EFFECT OF GREEN MICROSTRUCTURE ON THE DENSIFICATION AND MICROSTRUCTURAL EVOLUTION OF ALUMINA

By

TSUNG-SHOU YEH

A DISSERTATION PRESENTED TO THE GRADUATE SCHOOL OF
THE UNIVERSITY OF FLORIDA
IN PARTIAL FULFILLMENT OF THE REQUIREMENTS FOR
THE DEGREE OF DOCTOR OF PHILOSOPHY

UNIVERSITY OF FLORIDA

1989

ACKNOWLEDGEMENTS

I am indebted to Dr. M.D. Sacks, committee chairman, for his guidance and financial support during the course of this work. His patience in correcting this dissertation and his suggestions are especially appreciated. I would also like to thank Dr. R.T. DeHoff, Dr. D.O. Shah, Dr. J.H. Simmons, and Dr. E.D. Whitney, members of supervisory committee, for their useful suggestions.

I am also grateful to Dr. C.S. Khadilkar, Mr. H.W. Lee, Mr. D. Parker, Mr. O.E. Rojas, Mr. G.W. Scheiffele, and Mr. S.D. Vora for their help during the course of this study. Special thanks go to Dr. C. Khadilkar for allowing me to use the plotting program he developed. Thanks are also due to Mr. S.D. Vora, Dr. M. Dariel, and Mr. G.M. Johnson for proofreading my dissertation.

I would also like to express my sincere gratitude to my parents for their support and encouragement. I am most grateful to my wife Lu-Min for her understanding and constant support.

TABLE OF CONTENTS

page

ACKNOWLEDGEMENTS ii

ABSTRACT vi

I. GENERAL INTRODUCTION 1

II. GENERAL BACKGROUND 5

- Introduction 5
- Sintering Mechanism 5
- Sintering Research on Alumina 8
- Significance of This Study 15
- Suspension Processing 19
- Microstructural Evolution During Sintering 34
  - Grain Size Evolution During Sintering 35
  - Pore Size Evolution During Sintering. 41
  - Evolution of Pore-Solid Interfacial Area. 47
  - Evolution of Pore-Solid Interface Curvature 50
- Sintering Models 52

III. EXPERIMENTAL 59

- Powder Preparation and Characterization 59
- Suspension Preparation and Characterization 62
- Green Compact Formation and Characterization 66
- Sintering 68
- Sample Preparation for Ceramography 69
- Quantitative Stereology 70

IV. EFFECT OF PARTICLE PACKING 74

- Introduction 74
- Background 75
- Results and Discussion 87
  - Powder Characterization 87
  - Green Compact Characterization 101
  - Effect of Particle Packing on Sintering Kinetics 108

Effect of Temperature on Sintering Kinetics 129
Effect of Particle Packing on Microstructural Evolution 138
Comparison with Sintering Models 258

V. EFFECT OF PARTICLE SIZE DISTRIBUTION 273

Introduction 273
Background 273
Results and Discussion 283
Powder Characterization 283
Suspension Characterization 304
Green Compact Characterization 306
Densification Kinetics 312
Activation Energy 322
Volume Shrinkage 325
Effect of Particle Size Distribution on Microstructural Evolution 325
Effect of Particle Size on Sintering and Microstructural Evolution 400

VI. LOW TEMPERATURE SINTERING OF ALUMINA 410

Introduction 410
Results and Discussion 410

VII. SUMMARY AND SUGGESTIONS FOR FUTURE WORK 425

Summary 425
Suggestions for Future Work 429

APPENDIX A PROCEDURE FOR POWDER FRACTIONATION 434

APPENDIX B IMPREGNATION OF POROUS BODY FOR POLISHING 439

APPENDIX C DENSIFICATION DATA AND MICROSTRUCTURAL PROPERTIES FOR SCD, SCF, DPH, AND DPL SAMPLES 442

APPENDIX D DENSIFICATION DATA AND MICROSTRUCTURE PROPERTIES FOR NSD-30, ISD, AND BSD SAMPLES 448

REFERENCES 451

BIOGRAPHICAL SKETCH 464

Abstract of Dissertation Presented to the Graduate School of
the University of Florida in Partial Fulfillment of the
Requirements for the Degree of Doctor of Philosophy

EFFECT OF GREEN MICROSTRUCTURE ON THE DENSIFICATION AND MICROSTRUCTURAL EVOLUTION OF ALUMINA

By

Tsung-Shou Yeh

December 1989

Chairman: Dr. Michael D. Sacks
Major Department: Materials Science and Engineering

The effect of particle packing, particle size and particle size distribution on the densification behavior and microstructural evolution during sintering was investigated. High-purity, agglomerate-free alumina powders which had controlled particle size distributions were prepared by sedimentation classification. The effect of particle packing on sintering was studied using a powder with a very narrow particle size distribution. Green compacts with a wide range of packing characteristics were prepared using both suspension processing and dry pressing. Particle packing arrangements had significant effects on the densification kinetics and the path of microstructural evolution. In order to study the effect of particle size distribution, powders with constant median size and varying log-normal standard deviation were prepared. Powder compacts were prepared by slip casting concentrated, well-dispersed suspensions. Suspension rheology, green compact characteristics, densification and microstructural evolution were highly dependent upon the width of particle size distribution. Homogenous green bodies with high relative density and fine pore size were prepared by slip casting a fine-sized, agglomerate-free dispersion. Samples with nearly full density and fine grain size could be obtained at low sintering temperature.

CHAPTER I
GENERAL INTRODUCTION

Microstructure control of ceramic materials has become the subject of major interest in the field of high tech ceramics due to the fact that the useful mechanical, electrical, and optical properties of ceramic components are determined by the final microstructure of the sintered body. In order to obtain desired final properties, the understanding of the effects of green microstructure on densification kinetics and microstructural evolution during sintering is very important.

There are a variety of characteristics which determine the nature of the green microstructure, including (1) particle characteristics (i.e., specific surface area, particle shape, average particle size, particle size distribution), (2) pore characteristics (i.e., pore shape, average pore size, pore size distribution), and (3) particle packing characteristics (i.e., average packing density, local variations in packing density, presence of "defects" such as agglomerates and large pores). Previous experimental studies have generally been unsuccessful in isolating the effects of individual characteristics on sintering behavior; this is largely because of the inherent problem that most of the microstructural features listed above are interrelated. However, the difficulties are exacerbated by the fact that most powders used in experimental studies of sintering have highly non-ideal characteristics. For example, commercially-available powders invariably contain agglomerates which tend to have a dominant effect on the densification behavior and microstructural evolution, thereby masking the effects of other characteristics under investigation. In the present study, great effort has been made to prepare powders and powder compacts with model characteristics; therefore, the effects of particle packing, particle size and particle size distribution on sintering and microstructural evolution could be properly investigated.

The study was carried using model alumina powders which had high purity and which were processed to remove hard agglomerates and to produce controlled particle size distributions. Detailed powder characterizations were carried out in order to obtain complete information on powder characteristics. Quantitative stereology was used to obtain a complete characterization of the microstructures in each stage of sintering. Therefore, the evolution path of microstructural features can be clearly identified. This microstructural information can be used to evaluate the effect of processing parameters and green microstructures on sintering and microstructural evolution during sintering.

In Chapter II, general background on suspension processing, sintering and microstructural evolution is reviewed. The significance of this study is also presented. Detailed background on the effects of particle packing and particle size distribution on green microstructures and sintering will be given in each corresponding chapter. In Chapter III, detailed procedures for sample preparation, sintering and microstructural characterization are presented. General principles of quantitative stereology are also discussed.

The effect of particle packing on sintering and microstructural evolution is the focus of Chapter IV. Studies on particle packing effects have been performed using powder with a narrow particle size distribution; therefore, complications from the effect of particle size distribution can be eliminated. Compacts with various packing characteristics were prepared by slip casting and dry pressing. Detailed studies on the densification kinetics and microstructural evolution for the above samples are presented.

The effect of particle size distribution on powder processing and sintering is discussed in Chapter V. Powders with the same median size but varied width of the particle size distribution were produced. The effect of the width of size distribution on particle packing and suspension viscosity is discussed. Sintering studies were carried out on compacts with homogeneous green microstructures which were prepared by slip casting well-dispersed suspensions. Suspensions were prepared with high solids loading to prevent segregation of particles with varying size during consolidation. Detailed discussion on the effect of particle size distribution on densification kinetics and microstructural evolution is presented.

Decreasing particle size and increasing surface area are the general approaches used to increase the sinterability of ceramic powders. However, due to the presence of hard agglomerates in the fine powders, the benefit of decreasing size in sinterability is often diminished. In this study, an attempt has been made to prepare an agglomerate-free fine-sized powders. The effect of this extremely fine-sized powder on suspension processing and sintering is discussed in

Chapter VI. Comparison between the densification behavior of this sample and that of an α-Al_2O_3-seeded boehmite sample [Mes86] is also presented.

Finally, general summary and conclusions are presented in Chapter VII. Suggestions for future work are also given.

CHAPTER II
BACKGROUND

Introduction

A general review on suspension processing, sintering and microstructural evolution will be given in this chapter. Detailed reviews regarding to a specific subject (i.e., effect of particle packing on sintering, effect of particle size distribution on suspension processing and sintering, and suspension processing and sintering of ultra-fine size powder) will be given in each corresponding chapter.

Initially, sintering mechanisms will be discussed. Important aspects of the sintering of alumina will be reviewed. Then, the salient features of this study which make it significant and different from previously published work will be presented. General principles on suspension processing will be reviewed. The theoretical background and previous research work on microstructural evolution during sintering will be discussed. Finally, chosen sintering models which are important to this study will be reviewed.

Sintering Mechanism

Sintering processes have been used to integrate powders into strong and dense bodies since early human history; however, attempts toward the understanding of the physical fundamentals did not begin until the turn of the 20th century. In order to understand sintering processes, naturally, the first step should be to find out the driving forces of sintering. In 1905, Kepler first proposed that surface tension is the driving force for sintering when a liquid phase is present [Kep05]. In 1923, Smith proposed that surface tension is also the driving force for sintering samples without the presence of a liquid phase [Smi23]. A summary of the early work on sintering has been presented by Eitel, which included the pioneering work of Tammann and Hedvall and the subsequent work of Hutting, Volmer, Weyl, etc. [Eit54]. They recognized that sintering could occur by diffusion processes and the mobility of the diffusion species controlled the reaction rate.

The development of the first quantitative sintering model by Frenkel in 1945 [Fre45] initiated an extensive and fruitful research on sintering carried out by Kuczynski, Mackenzie and Shuttleworth, Rhines, Herring, Kingery, Cutler, Coble, etc. The major objectives of these studies were to identify the mechanism of material transfer and to predict the rate of geometric changes such as neck growth or sample shrinkage during sintering.

When ceramic powder is consolidated into a compact, vast amounts of contacts between particles are formed. Large negative curvatures are associated with the surfaces around the contact area (or neck). Because of surface tension, the surface which has negative curvature is subjected to a lower pressure (relative to a flat surface). The pressure differences (δP) can be expressed by the Laplace equation:

$$\delta P = \gamma_s \left(\frac{1}{R_1} + \frac{1}{R_2} \right) \tag{2.1}$$

where R_1, R_2 are the principal radii of curvature of the surface around the neck region and γ_s is the specific surface tension. The radius of curvature is assigned a negative value if the associated curvature is negative. For crystalline materials (which is the major interest in this thesis), the vacancy concentration on the neck surface is higher than the bulk value because of the pressure difference. This excess concentration of vacancies (C) immediately beneath a surface with negative curvature can be given by the Kelvin equation:

$$C = \frac{C_0 \gamma_s V_0}{k T} \left(\frac{1}{R_1} + \frac{1}{R_2} \right) \tag{2.2}$$

where C_0 is the vacancy concentration associated with a flat surface (which is assumed equal to the bulk concentration), V_0 is the volume of a vacancy, k is the Boltzmann's constant, and T is the absolute temperature.

During sintering process, due to the higher vacancy concentration at the neck surfaces, vacancies diffuse toward the nearby grain boundaries or toward other surfaces which have positive curvature. On the other hand, material is transferred to the neck regions and the necks grow. During these processes, the strength of the compacts increase and the surface area of the compacts decrease.

Vacancy diffusion can cause the approach of the centers of the adjacent particles, (i.e., the density of the compact increases) if the operating diffusion mechanisms are grain boundary diffusion and/or lattice diffusion and the grain boundaries are acting as vacancy sinks. If the convex particle surfaces are acting as vacancy sinks, only surface rounding will occur and densification can not be obtained. In addition, evaporation and condensation processes and surface diffusion also contribute to surface rounding only, no densification can be obtained through these processes. Normally, evaporation-condensation processes are not significant for oxide materials.

Sintering Research on Alumina

Alumina has long been a model material for ceramic research because of its widespread applications, the availability of high-purity powders and the possibility of reaching theoretical density by a small addition of magnesia. Based on the sintering research carried out with alumina, the understanding of the sintering processes of ceramics and the development of qualitative and quantitative sintering theories can be established. Vast numbers of studies on the sintering of alumina have been published, which cover almost every aspect of sintering. Only some important subjects which are the major concern for developing and advancing sintering processes will be reviewed.

Additives

It is well known that additives have significant effect on sintering kinetics and final microstructure. Searching for effective additives to benefit the sintering of alumina was one of the major research activities in the alumina sintering studies. Early work on the effect of additive on the sintering and grain growth of alumina was primarily carried out by the automobile industry because of the need to optimize spark plug manufacturing processes [Aus50, Com52, Jef42, McD38, McD41, Rei31]. In those studies, the major purpose of adding additives was to decrease porosity, increase strength and obtain uniform grain size in the sintered body. The effect of magnesia in increasing the sintered density and the strength of the sintered body was pointed out [Com52].

The earliest comprehensive reports on the effect of additives on the sintering and grain growth of alumina were published by Smothers and Reynolds in 1954 [Smo54] and by Cahoon and Christensen in 1956 [Cah56]. In the study reported by Smothers and Reynolds, 1 wt% of the additives were added to a commercial alumina with >99% purity and ~2.5 μm particle size. Some samples were also prepared by co-precipitation and calcination of chloride mixtures. Dry pressing was used to form the compacts. More than 30 additives were investigated and grouped into three categories--increasing grain size, decreasing grain sizing, or no significant effect. No significant conclusion was presented.

Cahoon and Christensen also performed similar research with emphasis on the effect of additives on exaggerated grain growth [Cah56]. They pointed out that magnesia strongly inhibited exaggerated grain growth, even when only a small amount (0.023 wt%) was added. They also observed that deterioration of mechanical strength occurred when exaggerated grain growth started. They showed that alumina bodies with zero apparent porosity could be obtained through magnesia doping. However, they also reported retardation of sintering by the addition of magnesia.

The beneficial effect of magnesia on enhancing densification kinetics and producing fully dense alumina was demonstrated by Coble [Cob61, Cob62a]. He prepared dry-pressed compacts from 0.3 μm Linde A alumina with 0.25 wt% magnesia. Theoretical density was obtained for samples sintered at 1675°C for ~250 min. Compared to an undoped sample, higher densification rate was obtained for the MgO-doped sample, and no exaggerated grain growth was obtained even when prolonged sintering time was used (up to 10,000 min at 1675°C). The undoped samples also exhibited normal grain growth up to ~560 min at 1675°C. Beyond this time, exaggerated grain growth was observed.

Since the discovery of magnesia as a sintering aid to produce fully dense alumina, vast amounts of studies have been devoted to identify the responsible mechanism. It is generally accepted that magnesia prevents the occurrence of pore-grain boundary separation; therefore, pores can remain in contact with grain boundaries in the late stages of sintering. Complete removal of the pore phase is then possible. Otherwise, if pores are trapped inside the grains (i.e., away from vacancy sinks), the shrinkage rate will become extremely low due to the long diffusion distance [Ale57, Bur57]. Samples practically stop densifying.

However, there is still controversy regarding the dominant mechanism(s) by which MgO inhibits pore-grain boundary separation. Possible mechanisms are (1) solute additives which segregate at the grain boundary and reduce the grain boundary mobility (solute-drag mechanism) [Bur80, Cah62, Jor64, Tay74]; (2) additives which enhance the densification rate relative to grain growth rate by changing the defect structure (solid solution mechanism) [Ben85, Har79, Joh78]; (3) additives which increase the surface diffusion coefficient and consequently the pore mobility, and therefore allow pores to migrate with grain boundaries until they are eliminated [Bai85, Ban80, Heu79, Rod89].

Recently, it has been pointed out by Harmer et al. that the additive effect on the sintering and grain growth of alumina may strongly depend on the purity of the starting alumina powder [Ben85, Zha87].

Since the discovery of the beneficial effect of MgO on alumina sintering [Cah56, Cob61, Cob62a], a great number of studies were carried out to search for other additives which can have the same beneficial effect as MgO [Bag70, Kes65, Raj73, Ros73, War67]. However, no replacement for MgO has been found.

Atmosphere

The densification rate and the achievable final density can be significantly affected by the sintering atmospheres [Cob62b]. Even though atmosphere may also affect the path of microstructural evolution during sintering, little study has been performed.

Densification rate. Coble [Cob62b] carried out a study on the effect of atmosphere on the densification behavior of 0.25 wt% MgO-doped alumina and found that similar densification kinetics were obtained for samples sintered in hydrogen and oxygen atmospheres. However, for alumina compacts containing 1000 to 4000 ppm MnO, Keski and Cutler reported an increase in densification rate with decreasing oxygen partial pressure [Kes68]. A decreasing oxygen partial pressure increased oxygen vacancy concentration and therefore increased the oxygen diffusion rate. Since oxygen was proposed to be the slower moving ion, densification rate could be increased when the oxygen vacancy concentration was increased.

Raja Rao and Cutler also observed an enhanced densification rate with decreasing oxygen partial pressure for iron-oxide-doped alumina compacts [Raj73]. They proposed that Al interstitials were the rate determining diffusion species and their concentration was increased when the oxygen partial pressure was decreased. Hence, densification rate could be increased.

Limiting density. Coble [Co62b] investigated the effect of various atmospheres on the sintering of alumina compacts containing 0.25 wt% MgO and showed that theoretical density could be obtained if the sintering atmospheres were hydrogen, oxygen, or vacuum. However, theoretical density could not be obtained in air, nitrogen, helium, or argon atmospheres. Paek et al. [Pae88] studied the densification behavior of MgO(0.1 wt%)-doped alumina compacts in O_2 and N_2 atmospheres. They also obtained higher density for samples sintered at O_2 atmosphere. The difference in final density was attributed to the differences in the solubilities of the gases in alumina.

In the late stages of sintering, isolated pores are formed when the open pore channels are pinched off. Gases are trapped in the closed pores at the ambient pressure and are compressed as further densification proceeds. If the solubility of the gases in the alumina is low, densification stops when the internal gas pressure (P) counterbalances the driving force for densification (i.e., when $P = 2\gamma / R$, where γ is the surface tension and R is the effective radius of curvature of the pores). Hydrogen and oxygen have relatively higher solubility in alumina; therefore, fully dense alumina can be obtained if hydrogen or oxygen atmosphere is used.

Paek et al. [Pae88] also observed slightly higher density for samples which were initially sintered at O_2 atmosphere to ~99% relative density, then replaced with N_2 atmosphere. Decreasing the oxygen concentration in the atmosphere will increase the oxygen concentration gradient, which will enhance oxygen diffusion toward sample surface.

Powder Characteristics

Powder characteristics (particle size and particle size distribution, surface area, agglomeration, purity, etc.) have significant influence on sintering and microstructural evolution. Nowadays, it is well accepted that agglomerate-free high-purity powders with fine particle size and optimum particle size distribution are essential for achieving high densification rate and fine sintered microstructure. This knowledge is established through the extensive research on the powder processing and sintering of alumina in the past half century.

The Bayer process is the major and best-known process for producing commercial high-purity alumina. Normally, large agglomerated powders are obtained from the Bayer process. Ball milling is used to break up agglomerates into primary particles. Before 1950, the common characteristics of the high-purity alumina powders produced by the Bayer process (e.g., Alcoa A-10) were large particle size ($> 5\ \mu m$) and low surface area ($< 0.2\ m^2/g$). A high sintering temperature was needed to sinter these powders. Some authors referred to these alumina powders as "non-reactive powders" [Flo78].

Because surface energy is the driving force for sintering, a reasonable approach to decrease sintering temperature and enhance densification kinetics should be to decrease the particle size of starting powder (i.e., increase the specific surface area). Herring's scaling law also indicates that sintering time can be significantly decreased if fine size powder is used [Her50]. The typical example of the high surface area powder (or so called "reactive" powder) is the Linde A alumina (which is derived from aluminum salts) introduced in the late 1950s. This powder has around 15-20 m^2/g surface area. Because of the discovery of magnesia as a sintering aid, fully dense alumina bodies could be obtained; however, high sintering temperatures (> 1650°C) were still needed [Bru62, Cob61].

In the late sixties, high surface area "reactive" alumina powders by the Bayer process were also introduced into the market (e.g., XA-139 from Alcoa or RC-HP from Reynolds Aluminum Company). Typically, these powders had ~0.3-0.5 μm median particle size and ~5-10 m^2/g surface area. However, due to the lack of understanding of the effect of powder characteristics on powder processing and sintering, the advantage of these "reactive" powders were not fully utilized.

It took some time to realize that surface area is not the only criterion for determining the sinterability of a powder. Other powder and green compact characteristics (such as powder aggregation, particle packing arrangement, etc.) also need to be taken into account. Even though the Linde A alumina powders had high surface area and should be "reactive," the powders were highly aggregated, which significantly reduced the obtainable green density and sinterability.

In addition to the retardation in densification kinetics, agglomerates also result in green microstructure heterogeneities and consequently cause differential sintering, low sintered density and large residue defects. These will significantly deteriorate mechanical properties of sintered bodies. More detailed discussion on the effect of agglomerates, particle packing, particle size and particle size distribution will be presented later in this thesis.

Significance of This Study

High Purity

Impurities which are contained in the as-received powders or introduced during processing can form liquid phases at the sintering temperature. Liquid phases can enhance exaggerated grain growth, and frequently extremely large grains with an elongated lath-like shape are obtained. Besides, high grain boundary mobility associated with liquid phases also causes pores trapped within large grains and makes high sintered density impossible. The need for high-performance, high-reliability ceramic components has driven the ceramic industry to improve powder-producing technology and to produce high-purity ceramic powders. With the availability of high-purity ceramic powders in recent years, more and more experiments carried out with high-purity powders showed tremendous difference in sintering behavior, grain growth kinetics and microstructural evolution. In the studies reported by Bennison and Harmer [Ben83, Har84, Ben85], it was shown that even in alumina samples prepared from 99.98% pure powder, lath-like large grains were still observed and small amounts of glassy phase in the grain boundaries were found. In order to minimize the complication of impurities and perform a better controlled study, ultra-high-purity powders (>99.99%) were used in this study. Careful experimental procedure was followed to prevent contamination during powder processing.

Complete Removal of Hard Agglomerates

Hard agglomerates, or aggregates, (where a group of primary particles are bonded by solid bridges as a result of sintering, fusion or chemical reactions) are the natural products of most ceramic powder manufacturing processes which involve calcination or other high-temperature processes. Even though extensive milling processes are used to break up hard agglomerates, noticeable amounts still exist in most commercial powders.

Aggregates are detrimental to powder compaction and sintering and have been the focus of many studies [Rho81, Sac82, Dyn83, Dyn84, Sac88a]. The effect of aggregates on the compaction behavior of alumina powder was reported by Dynys and Halloran [Dyn83]. They concluded that dry-pressed compact densities decreased with the increasing weight percentage of aggregates. The presence of aggregates also tends to retard the compaction rate during the compaction process. Sacks et al. investigated the effect of aggregates on the density and pore characteristics of slip cast green bodies of zirconia [Sac88a]. They found that the removal of large aggregates from as-received zirconia powder significantly increased the green density (from 36% to 47% relative density) and eliminated the large pores introduced by large aggregates.

Rhodes [Rho81] investigated the effects of aggregate size on the sintering behavior of yttria-stabilized zirconia and showed that the sintered density decreased with increasing of agglomerate size. He also demonstrated that full density could be obtained at low sintering temperature by using high green density compacts which are consolidated from agglomerate-free fine powders. Dynys and Halloran [Dyn84] also showed that the sintering rate and sintered density of dry-pressed alumina compacts decreased when the aggregate content was increased. Due to the existence of aggregates, highly inhomogeneous microstructures with large inter-aggregate pores were observed.

The powders used in the above investigations contained large quantities of aggregates. However, only a small amount, 0.1 wt% or less [Joh72], of aggregates can be found in well-controlled powders. Actually, even a small weight percent of agglomerates can produce a large number of defects in a ceramic component as shown by Johnson et al. [Joh72]. For example, assume that a ceramic powder contains 0.001 wt% of aggregates which have 50% relative density and 20 μm diameter. There will be around three thousand aggregate in a one cubic centimeter 60% dense green compact. If one percent of those agglomerates become critical defects after the green compact is densified, there will be ~30 critical defects in the sintered body (~0.6 c.c after densified). For a commercial ceramic component relatively large in size, a tremendous amount of defects will exist.

Milling is a well-known method which has been frequently used to break up aggregates and to increase the powder sinterability. In a study conducted by Sacks and Pask [Sac82], the sintering behavior of constant green density (~ 53 to 55 % relative density) mullite compacts consolidated from powders subjected to different degrees of milling (from 0.5 to 12 h) was reported. The break up of aggregates was demonstrated by the rapid reduction of particle size during milling. Densification kinetics were also greatly enhanced. However, milling becomes inefficient when particle sizes approach the micron range. It is difficult to achieve sub-micron size even when extended milling time is used. The introduction of impurities into the powder from the grinding media or mill liner is another disadvantage of milling processes (especially when long milling times are used to obtain fine particle size). Therefore, a suspension classification technique was adapted to prepare aggregate-free powders used in this study.

Well-Controlled Particle Size Distribution

In the present study, extensive efforts have been directed to obtain powders with varied particle size distribution. A very narrow size distribution powder was prepared for a particle packing study. As a result, particle packing can be isolated as a predominant variable for investigation without the complication from particle size distribution. On the other hand, powders with same median size but with varying widths of size distribution (geometric standard deviation in the range 1.3 to 2.4) were produced. To the best of this author's knowledge, this study is the first well-controlled experiment to study the effect of particle size distribution on the sintering of ceramic powders.

Better-Controlled Green Microstructure

By choosing consolidation methods and controlling the consolidation conditions, green compacts having various particle packings and degrees of homogeneity were produced. The effect of green microstructures on sintering kinetics and microstructural evolution during sintering can be more unambiguously studied by using controlled structures. In addition, the slip cast compacts prepared from well-dispersed suspensions have the homogeneous green microstructure (i.e., uniform packing of monosized particles) assumed in the development of most sintering models. Hence, those samples can be used to evaluate the effectiveness of the existing sintering models.

Homogeneous microstructures were also obtained for the samples used in the study of the effect of particle size distribution on sintering; therefore, factors (such as microstructural heterogeneities) which may mask the effect of particle size distribution were avoided. Particle size distribution can thus be isolated as a dominant parameter for detailed investigation.

Detailed Quantitative Characterization of Microstructural Evolution

Quantitative characterization of microstructural evolution during sintering is critical in determining what actually occurs during sintering and can also help to guide the modeling of sintering processes. In this study, a large effort has been devoted to the preparation of good polished cross sections and to the detailed quantitative characterization of microstructure (e.g., grain size and grain size distribution, pore size and pore size distribution, pore-solid interfacial area and curvature, etc.). These quantitative data on microstructures are also used as tools to evaluate the effect of processing parameters and green microstructures on sintering.

Suspension Processing

A suspension consists of particles (e.g., alumina powder) suspended in a liquid medium (e.g., water). Suspension processing was extensively used in this study for powder classification and for making homogeneous green compacts for sintering studies. Because complete and detailed discussions on suspension processing can be readily obtained in the literature [Hie77, Hun81, Hun87, Kha88, Kru52, Par73, Sat84, Ver48], only a general review on suspension processing (such as suspension stability and rheological behavior which are important in this study) will be presented.

The particle sizes of the powders used in this study were mostly in the range 1 μm to 0.01 μm. Suspensions formed with particles in this size range are termed colloidal suspensions. In a colloidal suspension particles are randomly moving due to Brownian motion. The properties of the colloidal suspension are mainly determined by the interaction forces between particles.

Dispersion vs. Flocculation

There are two kinds of forces between particles in the suspensions--attractive forces and repulsive forces. The van der Waals forces (i.e., dipole-dipole interactions, dipole-induced dipoles interactions, or London dispersion interactions), are attractive forces between particles. (Attractive forces between particles can be also due to the existence of surface charge of opposite sign. However, this is not within the scope of this study.) In the absence of repulsive forces, particles can clump together to form particle clusters described as "flocs." (Particle clusters can also be formed by flocculating agents such as long chain polymers. These are not treated in this thesis.) The suspension is described as a flocculated suspension.

In a dilute flocculated suspension, because of the formation of large flocs, particles settle to the bottom in a short time. In a more concentrated flocculated suspension, particles may form three-dimensional gel-like networks, and the settling of particles cannot occur. In the flocculated suspension, particles of various sizes or different compositions are randomly held together; therefore, size or component segregation can be prevented because large particles or high density components can not freely move. Controlled flocculation is frequently used in the storage of suspensions to prevent particle size segregation and the formation of dense sediment (which is difficult to redisperse). Normally, flocculated suspensions show higher viscosity, and the compacts prepared from flocculated suspensions also have lower green density.

If strong repulsive forces between particles can be established, particles can remain well separated in the suspension (unless they settle to the bottom due to gravity). This suspension is described as "dispersed" suspension. The benefits of a dispersed suspension are as follows:

1. At a constant solids loading, the viscosity of a dispersed suspension is lower.
2. Dispersed suspensions can be prepared with high solids loading. This offers several advantages during ceramic processing: (a) high throughput, (b) less amount of solvent (lower cost), (c) less solvent removal during drying processes (shorter drying period and less drying shrinkage).
3. Homogeneous and high density green compacts can be prepared from dispersed suspensions. (Subsequently, as will be demonstrated in this thesis, higher densification kinetics, lower sintering shrinkage, and better sintered microstructure can be obtained.)

Several mechanisms, such as steric stabilization and electrostatic stabilization, are available for establishing strong repulsive forces to produce a dispersed suspension. Because polymer is not used in this study, steric stabilization will not be discussed. A general review on the electrostatic stabilization is given below.

Mechanisms of Surface Charge Development

In order to overcome van der Waals attractive forces and to obtain a dispersed suspension, a high charge density on the surface of the suspending particles is needed for developing strong electrostatic repulsive forces. There are four major mechanisms through which charge can be developed at the solid/liquid interface [Hun87]:

1. Adsorption of ionized surfactants/electrolytes from the solution. For example, in a alumina suspension containing sodium citrate, the citrate ions can selectively adsorb on the alumina particle surface to establish a surface with a net negative charge.
2. Non-stoichiometric dissociation/adsorption at the surface of an ionic solid. A typical example is the silver iodide particle in water. The sign and magnitude of the surface charge depends on the concentrations of I^-/Ag^+ ions at the solid surface.
3. Isomorphic substitution. The clay/water system is a typical example.
4. Adsorption/dissociation of hydroxyl and hydrogen ions. This mechanism is the major charge determination mechanism for most oxide materials and is also the mechanism of importance in the current study (i.e., for the alumina/water system).

Depending on the processing and heat treatment history, the surface of alumina is hydroxylated to various extent. The surface of an alumina particle in an aqueous suspension can develop positive or negative charge by the following reactions:

$$-AlOH_{(surface)} + H^{+}_{(aqueous)} \Leftrightarrow AlOH_2{}^{+}_{(surface)}$$
$$-AlOH_{(surface)} + OH^{-}_{(aqueous)} \Leftrightarrow AlO^{-}_{(surface)} + H_2O$$

The H^+ and OH^- ions are called the potential determining ions. By changing the pH value (i.e., H^+/OH^- concentrations) of the suspension, the sign and magnitude of the surface charge can be changed. The pH value at which the surface charge is zero is defined as the point of zero charge (PZC).

Electrical Double Layer and the Repulsive Force Between Particles

In order to obtain electroneutrality, the net charge developed on the surface of the particles in a suspension must be balanced by an equal charge of opposite sign produced by counter ions in the solution. Some counter ions may physically adsorb on the particle surface due to the electrostatic attractive force (Stern layer). The other counter ions form a diffuse layer outside the Stern layer. The combination of the charged particle surface and the surrounding counter ions in the solution is called an electrical double layer.

When two particles approach each other (due to Brownian motion or an applied shear field), the electrical double layer starts to overlap. This will produce a repulsive force because of (1) the increase in the osmotic pressure due to the increase of the ions concentration between two particles, or (2) the increase of free energy due to the electrostatic force [Lyk68]. For two flat plates separated by distance d, the repulsion energy per unit area, V_R, can be approximated by the following equation:

$$V_{R(plate)} = \frac{64 n_0 kT}{\kappa} \left[\frac{\exp(Ze\psi_0/2kT) - 1}{\exp(Ze\psi_0/2kT) + 1} \right]^2 \exp(-\kappa d) \qquad (2.3)$$

where n_0 is the bulk ion concentration (number of ions/volume), k is the Boltzmann constant, T is the absolute temperature, Z is the valence of ions in a symmetrical electrolyte, e is the elementary charge, ψ_0 is the potential at the outer Helmhotz plane (Stern layer) which is used to represent the surface potential, κ is the Debye-Huckel parameter (i.e., the inverse of the "thickness" of the diffuse layer in the electrical double layer) which is given by:

$$\kappa^2 = \frac{e^2 \Sigma (n_{io} Z_i^2)}{\epsilon_r \epsilon_0 k T} \qquad (2.4)$$

where n_{io} is the bulk concentration of ions of type i, Z_i is the valence of ion i, ϵ_r is the relative dielectric constant, and ϵ_0 is the permittivity of vacuum.

In the case of interaction between two spherical particles with large values of κa (i.e., particle radius (a) is relatively large compared to the thickness of the diffuse layer), the total repulsive energy can be approximated by the following equation:

$$V_{R(sphere)} = \frac{64 \pi a n_0 kT}{\kappa^2} \left[\frac{\exp(Ze\ \psi_0/2kT) - 1}{\exp(Ze\ \psi_0/2kT) + 1} \right]^2 \exp(-\kappa d) \qquad (2.5)$$

From the above equations, it is clear that the major parameters which determine the repulsive force as a function of interparticle separation distance are the ionic strength (i.e., valence of ions and ion concentration), surface potential, ψ_0, and the size of the particle.

In a suspension with constant ionic strength, the repulsive force is mainly determined by the surface potential of the particles. However, the surface potential is not readily available. Therefore, in practical applications, a near surface potential (called the zeta potential) is used to monitor the magnitude of electrostatic repulsive forces. The zeta potential can be obtained by measuring the electrophoretic mobility in a microelectrophoresis apparatus, as will be described in the experimental section.

As mentioned before, the surface charge, and therefore the zeta potential, of oxide particles in a suspension can be adjusted by controlling the pH value of the suspension. Figure 2.1A shows a plot of zeta potential vs. pH for a high purity alumina powder [Sac88a]. The zeta potential is zero at pH $\approx$ 9 which is called the isoelectric point (IEP). For pH larger than IEP, the alumina surface is negatively charged and the zeta potential is also negative. For pH smaller than IEP, a positive charge is developed and a positive zeta potential is obtained. The magnitude of the zeta potential increases when the pH is farther away from the IEP.

The plot of zeta potential in Figure 2.1A shows a decrease in zeta potential in the low (< 3.8) or high (> 12) pH ranges. In order to reach low or high pH, a large amount of acid or base needs to be used (Figure 2.1B [Sac88a]) due to the high solids loading in the concentrated suspensions. Because the acid (or base) is an electrolyte which contributes ions to the solution, the ionic strength is significantly increased and the electrical double layer is compressed; therefore, the

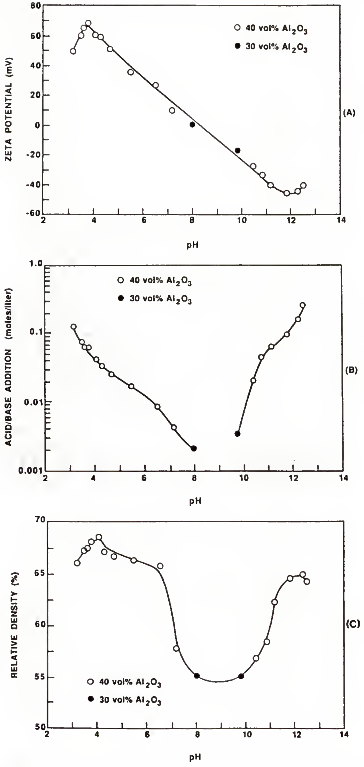

Figure 2.1 Plots of (A) zeta potential vs. pH, (B) acid or base concentration vs. pH, and (C) relative density of slip cast samples vs. pH of alumina suspensions (after M.D. Sacks, H.W. Lee, and O.E. Rojas [Sac88a].)

magnitude of the zeta potential is decreased. Even though the absolute values of the zeta potential in the low or high pH ranges are still pretty high, the repulsive forces decrease due to the significant increase of ionic strength. From the above discussion, it is clear that there is an optimal pH range (pH ≈ 4) for the processing of alumina suspensions with high solids loading.

The good dispersion of the high solids loading suspensions at pH ≈ 4 was also demonstrated by the high green density (~68% relative density) of the slip cast bodies (Figure 2.1C [Sac88a]). The flocculated suspension at pH ≈ 9 showed a much lower slip cast density (~55%) due to the absence of repulsive forces (Figure 2.1C).

Total Interaction Energy (DLVO Theory)

Normally, a well-dispersed suspension can be achieved at high zeta potential (i.e., high electrostatic repulsive force). However, due to the existence of van der Waals attractive forces, a summation of the repulsive forces and the attractive forces can give a more accurate indication of the stability of suspension. Based on DLVO (Derjaguin-Landau-Verwey-Overbeek) theory [Hun87, Ove52], the total interaction energy (V_T) is given by the sum of van der Waals forces (V_A) and the electrostatic interaction between electrical double layers (V_R):

$$V_T = V_R + V_A \tag{2.6}$$

where $V_A = - A / (12 \pi d^2)$ for the two flat plates configuration and $V_A = - A a / (12 d)$ for the two spheres case. (The negative sign represents an attractive force, A is the Hamaker constant, and a and d have been defined previously.) V_R was defined for the interactions between flat plates and between spheres in equations 2.3 and 2.5, respectively.

The repulsive forces vary as an inverse exponential function of the separation distance (equations 2.3 and 2.5) and the attractive forces vary as an inverse power of the separation distance. At short or long distances, the van der Waals attractive forces dominate. At the intermediate distances, the electrostatic repulsive forces dominate. In the case of moderate electrostatic repulsive forces and ionic strengths, a potential maximum can be obtained in the intermediate distance with two minima on each side. A typical schematic plot of the total interaction energy as a function of separation distance between two surfaces is shown in Figure 2.2 [Ove52]. The formation of the primary minimum is due to the strong Born repulsive forces which result from the overlap of electron clouds. The secondary minimum is due to the more rapid decay of the electrostatic repulsive forces while the van der Waals attraction is still effective.

If the height of the potential maximum, V_{max}, is much greater than the thermal energy of the particles (i.e., $V_{max} >> k\ T$), the potential barrier can prevent particles from permanent attachment when they encounter due to Brownian motion. The suspensions have good stability against flocculation. It was pointed out by Overbeek that potential barrier of the order of 5 to 15 kT is sufficient to maintain long-term stability [Ove82].

On the other hand, low zeta potential (i.e., low repulsive forces) or high ionic strength (i.e., compressed electrical double layer) can result in a monotonic decrease of total interaction energy with decreasing separation distance (i.e., no energy barrier). Flocculated

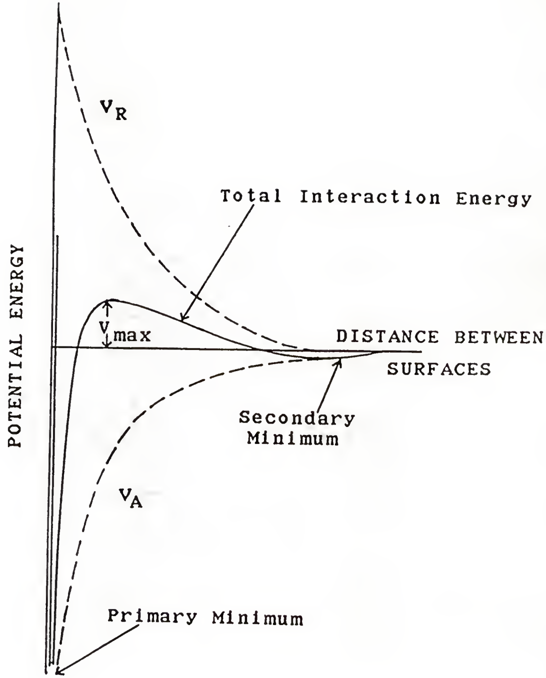

Figure 2.2 Schematic plots of total interaction energy vs. separation distance between two surfaces, based on DLVO theory.

suspensions will be obtained. It should be noted that weak flocculation can also be obtained by controlling suspension processing parameters (such as ionic strength) to make the secondary minimum larger than the thermal energy of particles. Suspensions flocculated at the secondary minimum can be easily redispersed (e.g., by dilution to decrease the ionic strength).

Suspension Rheology

Several methods (such as studying sedimentation behavior, measuring particle (or floc) size, etc.) can be used to characterize the state of dispersion of a suspension. The most useful and most frequently used method to characterize the suspension is rheological measurement. The rheological characteristics of a suspension can provide information about its interparticle forces, physical structure, and stability. Viscosity, which can be obtained in the rheological characterization, is a property that indicates the resistance to flow. Normally, the rheological behavior of a system is described in terms of the relation between shear stress (i.e., the tangential force applied per unit area) and shear rate (normally in reciprocal time units). The viscosity is defined as :

$$\text{viscosity} = \frac{\text{shear stress}}{\text{shear rate}} \tag{2.7}$$

Normally, four different types of flow behavior can be observed in various suspensions. Newtonian flow behavior is characterized by a linear relation between shear stress and shear rates and the viscosity is independent of the shear rate over a wide range of shear rates.

Pseudoplastic flow behavior shows a decrease of slope in the shear stress vs. shear rate flow curve and therefore a decrease of viscosity with increasing shear rate. This behavior is normally called shear thinning. Sometimes, shear thinning suspensions show time-dependent flow behavior and this behavior is called thixotropy. Normally, this is due to the breakdown of structures (such as floc structures in a flocculated suspension) under the applied shear stress. Thixotropy can be detected by the formation of a hysteresis loop between the shear stress vs. shear rate flow curves when the shear rates are increased from zero to a maximum value and then decreased to zero. The increase of the slopes of shear stress vs. shear rate flow curve (i.e., viscosity) with increasing shear rate is called dilatant or shear thickening. Bingham plastic flow behavior exhibits a yield stress which must be exceeded before the flow begins. Once the flow starts, the system shows linear relationship between shear stress and shear rate. The slope of the straight line portion in the shear stress vs. shear rate flow curve of Bingham systems is called the plastic viscosity. Often, pseudoplastic or dilatant types of flow behavior may be obtained after the yield stress is exceeded.

Well-dispersed suspensions. When the solids loading is low, well-dispersed suspensions normally show Newtonian flow behavior. When the solids loading is increased, pseudoplastic flow behavior may be obtained. Some typical reasons which can contribute to the pseudoplastic behavior are (1) the particles are anisotropic in shape, (2) electroviscous effects, and (3) Brownian motion. When the particles have fine size and high surface charge and the solution ionic strength is low, the electroviscous and Brownian motion effects can be very significant. More complete discussion on electroviscous effects will be given in chapter VI. When the solids loading is very high (50 vol% and above) and the repulsive forces between particles are strong, well-dispersed suspensions tend to show dilatant flow behavior.

Flocculated suspensions. At low solids loading, flocculated suspensions may show Newtonian flow behavior if the flocs remain as individual flow units without extensive interaction. However, the viscosity of a flocculated suspension will be higher compared to a well-dispersed suspension with the same solids loading. This is because some of the suspension liquid medium is trapped within the intra-floc voids and is not available for flow. The effective solids loading is increased.

When the solids loading is increased, the interactions between flocs become significant. When a shear force is applied, flocs and floc networks tend to break down and liquid trapped in the intra-floc voids is released; pseudoplastic flow behavior is obtained. If the flow units break down to the primary particles at the high shear rate, the viscosity of a flocculated suspension can approach the viscosity of a well-dispersed suspension with the same solids loading.

When even higher solids loading is used, a three-dimensional particle network will be formed throughout the whole body, and a yield stress is observed in the rheological flow curve.

Sedimentation Classification

A particle which is moving in a fluid experiences a resistance which depends on particle geometry (size and shape), fluid characteristics (density, viscosity), and particle velocity. If a particle is allowed to accelerate from rest under gravity, the drag force will continue to increase as the particle velocity increases, until eventually the drag force becomes equal to the gravitational force. At this point, the net force on the particle becomes zero and its velocity becomes constant. This constant velocity is known as the terminal velocity of the particle. According to Stokes' law, the terminal velocity is given by the following equation :

$$V_t = \frac{(D_s - D_f) g}{18 \eta} d_{st}^2 \tag{2.8}$$

where D_s is density of the solid, D_f is the density of the fluid, g is gravity, η is the viscosity of the fluid, and d_{st} is called the Stokes diameter which is the free-fall diameter under stokesian conditions (i.e., low Reynolds' number).

From Stokes' law, it is clear that larger particles have higher terminal velocities. Therefore, by choosing appropriate settling times and distances in a sedimentation process, larger particles can be separated from finer particles. By repeating the sedimentation procedure, a powder with a specific particle size distribution can be obtained. However, Stokes' law can not be strictly applied in sedimentation classification. Several factors can affect the accuracy of the Stokes' law such as:

1. Brownian motion. Brownian motion can significantly affect the motion of submicron particles in an aqueous suspension.
2. Hindered settling. In a concentrated suspension, the motion of particles is affected by adjacent particles. Hindered settling can be minimized by using dilute suspensions (2 vol% solids loading or less).

3. Container effect. The flow pattern around a particle will be affected if the particle is adjacent to the wall of the container. A larger container can minimize this problem. In addition, due to the constraint of the container, a back flow of fluid is produced to compensate for the motion of the particles and the fluid which is carried along with the particles. This back flow can bring large particles from the bottom to the top.
4. Suspension viscosity. The existence of the particles can change the effective viscosity of the suspending fluid.

In addition, ambient disturbances (such as vibration, temperature fluctuation, etc.) in the laboratory can also affect the applicability of Stokes' law. Normally, the settling time and distance needed for a specific powder classification need to be modified according to the result obtained.

Microstructural Evolution During Sintering

The path of microstructural evolution can be simply characterized by qualitative description of the existing geometric features at each stage of sintering. However, the extent of each geometric feature can be precisely quantified (such as grain size, surface area, etc.) using quantitative stereology. Accurate description and comparison of the path of microstructural evolution can be obtained. The evolution of a geometric feature can be presented as a function of sintering time, sintered densities, or even as a function of other geometric features. The effect of green microstructure on sintering can be easily examined by comparing the paths of microstructural evolution.

General background on the evolution of important microstructural features (such as grain size, pore size, interfacial area, etc.) during sintering will be reviewed below. The effect of particle packing and particle size distribution on microstructural evolution during sintering will be discussed in other chapters.

Grain Size Evolution During Sintering

Most of the research work on the grain size evolution during sintering can be summarized in two categories: (1) grain size change as a function of sintered density, (2) grain size change as a function of sintering time (i.e., grain growth kinetics).

Grain size vs. sintered density. Normally, sintering can be visualized as the combination effect of two competing processes: densification and coarsening. The densification process reduces the excess energy by reducing the amount of pore-solid interface, with increase in solid-solid interface. The grain size remains constant. The coarsening process reduces the excess energy by scaling up the microstructure (therefore, decreasing the amount of solid-pore and solid-solid interface). The grain size increases with increasing sintering time. It has been proposed that plots of grain size vs. sintered density (sometimes called grain size trajectories) can be used to evaluate the relative ratio of densification to coarsening and to measure the effect of processing parameters on sintering [Bro82, Har84, Wu84, Yan81]. Examples of grain size trajectories with different densification/coarsening ratios are shown in Figure 2.3. Trajectory A has higher densification/coarsening ratio; higher density can be reached with minimal grain growth. On the other hand, coarsening is significant

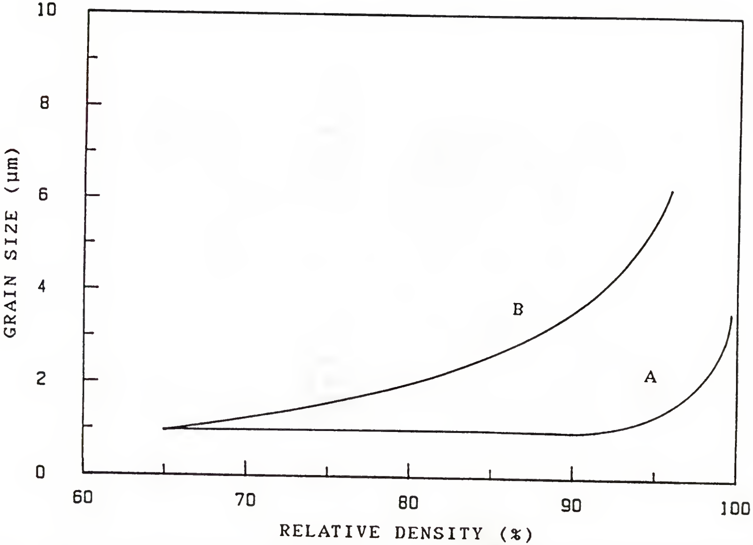

Figure 2.3 Schematic plots of grain size trajectories for (A) high densification/coarsening ratio and (B) low densification/coarsening ratio.

in trajectory B; larger grain size is obtained at a constant sintered density.

The grain size evolution following trajectory A is preferred when high density samples with fine microstructure are desired. Several approaches can be used to enhance densification/coarsening ratio as discussed below.

1. Increase sintering temperature. Assuming that the dominant mechanisms for densification and coarsening are lattice diffusion and surface diffusion, respectively, Brook et al. proposed that a higher densification/coarsening ratio can be obtained by using higher sintering temperatures [Bro82]. As lattice diffusion has a higher activation energy than surface diffusion, increasing the sintering temperature will favor lattice diffusion. Experimental results on alumina [Har79, Occ84] and zirconia [Wu84] supported their prediction. This approach can be useful as long as the densification mechanism of a system has higher activation energy than the coarsening mechanism. In order to predict the applicability of this approach to a system, the dominating mechanisms for densification and coarsening as well as the activation energies for each mechanism need to be known. However, complete information for most ceramic systems are still not available.
2. Use sintering aids. It has been shown that sintering aids can enhance the ratio of densification/coarsening rates. The most well-known example is the use of magnesia in alumina sintering. Several mechanisms have been proposed [Bro82] which can contribute to the increase of the densification/coarsening ratio. For

example, (a) additives which enhance lattice diffusion or grain boundary diffusion can raise densification kinetics; (b) additives which decrease surface diffusion or retard grain boundary migration can reduce coarsening rate. However, controversies still exist regarding the dominating mechanisms for the enhancement of densification over coarsening. Finding an effective sintering aid is still more or less a trial and error process.

3. Apply pressure during sintering. Hot pressing or hot isostatic pressing can be used to enhance densification kinetics and produce fine microstructure.
4. Control powder characteristics. Powder characteristics (such as purity, agglomeration, etc.) have important effect on grain size trajectory. For example, impurities can cause the formation of liquid phases at the grain boundaries which can promote exaggerated grain growth. Agglomerates can cause microstructural heterogeneities which consequently can hinder densification or promote localized grain growth. Grain size trajectories associated with a ratio of high coarsening/densification rates will be obtained.
5. Control green microstructure. Green microstructures (e.g., pore size and pore size distribution, packing density, etc.) have significant effect on the ratio of densification/coarsening rates. Detailed discussion will be presented in Chapter IV.

Grain size vs. sintering time (grain growth kinetics). It has been proposed that a parabolic grain growth law [Bro76, Bur52, Ree73]

$$G^2 - G_0{}^2 = K\ t \qquad (2.9)$$

can be used to describe the grain growth kinetics of pure single phase polycrystalline materials. G and G_0 are the average grain sizes at time t and t=0. K is a temperature-dependent growth-rate constant and t is the heat treatment time. The driving force for grain boundary migration is the curvature of the boundary which is proportional to the inverse of the average grain size. However, before reaching full density, powder compacts are porous and may contain more than 50 vol% of porosity in the early stages of sintering. Since pores are very effective in slowing down grain boundary migration, it is not surprising that porous compacts have lower grain growth rates. Therefore, the exponent in the grain growth kinetics equation should be larger than 2.

Greskovich and Lay [Gre71], studied grain growth in very porous alumina compacts and proposed that the grain growth mechanisms for very porous compacts involved, initially, the formation and growth of necks between contacting particles. Grain boundary developed between particles. The grain boundary became curved if the contacting particles were different in size. The grain boundary curvature created a driving force such that the boundary migrated through the smaller grains (i.e., small grains disappeared and large grains grew). By assuming that the migration of the grain boundary out of a filled neck occurs much faster than the growth of a neck (i.e., neck growth rate determines the grain growth rate), they proposed that the kinetic equation $G^n \propto t$ would still hold for grain growth in very porous compacts. The exponents are n = 3 and 4 when the growth rate determining mechanisms are volume diffusion and surface diffusion, respectively.

In high density samples, on the other hand, only isolated pores exist. Several attempts have been made to derive a grain growth equation under these circumstances [Bro76, Hil65, Nic66, Nic68]. Kinetic equations of the form

$$G^n - G_0^n = K\,t \tag{2.10}$$

were also obtained. In derivations of the above equation, several assumptions are normally adopted such as (1) pores are having spherical shape and locate at the intersection of two grains (i.e., grain faces), (2) pore size is proportional to grain size, or (3) pore number density at the grain boundary is proportional to $1/G^2$.

Normally, grain growth and densification occur simultaneously during sintering process. The grain growth kinetics should depend on the densification process, and vice versa. Attempts have been made to correlate density with grain growth kinetics. Assuming that the pore drag controls the grain boundary migration and surface diffusion controls the pore mobility, Howlett and Brook [How81] developed an equation

$$G^4 - Go^4 = \frac{K\,t}{(1 - D)^{4/3}} \tag{2.11}$$

to describe the relation between the density change and grain growth. D is the sintered density at time t and K is a constant determined by material parameters (such as surface diffusion coefficient, grain boundary energy, etc.) and sintering temperature. Harmer et al. [Ber86, Zha87] rearranged the above equation and obtained

$$\frac{dG}{dt} = \frac{K}{G^3\,(1 - D)^{4/3}} \tag{2.12}$$

where dG/dt is grain growth rate. They proposed that the slope in the plot of dG/dt vs. $1/(G^3(1-D)^{4/3})$ could be used to estimate the relative magnitude of surface diffusion coefficient. Berry and Harmer [Ber86] showed that the above equation gave a good fit to their densification and grain growth results for dry-pressed undoped and MgO-doped alumina compacts sintered at 1600°C in air. Zhao and Harmer [Zha87] sintered dry-pressed alumina compacts at 1620°C in nitrogen and found that the sintering results of undoped and FeO-doped samples gave a good fit to the above equation. However, they also reported that the sintering results of MgO-doped and MgO/FeO-codoped alumina samples did not fit the above equation. Instead, a simple cubic grain growth kinetics (i.e., $G^3 - Go^3 = Kt$) was followed.

In the present study, compacts with various green densities and microstructural homogeneities were prepared. These samples were used to evaluate the applicability of the above grain growth kinetic equations.

Pore Size Evolution During Sintering

Particle packing and particle size distribution have significant influence on pore geometry (e.g., coordination number, surface curvature, pore/grain size ratio, etc.) which can strongly affect the path of pore size evolution. A variety of pore structures have been observed in ceramic bodies and can be generally classified as (1) uniformly-distributed fine pores, (2) fine pore clusters, (3) large pores, or (4) combinations of the above pore features [Ono76]. Uniformly-distributed fine pores (i.e., pore sizes mostly smaller than the grain sizes), which are usually observed in compacts having a uniform packing of the particles, can normally shrink in size and finally disappear during the sintering process. However, depending on the packing density of the sample, various average pore sizes can be produced which can significantly affect the shrinkage rate [Kim87, Zhe89].

Pore clusters are those pores that exist as a group surrounded by denser matrix. This pore structure is a result of green microstructure inhomogeneity where the packing density of a localized region is somewhat lower than the surrounding matrix. Agglomerates with low packing density [Ben73] or intergranular regions (Wan76) are some typical examples. In order to eliminate these porous regions, a large amount of vacancies have to be transported from the pores to grain boundaries through diffusion processes. However, grain boundaries near the pores cannot be the recipient of all these vacancies because high vacancy concentration will build up in these grain boundaries. This will result in a decrease or even elimination of vacancy concentration gradient which will essentially stop vacancy flow. Therefore, long range diffusion is needed to uniformly dissipate the excess vacancies. Furthermore, large shrinkages needed for eliminating porous regions tend to be restrained by the surrounding matrix which is more dense and requires less shrinkage. In order to produce uniform shrinkage throughout the entire body, long range diffusion is essential. Consequently, densification rate will be retarded due to the slow kinetics of long range diffusion. Pore clusters can also coalesce into large pores which is even worse as can be seen in the following discussion.

The existence of large pores (i.e., those pores that are at least several times larger in diameter than the grain size) is one of the major reasons for the retardation of sintering kinetics and degradation of final properties of the sintered body. Incomplete crushing of granules, under-filling in dry pressing, entrapped air in casting or extrusion, and coalescence of smaller pores during sintering are a few examples that can cause formation of large pores. All large pores are very difficult to remove by sintering processes. One reason is that long range diffusion is needed in order to dissipate the vast amount of vacancies associated with large pores. The detrimental effects of large pores on densification can also be understood from thermodynamic considerations first introduced by Kingery and Francois [Kin67]. They considered the direction of mass transport based on the relative value of the chemical potential. Relative to a flat surface, a pore surface with negative curvature has lower chemical potential. Therefore, there is a tendency for material transport toward the pore and this pore will shrink. On the other hand, material flux will be away from the pores if the pore surface shows a positive curvature; hence, the pore size will increase. Considering a pore located at the grain corner and surrounded by various number of grains, they showed that the sign (i.e., positive or negative) and magnitude of the curvature of the pore surface are determined by the number of surrounding grains and the dihedral angle. For a chosen material with constant dihedral angle, they also demonstrated that the curvature of the pore surface will change from negative to positive if the number of surrounding grains becomes larger than a critical value. For a small pore (the ratio of pore diameter vs. grain diameter is small), the curvature of the pore surface is always negative; therefore, the pore will shrink and disappear during sintering. When the ratio of pore diameter vs. grain diameter increases, the number of grains surrounding the pore will increase. When the pore size become larger than a critical value, the curvature of the pore surface will become positive, and the pore tends to grow during sintering. Based on above consideration, Lange [Lan84a, Lan84b] proposed that grain growth was beneficial for samples with large pores to achieve high sintered density. Grain growth in the high density regions during sintering helped to reduce pore/grain size ratio and pore coordination number, hence large pores which was thermodynamically stable before grain growth became unstable and shrinkable.

Zhao and Harmer [Zha88] incorporated large-sized pores (~ 5 μm) into fine-sized (~ 0.45 μm) alumina compacts and investigated the densification kinetics and microstructural evolution. They found that the large-sized pores persisted even after extensive grain growth which translated the large pores from thermodynamically stable to unstable. By introducing 10 vol % zirconia particles to inhibit grain growth of alumina matrix, higher sintered density was obtained. They concluded that it was more favorable to inhibit grain growth than to promote it even though grain growth was more favorable considering the thermodynamic stability of pores. They suggested that grain size had strong effect on the kinetics of pore removal.

Mechanisms of materials transport during sintering (which may be affected by sintering temperature, atmosphere, impurities, etc.) also have important effects on pore size evolution. Generally speaking, surface diffusion or evaporation/condensation processes tend to produce pore coarsening without densification. On the other hand, lattice diffusion or grain boundary diffusion where grain boundaries act as vacancy sinks can result in pore shrinkage.

Because the grain boundaries act as vacancy sinks in the densification process, the maintenance of pore-grain boundary attachment is one of the major requirements for continued pore shrinkage. If pores break away from grain boundaries, it is more difficult for pores entrapped within the grains to shrink. Moreover, intragranular pores can grow through the Oswald ripening mechanism (i.e., larger pores grow by consuming smaller pores without changing the total pore volume) which makes the average pore size increase [Mas80].

In order to prevent pore-grain boundary separation, either the pore mobility needs to be increased or the grain boundary mobility needs to be decreased. Either approach can be achieved by using adequate additives. For example, if additives segregate at the grain boundary, this will create a dragging force to slow down grain boundary migration. On the other hand, if surface diffusion is the dominate mechanism for pore mobility, then additives which can enhance surface diffusivity will increase the pore mobility. Yan et al. [Yan83] also proposed that compacts prepared from narrow size distribution powders can reach high sintered density before the occurrence of pore-grain boundary separation. For compacts prepared from broad particle size distribution powders, he proposed that pore-grain boundary separation will occur at low density (~90% relative density) and that densification will virtually stop. However, controversy still exists regarding to the effect of particle size distribution on sintering and this will be the focus of discussion in Chapter V.

It was also proposed that grain growth during sintering can lead to pore coarsening through pore coalescence, where several smaller pores dragged by the migrating grain boundaries encounter and combine into a larger pores [Kin67]. In addition, differential densification in localized regions or particle rearrangement in the early stages of sintering can also increase the average pore size [Exn73, Exn79, Lan85, Wei86]. For example, agglomerates which have high packing densities and finer intra-agglomerate pore sizes will densify faster in the early stages of sintering. Pore space between agglomerates tends to open up to accommodate the shrinkage within the agglomerates. This was clearly demonstrated by Weiser and De Jonghe [Wei86] in the sintering of two-dimensional arrays of spherical copper powders.

Because most of the above mechanisms can simultaneously occur in a sintering system, the path of pore size evolution will be determined by the combined effect of the operating mechanisms. Page et al. utilized small angle neutron scattering to study the pore evolution during the late stage sintering of alumina sintered by glow discharge [Pag88]. They found that sintering occurred primarily through a reduction in the number of pores present with only a small change in the average pore size and size distribution.

Whittemore et al. [Whi74, Whi78, Whi80] observed pore coarsening for various materials in the early stages of sintering. Mercury porosimetry was used in their studies to monitor the change of pore size. On the other hand, a decrease of pore size was also reported for alumina and magnesia compacts characterized by mercury porosimetry [Ike87, Jan89, Whi83, Zhe89]. Mercury porosimetry actually measures the size of pore channels which connect void space. It is difficult to obtain the actual pore size information from mercury porosimetry. In addition, the well-known "Ink Bottle" effects [Orr69, Roo67] also makes interpretation of mercury porosimetry results difficult.

In order to obtain clear information about the pore size and pore size distribution, quantitative stereological measurements on polished cross section need to be used. Because quantitative measurements are laborious and time consuming, very limited work has been done. Tuohig [Tuo72] derived mean pore intercept size from pore-solid interfacial area measurement for UO_2 compacts. He observed relatively constant pore intercept size in the intermediate stages of sintering (up to around 90-95% relative density) with an increase in pore intercept size at higher density. Relatively constant pore intercept size was also observed for the sintering of copper compacts (~56% green density) in hydrogen [DeH66].

Evolution of Pore-Solid Interfacial Area (or Surface Area)

During sintering, a powder compact tends to minimize its pore-solid interfacial area in order to achieve minimum free energy. By assuming that material transfer driven by minimizing surface area will also produce densification*, Rhines and DeHoff [DeH66, Rhi62] proposed that surface area and density are linearly related during the intermediate stages of sintering and can be formulated into the following equation:

$$\rho = m\, S_v + \rho_{th} \tag{2.12}$$

where ρ is the density, S_v is the pore-solid interfacial area per unit volume, ρ_{th} is the theoretical density, and the slope m relates to the coarseness of the pore network. They showed that the absolute value of m (m is negative) decreased when the particle size of powder was decreased. They also proposed that this linear evolution path represented a specific path of minimal surface area that a system would pass through as the densification proceeded. It was also shown by DeHoff et al. [DeH66] that the slope of equation 2.12 is linearly related to the average pore intercept size. A constant slope implied that the mean pore intercept size should be constant during the course of sintering.

---

* This assumption implies that the shrinkage-producing diffusion mechanisms (i.e., lattice or grain boundary diffusion in which pore-solid interfaces act as vacancy sources and grain boundaries act as vacancy sinks) dominate the sintering process.

Depending on the particle packing conditions, green powder compacts can have various specific surface areas (e.g., higher packing density compacts have higher surface area per unit volume). It was proposed by Rhines et al. [Rhi69] that compacted green bodies were "surface excess" compared to loose stacked samples and should show a faster decrease of surface area in the early stages of sintering. Paths of the surface area evolution of the compacted samples tend to move toward the linear curve established by loose stack sintering of the same powder. Tuohig studied the paths of surface area change of UO_2 samples during sintering [Tuo72]. He observed that surface area-density plots of samples dry-pressed at various pressures formed an envelope of curves which merged in the high density region.

Burke et al. [Bur80] proposed that the evolution of pore-solid interfacial area can also be used to examine the relative ratio of densification vs. coarsening during sintering. If the pore-solid interfacial area is plotted as a function of sintered density, the paths of the interfacial area change fall into two categories (Figure 2.4):

1. Coarsening. Coarsening is characterized as a reduction in interfacial area without increase in density. The interfacial area

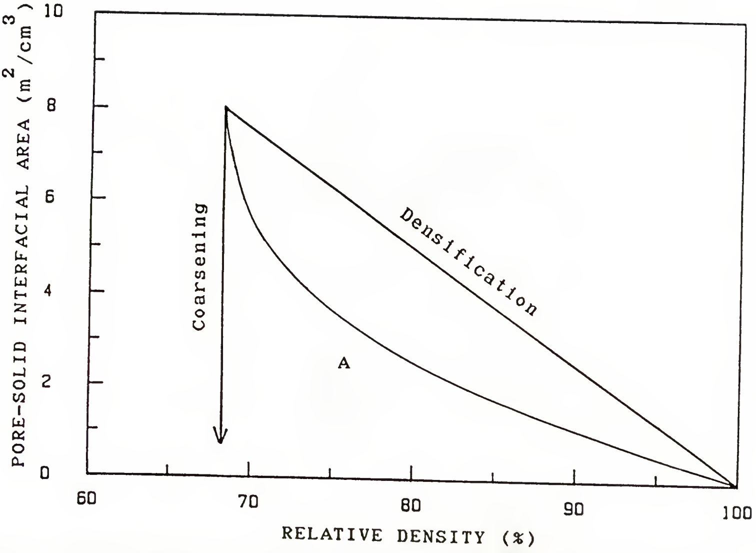

Figure 2.4 Schematic plots of trajectories of pore-solid interfacial area vs. relative density for densification process, coarsening process and the combination of both processes (curve A).

trajectory of such a process is a straight line parallel to the S_V axis.

2. Densification. These processes are represented by a straight line connecting the starting point and the final stage (i.e., zero interfacial area at 100% relative density) [DeH66, Rhi62].

The paths of interfacial area change of real compacts reflect the combined effect of both mechanisms and normally fall between these two extremes as described by curve A in Figure 2.4. The relative contribution of each mechanism can be judged from the shape of the curve. The more convex the trajectory towards the density axis, the larger is the contribution of coarsening.

Evolution of Pore-Solid Interface Curvature

The curvature at an infinitesimal surface element ds of a pore-solid interface (or an arbitrarily curved surface) can be defined by its two principal curvatures, K_1 and K_2. In the study of surfaces, the principal curvatures themselves may not be used; instead, the mean curvature or Gaussian curvature are frequently used. Mean curvature (H) is defined as:

$$H = (K_1 + K_2) / 2 \tag{2.13}$$

The integral of the mean curvature over the entire surface in an unit volume (S_V) is defined as integral mean curvature (M_V) [DeH77]:

$$M_V = \iint_{S_V} H \, ds \tag{2.14}$$

If edge segments (such as the intersections of grain boundaries with pore surfaces) are contained on the surface, the integral mean curvature (Me) along the lines in a unit volume (L) was shown to be [Cah67]

$$Me = \int_L (\chi / 2) \, dl \tag{2.15}$$

where χ is the dihedral angle at an infinitesimal line element dl of the edge. The general definition of the integral mean curvature (IMC) for a surface with edges is thus

$$M_V = \iint_{S_V} H \, ds + \int_L (\chi / 2) \, dl \tag{2.16}$$

It was proposed that the IMC of a sample can be estimated from the polished representative cross section [DeH67, DeH77]. This will be discussed in detail in chapter III.

Following the conventional notation, the curvature of a convex pore-solid interface (relative to the solid phase) is positive and a concave interface has a negative curvature. Depending on the microstructural characteristics of the sample, the IMC can be positive, zero, or negative. Considering a green body consolidated from equiaxed particles, the IMC has a large positive value since the pore-solid interface is mainly convex. During early stages of sintering, necks are formed at the particle contacts. Therefore, convex surfaces are consumed and saddle surfaces, which have one negative principal curvature, are produced. As a consequence, the magnitude of the IMC decreases. As the processes continue, the number of necks increases or the neck regions expand and the convex surfaces are further consumed. The IMC reaches zero when the amounts of positive and negative curvatures are equal.

When the sintering proceeds, surfaces with negative curvature keep increasing and surfaces having positive curvature continue to decrease, and the void space in the powder compact becomes smooth inter-connected pore channels. At some point, depending on the diameter/length ratio of the pore channel, the pore network starts to break up into segments or to close up and form isolated pores. Eventually, the void space will transform to only isolated pores, i.e., only negative curvature exists.

From the above discussion, it seems that the IMC will keep becoming more negative after it passes through the zero point. Actually, fine-sized pores in the compact are constantly eliminated during sintering. The pore volume gradually decreases. This process results in the decrease of the total negative curvature. The IMC shows a minimum at certain density ranges, depending on the ratio of the negative curvature producing/eliminating rates, and starts to decrease in absolute value when the density continues to increase. Finally, the system will reach zero IMC when full density is obtained. The above trend of IMC evolution was demonstrated by Tuohig for UO_2 compacts pressure sintered at 3,000 psi for 30 minutes at various temperatures [Tuo72]. In the same study, he also showed that finer microstructures obtained from finer size powder had more negative IMC values.

Sintering Models

Due to the extreme complexity of a sintering system, it is almost impossible to establish a theoretical model based on a real powder compact. The general approach of most model studies is to replace the complex internal geometry of a powder compact by a well-defined regular geometry with uniform grain and pore sizes. The most well-known example is the model introduced by Coble [Cob61, Cob63]. Coble's sintering model was based on an idealized geometric structure where grain structure was replaced by monosized Kelvin's tetrakaidecahedron. He further assumed that pore structure in the intermediate stage of sintering can be represented as cylindrical pores with the axes coincident with every grain edge. For the final stage of sintering, he assumed all corners of the polyhedral grains were occupied by spherical pores centered on the corner.

Using the above geometric model and assuming radial bulk diffusion from a circular vacancy source, Coble obtained an approximate equation

$$P_f - P_i = K (t_f - t_i) \qquad (2.17)$$

for both intermediate (continuous cylindrical pores) and final (isolated spherical pores) stages of sintering. P_i and P_f are the starting and final porosities, and t_i and t_f are the starting and final time. K is a constant containing temperature, material properties (e.g., surface tension, diffusion coefficient) and geometrical parameter (e.g., length of polyhedron edge). K had slightly different values for cylindrical and spherical pore configurations. According to the model, density should increase linearly with sintering time provided that the change in grain size is small. However, this linear relationship was not observed in the published sintering results. Because grain growth is commonly observed during the sintering processes, Coble adopted an empirical relation of grain size (G) vs. time (t)

$$G^3 = A\, t \qquad (2.18)$$

and introduced this equation into his model. He obtained a linear relationship between porosity and logarithm of time

$$P_f - P_i = K' \, (\ln(t_f) - \ln(t_i)) \qquad (2.19)$$

However, Coble did not clarify how the pore structure would evolve from the original geometry if the polyhedron grain grew in size.

Coble's model has found widespreading use since its introduction because most sintering data showed very good linear fit by plotting density as a function of logarithm of time. Based on this relationship, frequently, it was concluded that lattice diffusion was the dominating material transfer mechanism during sintering.

The observation that densification and grain growth occurred simultaneously during sintering provided the motivation to establish sintering models which can correlate densification with grain growth. One of the examples is the model developed by Rosolowski and Greskovich [Ros75]. Without specifying the geometric shape of grains, they assumed that all the pores could be described as circular cylinders centered on grain edges and developed a model which described the dependence of densification on grain growth during the intermediate stage of sintering. They proposed that the vacancy flux (F) which causes the shrinkage of pores can be described by

$$F = K_1 \, (l \, / \, R) + K_2 \, (l \, / \, R^2) \qquad (2.20)$$

where l is the length and R is the radius of the cylindrical pores, and K_1 and K_2 are constants which are related to the material properties (e.g., diffusion coefficients, surface tension, etc.) and sintering temperature. The first term and the second term of the above equation represent the contributions of volume diffusion and grain boundary diffusion, respectively. They further assumed (1) significant grain growth occurred during densification process which resulted in the growth of pores through coalescence, (2) the ratio of the average grain size to pore radius and pore length remained constant, (3) the ratio of the number of pores to the number of grains remained constant, and (4) loss of pore volume through elimination of small pores by diffusion was not significant. Finally, they obtained

$$(P - P_0)^* = K_1 C \int_{t_0}^{t} \left(\frac{1}{R} \right)_{av} \frac{1}{(G^3)_{av}} dt + K_2 C \int_{t_0}^{t} \left(\frac{1}{R^2} \right)_{av} \frac{1}{(G^3)_{av}} dt \qquad (2.21)$$

where P and P_0 represent the porosity of the sample at sintering time t and t_0, C is a constant, G is the grain size, and subscript "av" represents the average value. As noted by the authors, this equation is valid only when grain growth occurs (i.e., no densification can be obtained if grain growth does not occur).

Ikegami et al. [Ike78] also developed a model for densification with simultaneous grain growth. They assumed that grains and pores formed two interpenetrated homogeneous network structures. Every grain had pores as its neighbors and every grain boundary intersected with pores. All the mass diffused away from the grain boundary was transferred to the pore-solid interface and as a consequence the pore volume decreased. They also assumed that the width of grain size distribution remained constant throughout sintering. Based on the above assumptions, they derived an equation to describe the relation between relative density (D) and average grain size (G)

---

* In the original paper [Ros75], Ln(1-P) - Ln(1-Po) was reported which is a mistake in the integration.

$$\mathrm{Log}\left[\frac{D(1-D_0)}{D_0(1-D)}\right] = K_4 K_G \,\mathrm{Log}\left(\frac{G}{G_0}\right) \qquad (2.22)$$

where D_0 is the relative green density, G_0 is the initial particle size, K_G is a dimensionless parameter which depends on the width of the particle/grain size distribution, and

$$K_4 = S_V / ((1-D) S) \qquad (2.23)$$

where $S = S_V + S_G$, S_V is the pore-solid interfacial area and S_G is the grain boundary area. The above model also proposed that grain growth has to occur to densify a sample.

Instead of using simple and uniform geometry to replace the complex sintering system, Kuczyski proposed a statistical approach for the modelling of the intermediate and final stages of sintering [Kuc76, Kuc77]. He proposed that a compact in the intermediate stage of sintering could be best described as a body perforated by a specific length of cylindrical pores with various radii along their length. For the final stage, he assumed a body containing a specific number density of discrete spherical pores with various radii. He also assumed that the pores were distributed uniformly throughout the body of a compact and adopted the Zener's relation $G \propto (R / P)$ (where G is the average grain size, R is the pore radius, and P is the porosity) as the grain growth equation (i.e., grain growth is controlled by pore structure). He obtained equations of the same form for the intermediate and final stages

$$\left(\frac{P_0}{P} \right)^{n_i} = 1 + B_i t = \left(\frac{G}{G_0} \right)^{(n_i/m_i)} = \left(\frac{R}{R_0} \right)^{(n_i/(m_i-1))} \qquad (2.24)$$

where t is the sintering time, n, m and B are constants, and subscript i = 1 or 2 designates the intermediate or final stage, respectively. ($n_1 = 3\ X_1 / 2$, $n_2 = 2/3 + X_2$, $m_1 = (1 + X_1) / 2$, $m_2 = (2 + X_2) / 3$, where X_1 and X_2 are constants which can be obtained from the slopes of the plots of Ln G vs. Ln P*.) Kuczynski's model also proposed that grain growth and pore coarsening should occur simultaneously with the densification processes.

Johnson [Joh70] also proposed a generalized intermediate-stage sintering model without simplified assumption on microstructure geometry. He assumed that pore phase in the intermediate-stage sintering formed an interconnected three-dimensional network. Equilibrium angles existed at the intersections of grain boundaries and pore surfaces. Based on the above geometrical assumption, he assumed that the mass transfer mechanisms for the intermediate-stage sintering were the same as that of the initial-stage sintering. Therefore, he extended his initial-stage sintering model [Joh69] to the intermediate-stage sintering. He substituted the average neck radius by a fraction of grain size and the neck curvature by the average mean curvature (H_{av}) at the pore-solid interface. Finally, he obtained

---

* For the intermediate stage of sintering

$$\text{Ln } G \propto ((1 + X_1) / 2) \text{ Ln } P \ ;$$

for the final stage of sintering

$$\text{Ln } G \propto ((2 + X_1) / 3) \text{ Ln } P \ .$$

$$\frac{dV}{V\ dt} = K \cdot \frac{H_{av}}{(G/4)} (S_V\ D_v + b\ D_b\ L_V)$$

where V is the bulk volume of powder compact, t is the sintering time, K is a constant containing material parameters (e.g., surface tension) and temperature, S_V is the specific pore-solid interfacial area, L_V is the length of the grain boundary-pore intersection per unit volume, b is the width of grain boundary, D_v and D_b are the volume and grain boundary diffusion coefficients, respectively.

This model relates the densification kinetics to the instantaneous microstructural parameters which can be obtained through quantitative stereology. However, as pointed out by Exner and Petzow [Exn80], the chemical potential of vacancies (and hence the driving force for sintering) is determined by the local curvature at the pore-solid interface; therefore, using a curvature averaged over the entire pore-solid interface (which consists of convex and concave parts) may underestimates the active curvature.

CHAPTER III
EXPERIMENTAL

In this chapter, detailed procedures for powder preparation and characterization, suspension preparation and characterization, green compact consolidation and characterization, sintering, and microstructural characterization of sintered bodies will be presented. Quantitative stereology which was extensively used to follow the microstructural evolution will also be discussed.

Powder Preparation and Characterization

The powders used in this study were prepared by fractionation of commercially-available, high purity (>99.99%) alumina powders (Sumitomo AKP-15, AKP-30, and AKP-50).* Powders having narrow particle size distributions were prepared by a gravity-sedimentation process in which the coarsest and the finest particles were removed from the as-received powders. The sedimentation process was repeated many times not only to form the narrow size distribution, but also to ensure that "hard" agglomerates (which were in the coarsest fraction of the as-received material) were removed. Narrow size distribution powders with different median sizes (designated NSD-15 and NSD-30) were prepared from the as-received AKP-15 and AKP-30, respectively. Two broad size distribution powders which had the same median diameter as NSD-30, were prepared by blending agglomerate-free batches of varying median sizes which were obtained during the preparation of the narrow-sized powders. They were denoted as broad size distribution (BSD) and intermediate size distribution (ISD) according to their standard deviations. A very fine, agglomerate-free alumina powder (CSD) was also prepared by sedimentation of the as-received AKP-50. The detailed procedures for preparing powders with various particle size distributions are given in Appendix A.

---

* Sumitomo Chemical America, Inc., New York, NY.

Powder specific surface area was measured using nitrogen gas adsorption* (multipoint BET method). Powders were outgassed at 250°C for >10 h under flowing nitrogen to remove moisture or other volatile species. Surface area measurements were done at least two times for each sample. Crystalline phases of the alumina were determined by x-ray diffraction using a diffractometer** with a scanning rate of 6°/min or 1°/min.

The particle size and size distribution of the alumina powders were determined using the following methods: (1) gravitational x-ray sedimentation***, (2) centrifugal photo-sedimentation****, and (3) scanning electron microscopy (SEM)*****. For gravitational x-ray sedimentation measurement, approximately 1.5 vol% alumina dispersion at pH=4 was used. Ultrasonication* was also used to break down soft agglomerates. Samples for the centrifugal photo-sedimentation measurement were prepared in a similar fashion except much more dilute suspensions (below 0.1 wt% solids loading) were used.

---

* Model OS-7, Quantachrome Corp., Syosett, NY.

** Model APD-3720, Phillips Electronic Instrument Co., Mt. Vernon, NY.

*** Sedigraph Particle Size Analyzer, Micromeritics Instrument Corp., Norcross, GA.

**** Model CAPA-700, Horiba Instrument, Inc., Irvine, CA.

***** Model JSM-35CF, Japan Electron Optics Co., Ltd., Tokyo, Japan.

SEM photographs of alumina particles were used to obtain equivalent area diameter and equivalent perimeter diameter. A special sample preparation procedure was developed to produce well-separated particles which was required for unambiguous image analysis. First, a dilute dispersion (around 1 wt%) of alumina at pH=4 was prepared. After 30 min of ultrasonication, a drop of the alumina dispersion was introduced into 100 c.c. polyvinyl alcohol** (PVA) solution which had a concentration of 500 ppm. After mixing and 10 min ultrasonication, a drop of the alumina/PVA dispersion was placed on a glass slide which was cleaned with a chromic sulfuric acid solution. Excess dispersion was quickly removed to increase the drying rate. Samples were then dried in an oven at 60°C for 1 h. All samples were sputter coated with gold/palladium alloy to avoid charging of the sample during SEM observation. A minimum of twenty photographs were taken at random in order to obtain representative pictures. Projected area and perimeter of each particle were measured using a digitalizing tablet*** interfaced with a personal computer****. The equivalent area diameter (i.e., the diameter of a circle with same area) and equivalent perimeter diameter

---

* Model W-375, Heat Systems-Ultrasonics, Inc., Farmingdale, NY.

** Vinol 540, Air Products and Chemicals, Inc., Allentown, PA.

*** Model 9111A, Hewlett Packard, Palo Alto, CA.

**** Model HP-85, Hewlett Packard, Palo Alto, CA.

(i.e., the diameter of a circle with same perimeter) were calculated from the digitalized area and perimeter of each particle. More than 1000 measurements were carried out for each powder.

Suspension Preparation and Characterization

The dilute suspension of each powder obtained in the size classification process was concentrated in a water bath at 90°C under constant stirring. One fraction of the NSD-15 suspension was concentrated to around 15 Vol%, then the pH value was adjusted to ~9.0 to obtain a flocculated suspension for slip casting. The other fraction of the NSD-15 suspension was concentrated to around 45 Vol%, and was divided into two fractions. One fraction was saved for slip casting and the other fraction was filtered with a filtration apparatus* to remove water. The resultant powder cake was dried in an oven at 90°C for 24 h and then ground with a high-purity alumina mortar and pestle to obtain powder for dry pressing.

The NSD-30, ISD, BSD suspensions were first concentrated to 45 vol% for viscosity measurement. Subsequently the above suspensions were concentrated to around 51 vol% for slip casting. The CSD suspension was first concentrated to 38 vol% for viscosity measurement and then diluted to around 25 vol% for slip casting.

Electrophoresis

Electrophoresis was used to determine the suspension electrokinetic behavior. A concentrated suspension was centrifuged at

---

* Millipore Corp., Bedford, MA.

15000 rpm for 30 min to obtain essentially a particle free supernatant. A representative dilute suspension (approximately a few hundred ppm) was prepared by mixing the supernatant with a small amount of concentrated suspension. In some experiments, the ionic strength of the dilute suspension was controlled by adding potassium chloride.

The dilute suspensions were used to observe particles in a microelectrophoresis apparatus*. A thin-walled cylindrical cell was used. Constant current with adjustable voltage was applied through two electrodes which were inserted at the two ends of the cell. The voltage difference across the central cylindrical thin-walled tube was monitored through two other electrodes which were located right at the two ends of the cylindrical portion. The field strength in the central cylindrical tube was calculated from the measured voltage and the cell length (i.e., the effective distance between the two electrodes which were used for voltage measurement). The cell length was calibrated from the cell cross-sectional area and the observed voltage difference while the cell was filled with a standard solution (1×10^{-2}M KCl) and a known DC current was applied.

A He-Ne Laser source (3 mW) was used to illuminate particles. Particle velocities were measured at the top stationary level. The velocity was calculated by measuring the time required for particles to move 28 μm, i.e., the distance between lines of a grid in the microscope. The field polarity was reversed after each measurement. For each sample, a minimum of 80 individual measurements were taken (at several field strengths) to obtain an average electrophoretic mobility (electrophoretic mobility (μ) = velocity/field strength).

---

* Mark II, Rank Brothers, Cambridge, England.

The methods used to convert the electrophoretic mobility to zeta potential depend on the dimensionless parameter, κa, where κ is the Debye Huckel parameter and a is the particle radius. For large values of κa (e.g., $\kappa a > 200$), the Helmholtz-smoluchowski's equation [Ove52] was used :

$$\text{Zeta potential} = \frac{\mu\ \eta}{\epsilon_0\ \epsilon_r} \tag{3.1}$$

where η is the viscosity of the suspending media (D.I. water was used in this study), ϵ_0 is the permittivity of vacuum, and ϵ_r is the relative dielectric constant of the suspending liquid. For moderate values of κa (e.g., $0.1 < \kappa a < 50$) and high zeta potential, which was the case in the CSD powder, a graphical solution published by Wiersema et al. [Wie66] was used.

Rheological Measurement

Suspension rheological characteristics, shear stress vs. shear rate flow behaviors, were determined with a concentric cylinder viscometer*. All measurements were carried out with the same sensor system (i.e., ZB-30, inner cylinder O.D. is 29.36 mm, outer cylinder I.D. is 30 mm, gap size is 0.32 mm). Approximately 2 ml of suspension at pH ≈ 4.0 was used. The shear rate was increased from 0 to maximum in two minutes (up curve) and immediately decreased from the maximum to 0 in another two minutes (back curve). Plots of shear stress vs. shear rate were obtained at three maximum shear rate settings (i.e., 10, 100, and 1000 1/s) for each sample. The viscosities at each shear rate were determined using the relationship :

---

* Model RV-100/CV-100, Haake Inc., Saddle Brook, NJ.

$$\text{viscosity} = \text{shear stress} / \text{shear rate} \qquad (3.2)$$

It has been shown that the suspension viscosity is very sensitive to the solids loading when the volume fraction of solids is high (e.g., > 40 vol% solids loading) [Kha88, Kri72]. In order to meaningfully compare the rheological behavior of suspensions prepared from powders with various particle size distributions, extreme precaution was taken to ensure that each suspensions was prepared with the same solids loading, i.e., 45 ± 0.1 vol%. The solids loading of each suspension was accurately measured using the following procedure:

1. In a clean aluminum pan of known dry weight (W1), approximately 2 grams of suspension was poured. The total weight (W2) was taken immediately in order to minimize water evaporation.
2. The pan was heated on a hot plate and after complete removal of water, the total weight (W3) was taken.
3. Solids loading was calculated by the formula :

$$\text{Solids loading} = \frac{(W3 - W1) / \rho_{th}}{[(W3 - W1) / \rho_{th}] + (W2 - W3)/D_w} \qquad (3.3)$$

where D_w is the density of water at the measuring temperature and ρ_{th} is the theoretical density of alumina (3.98 g/cm^3, obtained by helium pycnometer for the as-received powders, was used in this study).

4. A minimum of three measurements were taken. Results showed ± 0.1 vol% agreement.

Each suspension was subjected to 2 h ultrasonication before the rheological measurement to ensure good dispersion. The viscosity of the suspension of the CSD powder was measured at 38 vol% solids loading. The solids loading was determined using the procedure described above.

Green Compact Formation and Characterization

Green compacts were formed using two methods--slip casting and dry pressing. Before slip casting, concentrated suspensions were ultrasonicated for two hours and aged on a rotating mixer for more than 24 hours. The pH value of the suspensions were checked just before slip casting. During slip casting, approximately 0.5 to 1.5 cm^3 (depending on the solids loading) of suspensions were poured into 3/4 inch I.D. plastic tubes set on absorbent plaster blocks. Nylon filter papers (about 0.22 μm pore size*) were placed between the plastic tubes and the plaster blocks to prevent contamination of the samples by the plaster blocks. Typically, the cast suspensions solidified within 5-10 min due to the high solids loading used in the slip casting operation. The cast bodies were air-dried for about 8 h. Then the compacts were removed from the tubes and further dried in an oven at 90°C for 24 h.

For dry pressing, about one gram of powder was cold compacted in a cylindrical tool steel die with 3/4 inch inner diameter. Thin teflon sheets were attached to the surfaces of the punches to decrease the contamination from the die. Two forming pressures, 0.1 MPa and 31 MPa, were used to obtain green compacts of ~41% and ~54% relative density, respectively.

---

* Fisher Scientific Co., Springfield, NJ.

The porosity and pore size distribution of the green compacts were characterized by mercury porosimetry*. A plot of the intruded volume vs. applied pressure was obtained. The maximum applied pressure was about 413 MPa. From the volume vs. pressure plot, a plot of specific pore volume frequency vs. pore radius was obtained. Standard values of specific surface tension (approximately 484 ergs/cm^2) and contact angle (approximately 140°) for mercury were used. The pore radius was calculated using following relation :

$$\text{pore radius (nm)} = 735 \,/\, \text{applied pressure (MPa)} \qquad (3.4)$$

The median pore radius was calculated from the pressure corresponding to 50% of maximum introduced volume (V_m). The relative density (RD) was calculated using the relationship :

$$RD = \frac{W_t \,/\, \rho_{th}}{V_m + (\, W_t \,/\, \rho_{th} \,)} \qquad (3.5)$$

where W_t is the weight of sample.

The porosity characteristics of the powder compacts was also determined by the Archimedes method using D.I. water as a suspending media. Relative densities were determined by dividing the bulk density with the alumina theoretical density. The bulk density (BD) and open porosity (%OP) were obtained using the following relations:

---

* Model SP-100, Quantachrome Corp., Syossett, NY.

$$BD = \frac{W_d \times D_w}{W_s - W_p} \tag{3.6}$$

$$\%OP = \frac{(W_s - W_d) / D_w}{(W_d / BD) - (W_d / \rho_{th})} \tag{3.7}$$

where W_d is the dry weight, W_s is the saturated weight, and W_p is the suspended weight of the sample in water. D_w is the density of water at the measuring temperature. All green compacts were calcined (700°C, 1 h for NSD-15; 700°C, 0.5 h for BSD, ISD, and NSD-30; 500°C, 1 h for CSD) to remove moisture and volatile species and to obtain sufficient strength for boiling in water. SEM was used to observed the top surface and fracture surface of the green compacts.

Sintering

Samples were sintered in air under isothermal conditions at temperature in the range 1100 to 1600°C. A box furnace* with $MoSi_2$ heating elements was used. Temperature readings were obtained through a type R thermocouple (i.e., Pt vs. Pt/13%Rh). A microprocessor** was used to control the furnace temperature.

The relative density and percent open porosity of sintered compacts were determined by Archimedes method as previously described. The surface areas of selected samples were determined by BET nitrogen gas adsorption method as mentioned earlier.

---

* Model DT-31, Deltech, Inc., Denver, Co.

** The MicRicon Process Control System, Research Inc., Minneapolis, MN.

Sample Preparation for Ceramography

In order to investigate the microstructural evolution over a range of sintered densities, flat polished sections without particle pull-outs are needed. However, it is difficult to obtain good polished cross sections for low density samples which were sintered at low temperatures and/or short times. A novel impregnation process was developed to minimize grain pullouts during grinding and polishing of highly porous samples. The detailed procedure is discussed in Appendix B.

After impregnation, samples were mounted on a sample holder which can hold up to 6 samples and hand ground with SiC powder slurries on glass plate to 1000 grit finish. The samples were then polished on a vibrating polisher* with diamond pastes (6, 1, and 0.25 μm, progressively) and nylon cloth. After obtaining a smooth, scratch-free surface, the mounted samples were placed in an oven at 200°C for 1 h to soften the mounting polymer. This enabled the removal of the sample from the polymer mounts. The samples were then subjected to a burn-out process to remove the impregnated polymer.

Samples were gradually heated in a furnace up to 800-900°C and held at that temperature for about 10 h to ensure complete burn-out of polymer. The heating schedules depended on the strength and sintering history of the samples. Lower heating rates and lower holding temperatures were used for more porous samples which had shorter sintering times or lower sintering temperatures. A very fast burn-out rate could result in disintegration of slightly sintered samples due to the vapors generated in the burn-out process.

---

* Vibromet I Polisher, Buehler Ltd. Lake Bluff, IL.

Thermal etching was used to reveal grain boundaries. Samples were thermal etched at temperatures in the range 1000 to 1450°C for 2-4 h. Normally, thermal etching temperatures were chosen to be at least 100°C lower than the sintering temperature, thereby preventing any microstructural change during thermal etching process. However, some samples were thermally etched at their sintering temperatures because clear grain boundary structures could not be obtained at lower temperature. In this case, the sintering time would be the original sintering time plus thermal etching time. An Au/Pd thin film was deposited by sputtering on the polished surface and SEM was used to take photographs for microstructural characterization. About 10 photographs were taken at random for samples with homogeneous microstructure (i.e., slip cast samples). About 20 photographs were used for samples with heterogeneous microstructure (i.e., dry-pressed samples). Negatives of each photograph were used to obtain enlarged (8 in x 10 in) prints for better accuracy during microstructural characterization. Standard quantitative stereology procedures were followed to obtain quantitative values of microstructural features.

Quantitative Stereology

Detailed treatments of quantitative stereology are readily available in the literature [DeH68, Und70]. Only a general review on the procedures for determining microstructural parameters will be presented.

Relative Density (Porosity)

A transparent plastic sheet with 10 x 10 square grid (100 intersecting points) was overlaid on the enlarged photographs. Points intersecting the pore regions were counted. At least 50 different fields were measured. The average point fraction equals to the porosity (P) of the samples. The relative density (RD) was obtained from the relation :

$$RD = 1 - P \tag{3.8}$$

Grain and Pore Intercept Size

A digitizing tablet* interfaced with a personal computer** and a specially developed computer program were used to obtained grain and pore intercept sizes. A transparent plastic sheet with equally spaced parallel lines was overlaid on the enlarged photographs. (Because microstructure showed no preferred orientation, a single direction for the parallel lines was adequate in this study.) The length of every intercept (grain or pore) was digitalized. After correcting for magnification, the intercept sizes were stored for further statistical analysis. Typically, approximately 500 intercept sizes were measured for homogeneous samples (i.e., slip cast samples) and approximately 1000 intercept sizes were measured for the heterogeneous samples (i.e., dry-pressed samples). Due to the very low pore population in the very high density samples (> 98% relative density), approximately 200 pore intercept sizes were measured for these samples.

Pore-Solid Interfacial Area and Grain Boundary Area

It has been shown that the area per unit volume (S_V) of a two-dimensional feature (e.g., solid-solid (grain boundary) interface or pore-solid interface) can be obtained using the following relation [DeH68, Und70]:

---

* Model 9111A, Hewlett Packard, Palo Alto, CA.

** Model HP-86, Hewlett Packard, Palo Alto, CA.

$$S_V = 2\ N_L \tag{3.9}$$

where N_L is the average number of intersections (made between the random test line and the planar feature on the polished cross section) per unit length of test line.

A transparent plastic sheet with equally spaced parallel lines was overlaid on the enlarged photographs. The number of intersections made between the test lines and the pore-solid interfaces (or grain boundaries) was recorded. Typically, approximately 800 intersections were measured. After correcting for magnification, the N_L values were obtained by dividing the total intersection number with the total length of the test line. Approximately 400 intersections of pore-solid interface were measured for the high density samples (>98% relative density).

The mean pore intercept size (PI), mean free path of pores (MFP, i.e., mean intercept length of solid phase without considering grain boundaries), mean grain intercept size (GI) could also be derived from the specific pore-solid interfacial area (S_V), specific grain boundary area (S_G), porosity (P), and relative density (RD) using the following relationships [DeH68, Und70]:

$$PI = 4\ P\ /\ S_V \tag{3.10}$$

$$MFP = 4\ RD\ /\ S_V \tag{3.11}$$

$$GI = 4\ RD\ /\ (\ S_V + 2\ S_G\ ). \tag{3.12}$$

The length (per unit area) of the perimeter of pores on the polished section (L_A) was derived using the following equation [DeH68, Und70]:

$$L_A = N_L \times (\pi / 2) \tag{3.13}$$

Integral Mean Curvature (M_V)

It has been shown by DeHoff and Rhines that the integral mean curvature of a curved surface can be obtained by counting the number of tangents formed between a test line and the contour of the surface while sweeping the test line through two-dimensional cross sections [DeH67, DeH68, DeH77]. In this study, tangents obtained on a convex contour (relative to solid phase) were denoted as positive and on a concave contour as negative. Integral mean curvature (M_V) can be obtained using the following equation

$$M_V = \pi \, T_{Anet} \tag{3.14}$$

where T_{Anet} is the net tangent count. For a close loop of any shape, the net tangent count will always equals two. Therefore, tangent count can be simplified as counting the number of close loops of pores on SEM photographs. However, for an incomplete loop, each individual tangent need to be counted. The integral mean curvatures were obtained using the relation :

$$M_V = \pi \, (T_{Anet}' - 2 \, N_A) \tag{3.15}$$

where T_{Anet}' is the net tangent count obtained from the incomplete loops of pore contour per unit area, and N_A is the number of complete loops per unit area on the two-dimensional cross sections.

CHAPTER IV
EFFECT OF PARTICLE PACKING

Introduction

Particle packing is one of the most important green compact characteristics that will have a determining effect on the final microstructures and properties. The effect of particle packing on the densification kinetics and microstructural evolution during sintering is the focus of this chapter.

Initially, two methods of forming powder compacts (i.e., dry pressing and slip casting) will be reviewed. The effect of powder consolidation method on particle packing characteristics will be discussed. Previous literature concerning the effect of particle packing on sintering and microstructural evolution will be discussed also.

Following the literature review, experimental results, discussion, and comparison of current results with reported data will be presented. Detailed characterization of the alumina powder is first presented. Characteristics of green compacts with homogeneous and heterogeneous packing prepared by slip casting and dry pressing will be shown. The effect of the various packings on the densification kinetics and microstructural evolution will be discussed. Extensive quantitative characterization of microstructural features (e.g., grain size and grain size distribution, pore size and pore size distribution, interfacial area, curvature, etc.) will be reported. Finally, comparison of current sintering results with existing sintering models will also be presented.

Background

Particle packing (i.e., the spatial arrangement of particles in a powder compact) determines the particle coordination number (the number of nearest neighbors), green density, pore size and pore size distribution, and the local curvature at the pore-solid interface of the green body. These microstructural characteristics strongly influence the magnitude of driving force for sintering, and therefore the temperature and time required. They also strongly influence the microstructure and properties that can be achieved in the final products. However, only in those systems with monosized spheres packed in an ordered fashion (such as simple cubic, face centered cubic, etc.), can a complete picture of the particle packing be easily visualized. In certain special cases (such as monosized spherical silica or titania), face-centered cubic or hexagonal close-packing has been observed within the domains in the green bodies prepared from well-dispersed suspensions. However, measured relative densities in bulk compacts are substantially lower than calculated from geometric considerations (e.g., ~65% compared to the theoretical value of ~74% for fcc packing), implying that a large volume percentage of packing defects (i.e., regions of disordered packing) exist.

Considering the irregular shape and broad size distribution of commercial powders, it is impossible to produce a compact with ordered packing. In order to clearly describe the packing characteristics in a powder compact, we need to describe the spatial position of each particle in three dimensions. At least, we need to know the number and relative position of the nearest neighbors of each particle. Considering the vast amount of particles in a sample, it is impossible to achieve that. Therefore, bulk properties (e.g. particle coordination number, pore characteristics, green density, etc.) are normally used as a qualitative indication about the status of particle packing. These properties are more or less related to each other. For example, when the green density increases, the average coordination number should also increase and average pore size should decrease (i.e., assuming the powder characteristics and consolidation conditions are kept constant).

Consolidation Conditions

For a given powder, the packing characteristics of the green compact are determined by the processing and consolidation conditions. Two of the most commonly used consolidation routes in ceramic processing (i.e., dry pressing and slip casting) were used in this study.

Dry pressing. Dry pressing is one of the most popular forming methods to consolidate ceramic powders into desired shapes because it can offer advantages such as high production rates, capability of achieving close dimensional tolerances and relatively low capital investment. A wide variety of ceramic components such as spark plug insulators, ceramic substrates and capacitors, nuclear fuel pellets, etc. are fabricated by dry pressing and subsequent sintering.

The typical procedures for dry pressing are (1) loading the powder (which may contain binders and lubricants and may be granulated) into a die, (2) compressing the powder into the desired shape by moving punches, (3) ejecting the powder compact from the die. During the compaction operation, the pressure applied by the moving punch can cause particles to slide, rearrange, and possibly even deform and fracture.

Compaction can also lead to deformation or break-up of agglomerates, collapse of porous regions or large pores, and an increase in the number of interparticle contacts. As a consequence, the relative density of the compacts increases, the average pore size decreases, the number of large pores also decreases, and the green strength increases.

The magnitude of the applied pressure is one of the most important factors in determining the microstructure and properties of the dry-pressed compacts. Normally, the compact density increases linearly with the logarithm of applied pressure. However, depending on the characteristics of the powder used, compaction curves showing a different mathematical form may be observed [Luk78, You82]. The increase in compact density with a increase in applied pressure is mainly due to the elimination of the larger pores which are formed between large agglomerates or are introduced by improper powder feeding. A typical example is the study carried out by Reed and Runk [Ree76] where the pore size distributions of dry-pressed Linde A alumina compacts were characterized using mercury porosimetry. A significant decrease in the volume of large pores was observed when the applied pressure increased from ~28 MPa to ~138 MPa.

Microstructural inhomogeneities are the most common drawbacks of dry-pressed compacts. These inhomogeneities can cause non-uniform shrinkage, distortion, or cracking during sintering. Large pores retard densification kinetics and limit the maximum sintered relative density that can be achieved. One of the causes of inhomogeneities is the frictional forces which occur between powder particles and between the powder and the die wall [Ree76]. Friction restricts powder rearrangement and results in non-uniform transmission of the applied pressure throughout the compaction zone. Thus, some regions of the compact will show lower packing densities and uncollapsed large pores due to lower compacting pressures.

Non-uniform powder filling of the die and non-uniformities in the powder (e.g., agglomerates) also causes microstructural inhomogeneities in dry-pressed samples. Ceramic powders (especially submicron powders) spontaneously form soft agglomerates in the dry state due to van der Waals attractive forces or adsorbed surface moisture. In addition, granules (one type of agglomerate) are usually produced intentionally (e.g., spray drying) to increase the flowability of the powder during the die filling operation. Many studies on the effects of powder agglomeration on green microstructures and densification of dry-pressed samples have been reported. It was clearly shown that large pores remained in the inter-agglomerate regions after dry pressing [Luk78, Wan76, You82]. During sintering, faster densification occurred in the intra-agglomerate regions due to the relatively higher packing density. On the other hand, inter-agglomerate pores were difficult to remove and large residual pores or pore clusters were often observed after extensive bulk densification [Wan76].

Slip casting. Slip casting has been a widely used ceramic forming technique for producing traditional ceramics for a long time. Because of its capability of forming green bodies with intricate shapes or thin-walled objects, it is still a popular process to fabricate highly sophisticated advanced ceramics (e.g., annular combustor for gas turbine engine). A typical slip casting process consists of (1) preparing a powder/liquid suspension (i.e., slip), (2) pouring this slip into a porous mold (usually made from plaster of Paris), (3) removing liquid from the suspension (i.e., by absorption into the mold) and allowing powder to consolidate against the mold surface*, (4) drying the powder compact in the mold to obtain sufficient strength for subsequent processing, and (5) removing object from the mold.

The advantage of suspension processing is that powders can be consolidated from a well-dispersed state. Soft agglomerates can be broken down (e.g., by ultrasonication) and particle-particle interactions can be controlled (e.g., by pH adjustment or the use of "dispersants"). By using well-dispersed suspensions and by choosing proper forming methods to consolidate the suspension into a powder compact, compacts with homogeneous** green microstructures can be produced.

Slip casting is a simple and inexpensive method to consolidate suspensions into powder compacts. However, when the suspension contains more than one component, those components having higher densities will have higher setting rates during slip casting and tend to segregate at the bottom. Furthermore, most powders have broad particle size distribution, large size particles also have higher settling rates and will also segregate at the bottom. In order to eliminate this segregation problem, several approaches have been reported. The most obvious solution is increasing the solution viscosity (e.g., adding soluble polymers) to decrease the settling rates of the particles in the liquid. However, this method also decreases the solvent removal rate which leads to low casting rates. High viscosity also make casting operation more difficult and slip may not fill small cavities in the mold.

---

* Thin wall objects can be obtained by pouring the excess slip out of the mold cavity when a suitable wall thickness has been formed. This is known as drain casting. Alternatively, by allowing the casting to continue until the whole mold cavity is filled, a solid cast body can be obtained.

** "Homogeneous" implies (1) homogeneous mixing between different powder phases when powders have more than one phase, (2) homogeneous mixing of different particle sizes because most powders have a distribution of particle sizes, and (3) homogeneous particle packing which results in a narrow pore size distribution.

As mentioned in Chapter II, controlled flocculation can also be used to prevent segregation. It has also been shown that homogeneous mixing of various flocculated suspensions can be obtained by high shear rate mixing (e.g., ultrasonication) and homogeneous green microstructure can be produced by consolidating these flocculated suspension [Car84, Lan87]. However, green compacts consolidated from flocculated suspensions show retarded densification kinetics and coarser sintered microstructure due to lower relative densities and larger pore sizes in the green state [Bar82, Kim87, Sac84]. Recently, it was shown by Cameron and Raj [Cam89] that the green densities of the compacts prepared from flocculated suspensions could be significantly increased by a compression deformation process and the densification kinetics could be significantly enhanced. However, these processes increase the complexities of compact preparation which will significantly decrease the productivity. Components with complicated geometry are also difficult to be fabricated using a compression deformation process.

After extensive studies on suspension preparation and consolidation, Sacks and co-workers [Sac85, Sac88a, Sac88b] proposed that slip casting of well-dispersed suspensions at high solids loading is a very effective way to produce homogeneous green bodies with high relative density. Sacks and Scheiffele [Sac85] studied the effect of suspension characteristics on the microstructure and properties of slip cast silicon compacts. They showed that by preparing well-dispersed suspensions (judged by low viscosity) through pH adjustments and ultrasonication, green bodies with low porosity, and small mean pore size could be obtained. In the same study, they also showed that by increasing the solids loading of the silicon suspensions to 56 vol%, homogeneous green bodies without particle size or component segregation could be obtained (even though the powders they used had very broad particle size distribution--ranging from above 10 μm to around 0.1 μm). The cast bodies also showed very high green density (above 75% relative density). Slip casting with high solids loading suspensions was also used to prepare SiC whisker-reinforced ceramic composites [Sac88a, Sac88b]. These samples showed homogeneous microstructure (no whisker segregation) and significantly higher green densities (i.e., compared to dry-pressed samples). The advantage of preparing green compacts through slip casting well-dispersed suspensions was also demonstrated by other studies [Aks84].

In summary, consolidation conditions have a significant effect on the packing characteristics of green bodies. In general, dry pressing produces inhomogeneous green microstructure--nonuniform particle packing, density gradients and the existence of large pores. Green compacts prepared from de-agglomerated, well-dispersed suspensions with high solids loading show homogeneous microstructure with high green density and fine pore size. Even though the majority of the reported sintering studies have been carried out using samples prepared by dry pressing, it should be pointed out that the aforementioned inhomogeneities make the system more complicated and difficult to analyze. The comparison of the sintering behaviors of dry-pressed samples and slip cast samples will be presented in this chapter.

Effect of Particle Packing on Sintering and Microstructural Evolution

Previous studies concerning the effect of particle packing on sintering are normally focused on the effect of green density and pore characteristics because these two properties are closely related to particle packing and are easily obtained. Bruch [Bru62] was among the first to study the effect of green density on sintering using Linde A alumina doped with 0.25 wt% magnesia. He dry pressed a series of samples with green density in the range from 22.4 to 52.8% relative density and isothermally sintered these samples at temperatures from 1450 to 1900 °C. He fitted his sintering data with an empirical equation, $P = Ct^n$, where P is the percent porosity after sintering, t is sintering time, and C and n are constants for constant temperature and green density. More negative n values represent faster densification kinetics. According to his sintering results, at a given temperature, "normal sintering" (for which $n = -0.4$) could be obtained for samples having green density larger than a critical value. For samples with lower green density, the absolute value of exponent n became less than 0.4. He called that "subnormal sintering." He concluded that densification rate strongly depended on green density.

Bruch [Bru62] also studied the grain growth behavior of the above samples and showed that at a constant sintered density, the grain sizes of samples with lower green densities were larger than that of high green density samples. Using constant heating rate sintering, Wang [Wan76] studied the grain size trajectories of dry-pressed alumina compacts with green densities in the range 32 to 48%. He showed that trajectories with a higher ratio of densification/coarsening rates were obtained for samples with higher green densities. Similar results were also reported by Occhionero and Halloran [Occ84] for dry-pressed alumina compacts sintered isothermally. In order to obtain the same sintered density, samples with lower green density must have a longer sintering schedule (temperature x time) compared to high green density samples; therefore, more grain growth occurs in lower green density samples. Occhionero and Halloran's study also showed that the green density affected the density for the onset of grain growth. Grain growth started at higher densities for higher green density samples.

Using both isothermal and constant heating rate approaches and focusing on the initial stage of sintering, Woolfrey studied the effect of green density on the sintering kinetics of UO_2 powder [Woo72]. He found that the linear shrinkage rate decreased steadily with decreasing green density for samples with green density below ~40 to 43% relative density. An approximately constant linear shrinkage rate was observed for samples with green density larger than the above values. Occhionero and Halloran [Occ84] and Zheng and Reed [Zhe89] also reported that linear shrinkage in the early stage of sintering is independent of green density for dry-pressed alumina compacts with relative densities in the range ~40% to 59%. However, as will be discussed later, using shrinkage as a criterion to study the effect of green density on sintering has some inherent problems and may result in misleading conclusions.

Bruch and Woolfrey both concluded that the decrease of sintering kinetics in low density samples was due to the existence of stable pores which were either formed during dry pressing [Woo72] or coalesced from pore clusters larger than some critical size (which depended on sintering temperature) [Bru62]. Woolfrey [Woo72] utilized mercury porosimetry to characterize the pore size of samples with relative densities in the range from ~30% to ~50%. He demonstrated that low density samples had a broad pore size distribution with the existence of large pores. No effect of green density on the activation energy for the sintering of UO_2 was observed in Woolfrey's study. However, Bruch reported that the activation energy for the sintering of low density alumina samples (i.e. subnormal sintering) was higher than that for normal sintering.

Sacks and Tseng [Sac84] performed a detailed study on the colloidal processing and sintering of monodispersed spherical silica powder and showed that green bodies with different packing status can be obtained by controlling the dispersing condition of silica powder in water. Green compacts prepared from dispersed suspensions (pH=10) had high green density (~60% relative density), uniform packing structure. Finer pore size was confirmed by mercury porosimetry. These compacts were sintered to full density at low temperature (1000°C for 24 h). On the other hand, samples prepared from flocculated suspensions (pH=3) had inhomogeneous green microstructure, low relative density (~45%), and larger pore sizes. A substantially lower densification rate and lower sintered density were obtained. Barringer and Bowen [Bar82] reported a study on the sintering of compacts prepared from monodisperse spherical titania powders. Their study also showed that fine grain size and high relative density (>99%) can be obtained at low sintering temperature, without the addition of sintering aid, by using a homogeneous, high density compact prepared from a well-dispersed suspension. Low sintered density was obtained from an inhomogeneous, low density compact prepared from a flocculated suspension.

Kimura et al. [Kim87] prepared alumina compacts by slip casting of suspensions with pH between 2 and 9. They showed that both the porosity and median pore size increased as the pH of the suspensions increased from 2 to 9 (i.e., changed from dispersed state to flocculated state). Sintering and microstructural evolution of compacts prepared from pH = 2 (green density was 64.8%) and pH = 9 (green density was 48.6%) were reported. Due to the higher packing density and finer pore size, the pH = 2 sample showed higher densification kinetics. Despite the significant difference in packing density, they reported that both samples showed similar sequence of microstructural development which was characterized as (1) formation of localized densified regions in the early stages of sintering (< 75% relative density), (2) the densified regions expanded and impinged each other as sintering proceeded, resulted in uniform microstructures (75 - 95% relative density), (3) development of columnar grains (> 95% relative density). They also showed that the arithmetic standard deviation of the grain size distribution increased linearly with increasing average grain size and both the pH = 2 and pH = 9 samples can be represented with a common line.

Cameron and Raj [Cam89] also studied the sintering behavior of alumina compacts prepared from dispersed suspensions (pH = 3) and flocculated suspensions (pH = 8.6). Significantly higher green density was obtained for the pH = 3 samples (64% vs. 51% for the pH = 8.6 sample) which resulted in higher densification kinetics and finer sintered microstructures. However, they showed that a significant increase in green density (from 51% to 62%) could be produced for the pH

= 8.6 sample through a compression deformation process. The pressed pH = 8.6 compacts showed similar densification kinetics and grain growth behavior as the pH = 3 sample. Due to the higher packing density, both the pH = 3 and pressed pH = 8.6 samples showed virtually no grain growth up to 92% relative density. On the other hand, the average grain size of the unpressed pH = 8.6 sample started increasing at ~75% relative density. The grain size trajectory of the pH = 8.6 samples showed higher ratio of coarsening/densification rates.

Zheng and Reed [Zhe89] investigated the sintering behavior of alumina compacts prepared from various compaction conditions. For the low density sample (50% green density) dry-pressed from spray-dried granules, they showed a significant increase in mean pore channel size (determined by mercury porosity) as the densification proceeded. For the dry-pressed compacts with higher green density (55% to 59% relative density), only slightly increase in mean pore channel size was observed. On the other hand, for samples consolidated from well-dispersed suspensions by pressure-filtration and post-compression (~63% green density), the mean pore channel size decreased as the sample densified. They suggested that essentially all of the pores in the samples prepared from suspensions were smaller than the critical size*, and hence shrinkage of pores could occur. In contrast, two classes of pores (one larger than critical size and the other smaller than critical size) existed in the dry-pressed samples. During sintering, the smaller pores were eliminated which led to an increase in the mean pore size of the dry-pressed samples.

---

* Kingery and Francois [Kin67] suggested that a critical ratio of pore size to grain size existed. Pores can shrink and disappear when the ratios of pore size to grain size are smaller than the critical ratio.

Even though green density has been used as an important indicator for the status of green compacts and many studies have been conducted to investigate the effect of green density on sintering, green density is an averaged bulk property which does not reveal microstructural heterogeneities. It has been shown by Sacks and Pask that green compacts with similar overall green density can have significant differences in sintering kinetics and final microstructure [Sac82]. Therefore, studying the effect of green density without detailed microstructural investigation may result in misleading conclusions.

Results and Discussion

Powder Characterization

It is well-known that commercial powders contain large hard agglomerates. As discussed in Chapter II, agglomerates can introduce heterogeneous green microstructure which will severely affect sintering kinetics and make sintering data more difficult to analyze. In this study, we have made an attempt to prepare model compacts for the study of the effect of particle packing on sintering. The first thing that needs to be done is to remove the agglomerates from the as-received powder. Therefore, the coarser portions of the as-received powder, which mostly consists of hard agglomerates, were removed by gravitational sedimentation. Figure 4.1 shows the SEM photographs of the agglomerates which were removed from the as-received powder. The collected agglomerates ranged in size from a few microns to several tens of micron. The microstructure of agglomerates can be clearly seen in the

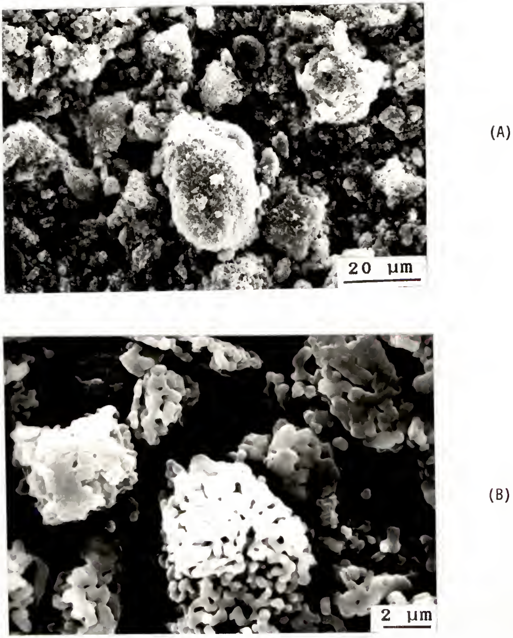

Figure 4.1 SEM micrographs of hard agglomerates removed from as-received (A) AKP-30 and (B) AKP-15 powders.

higher magnification photograph (Figure 4.1B). Some agglomerates showed porous structure in which primary particles had partially sintered. This kind of aggregated microstructure has also been reported by Dynys and Halloran in alum derived alumina powder [Dyn84]. The aggregates in their powder showed flaky shape; however, the aggregates found in current powders had more equiaxed shape (Figure 4.1A). This suggests that the manufacturing processes for the two powders are different. It can also be seen in Figure 4.1B that some regions of the agglomerates have been sintered to high relative density and primary particles are difficult to be identified. It is believed that the above hard agglomerates were formed during the high temperature calcination step of the powder manufacturing process and that these hard agglomerates were not broken up completely during the subsequent comminution operation. It should be noted that the majority of agglomerates found in the as-received AKP-30 powder are highly porous, with relatively few high density agglomerates. This may be due to the low calcination temperature (and/or short calcination time) used to produce AKP-30 powder.

As will be discussed in the next chapter, particle size distribution also has important effect in sintering kinetics. In order to avoid possible complications from using a powder with a range of particle sizes, fine particles in the as-received powder were also removed in order to obtain a powder with a narrow particle size distribution. Figure 4.2 shows a comparison of the particle size distribution of the as-received AKP-15 powder and the fractionated narrow size distribution powder (NSD-15) determined by X-ray gravitational sedimentation. The NSD-15 powder had an excellent fit to the log-normal distribution function over the entire range. This can be

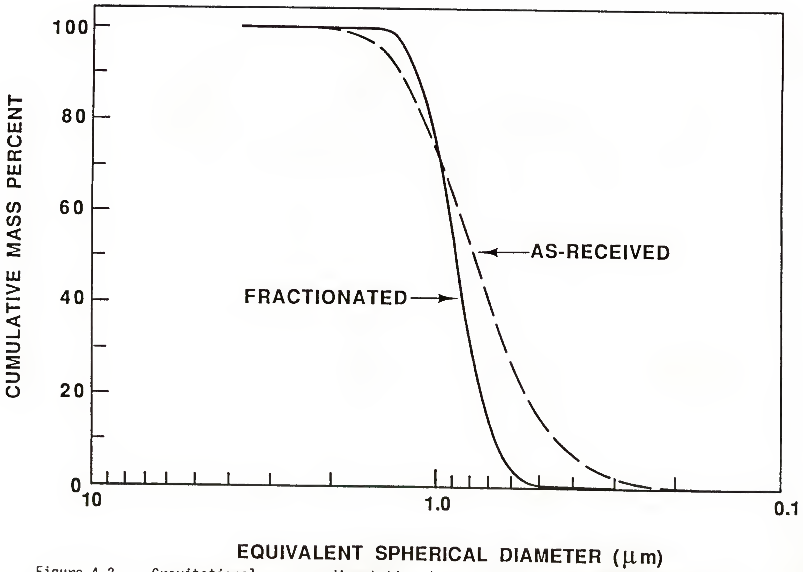

Figure 4.2 Gravitational x-ray sedimentation data for as-received AKP-15 powders and fractionated NSD-15 powders.

seen in Figure 4.3 where the size distribution data are plotted on a log probability scale. The median size of NSD-15 powder was 0.87 μm and the geometric standard deviation was only ~1.2 which demonstrates that NSD-15 powder had a very narrow size distribution. (For comparison, the geometric standard deviations of particle size distributions determined by X-ray gravitational sedimentation are around 1.3 and 1.5, respectively, for Stober silica with median size of 0.95 and 0.65 μm [Yeh85]. However, the geometric standard deviations for Stober silica size distributions determined by SEM measurement are normally ~1.1 [Kha88].)

A centrifugal photosedimentation method was also used to characterize the particle size distribution of the NSD-15 powder (Figure 4.4). The volume-basis median diameter was 0.75 μm which was slightly lower than the median diameter from X-ray gravitational sedimentation method. The geometric standard deviation was 1.34 which was slightly higher than the value from gravitational sedimentation. The data from the two methods can be more directly compared by converting the cumulative distribution in figure 4.2 to a distribution histogram (Figure 4.5).

Because the particles are not equidimensional (e.g., spheres), SEM was also used to obtain more information on particle size distribution. The distribution histograms of equivalent area diameters (D_a) and equivalent perimeter diameters (D_p) determined from projected images in SEM micrographs are shown in Figure 4.6 and Figure 4.7, respectively. The number-basis median diameter and geometric standard deviation of D_a were 0.83 μm and 1.20, respectively. (The number-basis mean diameter was also 0.83 μm.) In order to properly compare the number-basis equivalent

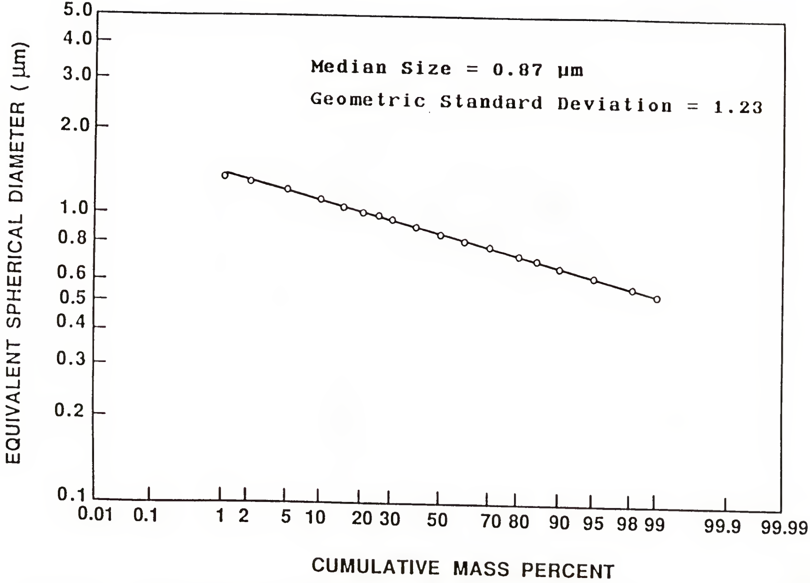

Figure 4.3 Particle size distribution plotted on a log-probability scale for the NSD-15 powders in Figure 4.2.

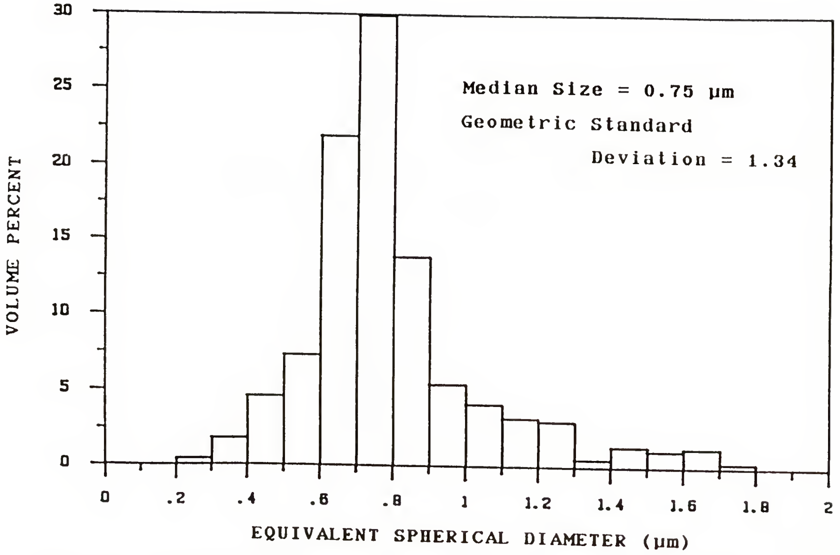

Figure 4.4 Histogram plot of the particle size distribution determined by centrifugal photosedimentation method for the NSD-15 powders.

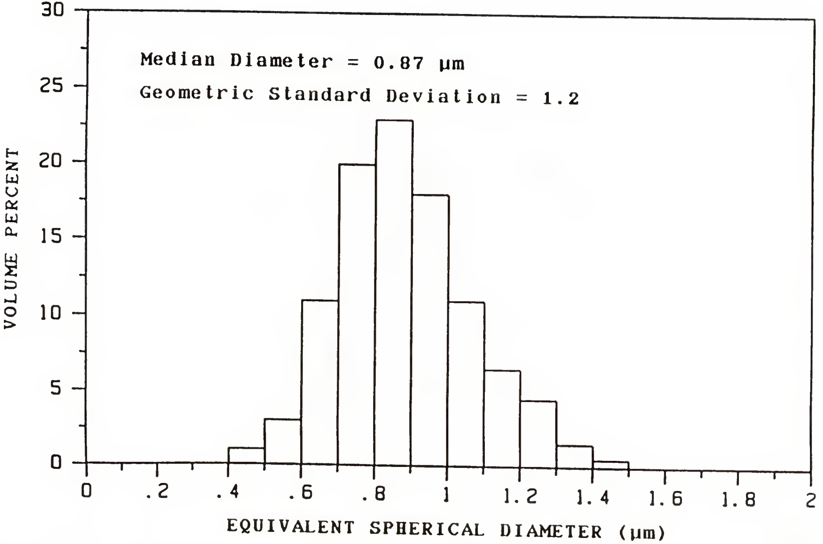

Figure 4.5 Histogram plot of the particle size distribution determined by gravitational x-ray sedimentation method for the NSD-15 powders.

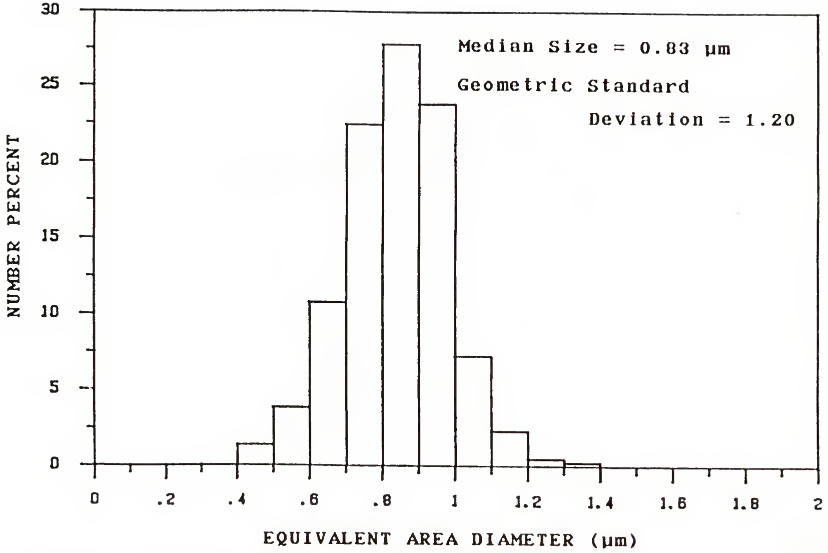

Figure 4.6 Histogram plot of the number-basis distribution of equivalent area diameter determined by SEM for the NSD-15 powders.

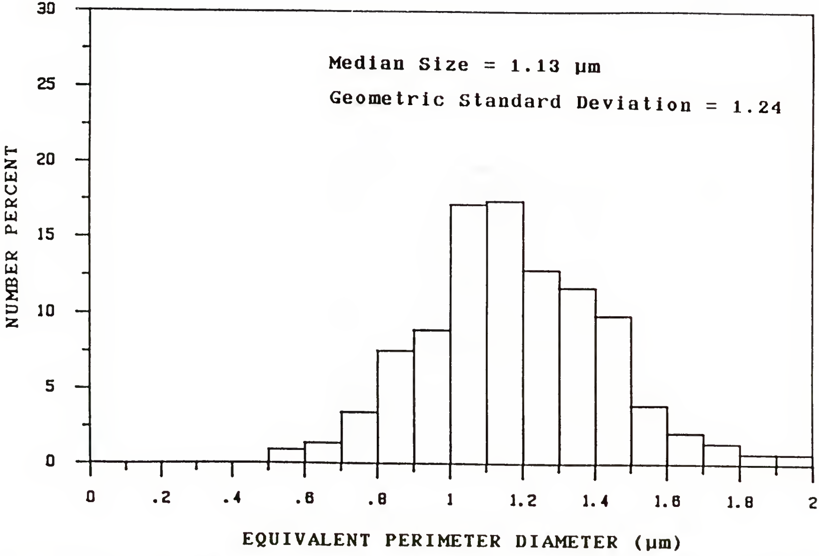

Figure 4.7 Histogram plot of the number-basis distribution of equivalent perimeter diameter determined by SEM for the NSD-15 powders.

area diameter with the volume-basis diameters determined by the sedimentation methods, the size distribution in Figure 4.6 was converted to a volume-basis distribution histogram* (Figure 4.8). The volume-basis mean diameter and median diameter were 0.91 and 0.85 μm, respectively. The geometric standard deviation was 1.18. These values are in good agreement with the data obtained from the gravitational sedimentation method. The number-basis median diameter of D_p was 1.13 μm (the number-basis mean was 1.18 μm) which was much larger than the aforementioned values. The reason is that the NSD-15 powder was not equiaxed in shape as can be seen in the SEM photographs in Figure 4.9. Therefore, the diameter of a circle having the same perimeter as the measured particle will be larger than the equivalent area diameter or the Stokes diameter. However, the geometric standard deviation of D_p was 1.24 which agreed very well with other measurements.

From the above discussion, it is clear that all the above sizing methods can give values that are in reasonable agreement. However, there are some fundamental differences among these methods that need to be pointed out:

1. In both sedimentation methods, particle size is determined from measuring the settling speed of particles in a liquid suspension. The dispersion state of the suspension can dramatically change the

---

* The volume of each particle in the ith size class was assumed to be equal to the volume of a sphere with diameter equal the median size of the size class. The volume frequency of ith size class

$$V_i = \frac{N_i \cdot \pi D_i^3/6}{\Sigma N_i \cdot \pi D_i^3/6}$$

where D_i is the median size of ith size class and N_i is the number frequency of ith size class.

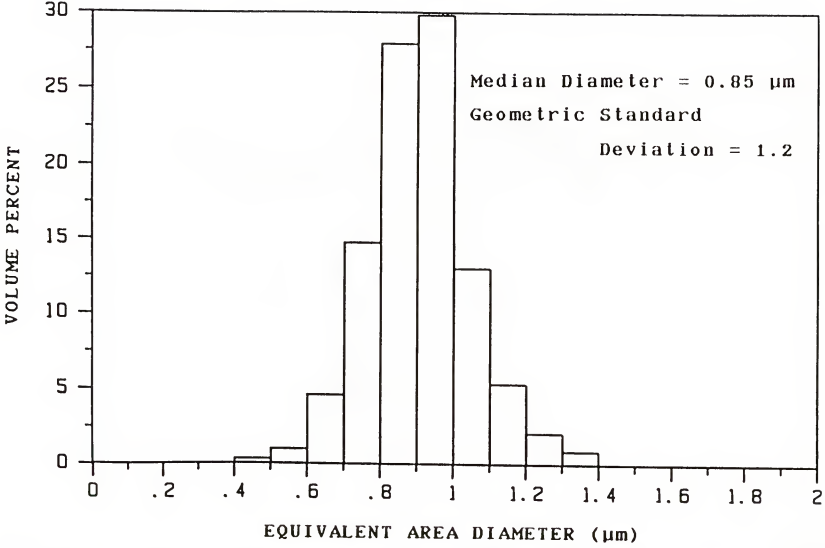

Figure 4.8 Histogram plot of the volume-basis distribution of equivalent area diameter determined by SEM for the NSD-15 powders.

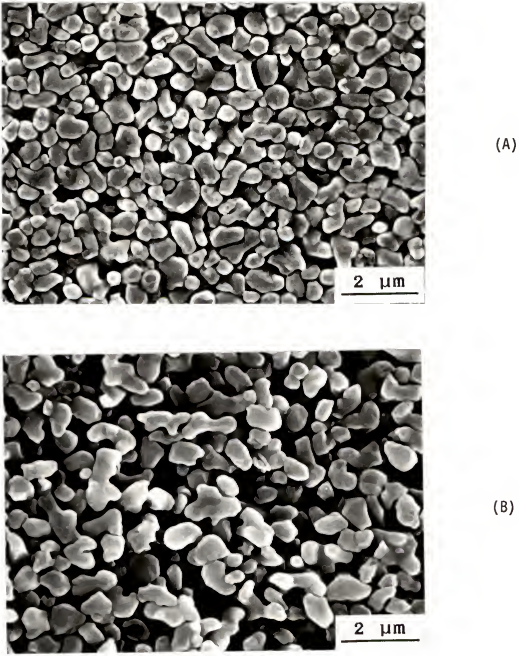

Figure 4.9 SEM micrographs for the top surfaces of (A) SCD sample and (B) SCF sample.

particle settling speed, and, consequently, change the measured particle size. Therefore, extreme precaution needs to be taken to ensure that a well-dispersed suspension is used. In the SEM method, direct observation of the dispersion state of particles is possible. Therefore, by using proper preparation procedures, measurement on each individual particle can be obtained.

2. Sedimentation methods utilize a large number of particles to determine the population in each interval of the size distribution. Therefore, more representative data can be obtained without much variation between measurements. The SEM measurement is much more laborious and is limited to smaller amount of particles. As a result, more data variation between measurements can be expected. Recently, due to the advancement in image analyzing techniques, large numbers of measurements are possible. However, careful sample preparation is needed in order to obtain SEM micrographs with well-separated particles which is essential for carrying out image analysis.
3. The diameter measured in the sedimentation methods is the Stokes diameter which is based on 3-dimensional physical properties of the particles. The diameter obtained from SEM measurement is based on the two-dimensional projection image. In addition, the population quantities in the SEM measurement are based on number fraction. The population quantities in the sedimentation methods are based on the attenuation of X-ray (which is related to the mass concentration of particles in suspension) or optical light (which is related to the cross section area of particle, particle size, and the extinction coefficient for that material.)

Green Compact Characterization

After agglomerate-free narrow size distribution powder was produced, green compacts with four different packing characteristics were prepared. Two sample series were prepared through suspension processing route (i.e., slip cast from well-dispersed and flocculated suspensions) and two series prepared by dry pressing method (i.e., dry pressed at high and low pressures).

Slip casting. The pore size distribution, i.e., the specific volume frequency vs. pore channel radius, obtained by mercury porosimetry of the two slip cast samples are shown in Figure 4.10. Samples slip cast from well-dispersed (pH = 4) suspension (SCD) had high green density (~64% relative density) and fine average pore channel radius (~95 nm). Samples slip cast from flocculated (pH = 9) suspension (SCF) had lower green density (~51% relative density), larger average pore channel radius (~172 nm) and broader pore size distribution. The above microstructure characteristics also can be clearly seen in the SEM photographs of the top surfaces of both compacts as shown in Figure 4.9. The micrograph of the SCD sample showed uniform particle packing and very high packing density. Particles arranged themselves, according to their shapes, to accommodate each other. Therefore, closed-packing between particles and a high average coordination number for each particle was possible. Because of these close-packing characteristics and fine pore channel sizes, curvatures on the pore surface were large. All of these features represented higher driving forces for sintering and faster densification kinetics could be expected.

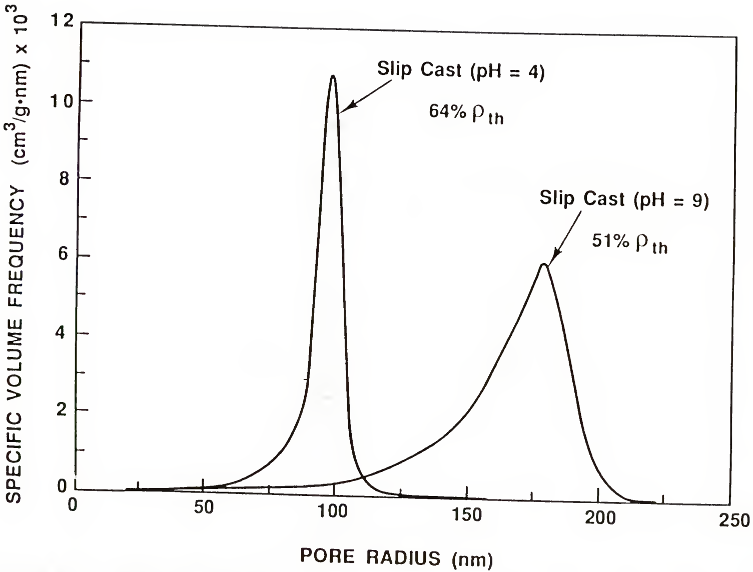

Figure 4.10 Plots of specific pore volume frequency vs. pore channel radius obtained by mercury porosimetry for SCD sample and SCF sample.

The green microstructure of SCF sample was also fairly uniform when viewed on a large scale (i.e., tens of microns or greater). No long range inhomogeneity or very large pores existed. However, at localized regions (i.e., in the micron range), it can be seen that most particles formed small clusters composed of several particles. The pore size within these clusters was small and the volume fraction of these pores is also small. The relatively larger pores between these clusters contributed to the majority of the pore volume and were seen as a peak with relative larger radius in the pore size distribution plot obtained by mercury porosimetry. The differences in the packing characteristics between the SCD and SCF samples played an important role in the sintering kinetics and microstructure evolution, as will be discussed later.

Dry pressing. Two compaction pressures were used to produce green bodies with different packing characteristics. Samples which had ~54% green relative density (designated DPH) were consolidated at a compaction pressure of ~31 MPa. These samples had the typical packing density of dry-pressed samples. Samples dry pressed at ~0.1 MPa (designated DPL) had ~41% green density and a very heterogeneous green microstructure. The pore size distributions obtained from mercury porosimetry for both dry-pressed samples are shown in Figure 4.11. Both samples showed broad pore size distributions that were bimodal, with a smaller peak at fine pore sizes and a major peak at larger sizes. The powder used for the dry pressing operation was obtained by breaking up and grinding powder cakes prepared by filtration of well-dispersed suspensions. Due to the incomplete break-up of the powder cake, granules having the same packing characteristics as the SCD sample (i.e., close

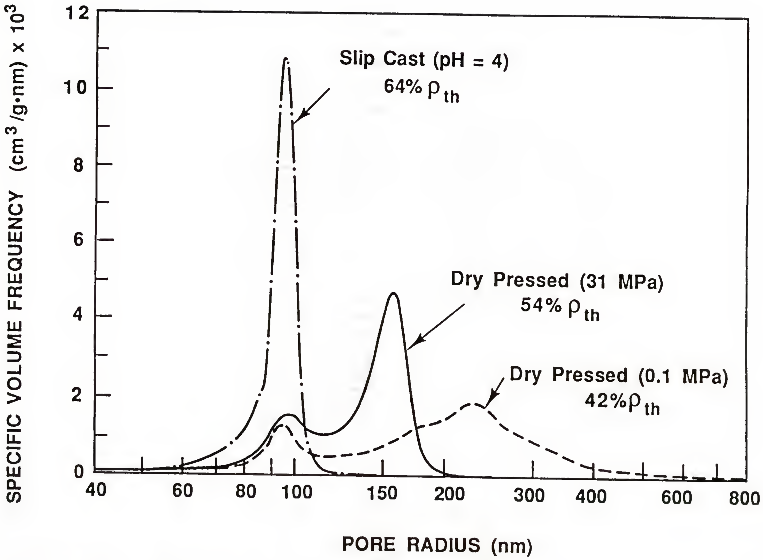

Figure 4.11 Plots of specific pore volume frequency vs. pore channel radius obtained by mercury porosimetry for SCD sample and dry-pressed samples.

packing) remained in the powder. These granules, which range in size from a few microns to more than 50 microns, will be referred to as "close-packed agglomerates". The pore sizes of these agglomerates account for the smaller peak in the distribution plots for the dry pressed samples (Figure 4.11). Note that the peak is at the same pore sizes observed in the distribution plot for the SCD sample. These agglomerates had a volume fraction of ~20% of the bulk volume of the dry-pressed compacts.

Aside from the close-packed agglomerates,the remaining structure of the dry pressed compacts was more porous and heterogeneous in nature and formed the major peak in the pore size distribution. The DPL samples had a very broad pore size distribution due to the very low pressing pressure. An SEM micrograph of the top surface of DPL samples is shown in Figure 4.12A. A very inhomogeneous microstructure with large agglomerates and large pores between these agglomerates can be seen. Microstructural inhomogeneities also can be clearly seen in the SEM photograph of the polished section of a slightly sintered sample (Figure 4.13A).

As the pressing pressure increases, the size and amount of large pores should decrease [Ree76]. Therefore, in the DPH samples, the extremely large pores were mostly eliminated. The pore sizes for the major peak in the distribution plot of the DPH sample were much smaller than that of the DPL sample. However, a bimodal pore size distribution still existed. This indicated that the close-packed agglomerates did not break down at this pressing pressure. Extremely large pores are not detected by mercury porosimetry for the DPH samples due to their low

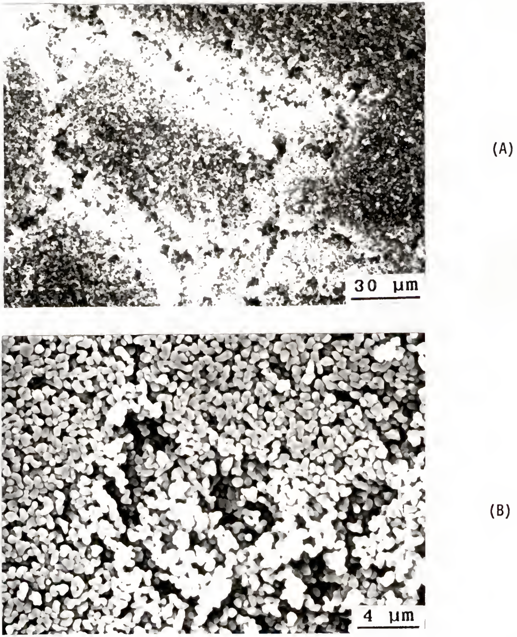

Figure 4.12 SEM micrographs for the top surfaces of (A) DPL sample and (B) DPH sample.

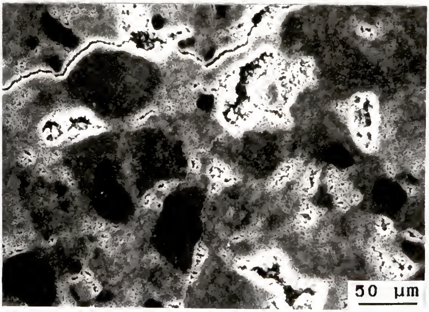

(A)

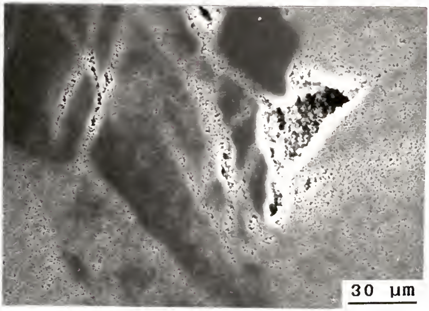

(B)

Figure 4.13 SEM micrographs of (A) DPL sample sintered at 1450°C, 0.5 h to 65.4% relative density and (B) DPH sample sintered at 1340°C, 1 h to 70.6% relative density.

concentration.* However, large pores in the DPH samples can be clearly seen in the SEM micrographs of green compacts (Figure 4.12B) and polished section of slightly sintered samples (Figure 4.13B).

The dark "grains" in Figure 4.13 are agglomerates with high packing density which densified much faster than surrounding matrix. Due to the differential shrinkage, cracking of the compact was observed in the dry-pressed samples (Figure 4.13A).

Effect of Particle Packing on Sintering Kinetics

Plots of relative density vs. sintering time at the temperatures of 1300, 1340, and 1450°C are shown in Figure 4.14, 4.15, and 4.16, respectively, for the slip cast and dry-pressed samples. At short sintering times, higher green density samples densify faster. For example, after sintering at 1340°C for 1 h, the relative density for the SCD samples (green density ~64%) increased ~19%, the DPH samples (green density ~54%) increased ~16%, the SCF samples (green density ~51%) increased ~15%, and the DPL samples (green density ~42%) increased ~13%. A similar trend (i.e., higher green density resulted in faster densification kinetics) was also observed in other studies [Bru62, Cam89, Kim87].

Plots of the densification rate** vs. sintering time are shown in

---

* The ink bottle effect [Orr69, Roo67] commonly observed in mercury porosimetry measurement can also hinder the possibility of observing large pores.

** The procedure for obtaining the densification rates is as follows: (1) manually drew smooth curves through the data points of the plots of relative density vs. sintering time (i.e., Figures 4.14 to 4.16), (2) digitized the smooth curve with a digitizing tablet interfaced with a personal computer, (3) fit segments of the

(continued...)

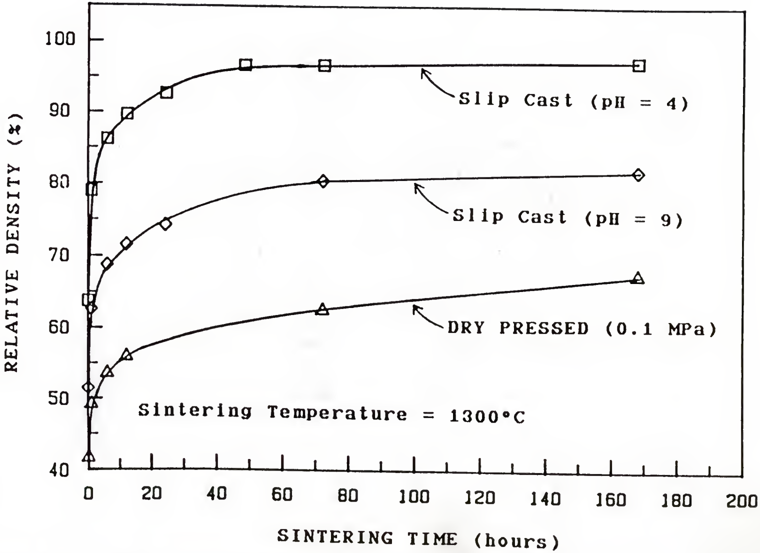

Figure 4.14 Plots of relative density vs. sintering time at 1300°C for the SCD, SCF and DPL samples.

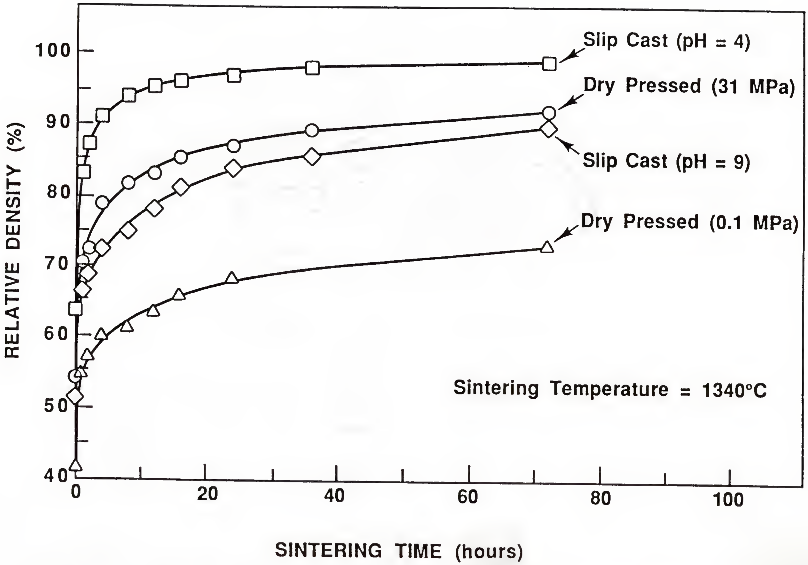

Figure 4.15 Plots of relative density vs. sintering time at 1340°C for the SCD, SCF, DPH, and DPL samples.

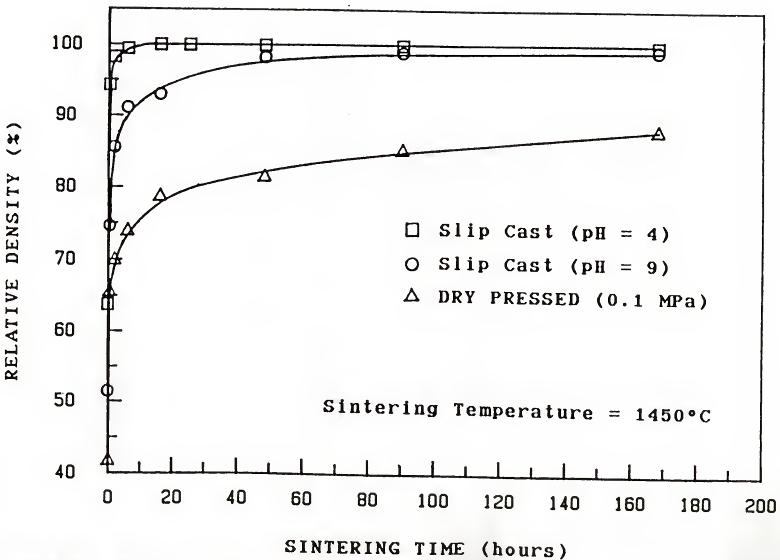

Figure 4.16 Plots of relative density vs. sintering time at 1450°C for the SCD, SCF and DPL samples.

Figures 4.17 to 4.19 for samples sintered at 1300, 1340, and 1450°C, respectively. In the early stages of sintering (i.e., at low sintering temperature and/or short sintering time) the SCD samples showed the highest densification rate and the DPL samples showed the lowest densification rate. The enhanced densification of the SCD sample in the early stages of sintering is consistent with the higher particle packing density and smaller pore channel size observed in the green body.

In addition to the enhanced densification rate in the early stages of sintering, the SCD samples also have the advantage that less shrinkage is required to achieve full density (due to the higher green density). Therefore, less sintering time or lower sintering temperatures are needed to reach high sintered density. For example, after 0.5 h sintering at 1450°C, the relative densities of SCD sample was 94.3%. With the same sintering schedule, the SCF and DPL samples only reached 74.6 and 65.4% relative density, respectively. Normally, densification rates fall off rapidly with increasing sintered density*. At high sintering temperature and/or long sintering time, the SCD sample had much higher sintered density; hence, the densification rates were the lowest which can be clearly seen in Figure 4.19.

As a consequence of the shorter sintering time and/or lower sintering temperature, finer sintered microstructure can be obtained for the SCD sample. This is illustrated in Figure 4.20 and 4.21 which show

---

**(...continued)
densification curves with polynomial equations (using a spline program), (4) take derivatives of the polynomial equations.

* For a sample with high sintered density, only small amount of pores are left; therefore, the distances between pores are large. Due to slow kinetics of long distance diffusion, the densification kinetics rapidly decreases.

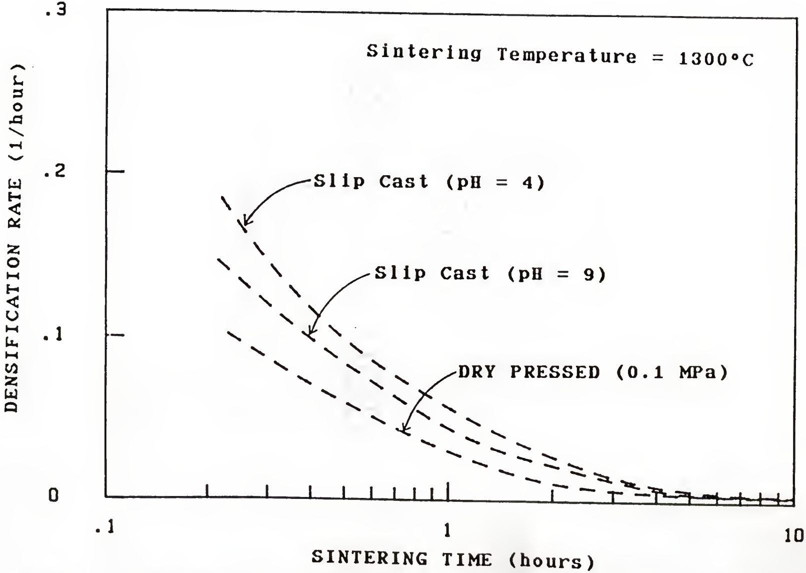

Figure 4.17 Plots of densification rate vs. sintering time at 1300°C for the SCD, SCF and DPL samples.

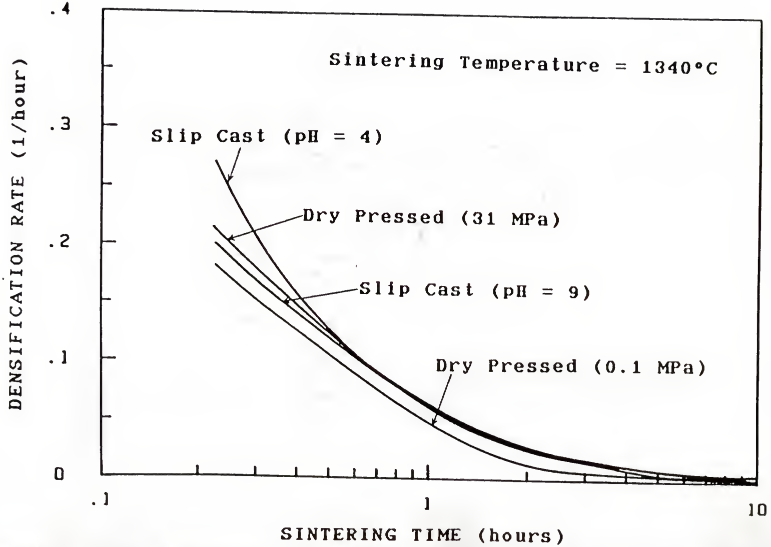

Figure 4.18 Plots of densification rate vs. sintering time at 1340°C for the SCD, SCF, DPH, and DPL samples.

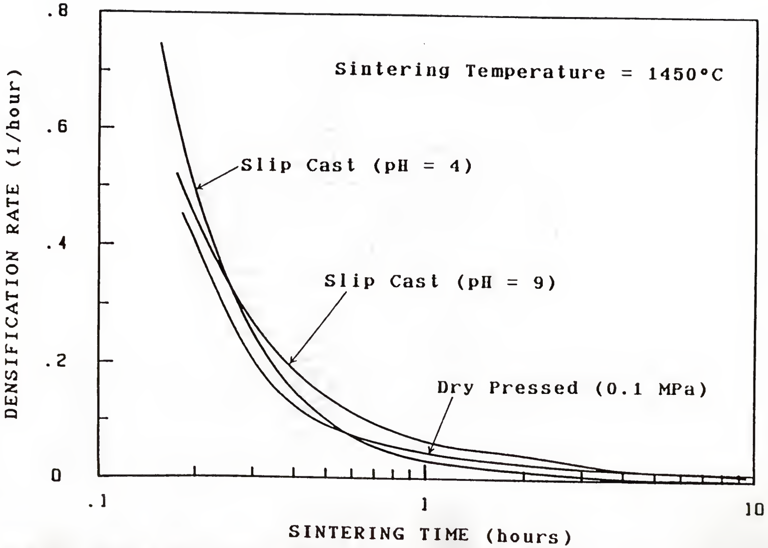

Figure 4.19 Plots of densification rate vs. sintering time at 1450°C for the SCD, SCF and DPL samples.

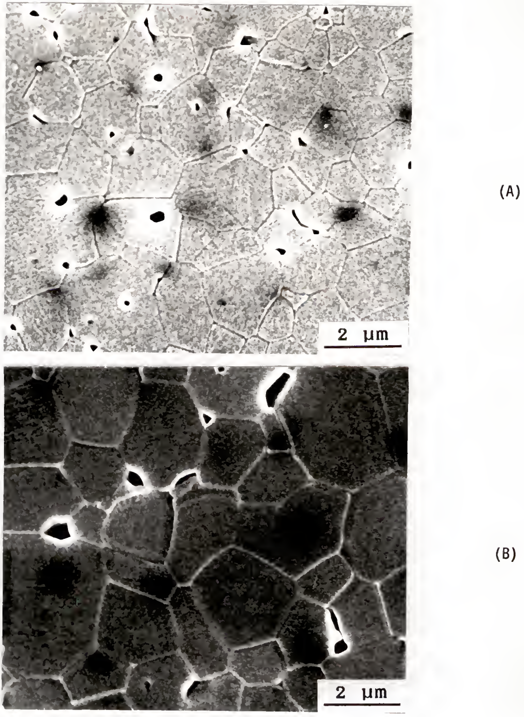

Figure 4.20 SEM micrographs of (A) SCD sample sintered at 1340°C, 36 h to 98.0% relative density and (B) SCF sample sintered at 1450°C, 48 h to 98.3% relative density.

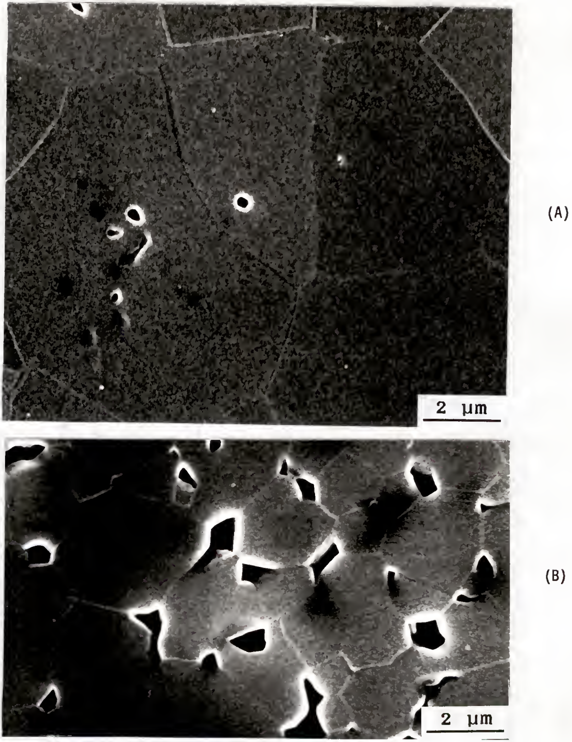

Figure 4.21 SEM micrographs of DPL sample sintered at 1450°C, 168 h to 97.8% bulk density : (A) Dense regions and (B) porous regions.

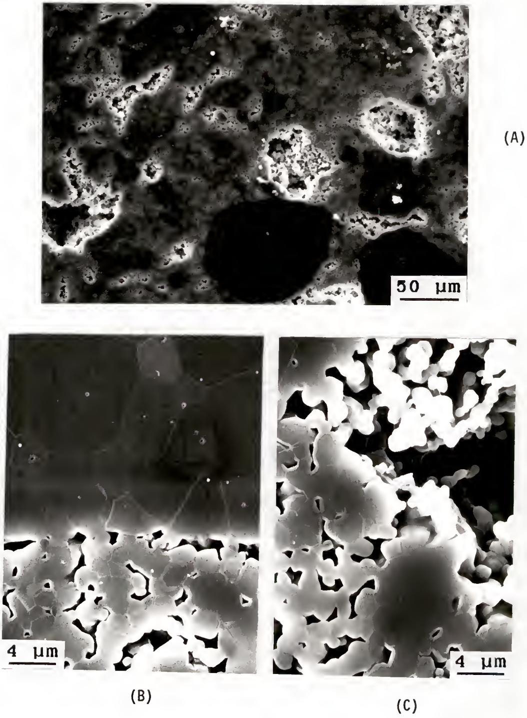

Figure 4.22 SEM micrographs of DPL sample sintered at 1600°C, 48 h to 89.2% bulk density (A) low magnification, (B) and (C) high magnification.

the SEM micrographs for samples sintered to ~98% relative density. The SCD sample sintered at 1340°C for 36 h had a mean grain intercept of 1.07 μm (Figure 4.20A). The SCF sample sintered at 1450°C for 48 h had a mean grain intercept of 1.83 μm (Figure 4.20B). Due to the relatively homogeneous green microstructures of both slip cast samples, homogeneous sintered microstructures were obtained.

Due to the heterogeneities and the existence of large pores in the dry-pressed samples, the DPH samples needed much longer sintering time (168 h at 1450°C) to reach ~98% relative density. As expected, the mean grain intercept was also larger (2.24 μm). The sintered microstructure also showed severe inhomogeneity--nearly fully dense regions (which had undergone extensive grain growth), Figure 4.21A, coexisted with highly porous regions (which had much smaller grain sizes), Figure 4.21B.

Because of the very low green density and existence of extremely large pores, the DPL samples only reached ~89% relative density even after 24 h sintering at 1600°C. No density increase was obtained at further sintering (e.g., 48 h at 1600°C). An extremely heterogeneous microstructure was obtained in these samples, as shown in Figure 4.22. Although the mean grain intercept was only ~2.8 μm, grain sizes larger than 10 μm were observed in the regions that were initially close-packed agglomerates (Figure 4.22B).

Plots of densification rate vs. relative density for samples sintered at 1300, 1340, and 1450 °C are shown in Figures 4.23, 4.24, and 4.25, respectively. All samples showed a rapid decrease in densification rate in the early stages of sintering. If we compare the densification rate of different samples at constant relative density, it is clear that the samples with higher green density have higher densification rate.

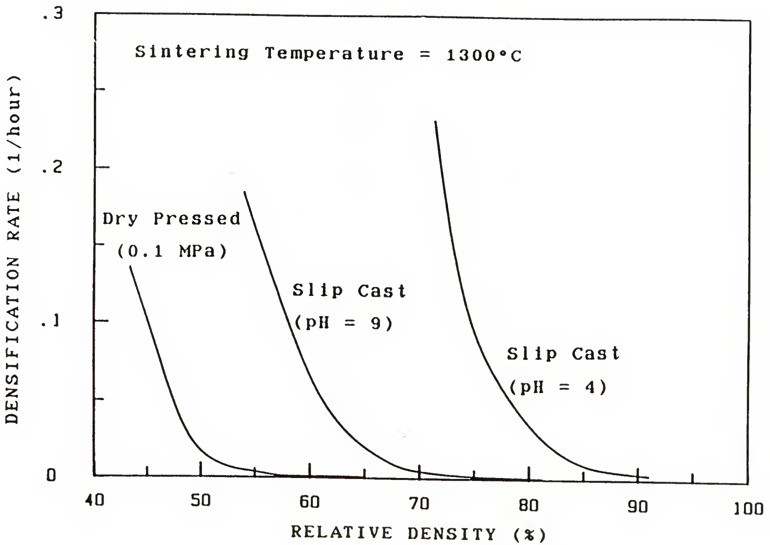

Figure 4.23 Plots of densification rate vs. relative density at 1300°C for the SCD, SCF, and DPL samples.

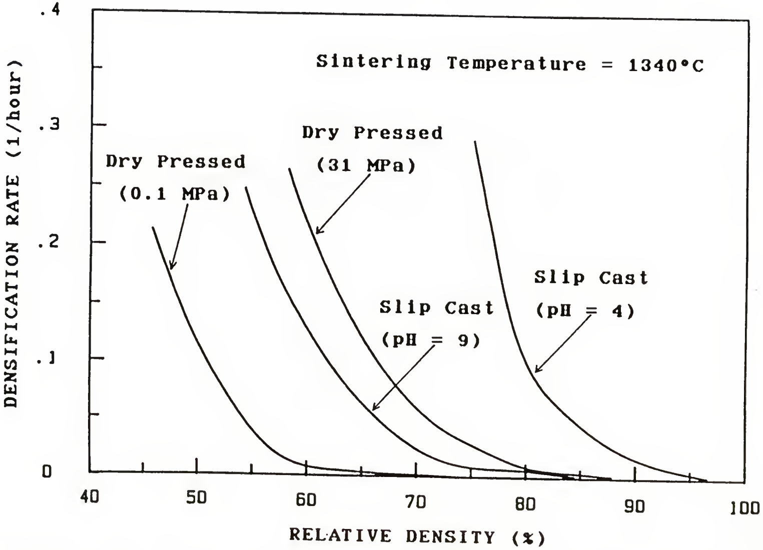

Figure 4.24 Plots of densification rate vs. relative density at 1340°C for the SCD, SCF, DPH, and DPL samples.

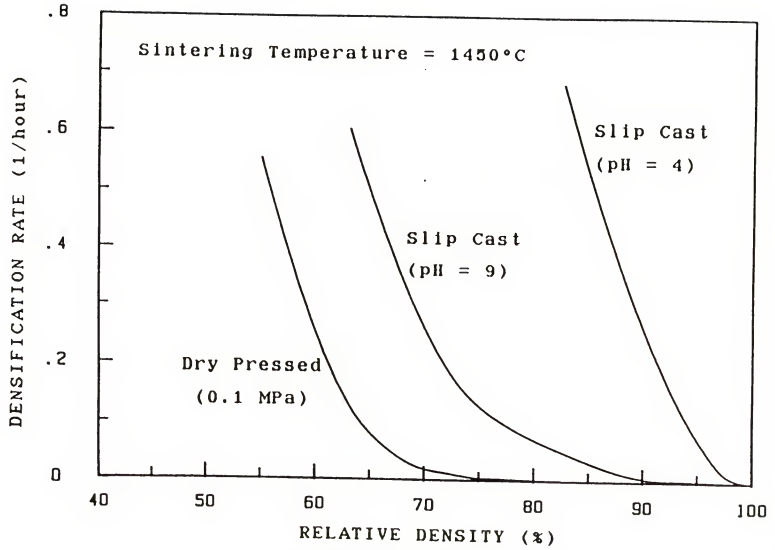

Figure 4.25 Plots of densification rate vs. relative density at 1450°C for the SCD, SCF, and DPL samples.

For example, at 1340°C (Figure 4.24), the SCD samples still show a high densification rate at ~90% relative density, while the densification rate of the other samples is already very low. This is because the SCD samples have higher green density and higher densification rate in the early stages of sintering. These samples reach high density in a shorter time, while maintaining a fine microstructure (i.e., fine grain and pore sizes). Therefore, higher densification rate is maintained at high relative density.

It is also interesting to directly compare the densification behavior for the DPH and SCF samples since they had similar relative density (i.e., ~54% for DPH sample and ~51% for SCF sample) but significant difference in microstructure homogeneities. The sintered densities of both samples and the density differences are shown in Table 4.1 for various sintering schedules. Due to the slightly higher green density and the existence of close-packed agglomerates (which can quickly densify), the DPH sample showed higher densification rate in the early stages of sintering. The maximum density difference was obtained at about 80% relative density (i.e., 1340°C, 12 h). However, the

Table 4.1 Comparison of Density Evolution Between SCF and DPH Samples

Sintering Schedule	Density of SCF Samples (D_{SCF})	Density of DPH Samples (D_{DPH})	$D_{DPH}-D_{SCF}$
Green Body	51.4	54.2	2.8
1340°C, 1 h	66.4	70.6	4.2
1340°C, 12 h	78.1	83.2	5.1
1340°C, 36 h	85.6	89.4	3.8
1340°C, 72 h	90.0	92.2	2.2
1375°C, 155 h	95.1	96.3	1.2
1450°C, 90 h	99.0	96.8	-2.2

densification rate of the DPH sample decreased faster and the density differences decreased with further sintering. The density of the SCF sample even became higher after 90 h sintering at 1450°C. The retardation on the densification of the DPH sample at high relative densities is probably due to the existence of large pores which are very difficult to be eliminated [Kin67, Zha88]. Furthermore, in order to reach full density, the volume shrinkage for the close-packed agglomerates (~64% green density) is about 36%. However, about 50% volume shrinkage is required for the more porous matrix (~50% green density) to reach full density. In the late stages of sintering, the close-packed agglomerates become fully dense while the surrounding matrix remain porous. The fully dense regions behave like inclusions toward the porous matrixes and densification is retarded. [Hsu86, Rah87, Raj84].

Volume shrinkage. Volume shrinkage (or linear shrinkage) is an important parameter in sintering studies and has long been used to report sintering kinetics. Measuring shrinkage alone (e.g., by using dilatometer) can be a fast and useful way to study the sintering behavior of samples with similar green density. However, extreme precaution must be taken in interpreting shrinkage data of samples having significant differences in starting density. For example, after 2 h sintering at 1340°C, the relative density of the SCD sample increased ~23% (i.e., from ~64% to ~87%), while the DPL samples increased only ~15% (i.e., from ~42% to ~57%). This suggested that the SCD sample had much higher densification rate in the first 2 h sintering at 1340°C. However, both samples have an equal value of volume shrinkage (~26%) in this period. It is surprising that same shrinkage kinetics can be obtained for samples with significant differences in green density and densification kinetics.

The finding that shrinkage kinetics can not be used to differentiate the early stages densification behavior of samples with various green densities is further demonstrated in Figures 4.26 to 4.28 in which plots of volume shrinkage vs. sintering time are shown for the sintering temperature of 1300, 1340, and 1450°C, respectively. At low sintering temperature (Figure 4.26) or short sintering time at higher temperature (Figure 4.27), all samples showed similar volume shrinkage kinetics. For the SCD samples, shrinkage stopped (and the shrinkage values were lower compared to the other samples) after ~70, ~20 and ~1 hours of sintering at the temperature of 1300, 1340, and 1450°C, respectively. This is because the SCD sample is approaching theoretical density and no further shrinkage can be obtained. The green density of the SCD sample was ~64% relative density and, therefore, the maximum volume shrinkage that could be (and was) achieved is ~36%. The DPL sample has ~42% green density and, therefore, ~58% volume shrinkage theoretically could be obtained for this sample. Therefore, it is reasonable to expect that the DPL sample should show higher volume shrinkage at prolonged sintering time and/or high sintering temperature. Due to the existence of extremely large pores (which limit the achievable density), the DPL sample did not show higher volume shrinkage compared to the SCF sample at the sintering temperature of 1340°C (Figure 4.27). However, slightly higher volume shrinkage was observed at 1450°C (Figure 4.28).

Occhionero investigated the linear shrinkage of alumina compacts with green densities in the range ~40 to ~55% relative density and also

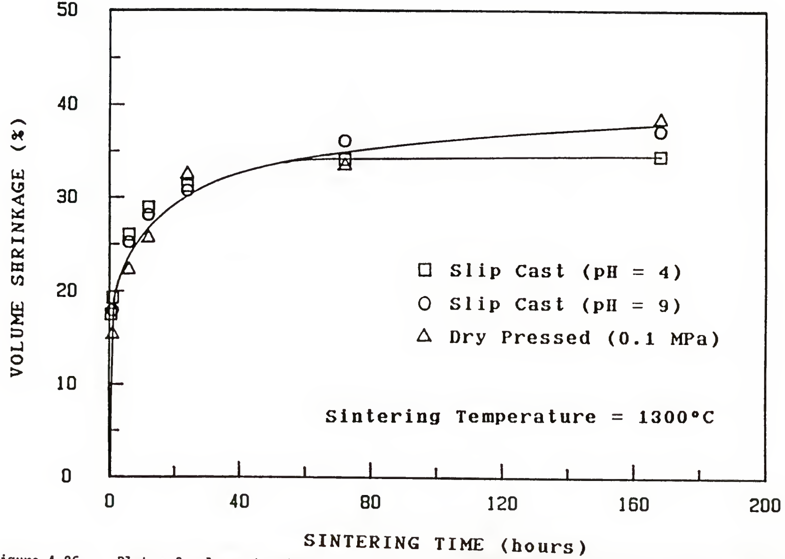

Figure 4.26 Plots of volume shrinkage vs. sintering time at 1300°C for the SCD, SCF and DPL samples.

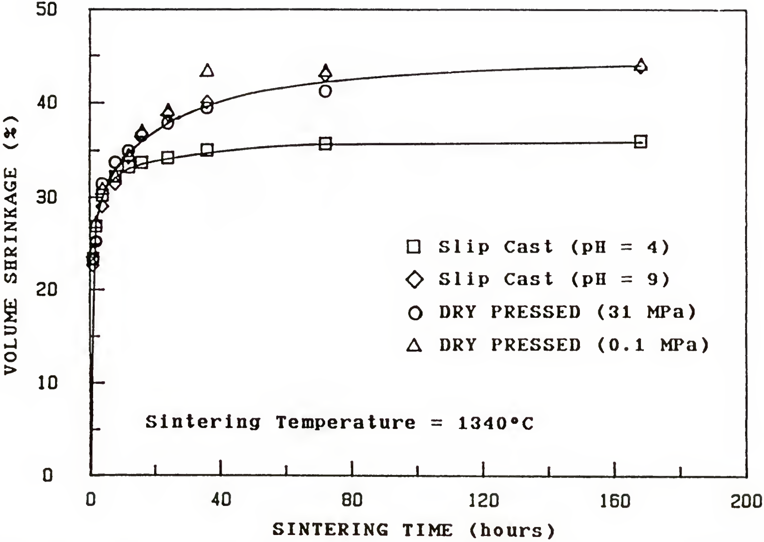

Figure 4.27 Plots of volume shrinkage vs. sintering time at 1340°C for the SCD, SCF, DPH, and DPL samples.

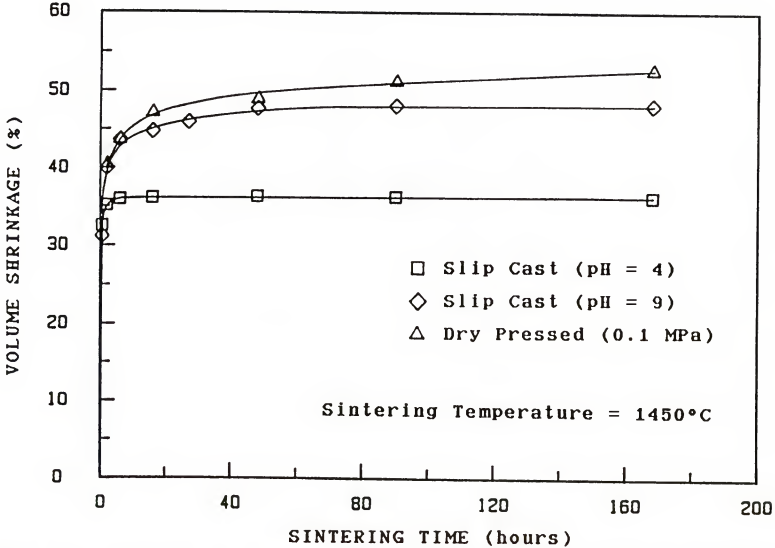

Figure 4.28 Plots of volume shrinkage vs. sintering time at 1450°C for the SCD, SCF and DPL samples.

found that green density had no effect on the initial stage shrinkage kinetics [Occ86]. Similar results were also reported by Zheng and Reed [Zhe89]. Carbone and Reed [Car78a] studied the shrinkage kinetics of zirconia compacts and also found that the linear shrinkage rate of the initial and intermediate stages were independent of the initial pore characteristics. Based on the shrinkage kinetics, they concluded that the initial- and intermediate-stage sintering behavior was independent of the initial pore characteristics. However, this conclusion is misleading since the green microstructure has dramatic effect on densification kinetics (as shown in Figure 4.17 to 4.19) and on the microstructural evolution (as will be discussed further below).

Effect of Temperature on Sintering Kinetics

Plots of relative density vs. sintering time at several sintering temperatures are shown in Figures 4.29, 4.30, and 4.31 for SCD, SCF, and DPL samples, respectively. It is obvious that higher densification rates were observed at higher temperatures. For example, for SCD samples, the relative density increased ~13%, ~23%, and ~34%, after 2 h sintering at 1260, 1340, and 1450°C, respectively. There is nothing surprising about these results since sintering rate is dependent upon diffusion coefficients, and diffusion coefficients increase exponentially with increasing temperature.

Plots of densification rate vs. relative density at various temperatures are shown in Figure 4.32, 4.33 and 4.34 for the SCD, SCF, and DPL samples, respectively. Comparing at a constant sintered density, samples for each packing condition showed higher densification rates at higher temperatures.

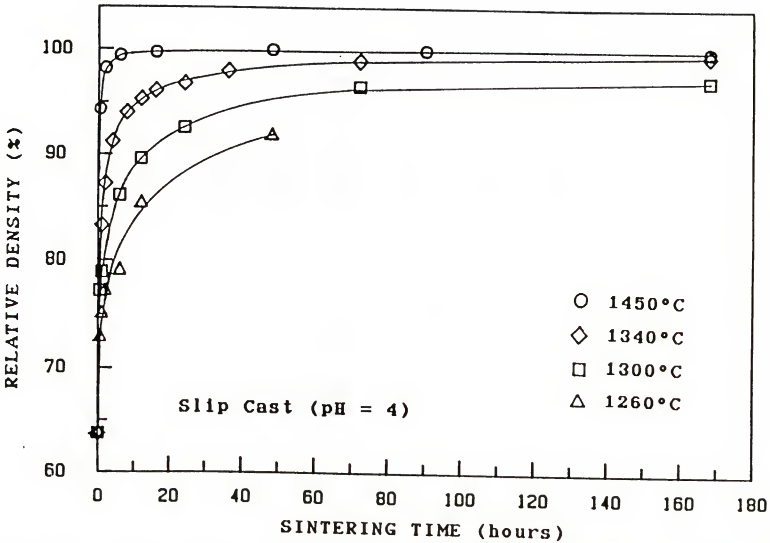

Figure 4.29 Plots of relative density vs. sintering time for the SCD sample sintered at 1260, 1300, 1340, and 1450°C.

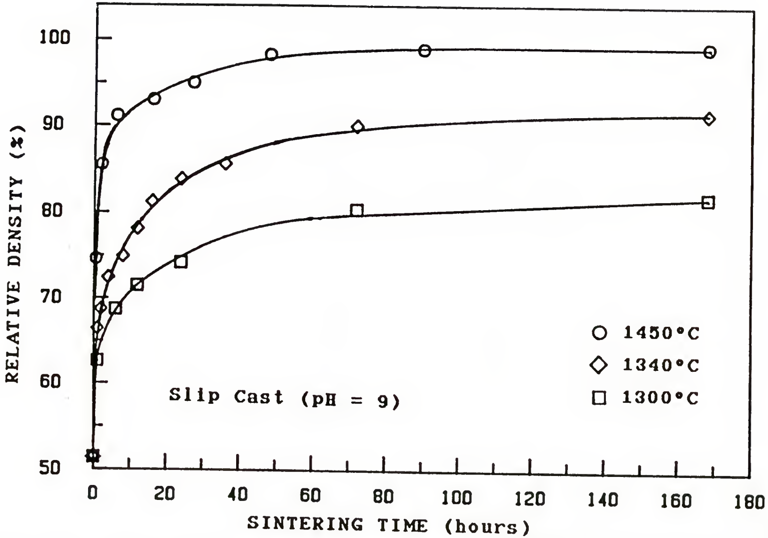

Figure 4.30 Plots of relative density vs. sintering time for the SCF sample sintered at 1300, 1340, and 1450°C.

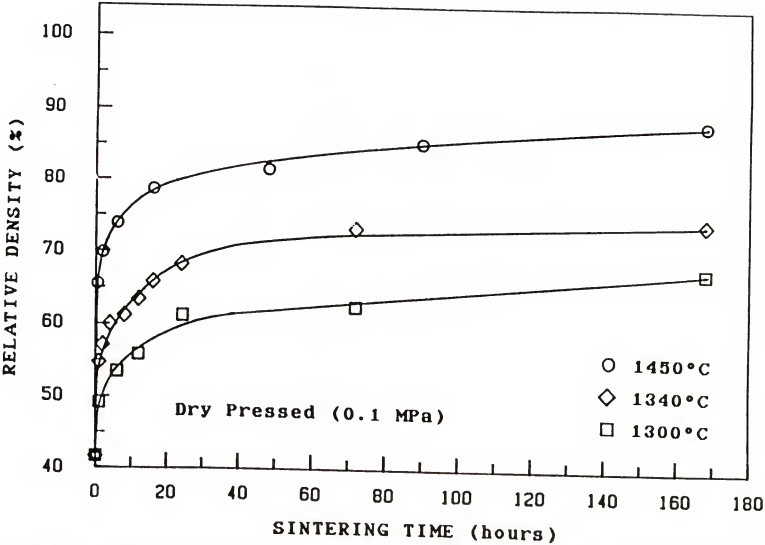

Figure 4.31 Plots of relative density vs. sintering time for the DPL sample sintered at 1300, 1340, and 1450°C.

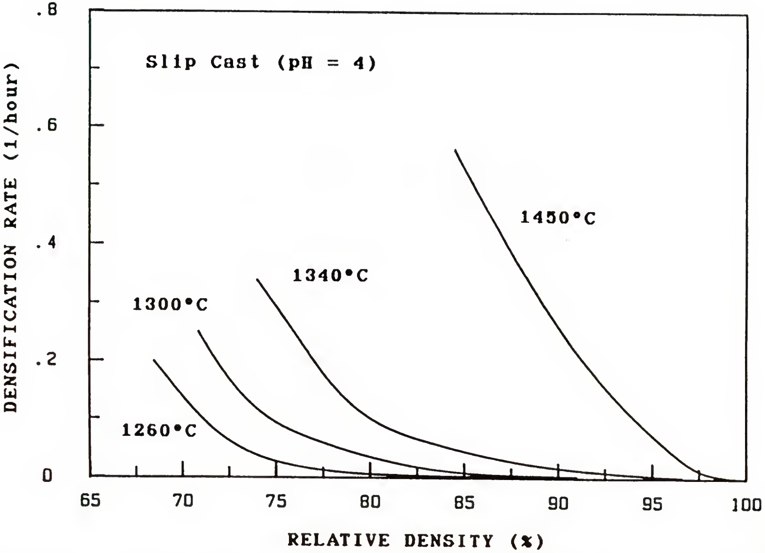

Figure 4.32 Plots of densification rate vs. relative density for the SCD sample sintered at 1260, 1300, 1340, and 1450°C.

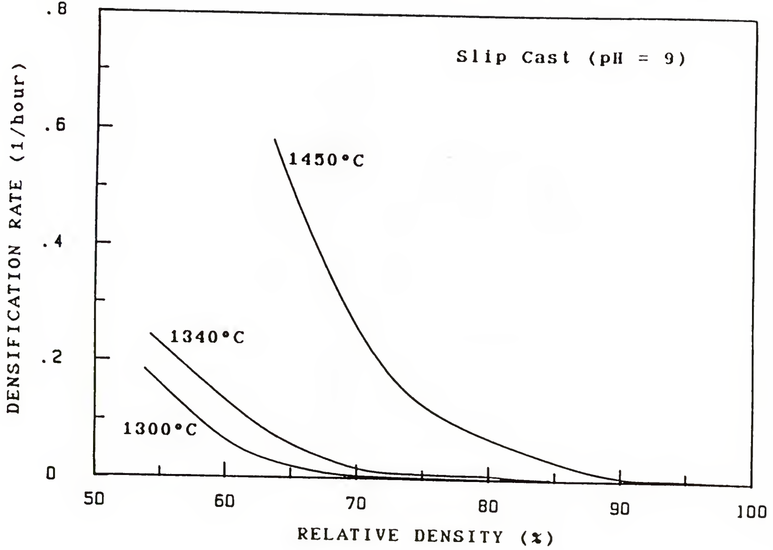

Figure 4.33 Plots of densification rate vs. relative density for the SCF sample sintered at 1300, 1340, and 1450°C.

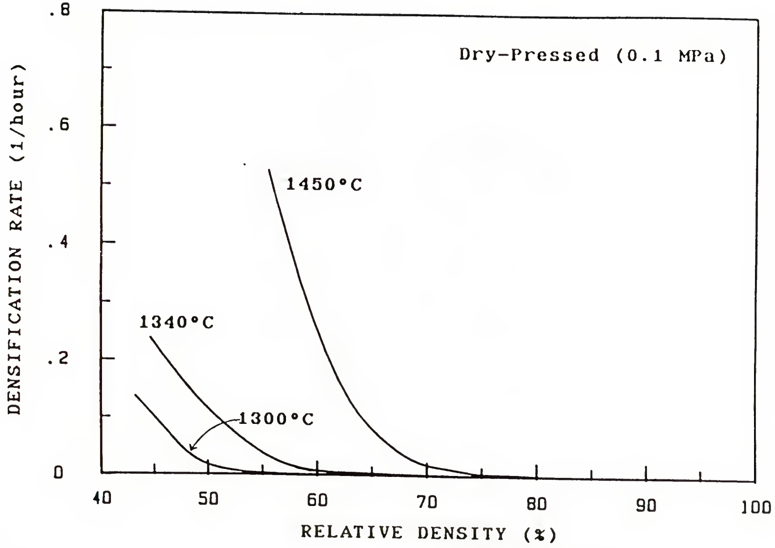

Figure 4.34 Plots of densification rate vs. relative density for the DPL sample sintered at 1300, 1340, and 1450°C.

By assuming that the reciprocal of sintering time (needed to obtain a given grain size) is proportional to the rate constant for grain growth, Coble derived apparent activation energy for grain growth [Cob61]. The same approach can also be used to obtain apparent activation energy for densification. It is assumed that the reciprocal of the sintering times needed to reach a given density at various temperatures are proportional to the rate constant of densification at that temperature. Therefore, by plotting ln(reciprocal time) vs. reciprocal absolute temperature, the apparent activation energy of densification can be obtained from the slope. Figure 4.35 shows plots of ln(reciprocal time*) vs. reciprocal absolute temperature for SCD, SCF and DPL samples sintered to 90%, 80% and 70% relative density, respectively. The apparent activation energies derived from the slopes are ~627, ~625, and ~596 KJ/mole for SCD, SCF and DPL samples, respectively. These values agree very well with the values reported by Bruch (~628 KJ/mole [Bru62]), Wang (~628 KJ/mole [Wan76]) and Janney and Kimrey (~575 KJ/mole [Jan89]). Bruch observed significantly higher apparent activation energy (~1150 KJ/mole) for the low green density samples (~22% relative density) [Bru62]. However, similar apparent activation energy was obtained in the present study for samples with various packing densities. Due to the extremely low green density for the sample used in Bruch's studies, very severe microstructural

---

* The sintering times needed to reach a given density for each sample (i.e., 90%, 80%, and 70% relative density for SCD, SCF and DPL samples, respectively) were estimated from the manually smoothed densification curves. The SCD samples sintered at 1450°C were not used to derive activation energy. Due to the extremely high densification rate, an accurate estimation on the sintering time (needed to obtain 90% relative density) cannot be achieved.

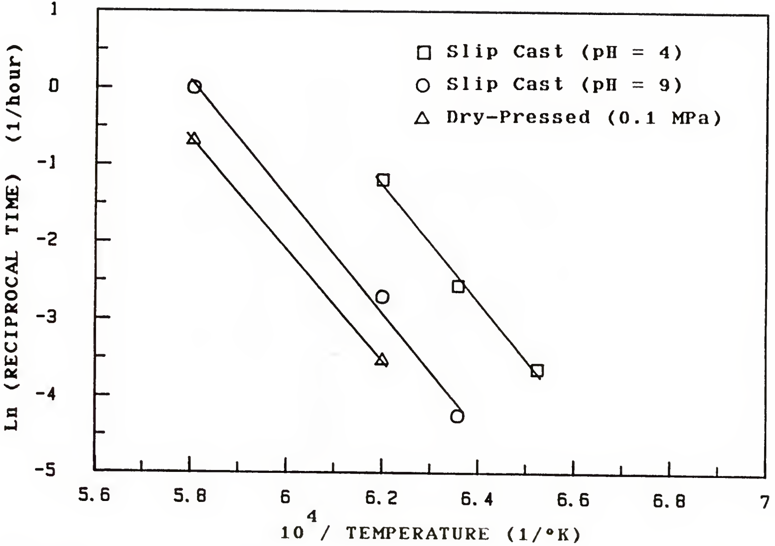

Figure 4.35 Plots of Ln(reciprocal sintering time) vs. reciprocal absolute temperature for the SCD, SCF, and DPL samples.

heterogeneities and larger voids should be obtained. This might be the reason that a significantly higher apparent activation energy was observed.

Effect of Particle Packing on Microstructure Evolution

Figures 4.36 to 4.43 show the SEM photographs for samples with different consolidation conditions at various density levels. The SCD samples showed homogeneous microstructures over the entire density range (Figures 4.36A, 4.38A, 4.41A, 4.42A). This is the direct consequence of the very good homogeneity obtained in the green bodies. In the early stages of sintering, the microstructures of the SCF sample showed small fully-dense clusters with relatively larger inter-cluster pores (Figures 4.36B and 4.38B). This is the result of the small high-packing-density clusters discussed previously. No large scale inhomogeneities were observed for the SCF samples.

Kimura [Kim87] studied the sintering and microstructural development of high purity alumina (AKP 15) samples slip cast from pH = 2 (i.e., dispersed) and pH = 9 (i.e., flocculated) suspensions. They observed duplex structure consisting of well- and poorly-sintered regions for both pH = 2 and pH = 9 samples in the early stages of sintering. The duplex structure observed in their study might be due to incomplete breakup/removal of agglomerates. A homomixer was used in their study for suspension preparation which is not effective in breaking up agglomerates. Therefore, even in pH = 2 and pH = 4 suspensions (which should be well-dispersed due to high zeta potential), agglomerates still existed. These agglomerates might result in the localized densification observed in their study. In the present study,

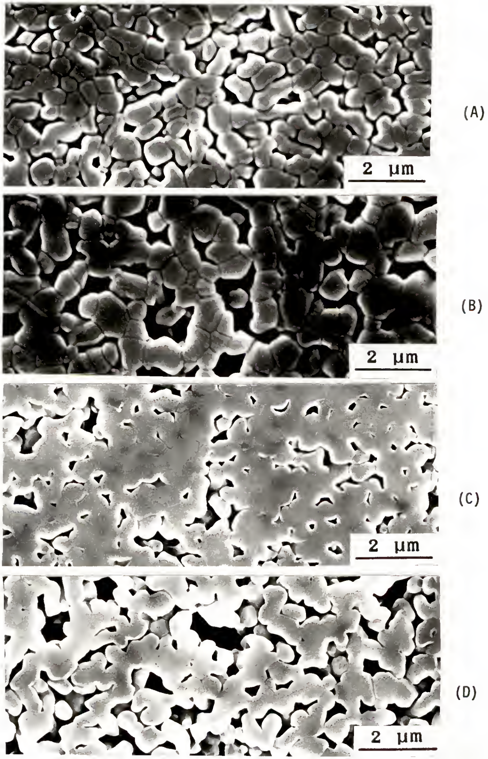

Figure 4.36 SEM micrographs of (A) SCD sample sintered at 1260°C, 0.5 h to 72.8% relative density, (B) SCF sample sintered at 1340°C, 8 h to 74.9% relative density, and (C) and (D) DPH sample sintered at 1340°C, 2 h to 72.5% relative density : (C) agglomerated regions and (D) porous regions.

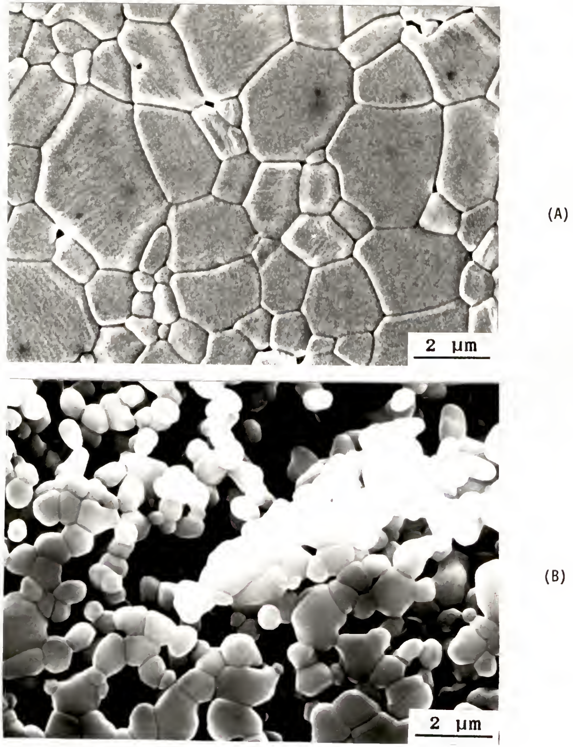

Figure 4.37 SEM micrographs of DPL sample sintered at 1450°C, 6 h to 73.8% relative density: (A) agglomerated regions and (B) porous regions.

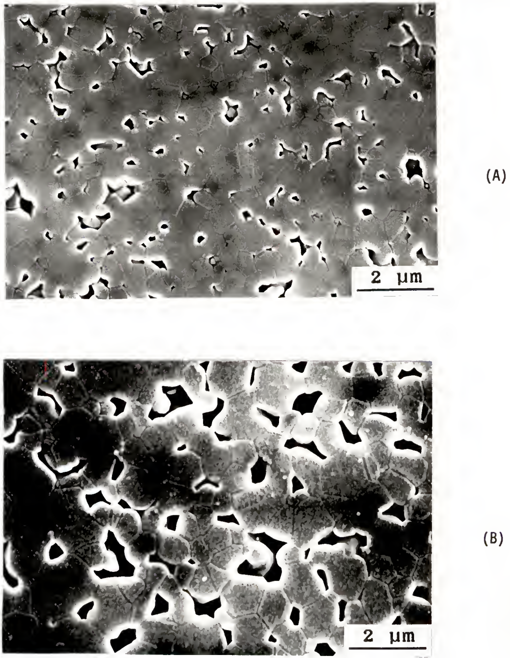

Figure 4.38 SEM micrographs of (A) SCD sample sintered at 1340°C, 2 h to 87.2% relative density and (B) SCF sample sintered at 1340°C, 36 h to 85.6% relative density.

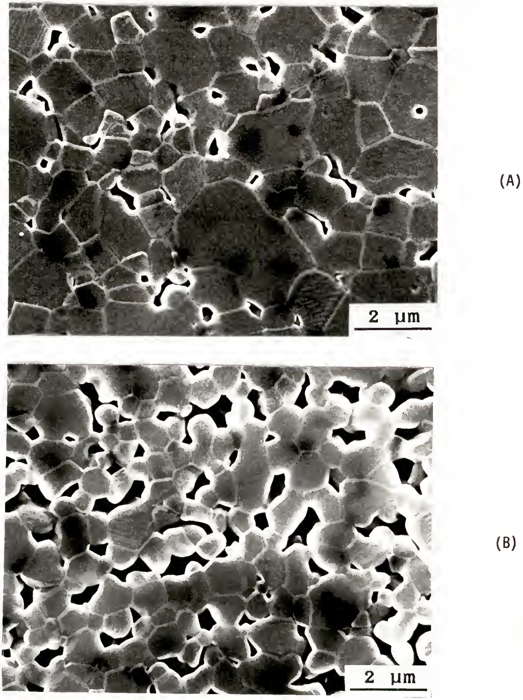

Figure 4.39 SEM micrographs of DPH sample sintered at 1340°C, 16 h to 85.4% relative density: (A) agglomerated regions and (B) porous regions.

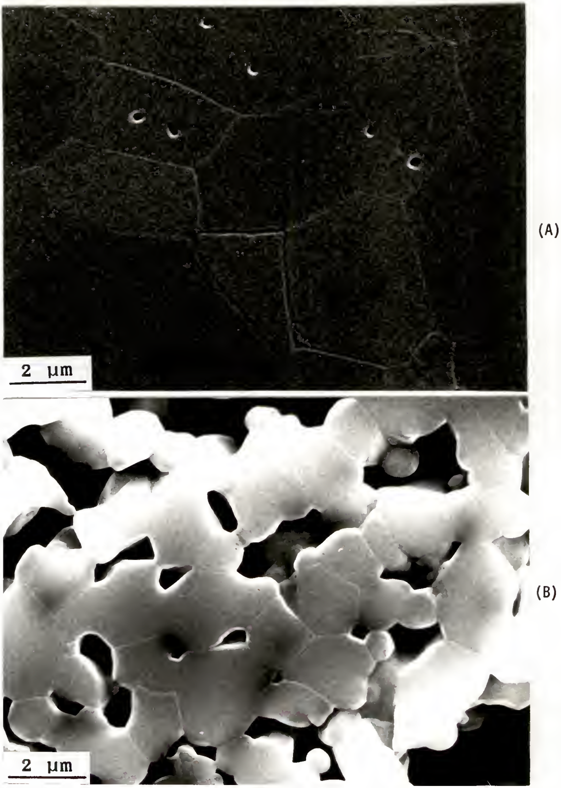

Figure 4.40 SEM micrographs of DPL sample sintered at 1450°C, 90 h to 85.2% relative density: (A) agglomerated regions and (B) porous regions.

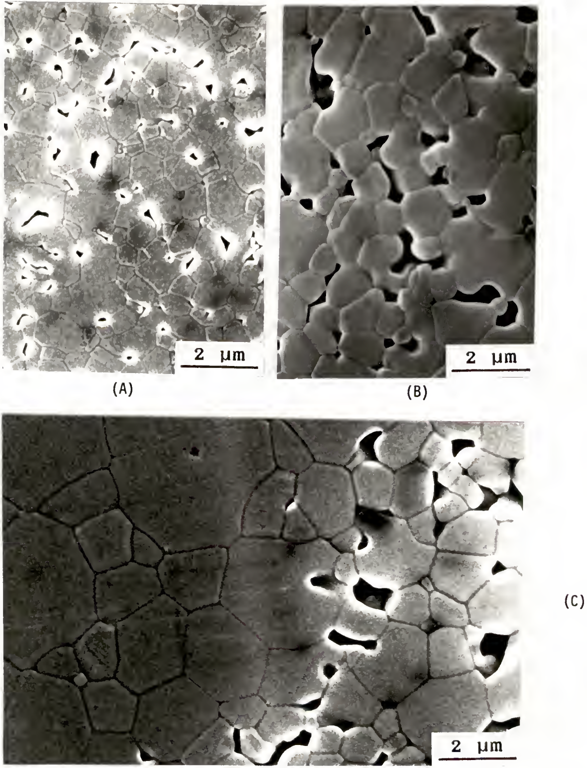

Figure 4.41 SEM micrographs of (A) SCD sample sintered at 1340°C, 4 h to 91.2% relative density (B) SCF sample sintered at 1450°C, 6 h to 91.1% relative density, and (C) DPH sample sintered at 1340°C, 72 h to 92.2% relative density.

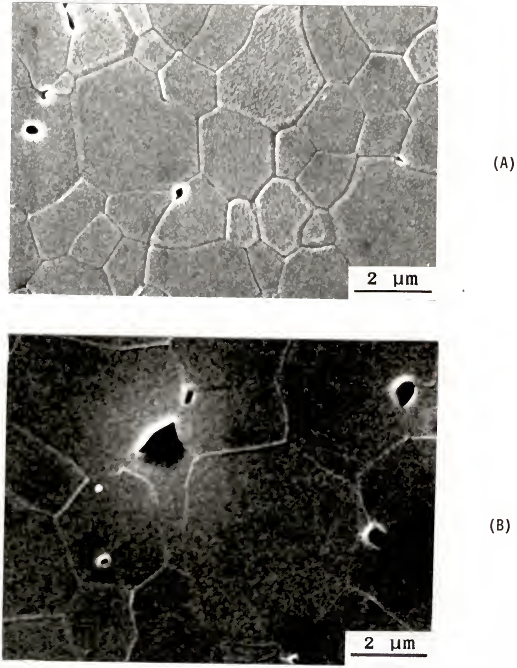

Figure 4.42 SEM micrographs of (A) SCD sample sintered at 1450°C, 6 h to 99.4% relative density and (B) SCF sample sintered at 1450°C, 168 h to 99.3% relative density.

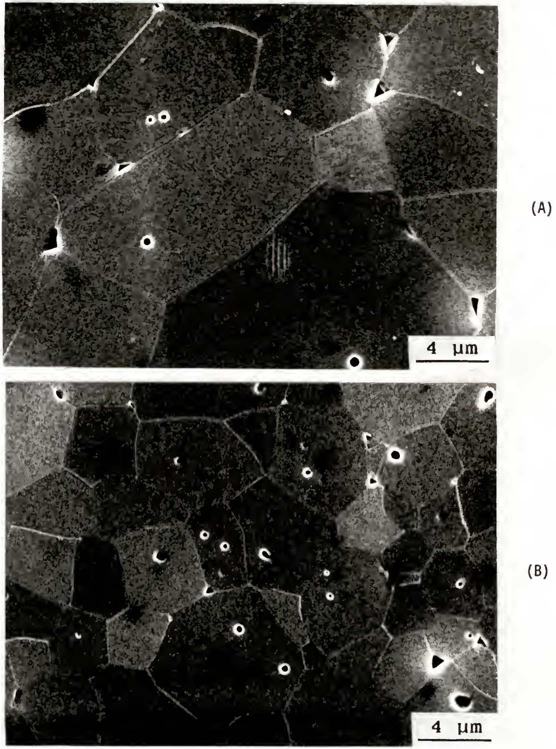

Figure 4.43 SEM micrographs of DPH sample sintered at 1600°C, 24 h to 99.3% relative density: (A) agglomerated regions and (B) porous regions.

because complete removal/breakup of agglomerates was achieved by powder classification and ultrasonication, homogeneous green microstructures were obtained for the slip cast compacts. Duplex structure was not observed. On the other hand, the DPH and DPL samples had severe heterogeneous green microstructures. These microstructural heterogeneities remained throughout the entire densification process and resulted in differences in microstructural development which can be clearly seen in the SEM photographs at various density levels (Figures 4.36C, 4.36D, 4.39A, 4.39B, 4.41, 4.43A, and 4.43B for the DPH samples; Figures 4.37A, 4.37B, 4.40A, and 4.40B for the DPL samples).

Despite the significant differences in microstructural homogeneities, all sintered samples in the present study showed equiaxed grains over the entire density range (Figures 4.36 to 4.43). Kimura et al. [Kim87] observed growth of elongated grains for samples with >95% relative density. The reason for the abnormal grain growth was not given. Bennison and Harmer [Ben83, Ben85, Har84] also observed elongated grains in samples prepared from less pure (99.98%) alumina powders. Glassy phases at the grain boundaries were observed in these samples. By using higher purity (> 99.99%) alumina powder, equiaxed grains were obtained.

Figure 4.44 shows plots of relative density values for the slip cast and dry-pressed samples which were determined by (1) the Archimedes displacement method and (2) quantitative stereological measurements of the pore volume fraction, Vp (i.e., the relative density equals 1-Vp). The straight line in Figure 4.44 represents ideal agreement between values determined by the two methods. All of the data in Figure 4.44 falls close to this ideal line which implies that representative

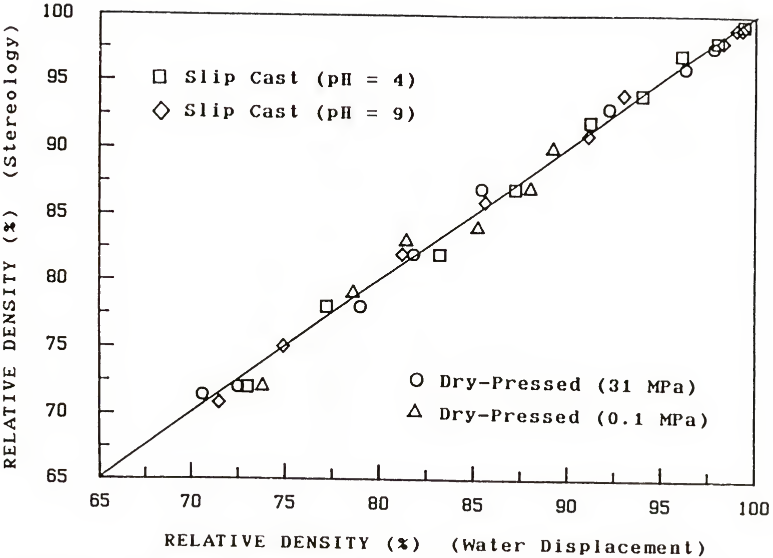

Figure 4.44 Comparison of relative densities determined by quantitative stereology and Archimedes water displacement method for SCD, SCF, DPH, and DPL samples.

microstructures were obtained for the quantitative stereological measurements. Quantitative characterization and detailed comparison of the effect of packing conditions on the evolution of various microstructural feature (e.g., grain size, pore size, ... etc.) throughout the densification process will be discussed in the following section.

Grain intercept size. Figure 4.45 shows plots of average grain intercept size vs. sintered relative density for slip cast samples. For the SCD sample, there was essentially no increase in the average intercept size until the relative density became higher than ~90%. In contrast, the average intercept size of SCF sample started increasing at ~75% relative density. Similar results were observed by Cameron and Raj [Cam89]. These differences in grain growth behavior are a consequence of the differences in the initial particle packing of the green compacts. First, as discussed before, the SCF sample had lower green density and lower densification rate and, therefore, a more extended sintering schedule (longer time or/and higher temperature) is needed in order to reach same density level as SCD sample. Therefore, more grain growth occurs in the SCF sample. Second, the SCF sample had a less homogeneous green microstructure (i.e., small clusters with higher packing density and finer pore size and regions containing larger intercluster pores). During sintering, the clusters densify rapidly and support grain growth, but the overall bulk density remains low due to the larger intercluster pores. Thus, the average intercept size increases at a relatively low density. In contrast, the SCD sample had higher packing density, more homogeneous microstructure, and smaller pore size; therefore, high

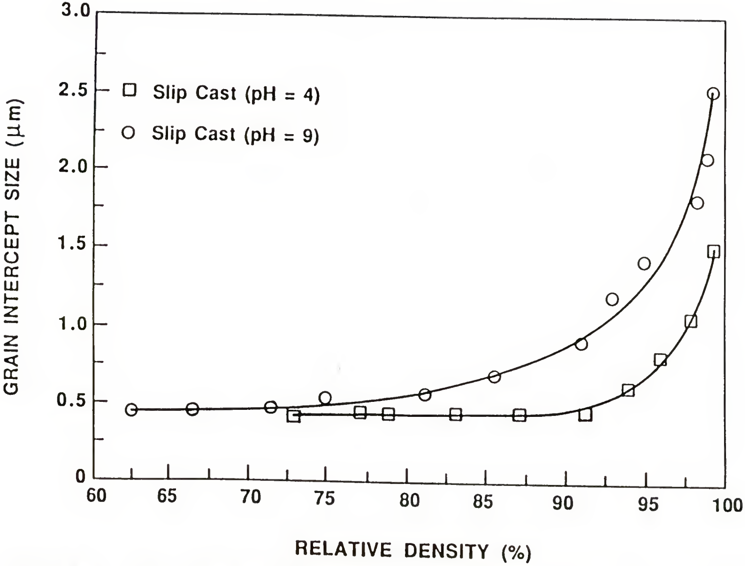

Figure 4.45 Plots of average grain intercept size vs. relative density for SCD and SCF samples.

densification rate could be obtained uniformly over the entire sample and high density could be reached without significant grain growth.

Below ~ 90% relative density, pore morphology of both slip cast samples consisted primarily of interconnected pore channels. This is illustrated by the plot of percentage of open porosity vs. sintered density shown in Figure 4.46. Almost all of the porosity remains open in samples with relative density ≤ 90%. It is well-accepted that continuous pore channels are very effective in preventing grain boundary migration. This also accounts for the fine grain size obtained for the SCD sample with less than 90% relative density. Figure 4.46 also shows that the percentage of open pores decreases rapidly above ~90% relative density. Virtually only closed pores remain when the sample reaches ~95% relative density. The increase in the percentage of closed pores represents the collapse of continuous pore channels into isolated pores. The isolated pores offer less resistance to retard grain boundary migration. Therefore, the grain size of both samples rapidly increased when density became larger than ~95% relative density. The decreased drag force on the grain boundaries should result in the onset on pore-grain boundary separation. Plots of number percentage of intragranular pores vs. sintered density for both slip cast samples are shown in Figure 4.47. As expected, the number percentage of intragranular pores increased rapidly after the density became larger than ~97% relative density.

Figure 4.48 shows plots of average grain intercept size vs. sintered density for the dry-pressed samples, and for comparison, the SCD sample. The average intercept size starts to increase at much lower relative densities for the dry pressed samples compared to the SCD sample. For the DPH sample, this increase begins at less than 78%

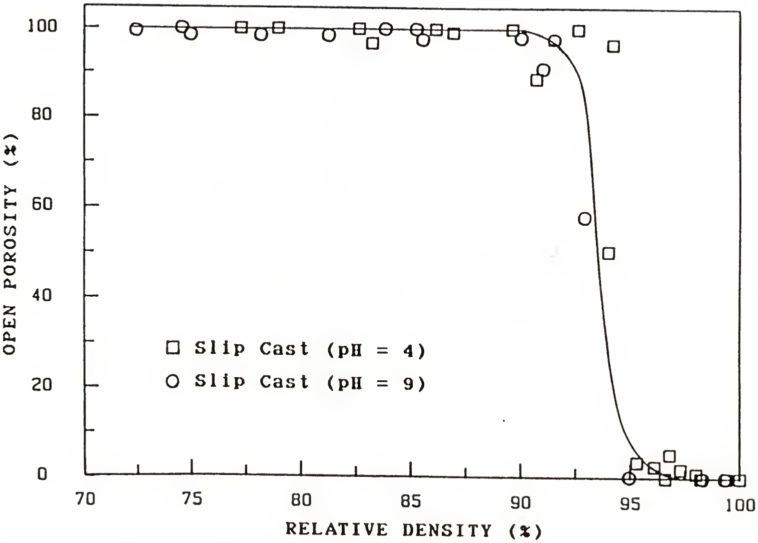

Figure 4.46 Plots of percentage of open porosity vs. relative density for SCD and SCF samples

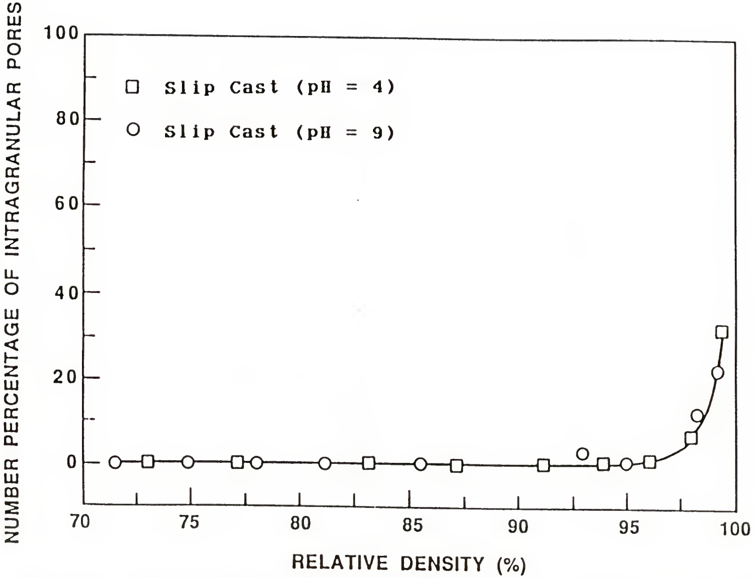

Figure 4.47 Plots of number percentage of intragranular pores vs. relative density for SCD and SCF samples

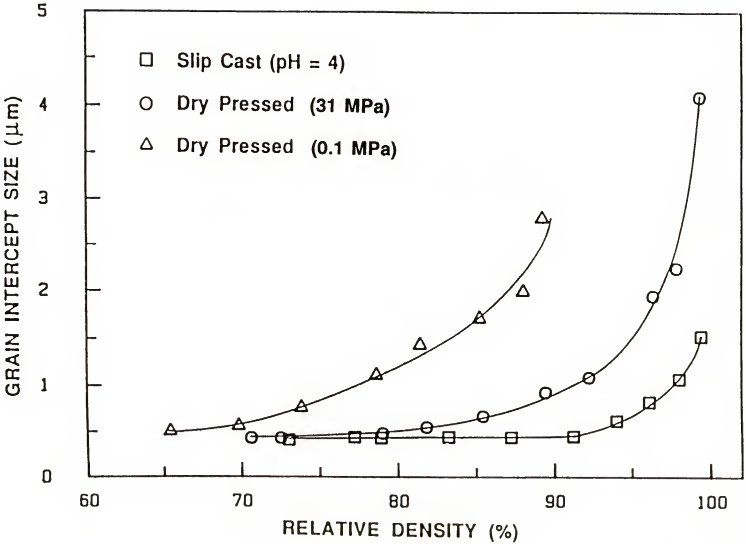

Figure 4.48 Plots of average grain intercept size vs. relative density for SCD, DPH, and DPL samples.

relative density. This behavior is due to the occurrence of grain growth in the agglomerated regions of the compact. As noted earlier, agglomerated regions can reach high relative density, even though the overall bulk density may remain low. This can be clearly seen in Figure 4.39 which shows a DPH sample sintered to ~85% relative density. The grain size in the close-packed agglomerated regions is much larger than the grain size in the more porous regions. At high relative densities, significantly larger average intercept sizes were obtained for the DPH sample.

Figure 4.49 compares the grain size trajectories (i.e., plots of average intercept size vs. relative density) for the DPH and SCF samples. The data is similar up to ~90%. At higher densities, the agglomerated regions of the DPH sample had reached full density which resulted in very rapid grain growth in these regions. Therefore, much larger average intercept sizes were obtained for the DPH sample.

The DPL sample undergoes a great deal of differential sintering due to the low green density and severe microstructural inhomogeneities. Therefore, the average grain intercept size is expected to begin increasing at very low overall relative density. A plot of grain intercept size vs. relative density for the DPL samples is shown in Figure 4.48. The average intercept size began to increase at relative densities below 65%. After 6 h sintering at 1450°C, this sample reached only ~74% overall relative density. In the same time, significant grain growth occurred in the close-packed agglomerated regions (which were already fully dense, Figure 4.37). Therefore, the average intercept size was twice that of the SCD sample at the same bulk density. Even after 48 h sintering at 1600°C, the relative density increased to only ~89%.

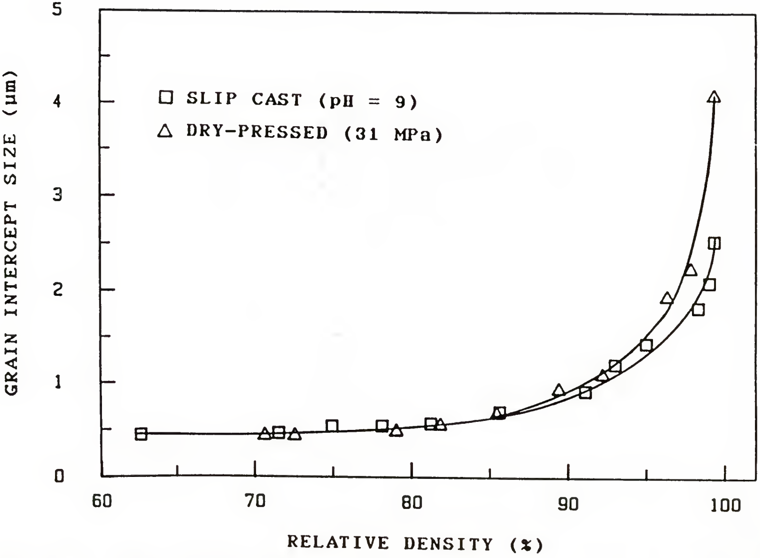

Figure 4.49 Plots of average grain intercept size vs. relative density for SCF and DPH samples.

However, grains larger than 10 micron were obtained in the fully dense regions and the average grain intercept size was ~2.8 μm.

The critical density for pore-grain boundary separation (about 95-97% relative density) is reached in the close-packed agglomerates of the dry pressed sample, even though the overall bulk density remains low. For example, after 2 hours sintering at 1450 °C, the bulk density of the DPL sample was around 70% relative density, while the close-packed agglomerates were 98% dense. Therefore, for the dry-pressed samples, it was expected that the intragranular pores would be obtained at low bulk density. Figure 4.50 shows plots of the number percentage of intragranular pores vs. relative density for the dry-pressed samples and the SCD samples. For the DPL sample, the number percentage of the intragranular pores began to increase below 80% relative density. Due to the higher dry-pressing pressure, the DPH sample had a more homogeneous green microstructure compared to the DPL sample. The percentage of the intragranular pores did not increase significantly until much higher densities. As expected, an increase in the percentage of intragranular pores was not observed in the homogeneous SCD samples until even higher densities.

Plots of percentage of open porosity vs. relative density for the DPH and DPL samples are shown in Figure 4.51. At less than 90% relative density, most of the pore volume of both dry-pressed samples was open pore. Even though a significant number fraction of intragranular pores were obtained for the DPL sample with < 90% relative density (Figure 4.50), the volume fraction of these pores was insignificant because they were mainly fine-sized pores in the agglomerated regions (Figures 4.37). However, compared to the slip cast samples (Figure 4.46), the dry-

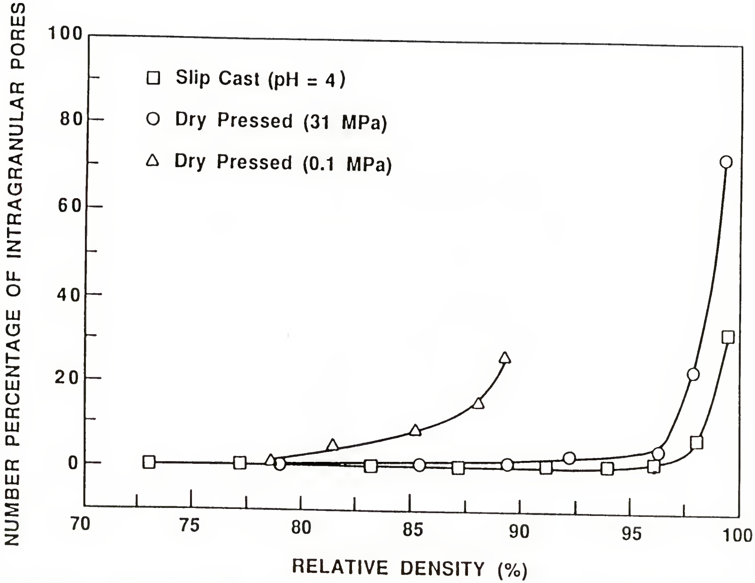

Figure 4.50 Plots of number percentage of intragranular pores vs. relative density for SCD, DPH, and DPL samples

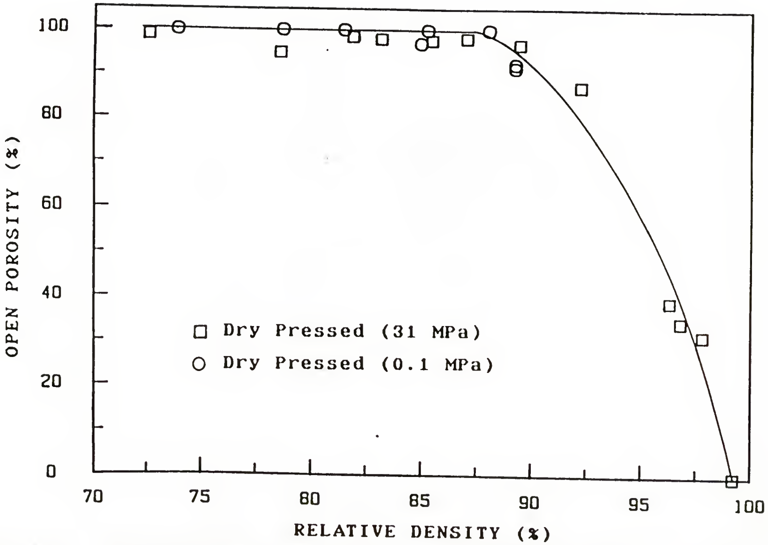

Figure 4.51 Plots of percentage of open porosity vs. relative density for DPH and DPL samples

pressed samples still showed slightly higher percentage of closed pore at < 90% relative density. The open porosity for the dry-pressed samples also started to decrease rapidly at slightly lower relative density. However, at ~98% relative density, the DPH sample still contained ~30 - 40% open porosity. In contrast, only closed pores were left for the slip cast samples (Figure 4.46). The greater amount of open porosity in the high density DPH samples may be due to the existence of large pores which are more difficult to close up. Some cracks introduced by differential shrinkage (Figure 4.13) may also contribute to the open porosity.

Gupta [Gup72] analyzed the grain growth data of Cu, Al_2O_3, BeO, and ZnO in the density range 60 to 90% relative densities and concluded that a linear relation existed between grain size and sintered density. However, as illustrated by Figures 4.45 and 4.48, the powder processing conditions and particle packing in the green microstructure have dramatic effect on the relation between grain size and relative density. By carefully controlling the powder characteristics and consolidation conditions, densification can proceed up to ~90% relative density with virtually no grain growth (e.g., SCD sample). On the other hand, for the dry-pressed sample with heterogeneous green microstructure (e.g., DPL sample), extensive grain growth can occur in the early stages of sintering. Therefore, it is improper to postulate that the grain growth behavior in the intermediate stage of sintering will follow a common linear relationship in the grain size vs. density plot. In addition, the grain growth data in Gupta's paper had a similar trend as the DPL sample in the present study. This may indicate that the samples used in Gupta's paper had heterogeneous green microstructures.

Mister and Coble [Mis68] suggested that exaggerated or abnormal grain growth can be initiated by density fluctuations in the sample and that this condition may exist even with monosized, high purity powders. They postulated that the high densification rate associated with high green density regions helped these regions to achieve a high density earlier than the lower green density regions did. The restraint of grain growth by pores was removed in the high density regions. Large grains formed would then grew into the smaller matrix grains. In the present study, indeed, two levels of grain growth rates were observed--high grain growth rates within the agglomerates and low grain growth rates in the porous matrix. This can be clearly seen in Figure 4.22B in which micrographs for a DPL sample sintered at 1600°C for 48 hours are shown. Even though a large average grain size was obtained within the close-packed agglomerated regions, the grain size distribution was uniform and "exaggerated" grains were not observed. This implied that the uniform large grain size in the agglomerated regions was obtained through normal grain growth (i.e., exaggerated grain growth* did not occur despite the prolong sintering at high temperature). The large-sized grains were limited to the high density regions. Clear boundaries between large grain (dense) regions and fine grain (porous) regions remained (Figures 4.22). The probable reason is that the fine grain matrix still had high porosity which would restrain the migration of grain boundaries.

---

* Normally a grain growth process is called "exaggerated grain growth" when a small fraction of the grains consume their neighboring grains (which are uniform in size) and become extremely large [Kin76]. For alumina, exaggerated grain growth usually produces elongated (lath-like) grains.

Figure 4.52 shows plots of grain intercept size vs. sintering time at 1450°C for the SCD, SCF, and DPL samples. The SCD sample showed the highest grain growth rate because of its rapid densification rate. This sample reached ~99% density after 6 h at 1450°C. The removal of pores allowed grain growth to occur. In contrast, the SCF sample only reached ~ 91% relative density after 6 h at 1450°C, and only minimal grain growth had occurred. This trend is further exaggerated in the DPL sample which reached only 74% relative density after 6 h at 1450°C. Although the average grain intercept size is low (0.76 μm) at this density, the close-packed agglomerates had grain sizes similar to that of SCD sample (Figure 4.37A vs 4.42A). Figure 4.53 shows plots of grain intercept size vs. sintering time at 1340°C for the SCD, SCF and DPH samples. At short sintering time, no grain growth was observed. Similar grain intercept size was obtained for samples with various particle packing. After grain growth started (at ~2 to 4 hours of sintering), results were similar to the data obtained at 1450°C, i.e., the SCD sample showed a higher grain growth rate than the SCF sample. Compared to the SCF sample, the DPH sample had higher grain growth rate which may due to the rapid grain growth in the densely-packed agglomerated regions.

Following the treatment of Coble [Cob61], the apparent activation energy for grain growth can be obtained from grain size data at different temperatures. It is assumed that the reciprocal of sintering time (to reach a constant grain size) is proportional to the rate constant for grain growth. Therefore, by plotting the ln (reciprocal time) against reciprocal absolute temperature, the apparent activation energy can be obtained from the slope. The sintering time needed to obtain one micron grain intercept size for the SCD sample was ~36 hours

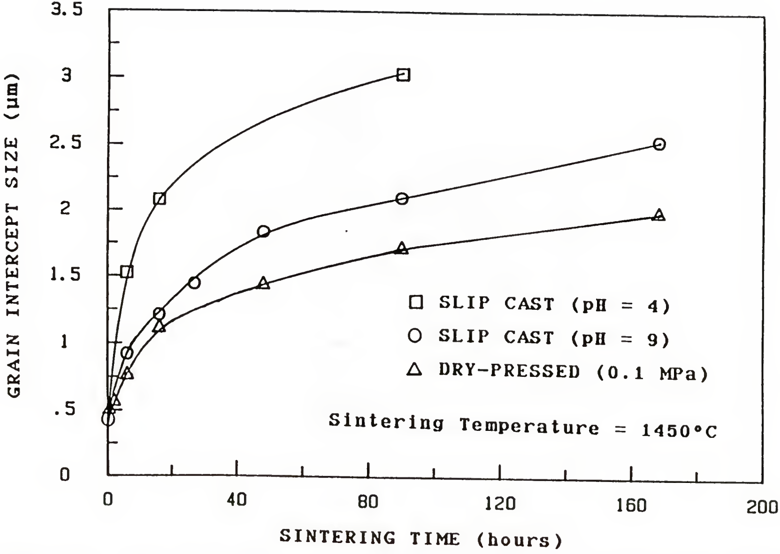

Figure 4.52 Plots of average grain intercept size vs. sintering time at 1450°C for SCD, SCF, and DPL samples.

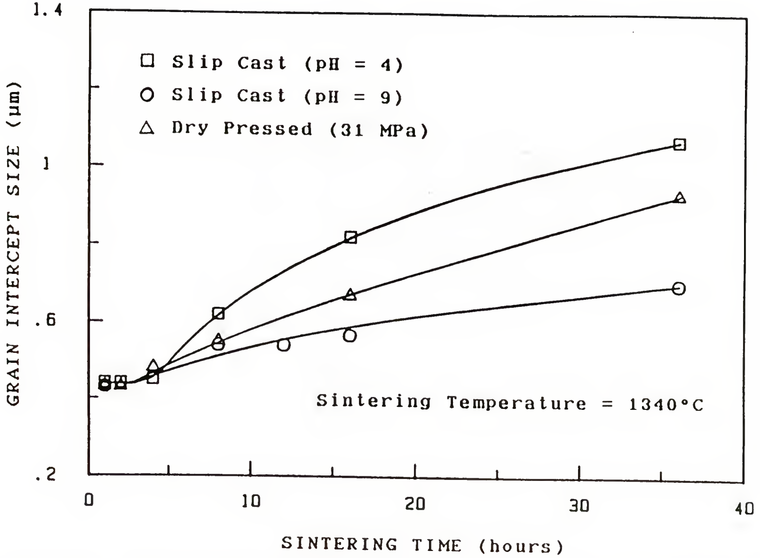

Figure 4.53 Plots of average grain intercept size vs. sintering time at 1340°C for SCD, SCF, and DPH samples.

at 1340°C and ~2 hours at 1450°C. For the SCF sample, same grain intercept size (~0.7 μm) was obtained using the above two sintering schedules. The apparent activation energies obtained for both samples was ~599 KJ/mole which agreed very well with Coble's value (641 KJ/mole).

Grain intercept size distribution. It has been shown in Figure 4.45 that the average grain intercept size of the SCD samples remained essentially constant until the relative density reached ~90%. In the same density range, the grain intercept size distribution also showed virtually no change (Figures 4.54 and 4.55). Upon further densification, the grain intercept size distribution became broader with decreasing population in small intercept size and growth in the coarse end as shown in Figure 4.56 to 4.58. In contrast, the grain intercept size distribution of the SCF sample started to broaden at only ~75% relative density (Figures 4.59 to 4.61). Significantly broadened size distributions were obtained when the sintered samples approached full density (Figures 4.62 and 4.63). For example, at ~99% relative density, the SCD sample only had maximum grain intercept size of ~5 μm (Figure 4.58); in contrast, the grain intercept size distribution of SCF sample extended up to ~9 μm (Figure 4.63). Due to the longer sintering time and/or higher sintering temperature needed to densify the SCF sample, the SCF sample showed coarser microstructure compared to SCD sample. However, as noted earlier, both slip cast samples had uniform sintered microstructures. This is because both slip cast samples had relatively uniform green microstructures.

The grain intercept size distributions for DPH sample at various relative densities are shown in Figure 4.64 to 4.68. At lower density (e.g., 73% relative density), no grain growth was observed for both close-packed agglomerated regions and porous regions (Figure 4.36). The grain intercept size distribution (Figure 4.64) was similar to that of the SCD and SCF samples (Figures 4.54 and 4.59). Slight broadening of the grain size distribution was observed in the ~79% relative density sample (Figure 4.65).

The grain intercept size distributions for close-packed regions and the more porous regions of a sample with ~82% overall bulk density are shown in Figures 4.69 and 4.70, respectively. Compared to the porous regions, the close-packed regions had a smaller percentage of fine grains (< 0.75 μm) and a larger percentage of coarser grains (> 0.75μm). This difference in average grain intercept size and grain intercept size distribution for the closed-packed and the porous regions remained throughout the densification process. Figures 4.71 and 4.72 show the comparison for a sample with ~98% density.

Due to rapid grain coarsening in the high density agglomerates, large grains started to appear as "tail" in the grain intercept size distribution plots for samples with density higher than 82% (Figures 4.66 to 4.68). Therefore, at > 82% relative density, the DPH samples showed broader grain intercept size distributions, larger maximum intercept sizes and higher percentages of large intercepts when compared to the SCF samples with similar relative density. This is consistent with the larger average grain intercept sizes for the DPH samples in the high density ranges (Figure 4.49).

The above trend was further exaggerated in the DPL samples which have even more heterogeneous green microstructures. Histograms of grain intercept size distribution of DPL samples are shown in Figures 4.73 to

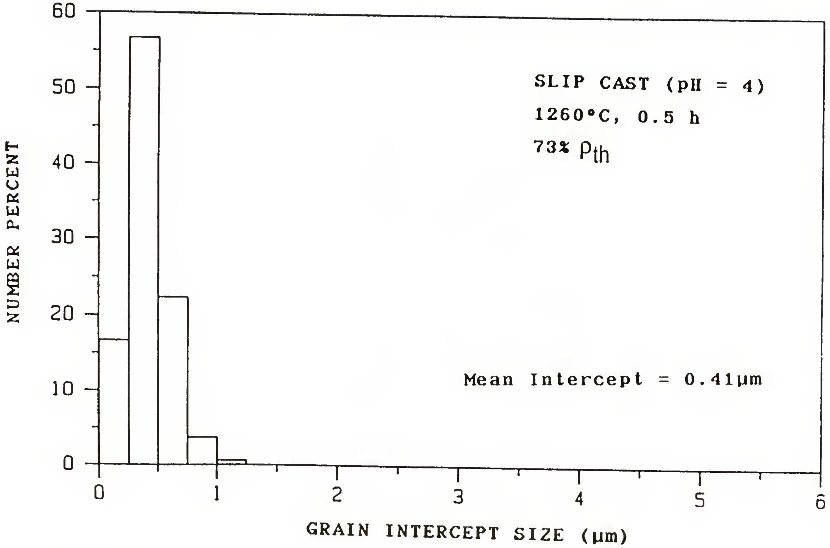

Figure 4.54 Histogram plot of the grain intercept size distribution for SCD sample sintered at 1260°C, 0.5 h to 72.8% relative density.

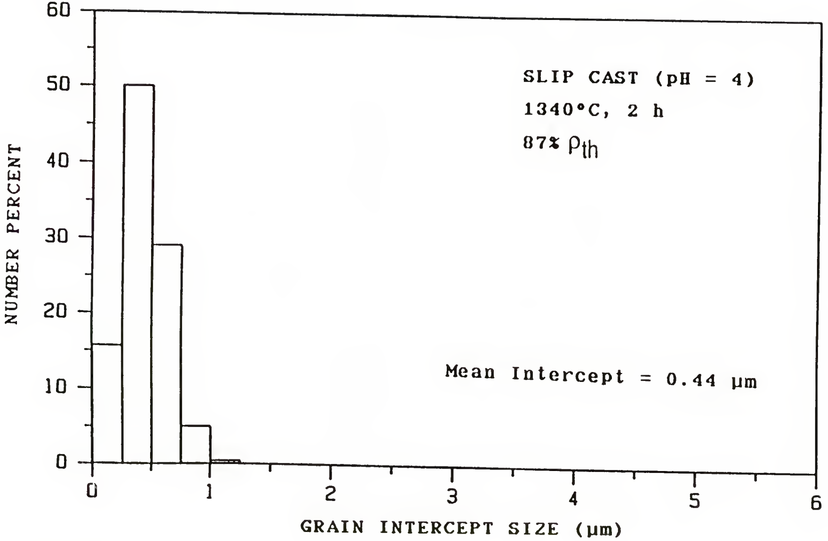

Figure 4.55 Histogram plot of the grain intercept size distribution for SCD sample sintered at 1340°C, 2 h to 87.2% relative density.

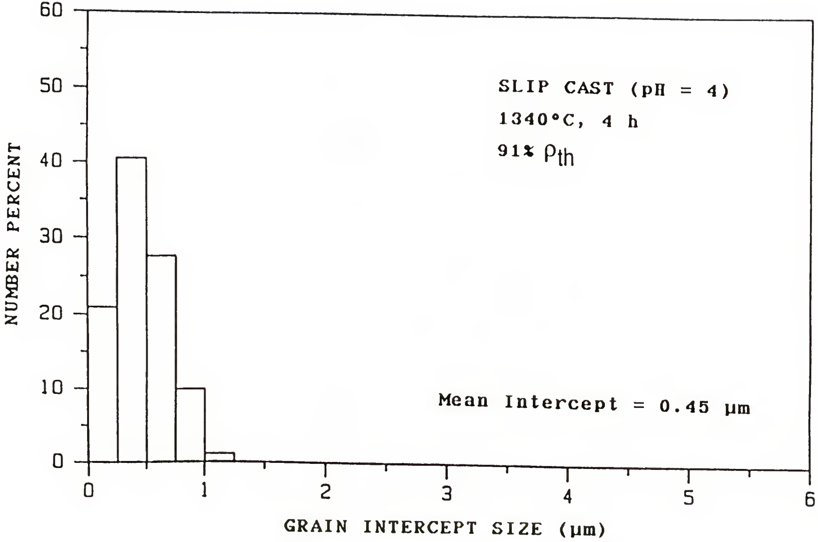

Figure 4.56 Histogram plot of the grain intercept size distribution for SCD sample sintered at 1340°C, 4 h to 91.2% relative density.

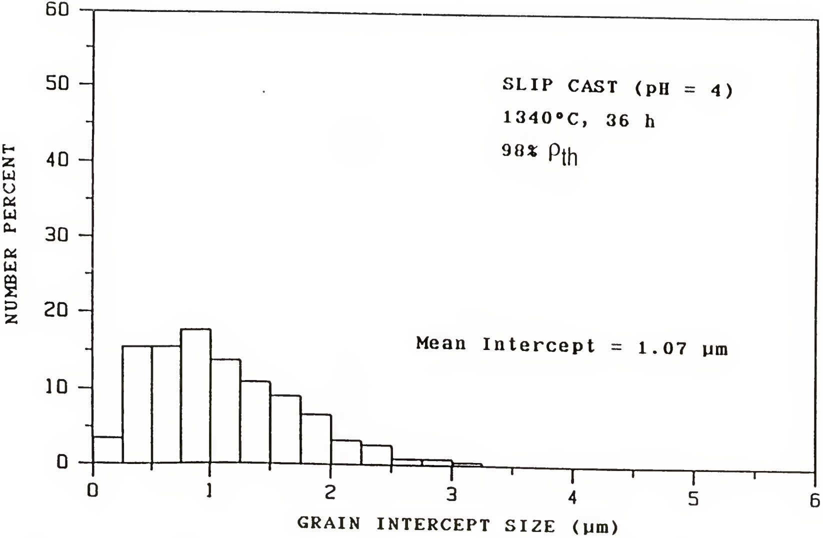

Figure 4.57 Histogram plot of the grain intercept size distribution for SCD sample sintered at 1340°C, 36 h to 98.0% relative density.

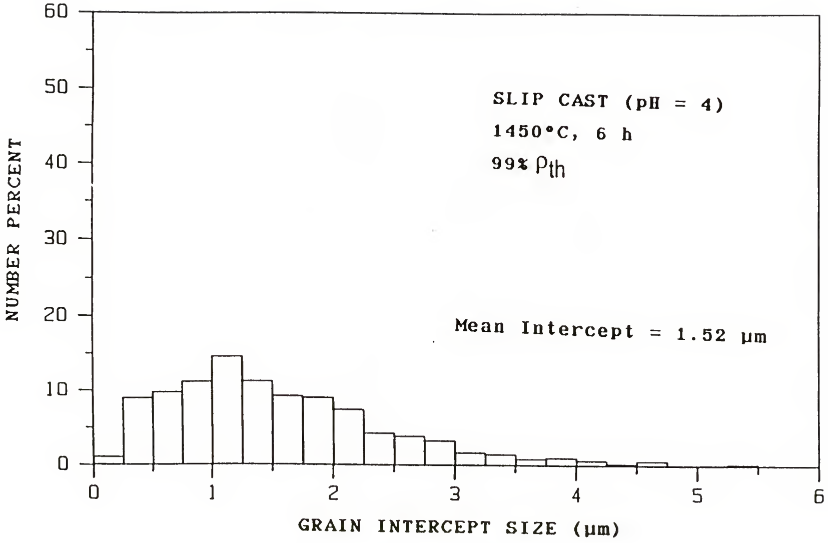

Figure 4.58 Histogram plot of the grain intercept size distribution for SCD sample sintered at 1450°C, 6 h to 99.4% relative density.

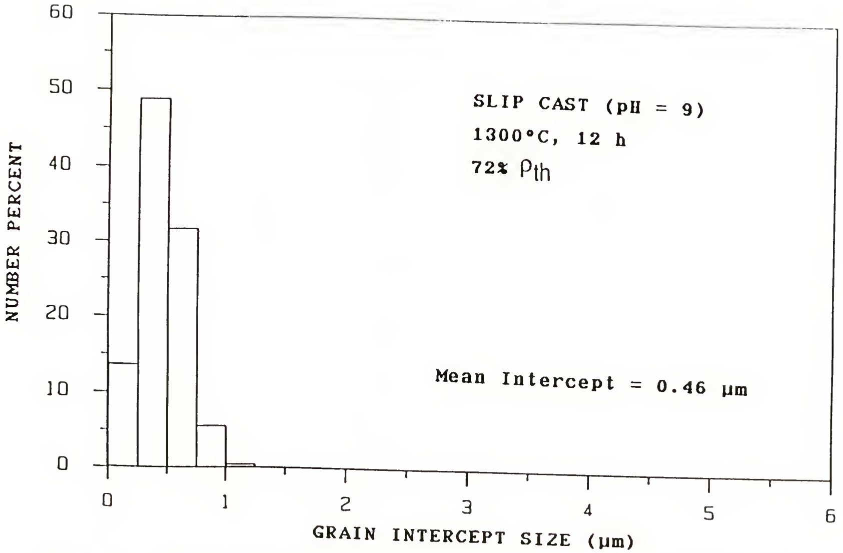

Figure 4.59 Histogram plot of the grain intercept size distribution for SCF sample sintered at 1300°C, 12 h to 71.5% relative density.

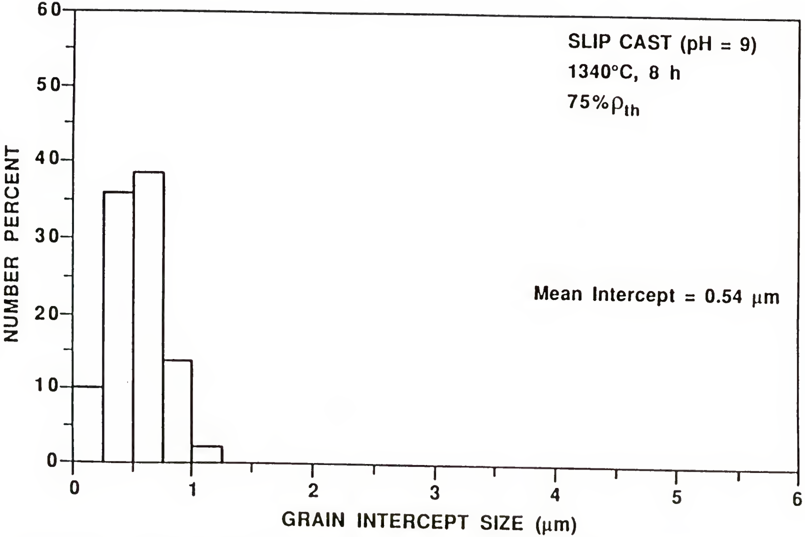

Figure 4.60 Histogram plot of the grain intercept size distribution for SCF sample sintered at 1340°C, 8 h to 74.9% relative density.

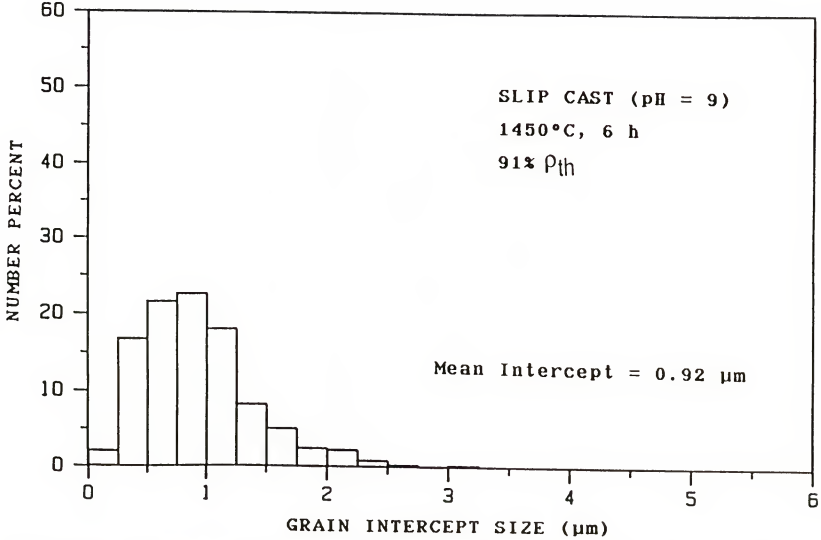

Figure 4.61 Histogram plot of the grain intercept size distribution for SCF sample sintered at 1450°C, 6 h to 91.1% relative density.

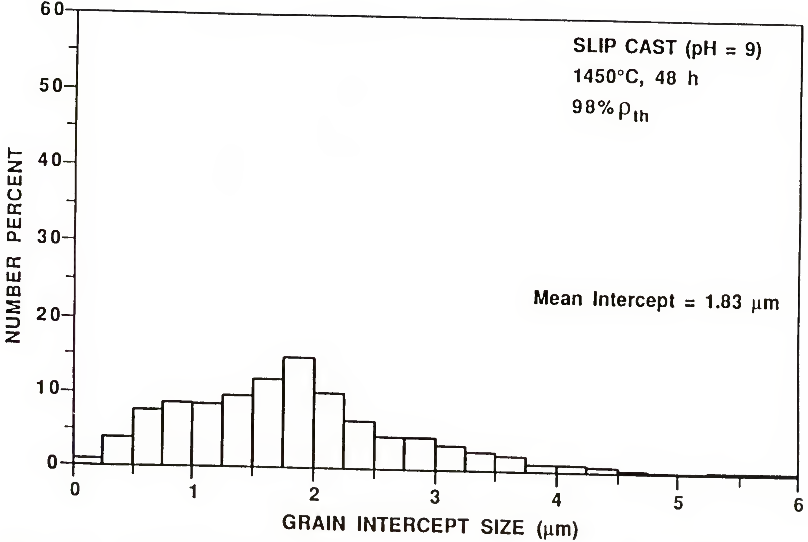

Figure 4.62 Histogram plot of the grain intercept size distribution for SCF sample sintered at 1450°C, 48 h to 98.3% relative density.

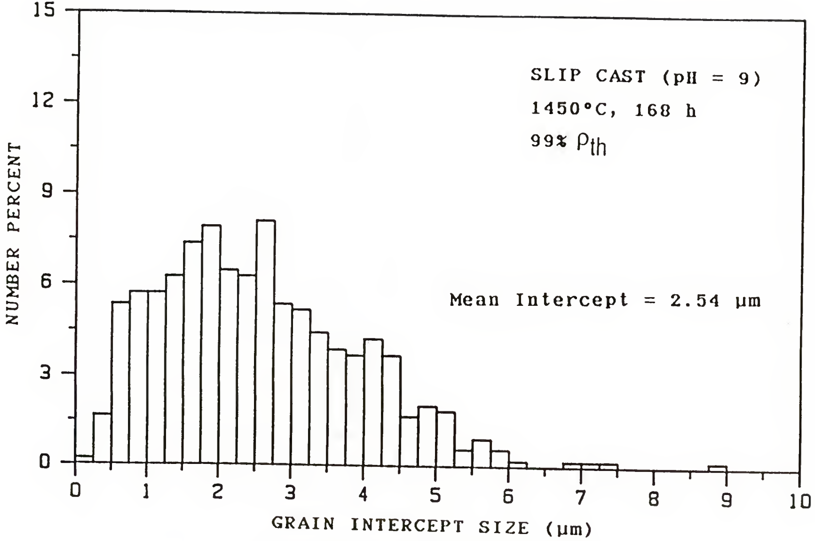

Figure 4.63 Histogram plot of the grain intercept size distribution for SCF sample sintered at 1450°C, 168 h to 99.3% relative density.

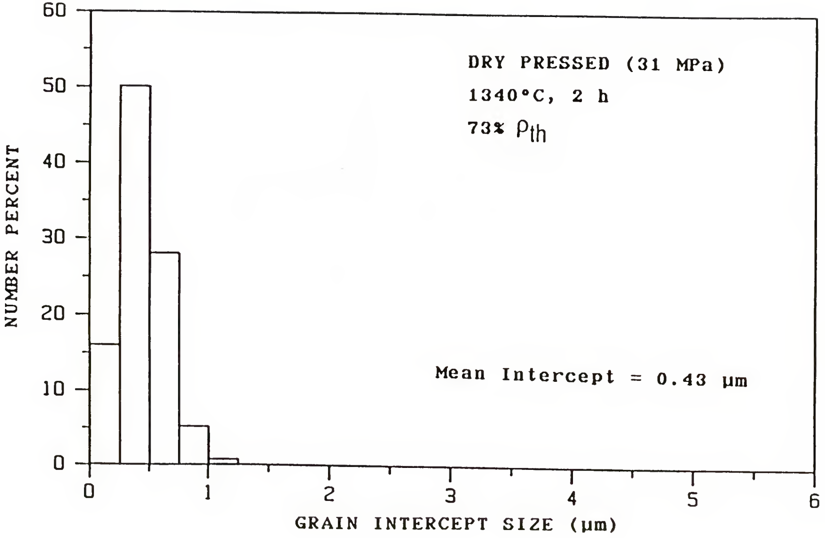

Figure 4.64 Histogram plot of the grain intercept size distribution for DPH sample sintered at 1340°C, 2 h to 72.5% relative density.

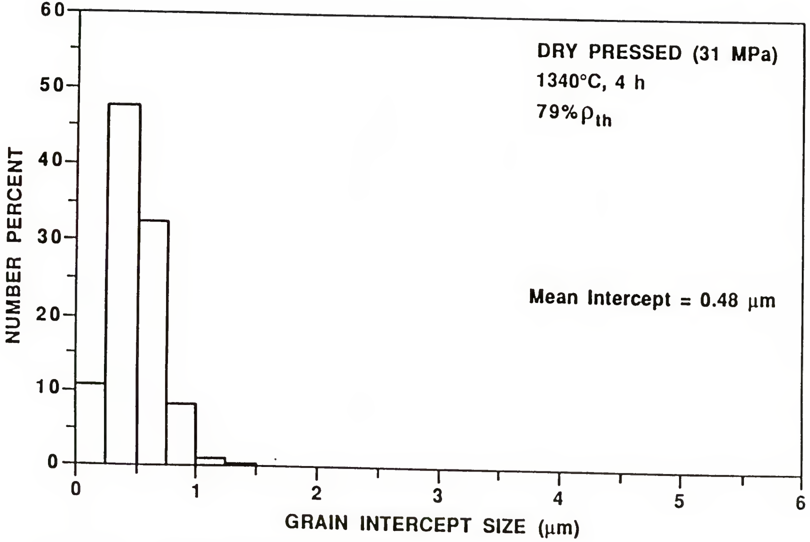

Figure 4.65 Histogram plot of the grain intercept size distribution for DPH sample sintered at 1340°C, 4 h to 79.0 % relative density.

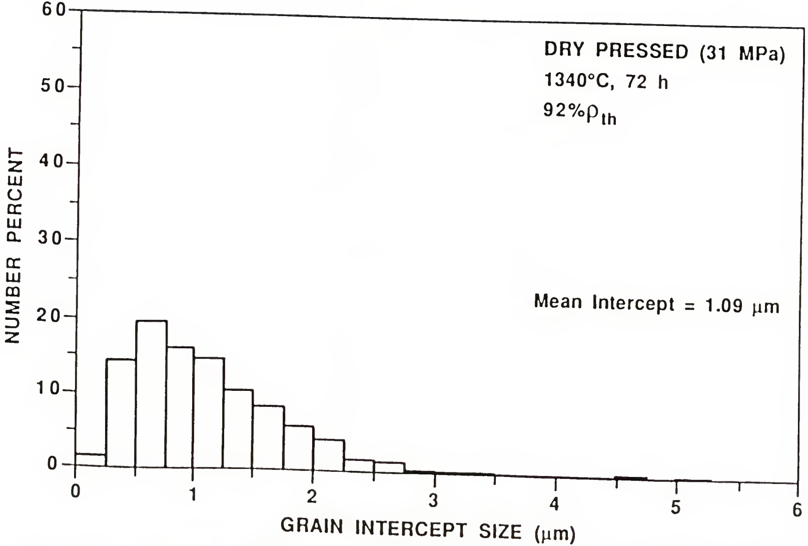

Figure 4.66 Histogram plot of the grain intercept size distribution for DPH sample sintered at 1340°C, 72 h to 92.2% relative density.

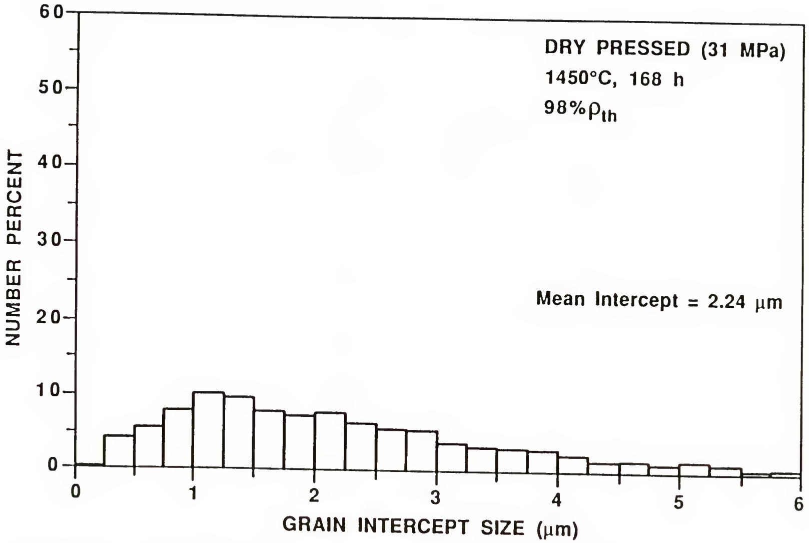

Figure 4.67 Histogram plot of the grain intercept size distribution for DPH sample sintered at 1450°C, 168 h to 97.8% relative density.

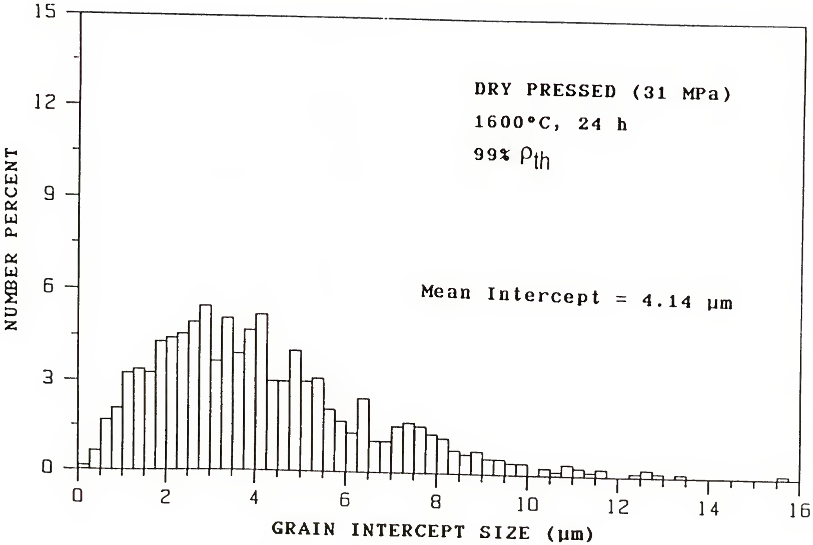

Figure 4.68 Histogram plot of the grain intercept size distribution for DPH sample sintered at 1600°C, 24 h to 99.3% relative density.

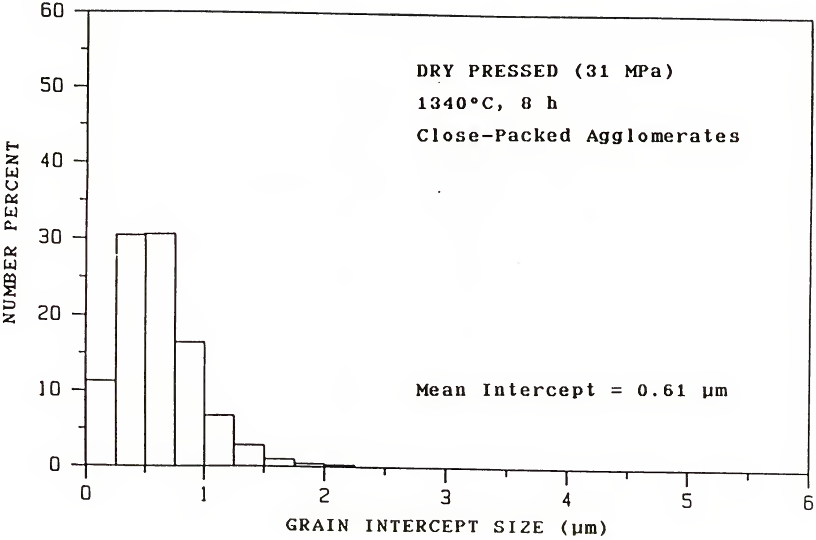

Figure 4.69 Histogram plot of the grain intercept size distribution for the close-packed agglomerated regions of DPH sample sintered at 1340°C, 8 h to 81.8% overall bulk density.

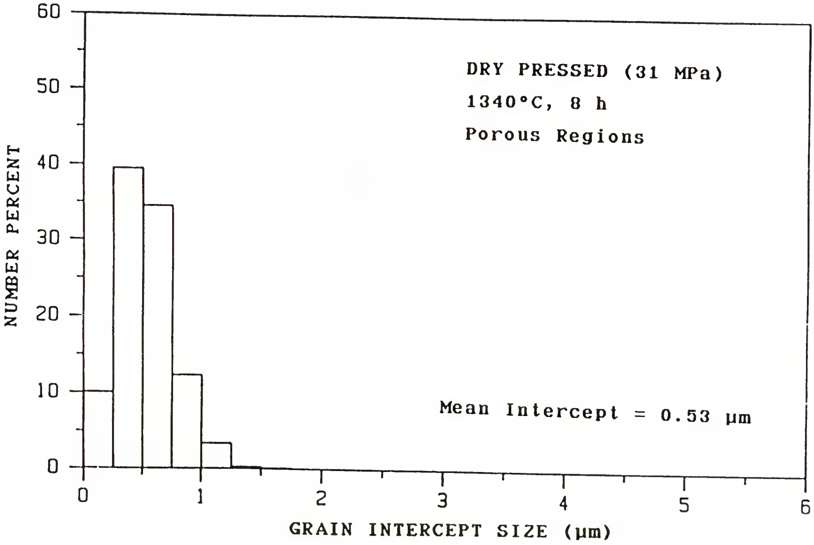

Figure 4.70 Histogram plot of the grain intercept size distribution for the porous regions of DPH sample sintered at 1340°C, 8 h to 81.8% overall bulk density.

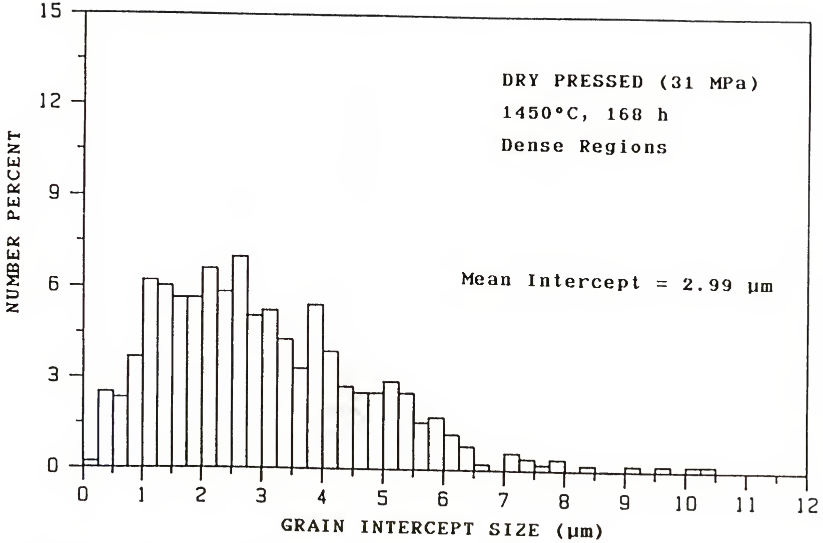

Figure 4.71 Histogram plot of the grain intercept size distribution for the close-packed agglomerated regions of DPH sample sintered at 1450°C, 168 h to 97.8% overall bulk density.

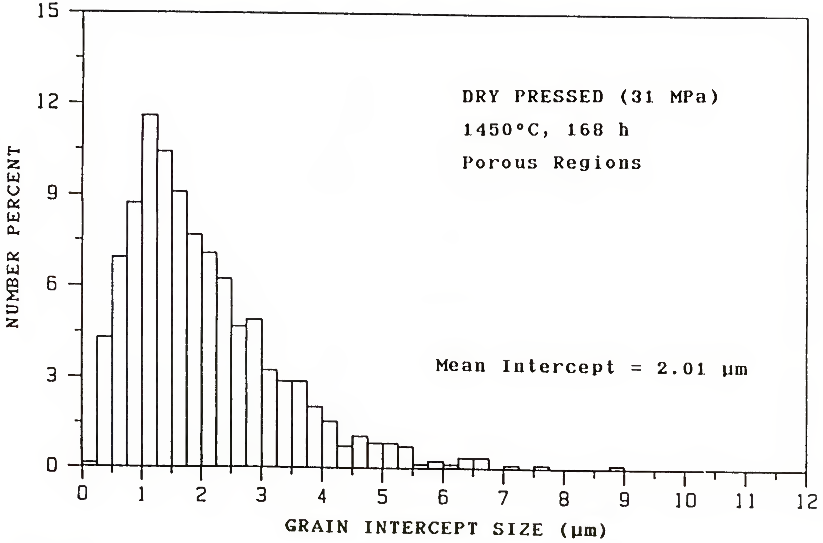

Figure 4.72 Histogram plot of the grain intercept size distribution for the porous regions of DPH sample sintered at 1450°C, 168 h to 97.8% overall bulk density.

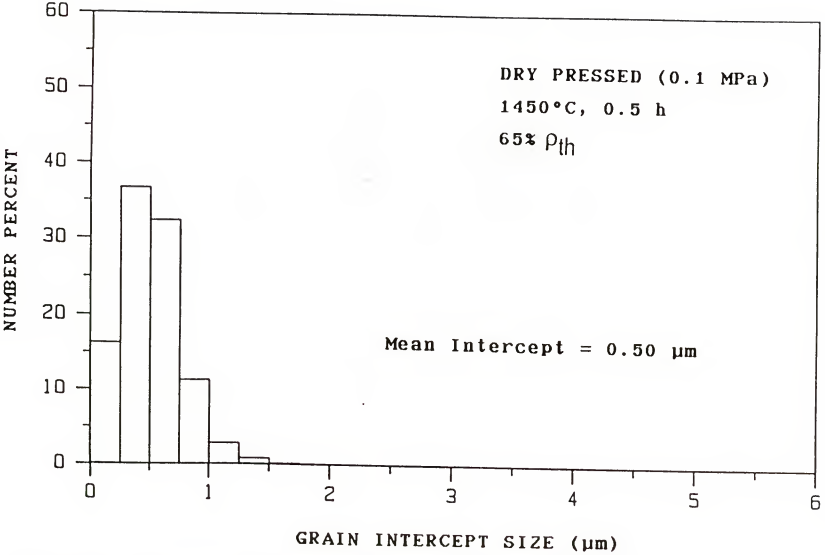

Figure 4.73 Histogram plot of the grain intercept size distribution for DPL sample sintered at 1450°C, 0.5 h to 65.4% relative density.

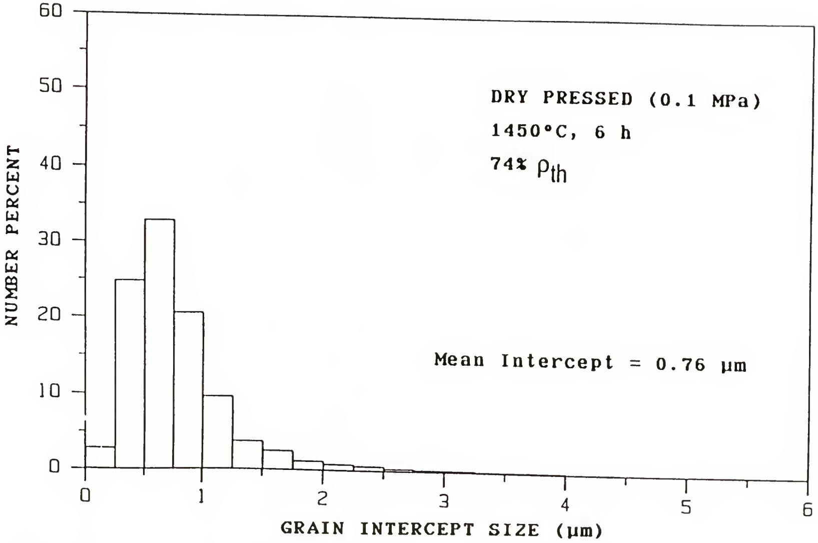

Figure 4.74 Histogram plot of the grain intercept size distribution for DPL sample sintered at 1450°C, 6 h to 73.8% relative density.

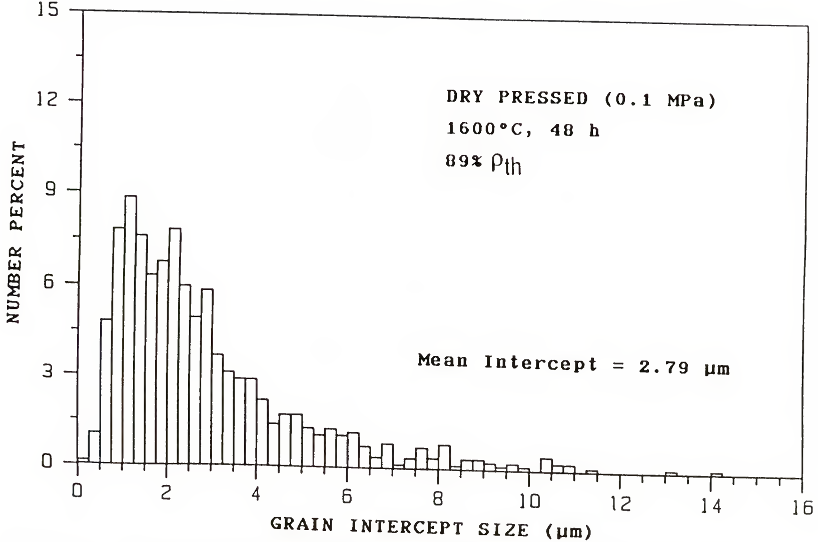

Figure 4.75 Histogram plot of the grain intercept size distribution for DPL sample sintered at 1600°C, 48 h to 89.2% relative density.

4.75. Broadening of grain intercept size distribution was observed at very low bulk density (i.e., < 65%, Figure 4.73). At 89% relative density, extremely large grains were obtained in the fully dense regions while small grain size remained in the porous regions (Figure 4.22). This resulted in a very broad grain intercept size distribution (Figure 4.75).

The effect of various particle packings on the evolution of the grain intercept size distribution can be further demonstrated in Figures 4.76 and 4.77 in which plots of geometric standard deviation* (σ_g) of the grain intercept size distribution vs. relative density are shown. The σ_g of the SCD sample remained relatively constant until ~85% relative density. At higher density, the σ_g started to increase. It seems that the increase of σ_g is closely related to the onset of grain growth. The grain growth was obtained at much lower relative density (~75%) for the SCF sample, the σ_g also started to increase at lower density. Before the occurrence of grain growth, low σ_g values were obtained for both samples because the starting powder had a narrow particle size distribution. During grain growth process, relatively larger grains had more driving force for growth. In the same time, the relatively smaller grains were "consumed" and decreased in size.

---

* Geometric standard deviation (σ_g) was obtained by using the equation

$$\text{Log}\ \sigma_g = \left(\frac{\sum_{i=1}^{N} (\text{Log}\ d_i - \text{Log}\ d_g)^2}{N - 1} \right)^{1/2}$$

where N is the number of grain intercept, d_i is the ith grain intercept, and d_g is the geometric mean intercept. The magnitude of σ_g is proportional to the width of the grain intercept size distribution when the distribution data are plotted on logarithmic scale.

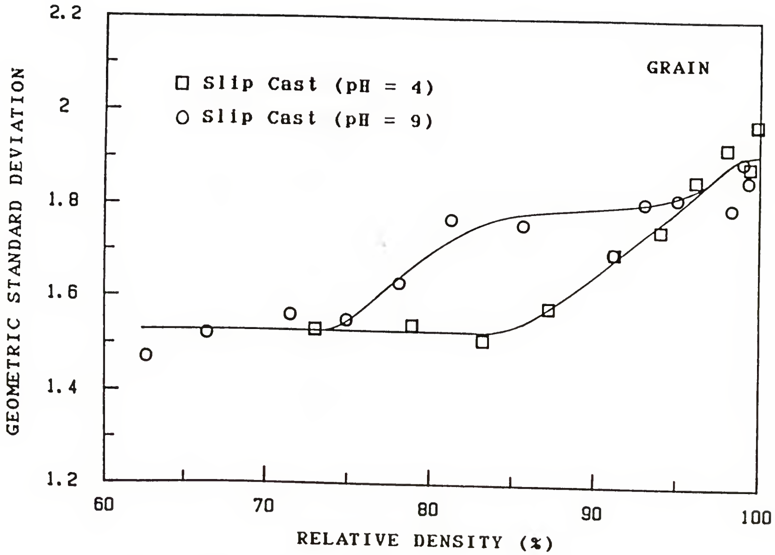

Figure 4.76 Plots of geometric standard deviation of grain intercept size distribution vs. relative density for SCD and SCF samples.

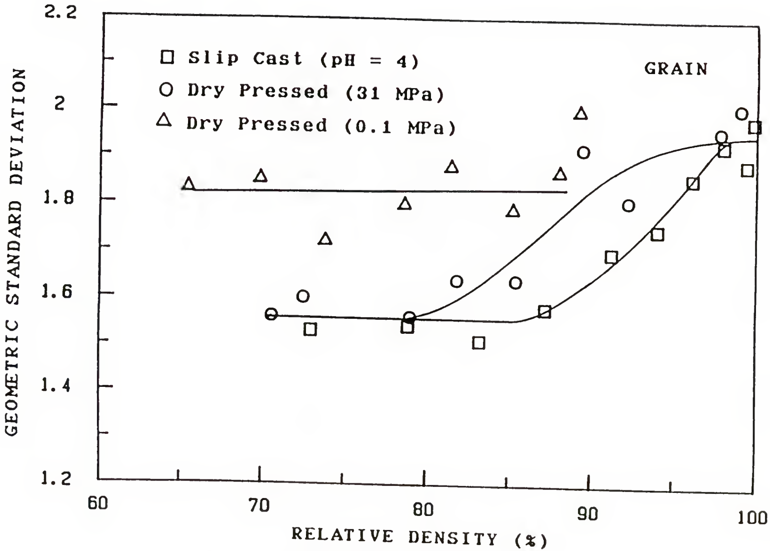

Figure 4.77 Plots of geometric standard deviation of grain intercept size distribution vs. relative density for SCD and DPH, and DPL samples.

Therefore, the grain size distribution became broader and higher σ_g values were obtained.

The σ_g value of the DPH sample started to increase at ~80% relative density (Figure 4.77) which is also consistent with the onset of grain growth. For the DPL sample, the σ_g value remained at a relatively constant large value (~1.8) over the density range in which grain intercept size was measured (i.e., ~65 to 89% relative density). This reflects the fact that growth started at very low relative densities (< 65%). It is expected that lower σ_g values would be obtained for samples with densities below 65%.

In Figures 4.76 and 4.77, it seems that the σ_g value increases and approaches a stable range of values (~1.8 to 2.0) as the grain growth begins. This can be further confirmed by plotting σ_g vs. grain intercept size as shown in Figure 4.78.

Kimura et al. [Kim87] studied the grain growth behavior during sintering for slip cast alumina compacts and showed that a linear relationship between arithmetic standard deviation (σ_a) of grain size distribution and grain size was obtained despite the different packing density of various green compacts. Plots of σ_a* vs. grain intercept size for the slip cast and dry-pressed samples in the present study are shown in Figure 4.79. An approximately linear relation between σ_a and grain

---

* Arithmetic standard deviation (σ_a) was obtained by using the equation

$$\sigma_a = \left(\frac{\sum_{i=1}^{N} (d_i - d_a)^2}{N - 1} \right)^{1/2}$$

where N is the number of grain intercept, d_i is the ith grain intercept, and d_a is the mean intercept size.

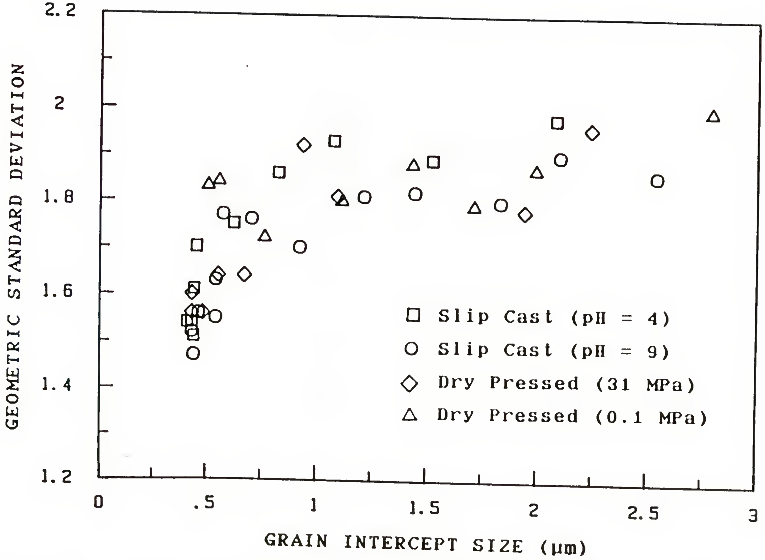

Figure 4.78 Plots of geometric standard deviation of grain intercept size distribution vs. grain intercept size for SCD, SCF, DPH, and DPL samples.

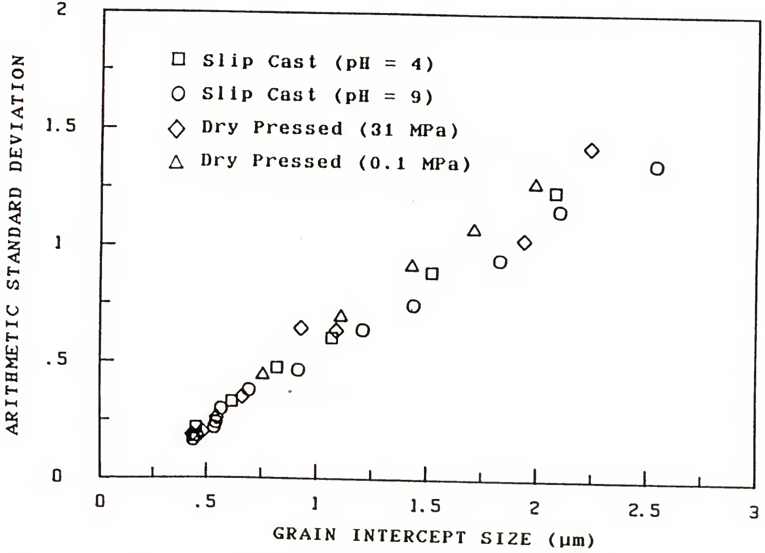

Figure 4.79 Plots of arithmetic standard deviation of grain intercept size distribution vs. grain intercept size for SCD, SCF, DPH, and DPL samples.

intercept size was observed. A constant ratio between σ_a and grain intercept size indicates that a common distribution curve will be obtained if grain intercept sizes in various size distributions are divided by the mean size of each size distribution (i.e., distributions are normalized*). This is controversial with the results of geometric standard deviation. It was suspected that the change of the ratio between σ_a and grain intercept size was not clearly delineated in the plots of σ_a vs. grain intercept size. This is confirmed in Figure 4.80 in which plots of the ratio of σ_a to grain intercept size vs. grain intercept size are shown**. The ratio, which represents the width of the normalized size distribution, rapidly increased as the grain growth began and approached a steady value between 0.5 and 0.65. This is consistent with the σ_g results in Figure 4.78. A significantly larger ratio was observed for the DPL sample with large grain intercept size (solid triangle in Figure 4.80) which was sintered at 1600°C for 48 h. This indicates that the normalized grain intercept size distribution for this sample is broader. This is due to the fact that extremely large grain sizes are obtained in the close-packed agglomerated regions while fine grains remain in the porous regions.

Plots of the ratio of arithmetic standard deviation to grain intercept size vs. relative density for the slip cast and dry-pressed

---

* In order to properly compare the grain intercept size distributions of samples with significantly different mean intercept size, the intercept size of each sample need to be normalized to eliminate the effect of mean value. This can be achieved by dividing each intercept size with the mean intercept size.

** The ratio of σ_a to mean size is also called the "coefficient of variation" of the distribution. In the present case, this ratio is proportional to the width of the normalized grain intercept size distribution.

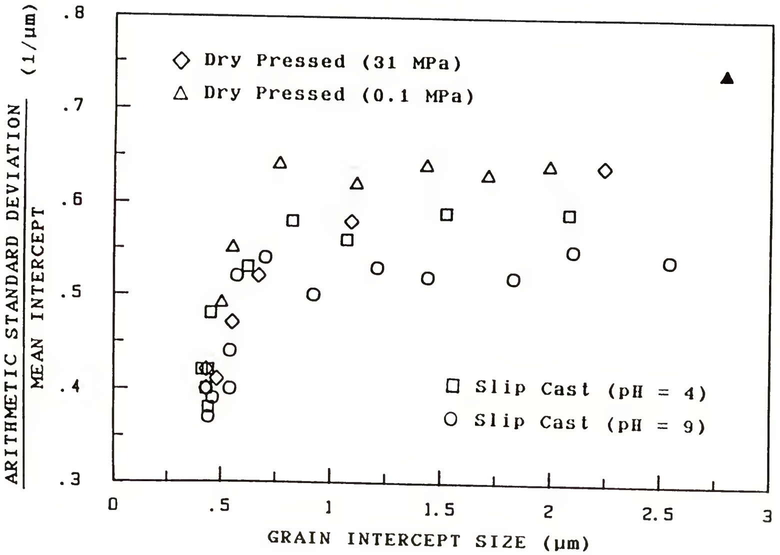

Figure 4.80 PLots of the ratio of arithmetic standard deviation of grain intercept size distribution to mean intercept vs. mean intercept for SCD, SCF, DPH, and DPL samples.

sample are shown in Figures 4.81 and 4.82, respectively. The trends of the broadening of the normalized grain intercept size distributions (in linear scale) were similar to that judged from the geometric standard deviations (Figures 4.76 and 4.77). The broadening of the grain intercept size distribution for the DPL samples was also observed at lower density range in Figure 4.82.

The broadening of grain intercept size distribution can also be shown by comparing the distribution histogram of normalized grain intercept size (i.e., $G/\bar{G}$, where G is the grain intercept size and $\bar{G}$ is the mean intercept size) for samples before and after the onset of grain growth. This can be illustrated with the SCD samples at ~87% relative density (i.e., before the onset of grain growth, $\bar{G} = 0.44\ \mu m$) and ~96% relative density (i.e., after significant grain growth, $\bar{G} = 0.82\ \mu m$). Figures 4.83 to 4.86 show the distribution histograms for the above samples in linear scale (Figures 4.83 and 4.84) and log scale (Figures 4.85 and 4.86). The broadening of size distribution for sample with ~96% relative density (Figures 4.84 and 4.86) is clearly shown by the decrease in the number percentage of normalized grain sizes at the center of distributions (i.e., $G/\bar{G} \approx 1$ or $\text{Log}(G/\bar{G}) \approx 0$) and the increases in the percentages of fine and large normalized grain sizes.

Pore intercept size and pore intercept size distribution. Figure 4.87 shows the pore intercept size vs. relative density for the SCD and SCF samples. Both samples showed fairly constant average pore intercept size over the entire density range. This is consistent with the observations of DeHoff et al. [DeH66], Tuohig [Tuo72], and Page et al. [Pag88]. As discussed in Chapter II, various mechanisms can result in pore shrinkage or pore coarsening. The constant pore intercept size

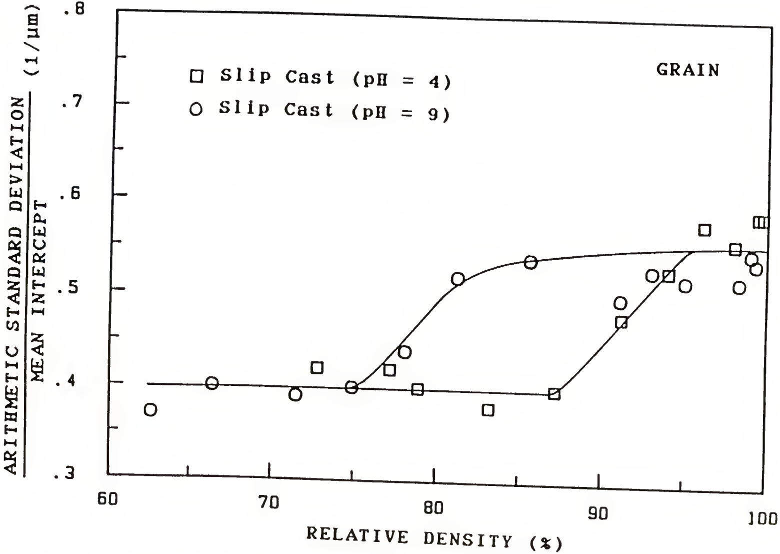

Figure 4.81 PLots of the ratio of arithmetic standard deviation of grain intercept size distribution to mean intercept vs. relative density for SCD and SCF samples.

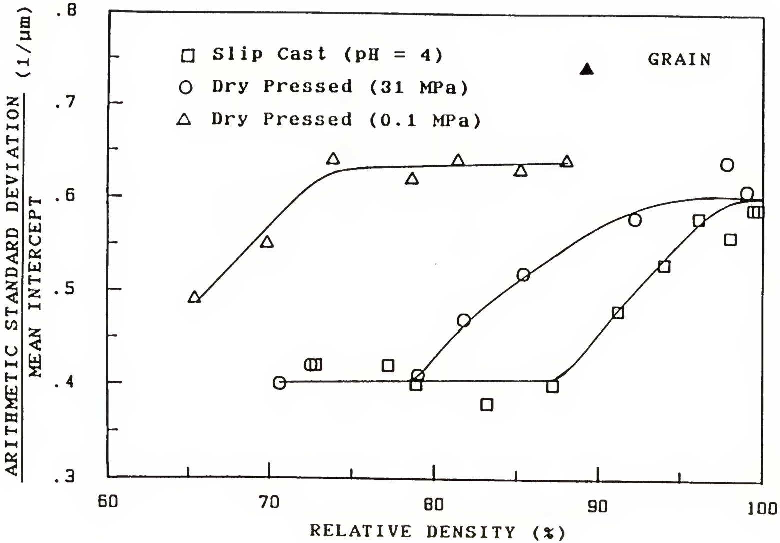

Figure 4.82 PLots of the ratio of arithmetic standard deviation of grain intercept size distribution to mean intercept vs. relative density for SCD, DPH, and DPL samples.

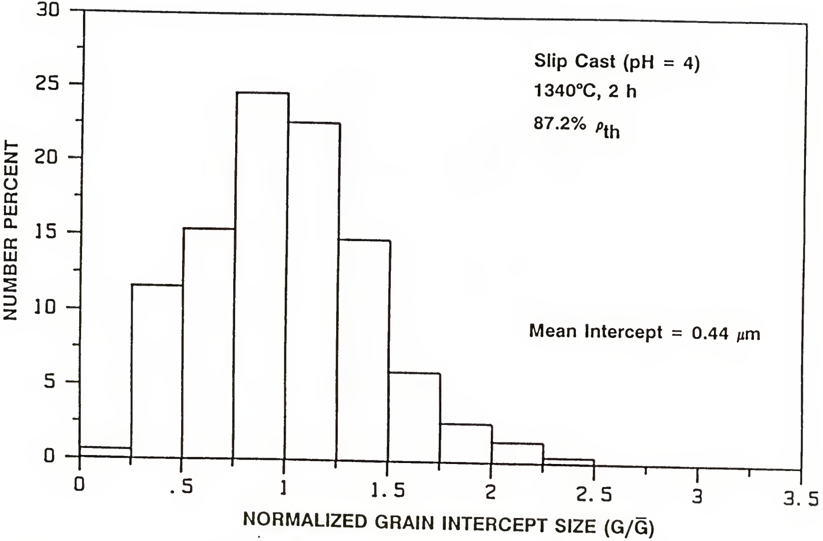

Figure 4.83 Histogram plot of the normalized grain intercept size distribsution (G/Ḡ) for SCD sample sintered at 1340°C, 2 h to 87.2% relative density (Ḡ = 0.44 μm).

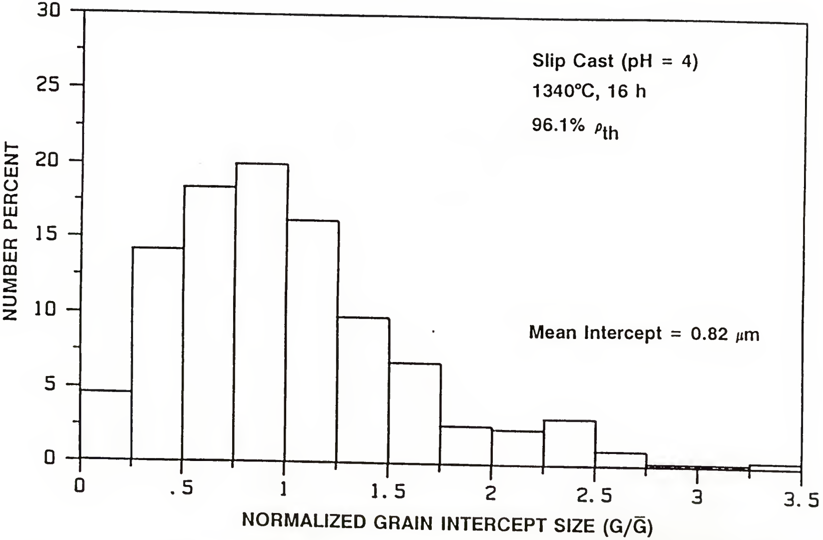

Figure 4.84 Histogram plot of the normalized grain intercept size distribsution $(G/\bar{G})$ for SCD sample sintered at 1340°C, 16 h to 96.1% relative density ($\bar{G}$ = 0.82 μm).

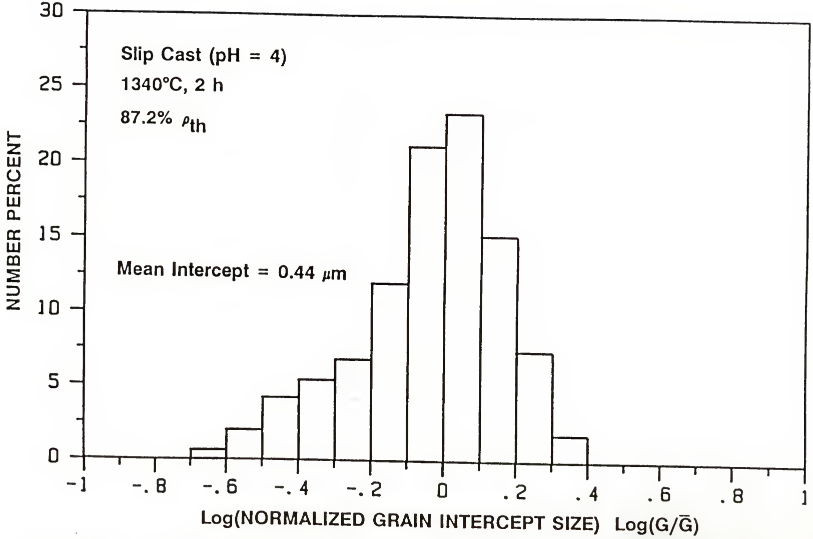

Figure 4.85 Distribution histogram of the normalized grain intercept size distribsution ($G/\bar{G}$) plotted in log scale for SCD sample sintered at 1340°C, 2 h to 87.2% relative density ($\bar{G}$ = 0.44 μm).

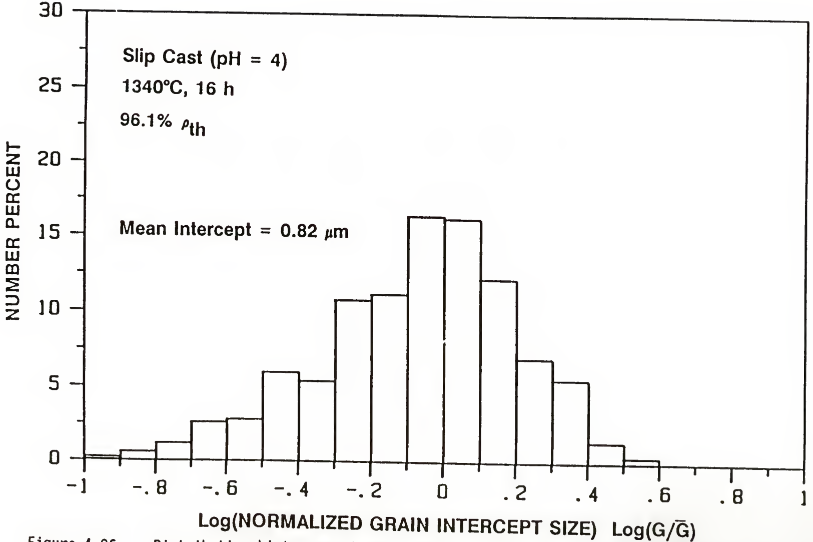

Figure 4.86 Distribution histogram of the normalized grain intercept size distribsution ($G/\bar{G}$) plotted in log scale for SCD sample sintered at 1340°C, 16 h to 96.1% relative density ($\bar{G}$ = 0.82 μm).

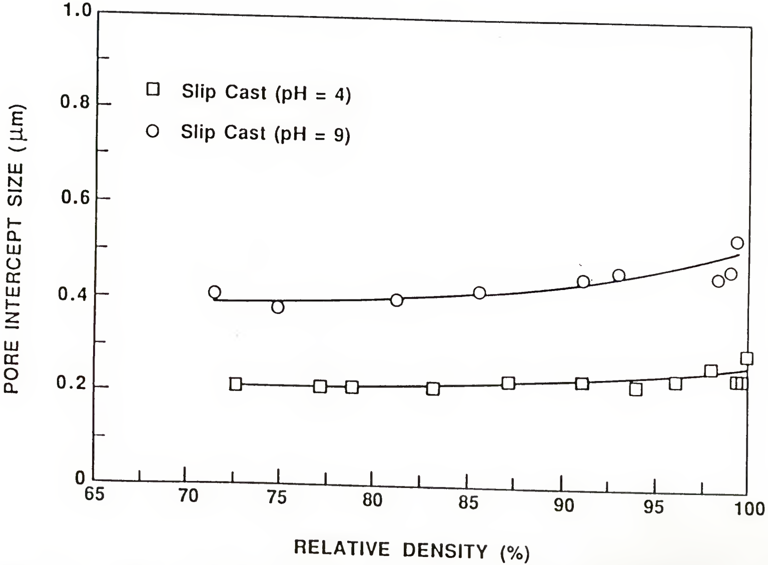

Figure 4.87 Plots of average pore intercept size vs. relative density for SCD and SCF samples.

observed in the present study indicated a balance between pore-shrinking mechanisms and pore-coarsening mechanisms. Furthermore, during densification process, pores with radii smaller than the critical size [Kin67] tend to shrink. This will decrease the average pore size. However, the elimination of fine-sized pores tended to increase the average pore size. These two processes can also contribute to the observation of constant pore size. However, a slight increase of the pore intercept sizes was observed for both slip cast samples in the high density range. This may indicate that pore coalescence becomes more important in the high density range where significant grain growth was observed.

The pore intercept size for the SCF sample (~0.4 to 0.5 μm) is approximately twice that of the SCD sample (~0.2 to 0.3 μm). A similar difference was observed in the median pore channel radius obtained by mercury porosimetry (~0.17 vs. ~0.095 μm for the SCF and SCD samples, respectively). The pore intercept sizes obtained by microscopy are more than twice the values obtained by mercury porosimetry. This is because the size obtained by porosimetry represents the size of the channels which allow the flow of a liquid between particles, not the size of the interstitial void formed by a cluster of particles.

If the SCD and SCF samples are compared at the same density level, the larger pore size of the SCF sample indicates that the pore population (i.e., number of pores per unit volume) is smaller and that the average distance between pores is larger. The larger pore size in the SCF sample also implied smaller curvature of the pore/solid interface. These microstructural characteristics partly accounted for the slower sintering kinetics for the SCF sample.

The pore intercept size distribution of the SCD sample are shown in Figures 4.88 to 4.91. Even though no significant change in intercept size distribution was observed over the entire density range. The percentage of fine-sized pores decreased slightly and the percentage of intermediate-sized pores increased slightly as the density increased. A slight decrease in the percentage of large pore sizes was also observed in the high density sample (Figure 4.91). Therefore, slight decrease in the width of the pore intercept size distribution was obtained for samples with high sintered density. The pore size distributions of the SCF sample (Figures 4.92 to 4.95) showed a similar trend except that the pore size distributions were broader (with a longer "tail" in the large pore range).

Lange and Davis reported pore coarsening in the initial stage sintering of ZrO_2 (with 6.6 mol% of Y_2O_3) [Lan84]. The pore size data in their studies were obtained by mercury porosimetry. In the early stages of sintering, due to the local densification of the relatively close-packed domains, the pore channels between these domains can open up. This accounts for the increase in size obtained by mercury intrusion. Since the pore intercept size for the initial stage sintering was not obtained in the present study, a comparison with these results can not be made.

It is interesting to note that very rapid grain growth occurred for the SCD and SCF samples as the relative density increased from ~98% to ~99% (Figures 4.45, 4.57, 4.58, 4.62, and 4.63). However, only slight change in pore intercept size and pore intercept size distribution was obtained in the same density range (Figures 4.87, 4.90, 4.91, 4.94, and 4.95). In most grain growth models for the late stages of sintering, it

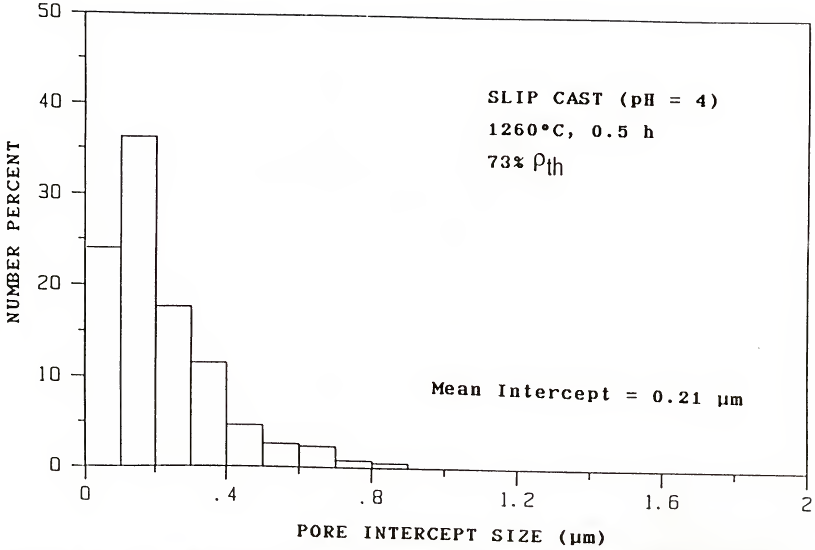

Figure 4.88 Histogram plot of the pore intercept size distribution for SCD sample sintered at 1260°C, 0.5 h to 72.8% relative density.

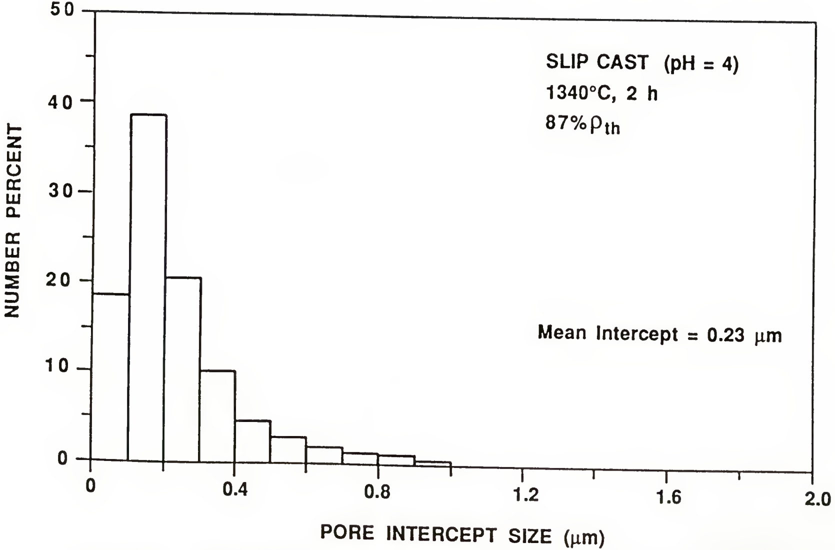

Figure 4.89 Histogram plot of the pore intercept size distribution for SCD sample sintered at 1340°C, 2 h to 87.2% relative density.

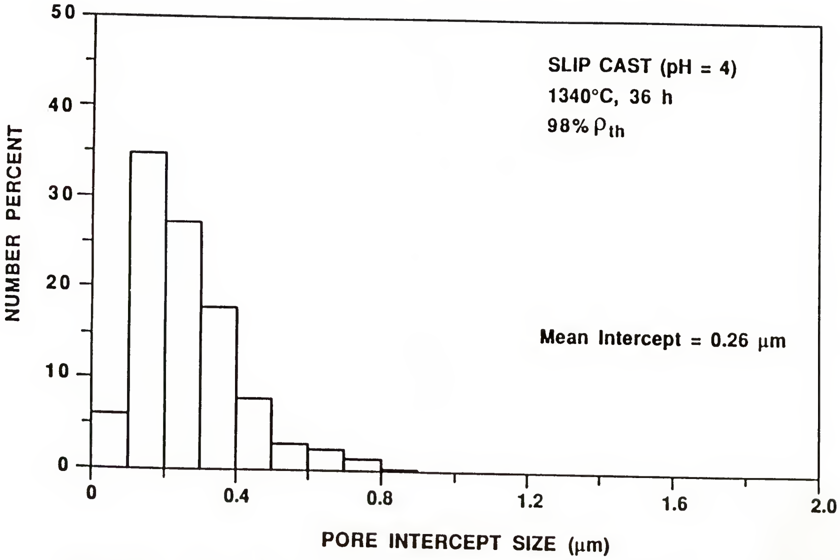

Figure 4.90 Histogram plot of the pore intercept size distribution for SCD sample sintered at 1340°C, 36 h to 98.0% relative density.

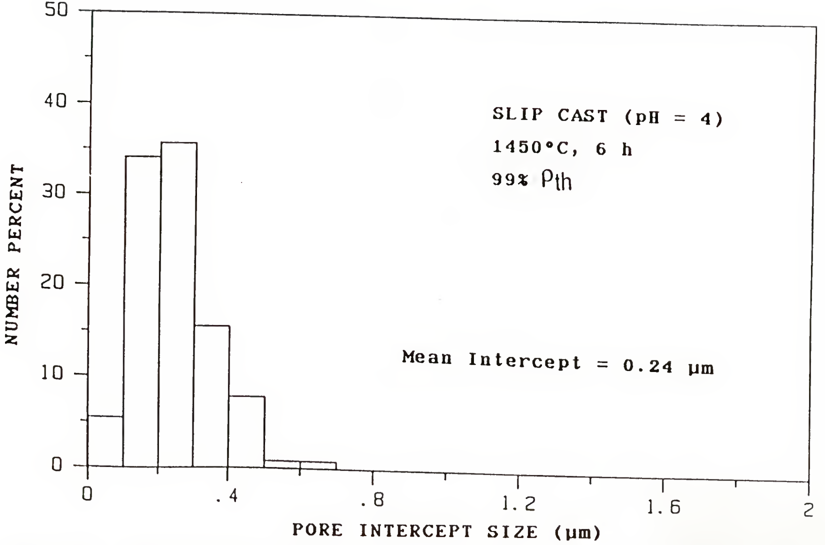

Figure 4.91 Histogram plot of the pore intercept size distribution for SCD sample sintered at 1450°C, 6 h to 99.4% relative density.

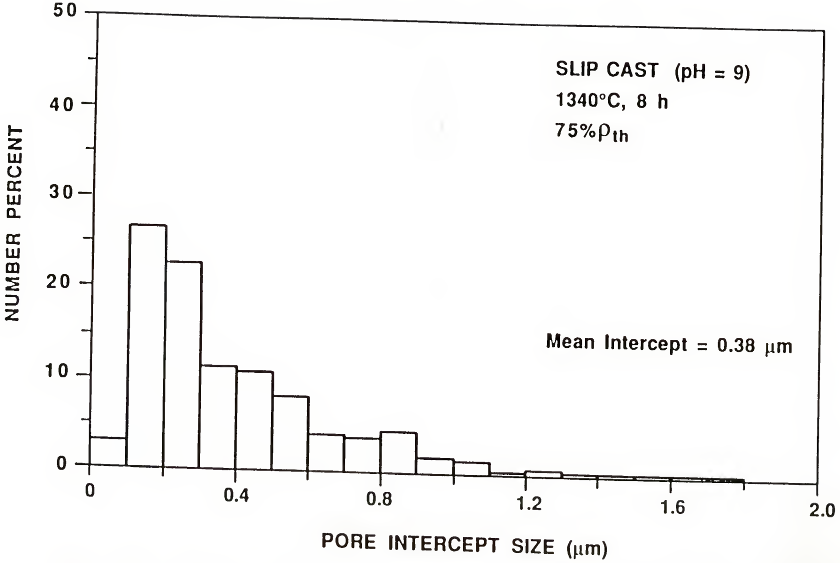

Figure 4.92 Histogram plot of the pore intercept size distribution for SCF sample sintered at 1340°C, 8 h to 74.9% relative density.

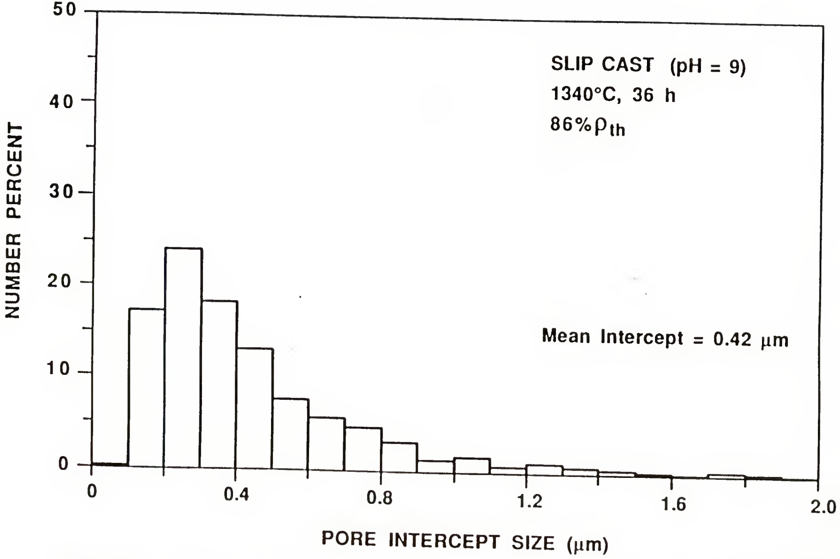

Figure 4.93 Histogram plot of the pore intercept size distribution for SCF sample sintered at 1340°C, 36 h to 85.6% relative density.

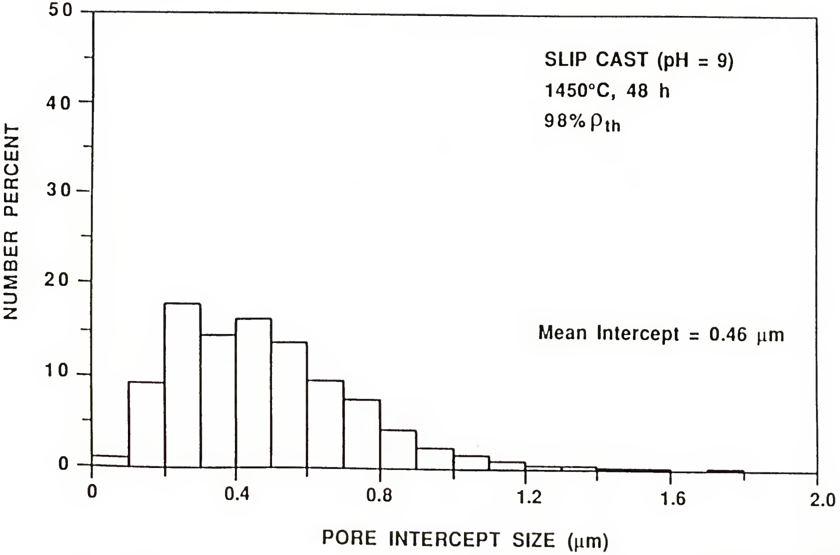

Figure 4.94 Histogram plot of the pore intercept size distribution for SCF sample sintered at 1450°C, 48 h to 98.3% relative density.

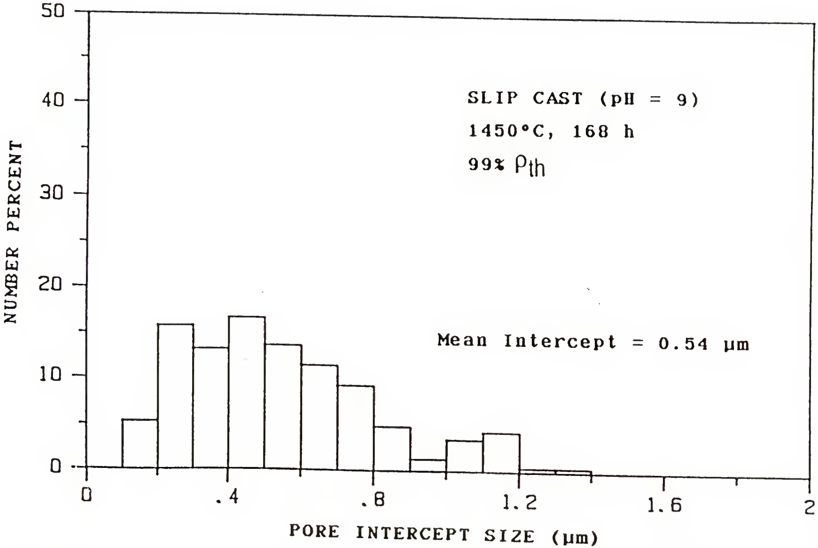

Figure 4.95 Histogram plot of the pore intercept size distribution for SCF sample sintered at 1450°C, 168 h to 99.3% relative density.

is generally assumed that the ratio of grain size vs. pore size is constant [Bro76]. However, in the present study, a increase in the ratio of grain sizes vs. pore size was obtained as the grain size increased.

Figure 4.96 shows plots of the average pore intercept size as a function of relative density for the dry-pressed samples and, for comparison, the SCD sample. The average pore intercept size of the DPL sample increased significantly with increasing density. This is a consequence of the heterogeneous green microstructure for this sample. During sintering, small pores in the close-packed agglomerated regions can be rapidly removed. For example, at ~74% overall bulk density, virtually full density was obtained in the close-packed agglomerated regions (Figure 4.37A). The average pore size was determined almost exclusively from the porous (inter-agglomerate) regions. The pore intercept size of the DPL sample was ~0.76 μm at ~74% relative density while the SCD sample had only ~0.2 μm pore intercept size. At further sintering, due to the severe heterogeneities packing density in the porous regions (Figure 4.37B), Some pores may open up due to localized densification. In addition, extremely large pores will not shrink because they are much larger than the critical radius at which shrinkage can occur [Kin67]. Consequently, the average intercept size increased.

In the DPH sample , the initial average pore radii were smaller and the number of very large pores was also smaller (compared to the DPL sample). Thus, more pores were in the "shrinkage regime" and the average pore size increased only moderately during densification (Figure 4.96).

From mercury porosimetry, it was shown that the dry-pressed samples have a bimodal pore size distribution (Figure 4.11), i.e., due to the presence of both finer intraagglomerate pores and coarser

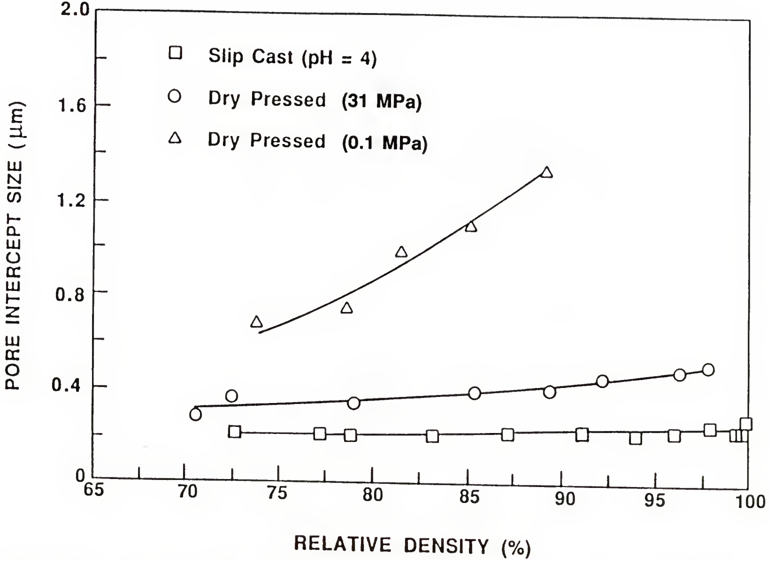

Figure 4.96 Plots of average pore intercept size vs. relative density for SCD, DPH, and DPL samples

interagglomerate pores. This bimodal pore size distribution remained through most of the densification process. The pore size histograms of the porous (interagglomerate) regions and the high density (intraagglomerate) regions at ~98% density are shown for the DPH sample in Figures 4.97 and 4.98, respectively. The high density regions had fine pore size and narrow pore size distribution which was similar to the pore intercept size distribution of SCD sample (Figure 4.91). The inter-agglomerate regions show large pore size and broader pore size distribution.

The evolution of pore intercept size distribution are shown in Figures 4.99 to 4.101 for the DPH sample and in Figures 4.102 to 4.104 for the DPL sample. Similar pore intercept size distributions were obtained for DPH sample in the density range ~73% to ~85% relative density. At higher density, a decrease in the number percent of fine pores and a slight increase in the number percent of larger pores were observed. For the DPL sample, a decrease in the number percent of fine pores and an increase in the number percent of large pores were observed when the densification proceeded. This is consistent with the significant increase of the average pore intercept size for the DPL sample (Figure 4.96).

It should be noted that similar pore intercept sizes and intercept size distributions were obtained for the SCF and DPH samples. This is the consequence of similar green density obtained in both samples. However, as shown before, a small number of large pores was observed for the DPH sample (Figure 4.13B). Due to the small concentration of these large pores, they can not be shown in number-basis distribution histograms.

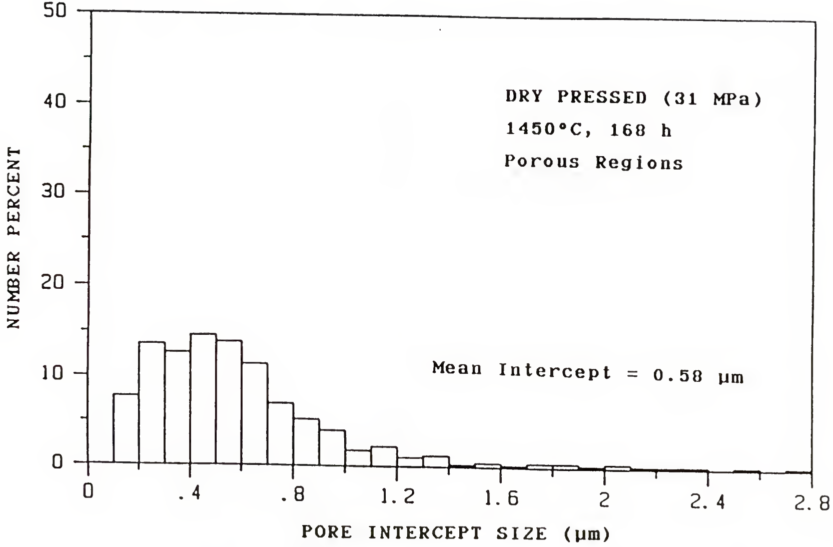

Figure 4.97 Histogram plot of the pore intercept size distribution for the porous regions of DPH sample sintered at 1450°C, 168 h to 97.8% overall bulk density.

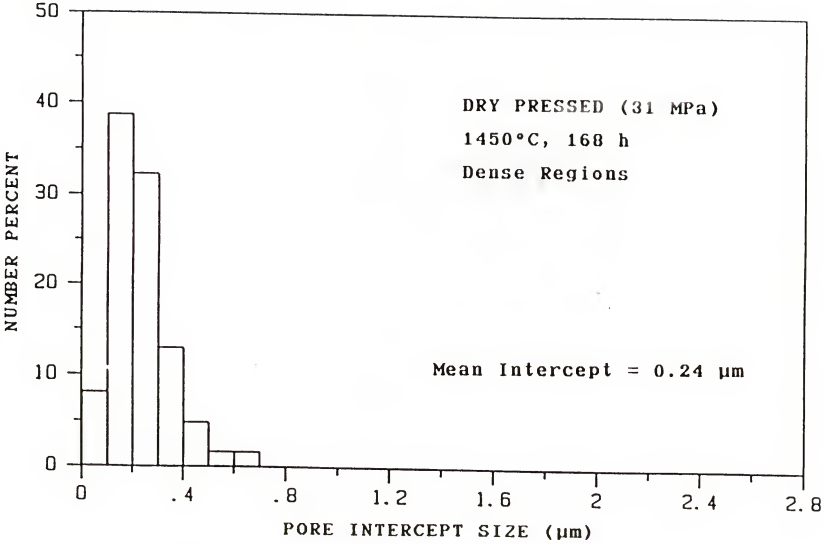

Figure 4.98 Histogram plot of the pore intercept size distribution for the close-packed agglomerated regions of DPH sample sintered at 1450°C, 168 h to 97.8% overall bulk density.

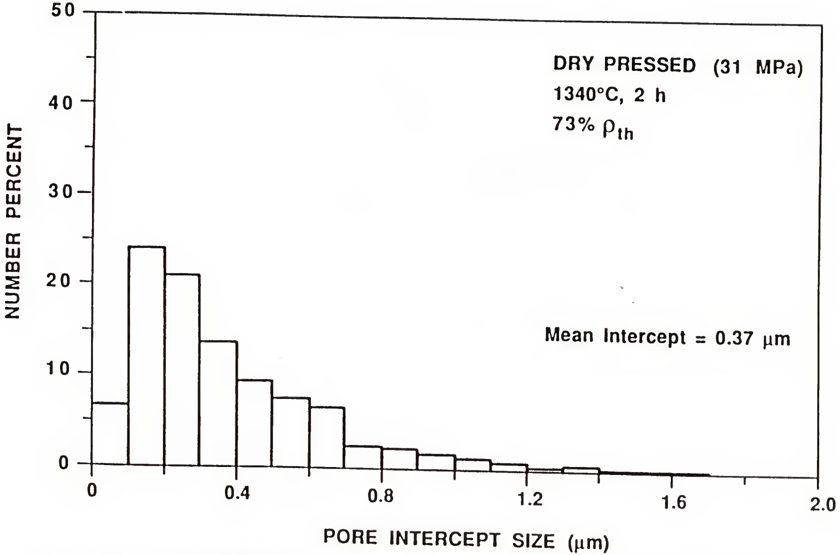

Figure 4.99 Histogram plot of the pore intercept size distribution for DPH sample sintered at 1340°C, 2 h to 72.5% relative density.

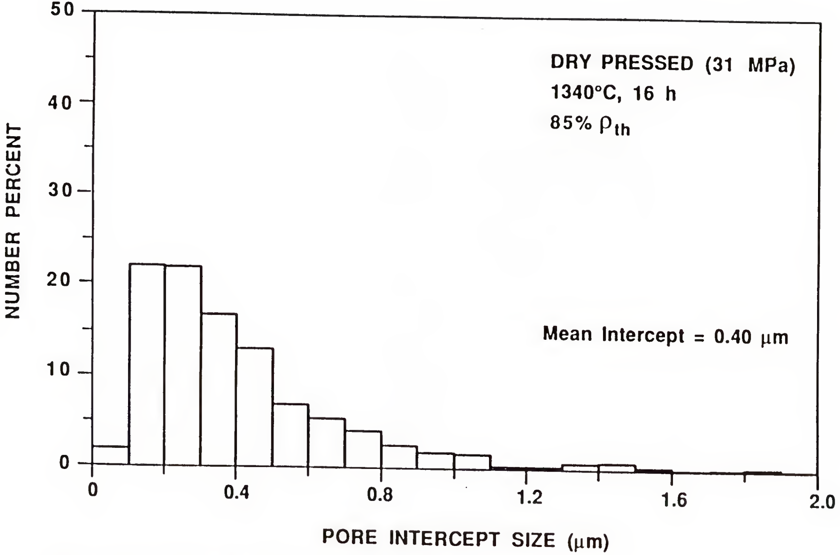

Figure 4.100 Histogram plot of the pore intercept size distribution for DPH sample sintered at 1340°C, 16 h to 85.4% relative density.

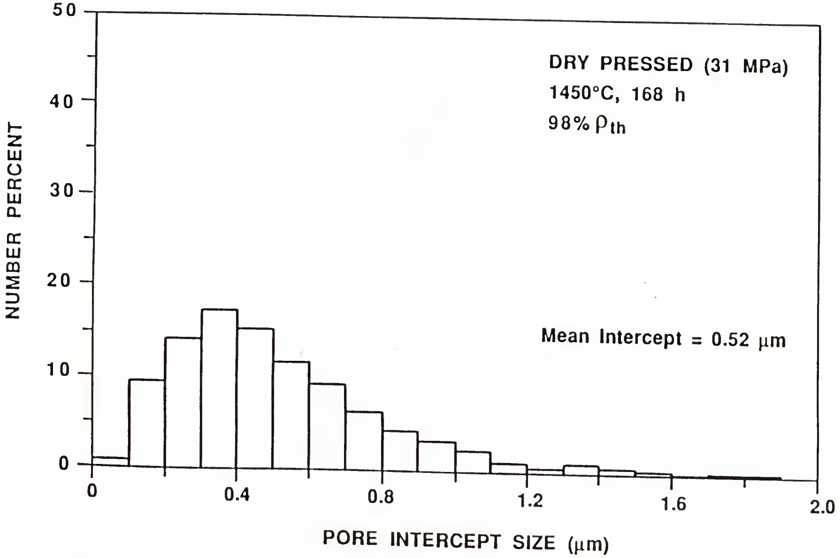

Figure 4.101 Histogram plot of the pore intercept size distribution for DPH sample sintered at 1450°C, 168 h to 97.8% relative density.

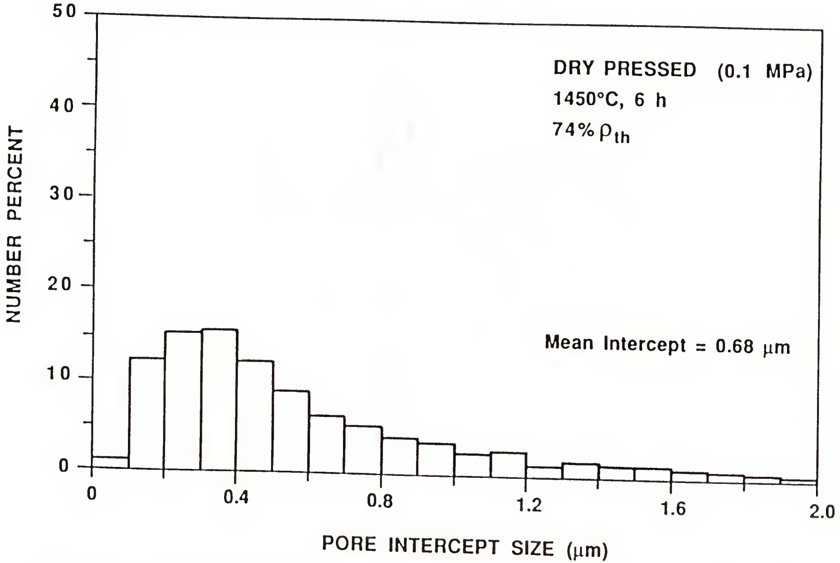

Figure 4.102 Histogram plot of the pore intercept size distribution for DPL sample sintered at 1450°C, 6 h to 73.8% relative density.

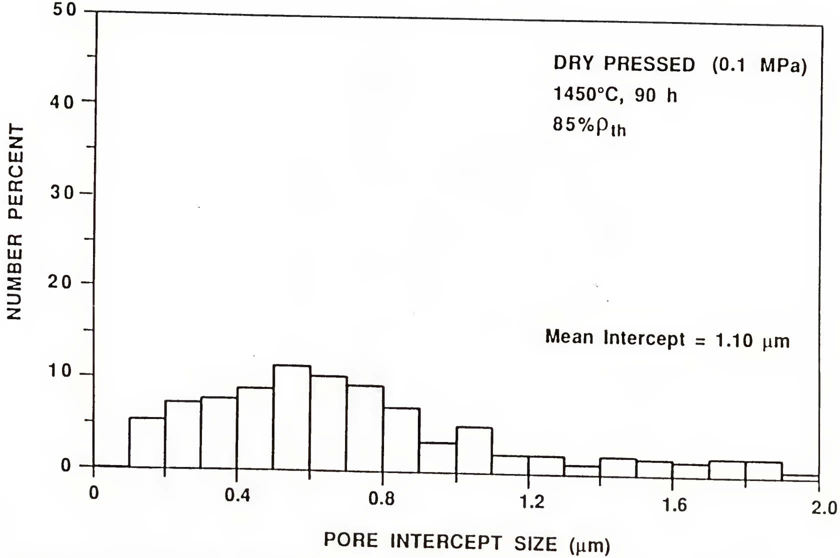

Figure 4.103 Histogram plot of the pore intercept size distribution for DPL sample sintered at 1450°C, 90 h to 85.2% relative density.

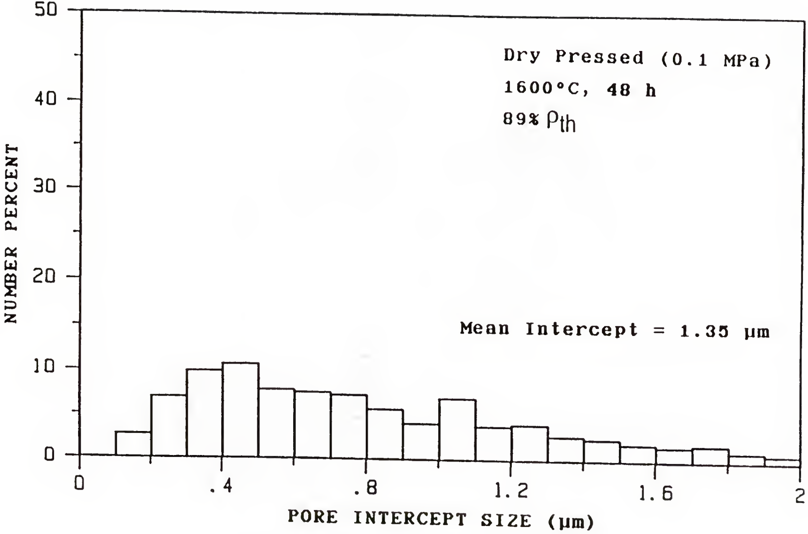

Figure 4.104 Histogram plot of the pore intercept size distribution for DPL sample sintered at 1600°C, 48 h to 89.2% relative density.

Plots of arithmetic standard deviation (σ_a) of the pore intercept size distribution vs. relative density are shown in Figure 4.105 for the SCD, SCF and DPH samples. For each sample, a relatively constant σ_a value was obtained over the entire density range. Because the pore intercept sizes of the above samples were also relatively constant over the same density range (Figures 4.87 and 4.96), the ratio of σ_a to pore intercept size for each sample was expected to remain relatively constant. This is confirmed in Figure 4.106 in which plots of the ratio of σ_a to pore intercept size vs. relative density are shown. A constant ratio indicated that the pore intercept size distribution of each sample remained relatively unchanged throughout the densification process. This is consistent with the pore intercept size histograms shown previously. It should be noted that a slight decrease of the ratio of σ_a to pore intercept size with increasing relative density can still be noticed. This is the consequence of the slight increase of pore intercept size with increasing relative density.

In Figure 4.105, it is also shown that the σ_a values of the SCF and DPH samples are about twice of that of the SCD sample. Because the pore intercept size of the SCF and DPH samples are also about two-fold larger than that of the SCD sample, a common line was obtained in Figure 4.106. This indicates that a common pore intercept distribution curve will be obtained if pore intercept size distributions are normalized by dividing each intercept size with the mean size of the distribution.

Plots of the geometric standard deviation (σ_g) of the pore intercept size distribution vs. relative density for the SCD, SCF, and DPH samples are shown in Figure 4.107. A relatively constant σ_g values

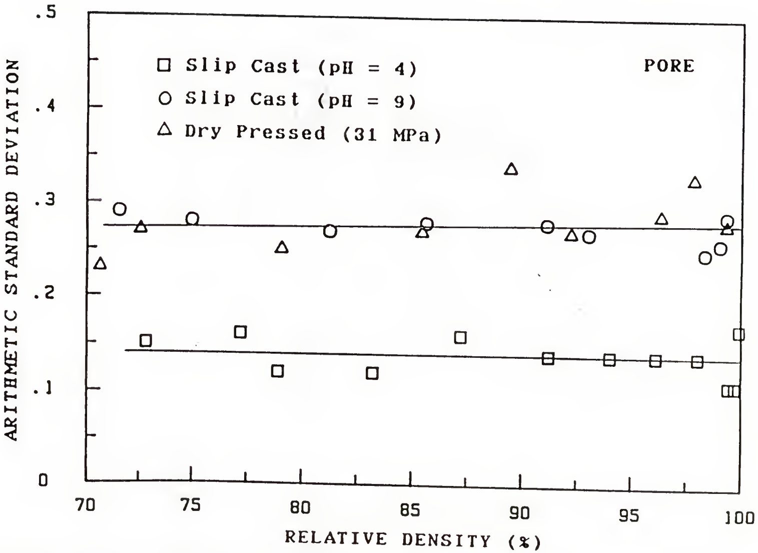

Figure 4.105 Plots of arithmetic standard deviation of pore intercept size distribution vs. relative density for SCD, SCF, and DPH samples.

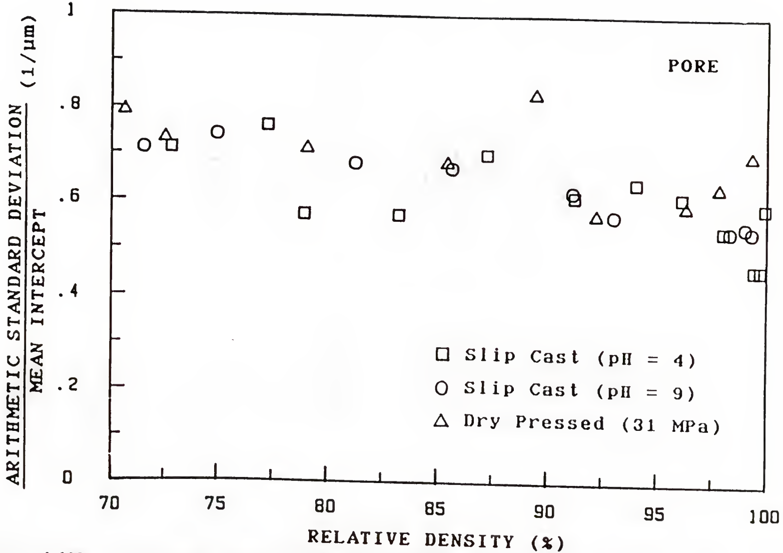

Figure 4.106 PLots of the ratio of arithmetic standard deviation of pore intercept size distribution to mean intercept vs. relative density for SCD, SCF, and DPH samples.

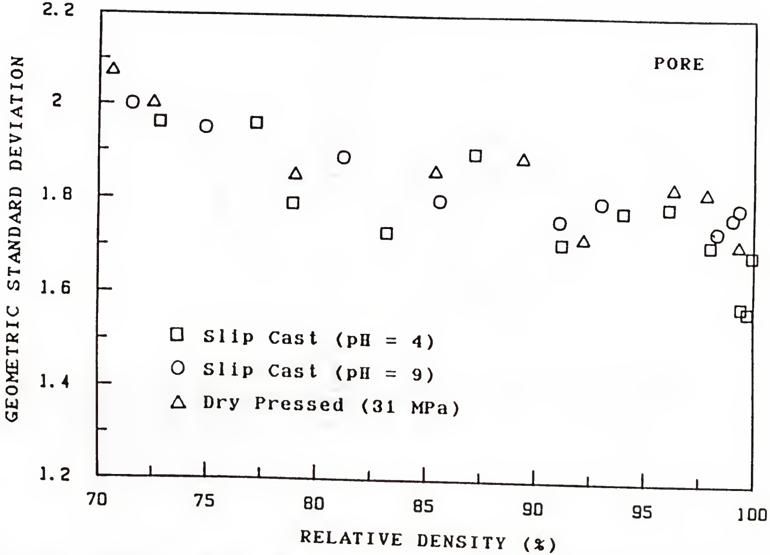

Figure 4.107 Plots of geometric standard deviation of pore intercept size distribution vs. relative density for SCD, SCF, and DPH samples.

were also obtained which was consistent with the results in Figure 4.106.

Even though σ_g and the ratio of σ_a to pore intercept size were relatively constant over the density range investigated, a slight decrease in both values was observed. This indicated a slight decrease in the width of pore intercept size distribution as the sintered density increased. This might be associated with the elimination of the fine-sized pores.

Pore-solid interfacial area. The effect of particle packing on microstructural evolution can also be seen in the plots of pore-solid interfacial area vs. sintered density. It has been shown that the SCD sample had finer microstructure (i.e., finer grain size and finer pore size) at any particular relative density. The finer pores should also result in a higher value of the specific pore-solid interfacial area. This is illustrated in Figures 4.108 and 4.109 which compare the pore-solid interfacial area (obtained by quantitative stereology) of the SCD samples with that of the SCF (Figure 4.108) and the dry pressed samples (Figure 4.109). The trajectory of the interfacial area vs. relative density curve of the SCF sample was lower than that of the SCD sample over the entire densification range, indicating that the SCF sample had coarser pore structure. Based on the argument proposed by Burke [Bur80], it can be concluded that the SCD sample had higher densification/coarsening ratio. Indeed, microstructure observations confirm this conclusion.

It can also be seen from Figure 4.108 that a good linear relationship between the interfacial area and density is obtained for each sample. This agrees with the prediction proposed by DeHoff et al.

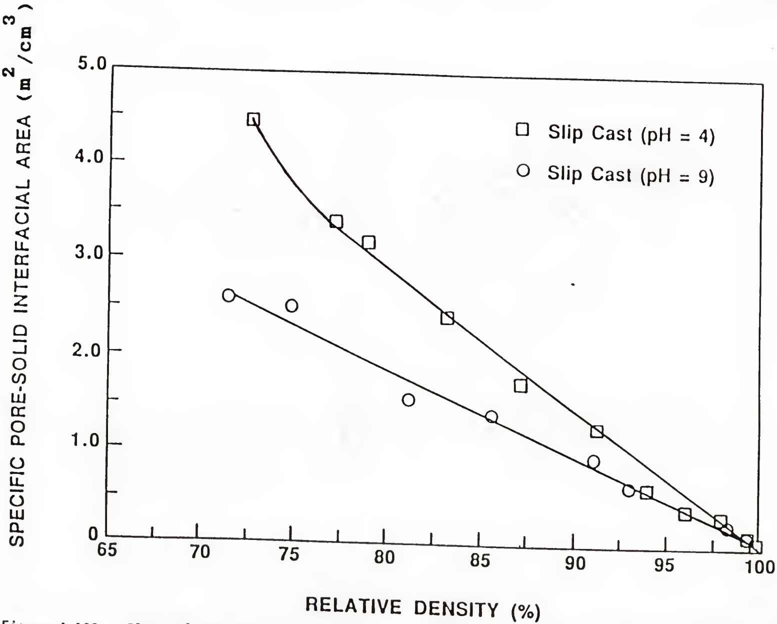

Figure 4.108 Plots of specific pore-solid interfacial area vs. relative density for SCD and SCF samples.

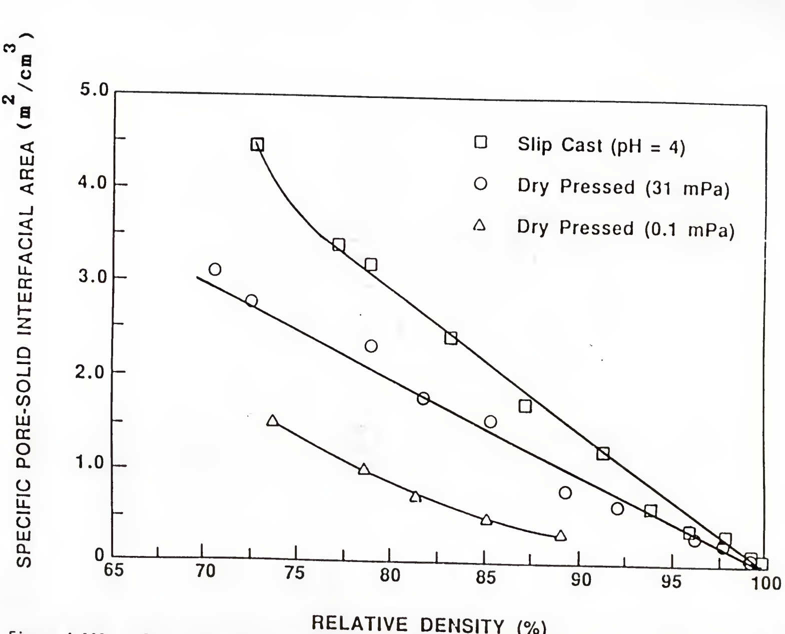

Figure 4.109 Plots of specific pore-solid interfacial area vs. relative density for SCD, DPH, and DPL samples.

[DeH66]. They showed that the slope of the linear curve is inversely proportional to the pore intercept size. The larger slope for the SCD sample indicated a finer pore intercept size. The constant slope also represented a constant pore intercept size. These results are consistent with the pore intercept size measurement.

The trajectory of the pore-solid interfacial area vs. relative density for the DPL sample (Figure 4.109) was much lower than that of the SCD sample and was consistent with the previous data on grain and pore intercept sizes which showed that these samples underwent extensive coarsening. The DPH sample showed a trajectory intermediate between the DPL and SCD samples which was consistent with the grain and pore intercept size data discussed previously. Similar values of pore-solid interfacial area were obtained for the SCF and DPH samples over the entire densification process. This is the consequence of the similar green densities obtained for these two samples. Because the pore-solid interfacial area is an averaged bulk properties, the differences in homogeneities between these two samples were not shown.

The pore-solid interfacial area trajectory of the DPH sample also showed a good linear relationship. However, the trajectory of the DPL sample did not have a good fit to a linear relationship. These results were also consistent with the pore intercept size measurements (i.e., the DPH sample had relatively constant pore intercept size and the DPL sample showed significant pore coarsening).

Studies of the trajectories of pore-solid interfacial area vs. relative density were also reported by Shaw and Brook for alumina compacts prepared from dry-pressing. Because the powders used in their study had much higher initial surface area (i.e., 6 m^2/g vs. 3.4 m^2/g in this study); the pore-solid interfacial area values should be higher than those reported in the present study when samples have constant density. However, the trajectory of pore-solid interfacial area obtained in their study is similar to that of the DPH samples in the present study. This resulted from the significant lower green density (30% relative density) of their samples. Lower density indicated larger pore sizes and more heterogeneous microstructure in the green body. In order to reach comparable densities with the samples in the present study, significant higher sintering temperatures (i.e., 1525°C) were used, and therefore more coarsening was obtained. However, the trajectories of pore-solid interfacial area in their study are still higher than that of the DPL sample in the present study. This is the direct consequence of the higher initial surface area of the powder used in their study.

The pore-solid interfacial area data can be used to calculate pore intercept sizes (using equation 3.10). Comparison of these intercept values with the values obtained by the linear intercept method are shown in Figures 4.110 to 4.113. The agreement between the values is excellent.

From pore-solid interfacial area data, the mean free path (MFP) between pores (i.e., the mean intercept length of solid phase without considering grain boundary) can be obtained using equation 3.11. Plots of MFP vs. relative density are shown in Figure 4.114 for the SCD and SCF samples. As expected, the SCF sample had larger MFP values over the entire densification range. It has been shown that the green compact of the SCF sample had small close-packed clusters. Finer internal pores associated with these clusters can be removed during the earlier stages of densification. The development of dense domains results in larger MFP

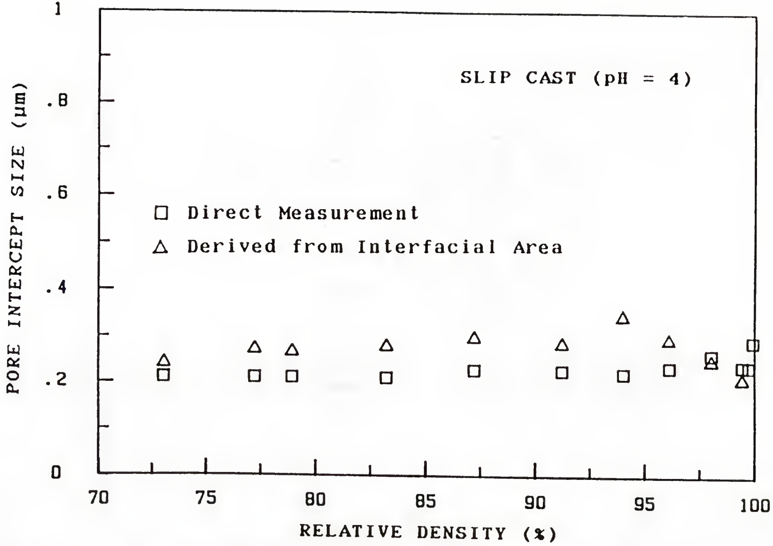

Figure 4.110 Comparison of pore intercept size calculated from pore-solid interfacial area with that obtained by direct linear intercept measurement for SCD sample.

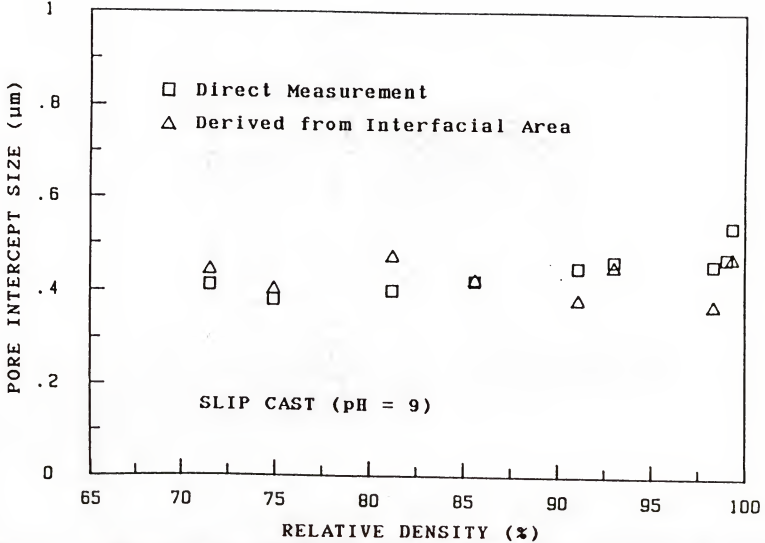

Figure 4.111 Comparison of pore intercept size calculated from pore-solid interfacial area with that obtained by direct linear intercept measurement for SCF sample.

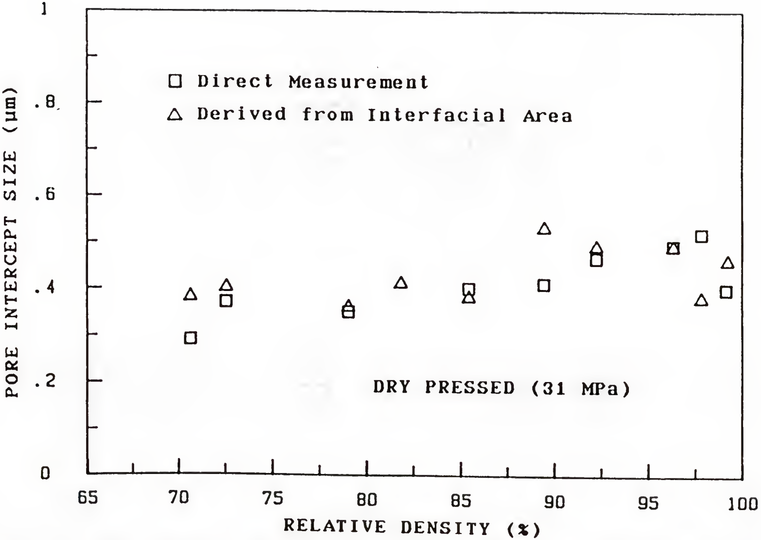

Figure 4.112 Comparison of pore intercept size calculated from pore-solid interfacial area with that obtained by direct linear intercept measurement for DPH sample.

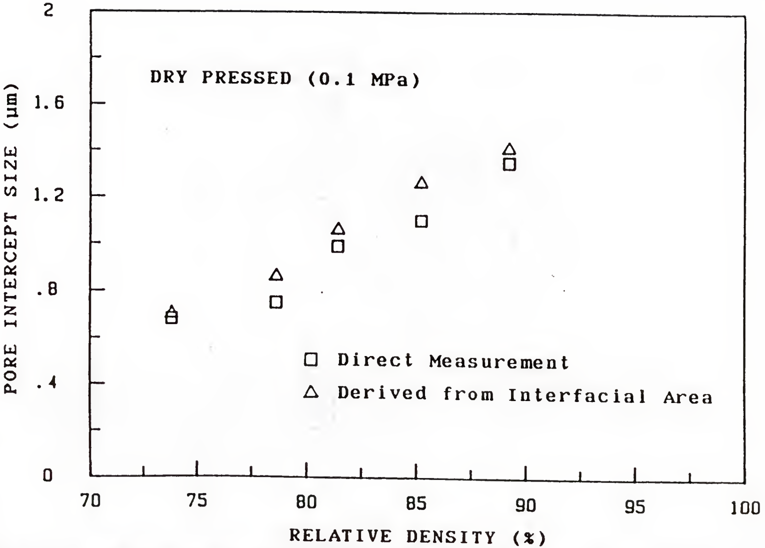

Figure 4.113 Comparison of pore intercept size calculated from pore-solid interfacial area with that obtained by direct linear intercept measurement for DPL sample.

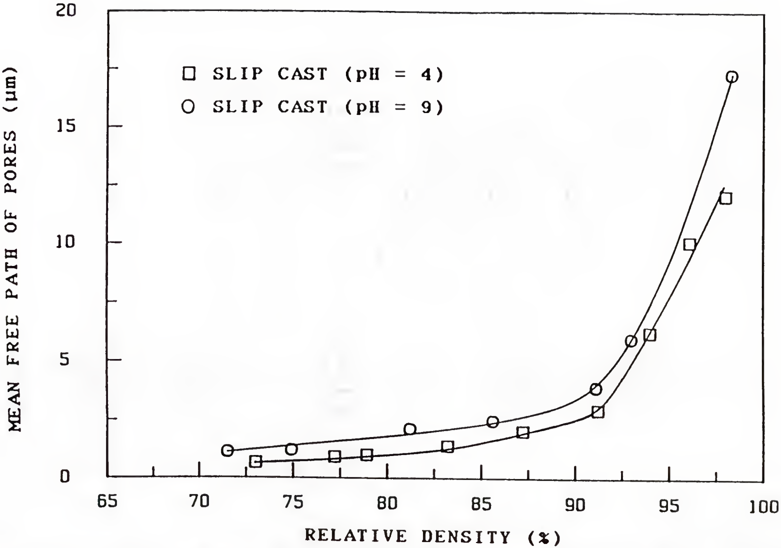

Figure 4.114 Plots of mean free path of pores vs. relative density for SCD and SCF samples.

values for the SCF sample. The larger MFP, along with larger average pore intercept sizes, indicates that SCF samples have lower pore concentration compared to SCD samples at any given relative density. This is confirmed in Figure 4.115 which shows plots of number of pores per unit area (at the cross section plane) vs. relative density for the two samples.

It should be noted that the number of pores per unit area decreased relatively slowly for the SCD sample when the relative density increased from ~73% to ~87%. The possible reason was that the pore channels are more branched and irregularly-shaped in this density range. During sintering, the number of branches or the length of the branches decreased; therefore, the shape of the pores on a two dimensional section became more rounded. However, the number of pores only showed a slight decrease. This is supported by measurements of the pore "shape factor" over this density range (Figure 4.116). The shape factor was obtained by dividing the mean perimeter length of the pores with the mean pore intercept length. Branched or irregularly-shaped pores will have a larger shape factor value; on the other hand, rounded pores will have smaller shape factor value. The shape factor of the SCD sample showed a rapid decrease up to ~87% relative density which is consistent with our speculation. At high density, the shape factor of the SCD sample remained relatively constant at the value of ~4 which is the shape factor for a circle*. In the high density regime (> 90% density), densification occurs primarily by the shrinkage and elimination of

---

* The mean intercept length of monosized circles with diameter D is $\pi D/4$. Therefore, the ratio of perimeter of a circle to mean intercept length (i.e., shape factor) is 4.

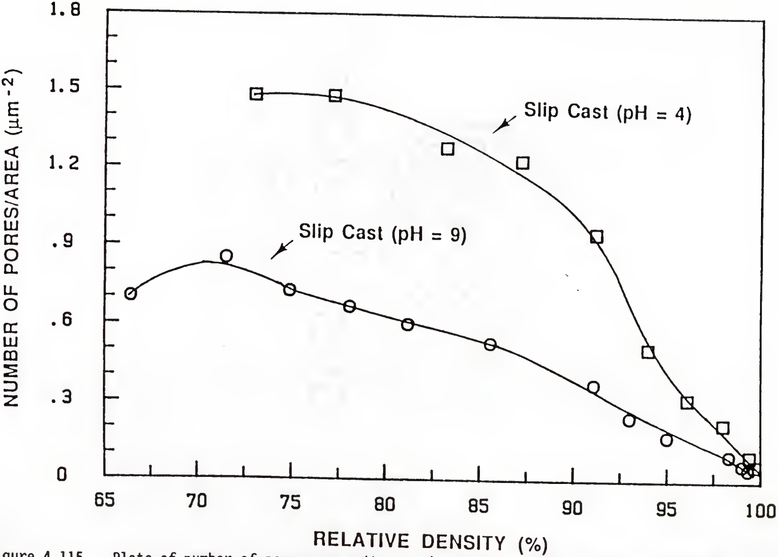

Figure 4.115 Plots of number of pores per unit area (on cross section plane) vs. relative density for SCD and SCF samples.

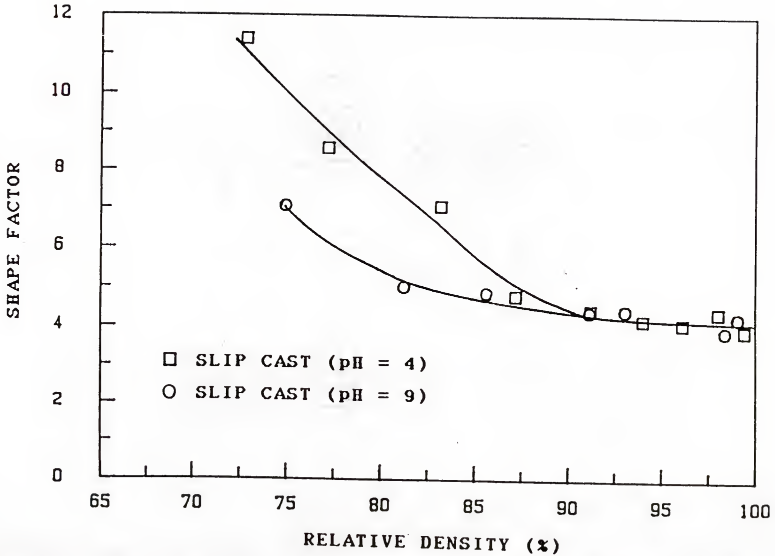

Figure 4.116 Plots of shape factor of pores on cross section plane vs. relative density for SCD and SCF samples.

pores. This is indicated by the decreasing number of pores per unit area as shown in Figure 4.115.

The shape factor for the SCF sample with less than ~87% relative density was smaller compared to the SCD sample. This reflected that the pores of the SCF sample in this density range were less irregular in shape which might be due to the more extended sintering schedule (time x temperature) experienced by the SCF sample. Above ~87% relative density, the shape factor values were essentially the same for the SCD and SCF samples.

Plots of the MFP between pores and the number of pores per unit area for dry-pressed samples are shown in Figure 4.117 and 4.118, respectively. The MFP was much larger for the DPL sample which was consistent with its much coarser microstructure (Figures 4.48 and 4.96) and its very low value of the number of pores per unit area (Figure 4.118). As with other microstructure features, the DPH sample showed values of the MFP and the number of pores/area that are intermediate between the DPL and the SCD samples.

Plots of shape factor of pores vs. relative density for the dry-pressed samples and SCD sample are shown in Figure 4.119. Similar to the SCF sample, the DPH sample showed lower shape factor values than the SCD sample when relative density was below ~85%. At higher density, the shape factor values of the DPH sample approached that of the SCD sample. This also indicated a more rounded pore structure. Significantly lower shape factor values were obtained for the DPL sample. Although the lowest shape factor value should be 4, shape factors smaller than 4 were obtained for the DPL sample. This probably resulted from increased

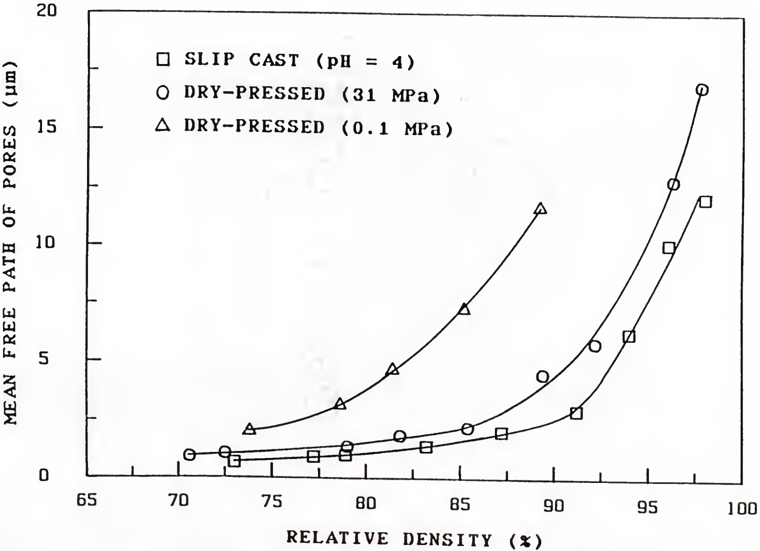

Figure 4.117 Plots of mean free path of pores vs. relative density for SCD, DPH, and DPL samples.

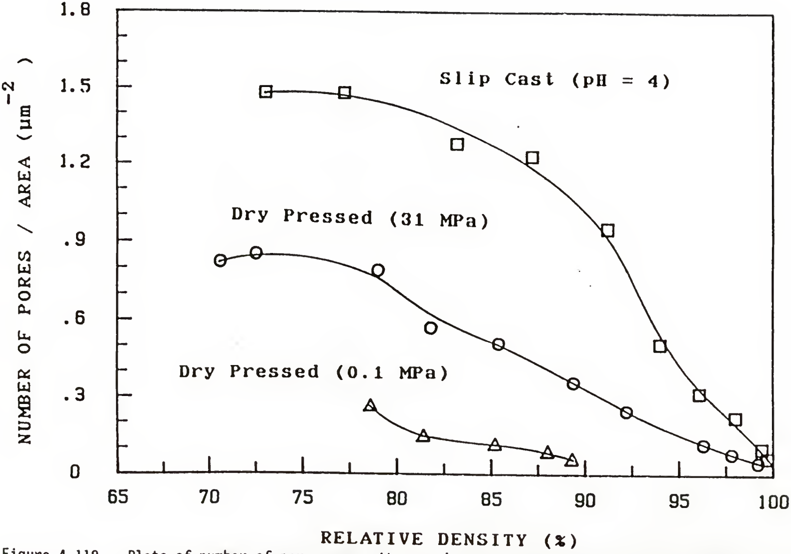

Figure 4.118 Plots of number of pores per unit area (on cross section plane) vs. relative density for SCD, DPH, and DPL samples.

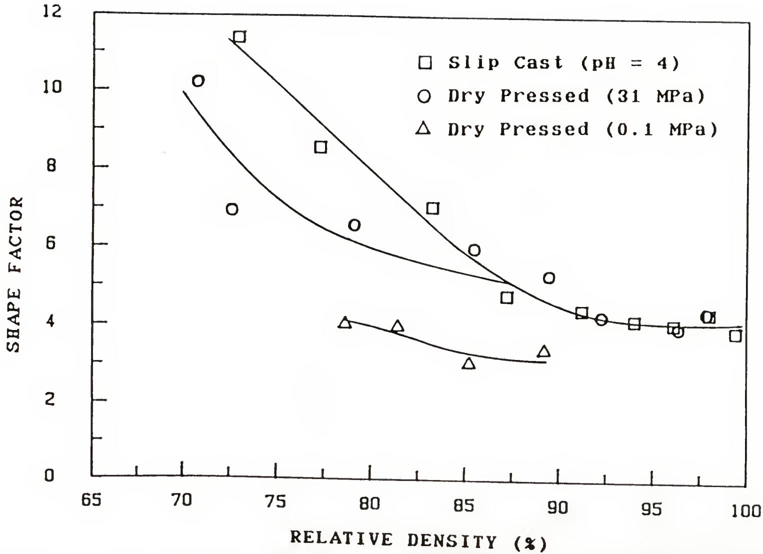

Figure 4.119 Plots of shape factor of pores on cross section plane vs. relative density for SCD, DPH, and DPL samples.

experimental error in the measurements due to the severe microstructural heterogeneities in the DPL samples.

Grain boundary area (GBA). Plots of GBA vs. relative density for slip cast samples are shown in Figure 4.120. In the early stages of sintering, only small amounts of grain boundary area were formed in the neck regions; therefore, both samples had low GBA values. As densification proceeded, the GBA increased due to the growth of neck regions and the formation of new necks. Because the SCF samples had lower green densities than the SCD samples, larger density increase was needed in order to reach a similar density as the SCD samples. A larger density increase indicated that more grain boundaries were formed. Therefore, slightly higher GBA values were observed for the SCF samples when the sintered density was smaller than ~78%. The GBA reached a peak value at ~90% density for the SCD sample and at ~80% density for the SCF sample. Decreases in GBA were observed upon further densification. The decreases reflected the onset of grain growth. This is consistent with the grain size results (Figure 4.45) which showed increases of grain size in the same density range. The much higher peak value (~3.5 m^2/cm^3) for the SCD sample is another indication of its fine grain microstructure. The high green density and fast densification rate (i.e., higher densification/coarsening ratio) for the SCD sample also pushed the peak position to higher density (i.e., the onset of grain growth was delayed).

Figure 4.121 shows plots of GBA as a function of relative density for dry-pressed samples. The DPL sample had very low GBA value and the peak value occurred at very low density (<75% relative density). This was consistent with the extensive coarsening and large grain size

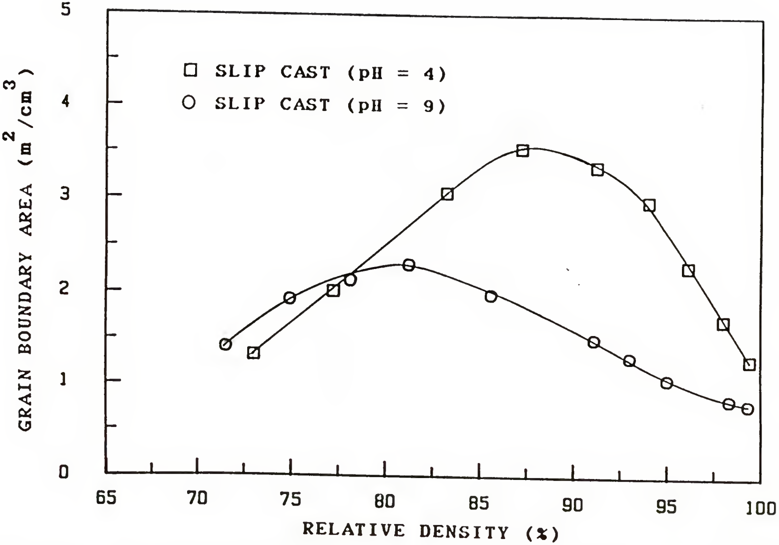

Figure 4.120 Plots of grain boundary area vs. relative density for SCD and SCF samples.

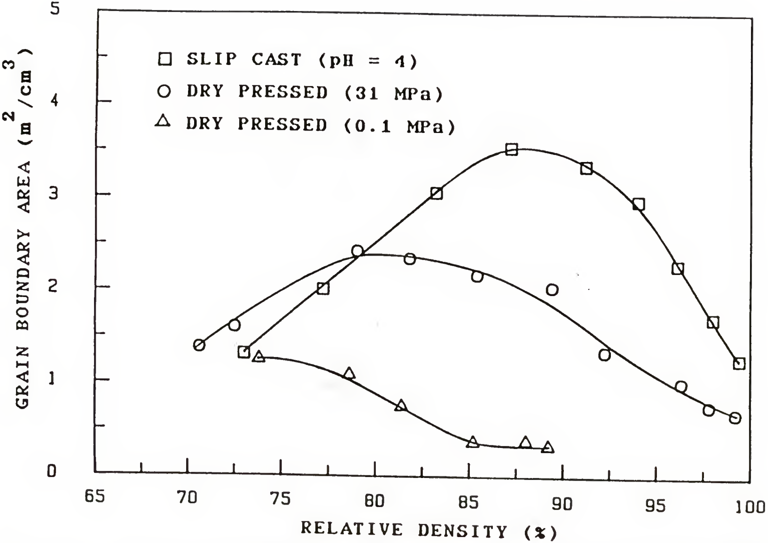

Figure 4.121 Plots of grain boundary area vs. relative density for SCD, DPH, and DPL samples.

observed in the DPL sample. The DPH sample had higher GBA value and the peak appeared at a higher density. This indicated that the DPH sample had finer microstructure and the onset of coarsening process was delayed. However, as shown in the same figure, the SCD sample had a much finer sintered microstructure and better resistance against coarsening.

Studies of the evolution of GBA during densification was also reported by Shaw and Brook for alumina compacts prepared from dry pressing [Sha86]. Because the powders used in their study had much finer particle sizes (i.e., the equivalent surface area diameter was ≈ 0.25 μm), therefore, much higher GBA values should be expected in their samples compared to the samples in the present study. However, the trajectory of GBA for the samples in their study fall between that of the DPH and DPL samples in the present study. This is the consequence of very low green density, as being discussed previously in regards to the evolution of pore-solid interfacial area.

It has been shown that grain intercept size can be derived from grain boundary area and pore-solid interfacial area (equation 3.12). Figures 4.122 to 4.125 show comparison between the grain intercept size values obtained from the interfacial areas and values obtained by the linear intercept method for samples with different consolidation conditions. Extremely good agreement between these two methods was obtained for most of the samples. However, the grain sizes derived from the interfacial area had higher value than the linear intercept grain size for the DPL sample with density in the range ~85 - 90%. This discrepancy may be due to the extremely heterogeneous microstructure of this sample which decreases the accuracy of the stereological measurements.

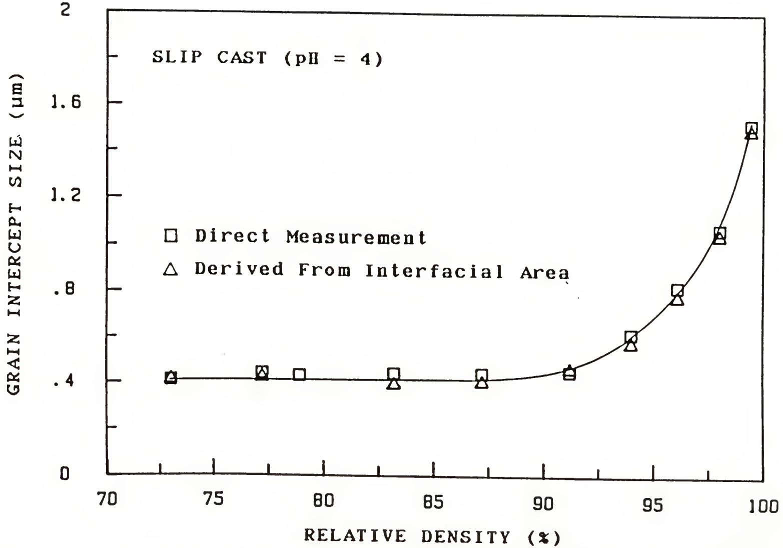

Figure 4.122 Comparison of grain intercept size calculated from interfacial area with that obtained by direct linear intercept measurement for SCD sample.

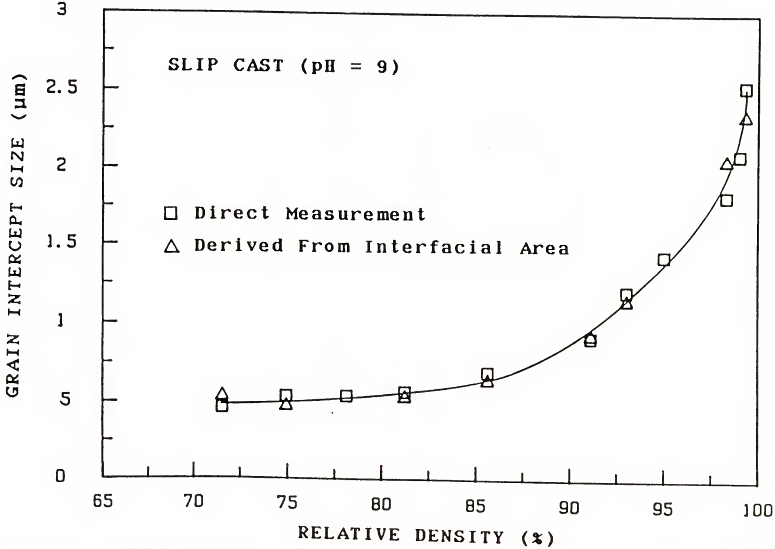

Figure 4.123 Comparison of grain intercept size calculated from interfacial area with that obtained by direct linear intercept measurement for SCF sample.

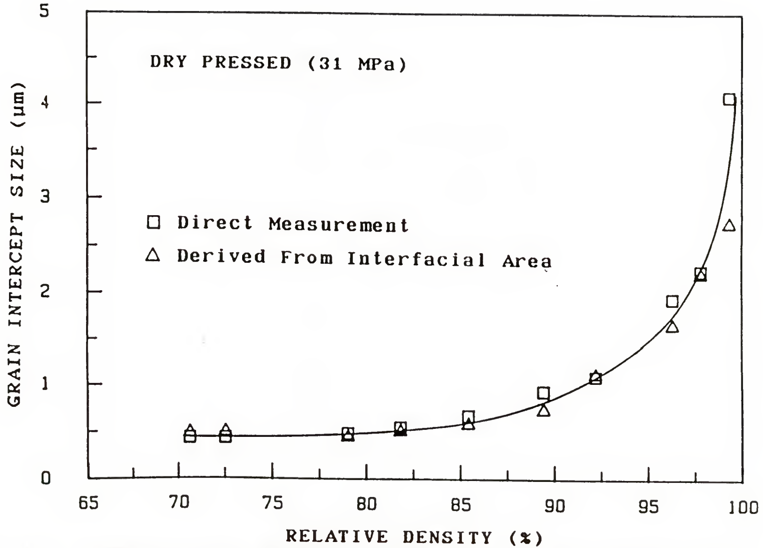

Figure 4.124 Comparison of grain intercept size calculated from interfacial area with that obtained by direct linear intercept measurement for DPH sample.

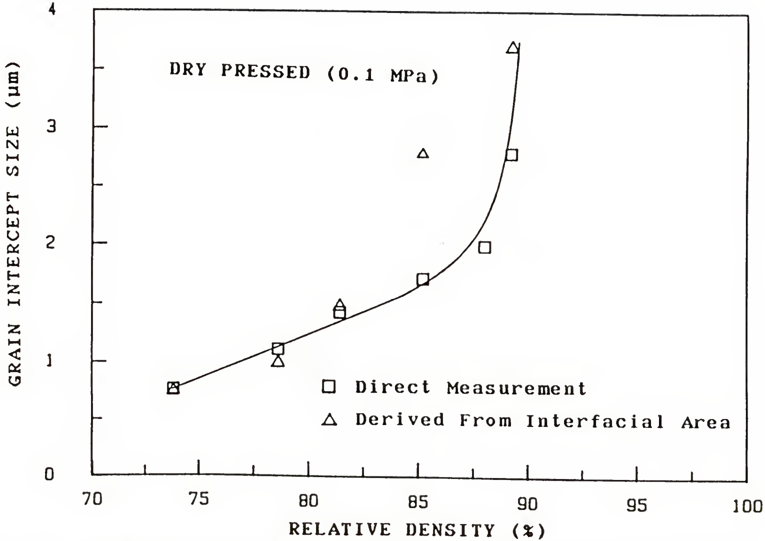

Figure 4.125 Comparison of grain intercept size calculated from interfacial area with that obtained by direct linear intercept measurement for DPL sample.

Integral mean curvature (IMC). Plots of IMC vs. sintered density for the SCD and SCF compacts are shown in Figure 4.126. The SCF sample showed a negative minimum IMC value at around 71% relative density. A minimum value was also expected for the SCD sample. However, because low density data was not obtained, the minimum value for the SCD sample was not shown. The absolute value of IMC decreased as densification proceeded. This indicated a decrease of the number of pores per unit volume. The more negative IMC value for the SCD sample represented finer pore structure [TU072] which was consistent with previous results. As discussed in Chapter II, both samples should have positive IMC value at green state. The SCD green compact should have larger IMC value due to the larger number of particles per unit volume (i.e., higher green density). However, the SCD sample reached a more negative value at only ~11% relative density increase (from ~64% relative density to ~75% relative density). On the other hand, the SCF sample showed around 20% density increase (from ~51% relative density to ~71% relative density) to obtain the less negative minimum IMC value. The rapid decrease of the IMC for the SCD sample indicated rapid formation and growth of the neck regions [Gre69, Tuo72]. This is consistent with the higher densification rate and rapid increase in grain boundary area observed for the SCD samples.

Figure 4.127 shows plots of the IMC vs. relative density for the two dry-pressed samples and the SCD sample. The DPL sample had very low absolute value of IMC which indicated a coarse pore structure [Tuo72]. This is consistent with the previous results on pore intercept size (Figure 4.96) and pore-solid interfacial area (Figure 4.109). The DPH sample had a more negative value and, therefore, finer pore structure.

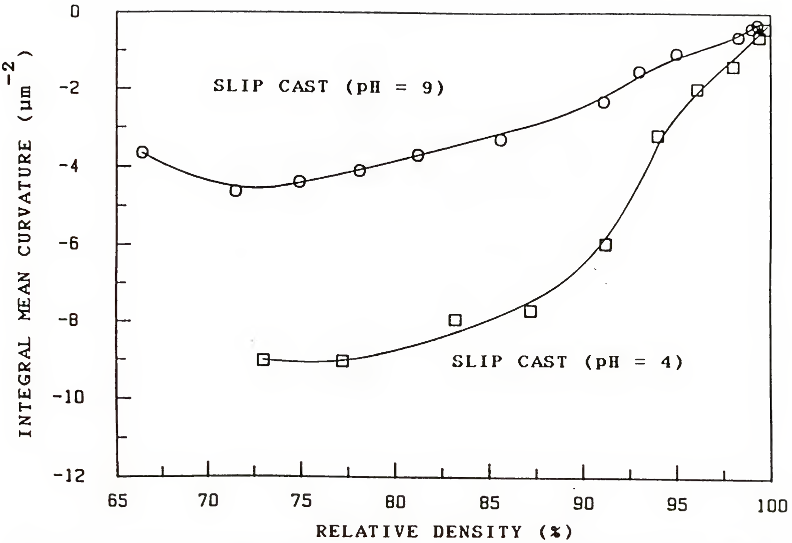

Figure 4.126 Plots of integral mean curvature vs. relative density for SCD and SCF samples.

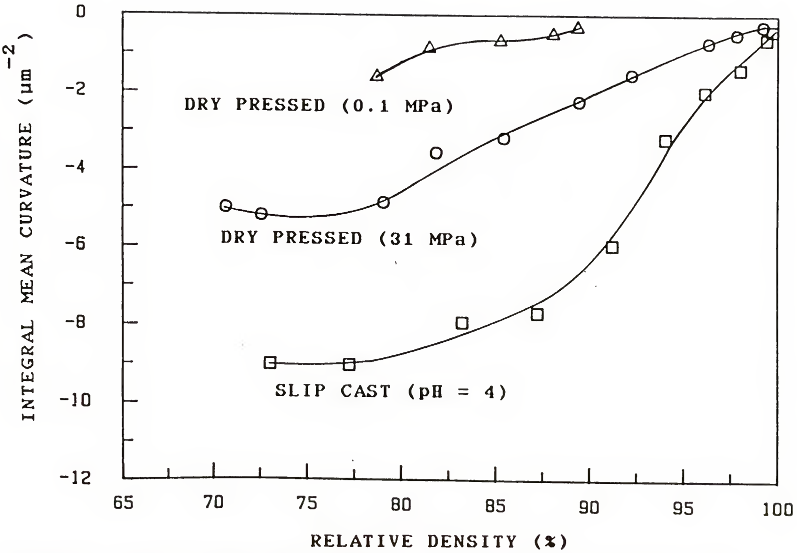

Figure 4.127 Plots of integral mean curvature vs. relative density for SCD, DPH, and DPL samples.

However, it is still coarser than the SCD sample. The DPH sample also showed ~18% density increase (from ~54% relative density to ~72% relative density) to reach the minimum value which was consistent with the relatively slower densification rate compared to the SCD sample.

Comparison with Sintering Models

The SCD sample showed very uniform microstructure and narrow grain size and pore size distributions. These microstructural characteristics begins to approach the ideal geometric assumptions proposed in most sintering models. Hence, it can be used to evaluate the validity of the densification and grain growth models in the literature. On the other hand, the dry-pressed sample, especially the DPL sample, had extremely heterogeneous microstructures which can be used to examine the effect of inhomogeneity in model fitting. In addition, extensive quantitative microstructure characterization has been carried out in this study which will provide complete information which is needed for the evaluation of the assumptions and the predictions of models. The intermediate and final stage of sintering will be the focus of the present study because only limited information was collected for the initial stage of sintering.

Densification kinetics. Based on polyhedral grains and cylindrical pores (intermediate stage) or spherical pores (final stage), Coble developed a widely used intermediate stage sintering model and proposed that density should increase linearly with sintering time (i.e., constant densification rate) if grain size remained constant. As discussed before, the SCD sample showed essentially constant grain intercept size up to ~90% relative density (around 4 h sintering at

1340°C or 12 h sintering at 1300°C). Plots of relative density vs. sintering time were shown in Figure 4.14 and 4.15. It is clear that densities did not vary linearly with sintering time. The continuous decrease in densification rate was also demonstrated in Figures 4.17 and 4.18. The non-linear behavior of density vs. sintered time at constant grain size was also obtained in all other samples regardless of the particle packing conditions and has also been observed by other investigators [Cam88].

A linear relationship was observed in plots of relative density vs. the logarithm of sintering time. Figures 4.128 and 4.129 show results for various samples sintered at 1300°C and 1340°C, respectively. Least square fits gave correlation coefficients greater than 0.99. It should be pointed out that a deviation from a linear curve was observed for SCD samples at high sintered density. Figure 4.130 shows plots of relative density vs. logarithm of sintering time for samples sintered at 1450°C. The linear relation was obtained for only DPL sample. According to Coble's model, a linear relationship between density and log(sintering time) is obtained only when the empirical grain growth equation $G^3 \propto t$ is effective. However, linear relationships between density vs. log(sintering time) were obtained at constant grain size stages for most of the samples sintered at 1300°C and 1340°C. On the other hand, for the SCD sample at high sintered densities (> 95% relative density) or for the SCF sample sintered at 1450°C, grain growth virtually followed the empirical equation $G^3 \alpha t$; however, linear relations between density vs. Log (sintering time) were not obtained. From the above discussion it is clear that linear relations between density and log(sintering time) can not be used as a criterion to

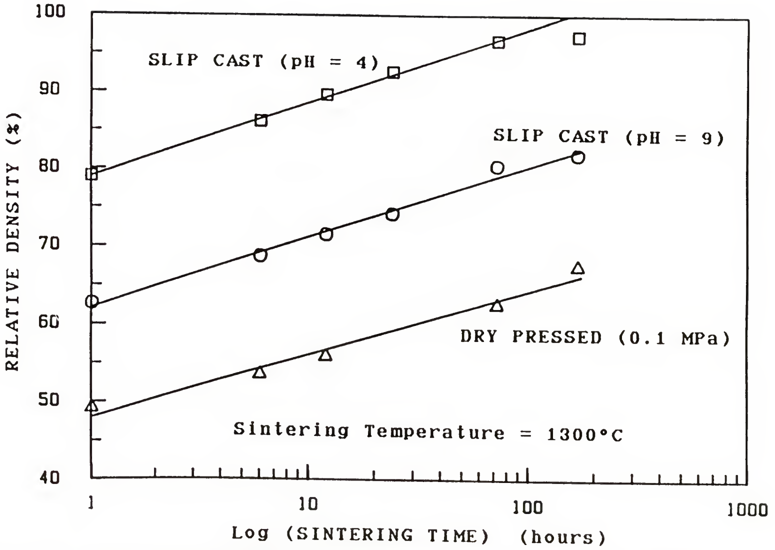

Figure 4.128 Plots of relative density vs. logarithm of sintering time at 1300°C for SCD, SCF, and DPL samples.

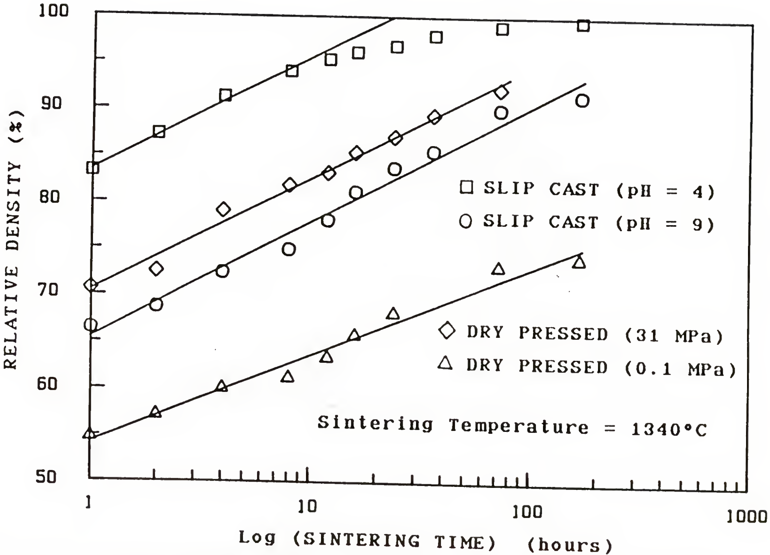

Figure 4.129 Plots of relative density vs. logarithm of sintering time at 1340°C for SCD, SCF, DPH, and DPL samples.

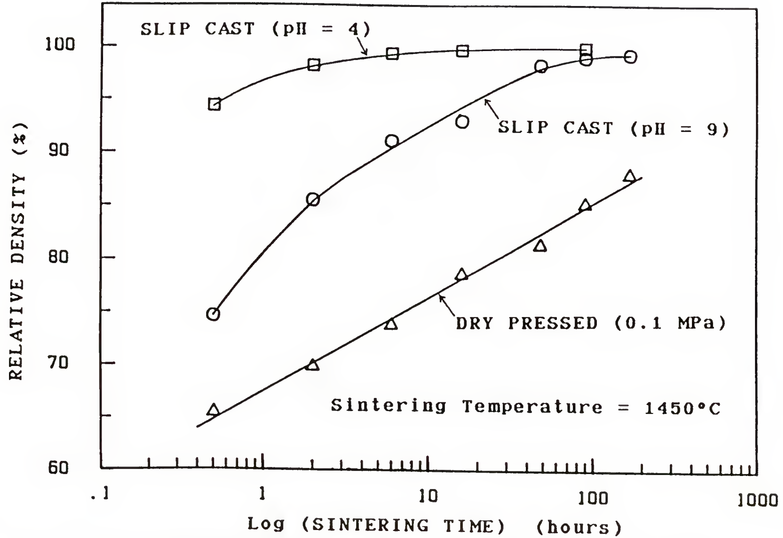

Figure 4.130 Plots of relative density vs. logarithm of sintering time at 1450°C for SCD, SCF, and DPL samples.

propose that Coble's model is correct or that lattice diffusion is the dominant sintering mechanism. Density α log(sintering time) should be treated as an empirical equation for describing sintering kinetics.

Based on homogeneous grain/pore structures, Rosolowski and Greskovich [Ros75] and Ikegami et al. [Ike78] developed densification/grain growth models for intermediate-stage sintering. Their models can be best evaluated using the sintering results of the SCD sample which showed very homogeneous microstructures. In the model developed by Rosolowski and Greskovich [Ros75], they assumed that significant grain growth would occur during intermediate stage densification. However, it has been clearly shown that significant densification could be obtained with virtually no grain growth. The pore coarsening proposed in their model was not observed in the SCD sample, either. In the model developed by Ikegami et al. [Ike78], as discussed in Chapter II, they obtained

$$\mathrm{Log}\left(\frac{D(1-Do)}{Do(1-D)}\right) \propto \mathrm{Log}\left(\frac{G}{Go}\right)$$

which suggested that no densification could be obtained (i.e., D = Do) if the grain size remained unchanged (i.e., G = Go). Again, it is not correct according to the densification results of the SCD sample. On the other hand, significant grain growth was observed in the DPL sample. However, grain growth occurred only in some localized regions which was the result of the extremely heterogeneous particle packing. Because the particle packing in the DPL sample was inconsistent with the geometrical assumption adopted in the above models, this sample can not be used to evaluate the above models.

In the statistical sintering model developed by Kuczynski for the intermediate and final stages of sintering [Kuc76, Kuc77], he also proposed that grain growth and pore coarsening should accompany densification. As discussed above, constant grain intercept size and pore intercept size were obtained for the intermediated stage sintering of the homogeneous SCD compact. For the SCD sample with > 95% relative density, the majority of the pores were rounded closed pores (Figure 4.46) which approached the geometrical assumption of Kuczynski's late-stage model. However, a relatively constant pore intercept size was still observed which also did not agree with the pore coarsening proposed by Kuczynski for the final stage sintering.

Rapid grain growth was obtained for the SCD sample in the final stages of sintering; therefore, it can be used to evaluate the densification and grain growth equation

$$\mathrm{Ln}\ G \propto -\left(\frac{2 + X_2}{3}\right) \mathrm{Ln}\ P$$

developed by Kuczynski for the late stage of sintering. Plots of the Ln G vs. Ln P for the SCD sample in the closed-pore stages (> 95% relative density) is shown in Figure 4.131. Least square fits showed good linear relationship between Ln G and Ln P with correlation coefficients > 0.995. The x_2 values obtained from the slopes are -0.461 and -0.856 for the sintering temperature of 1340 and 1450°C, respectively. Kuczynski [Kuc76, Kuc77] also proposed that a linear relation should be obtained between $(P_0/P)^{n_2} - 1$ and t. For the final stages of sintering, n_2 =

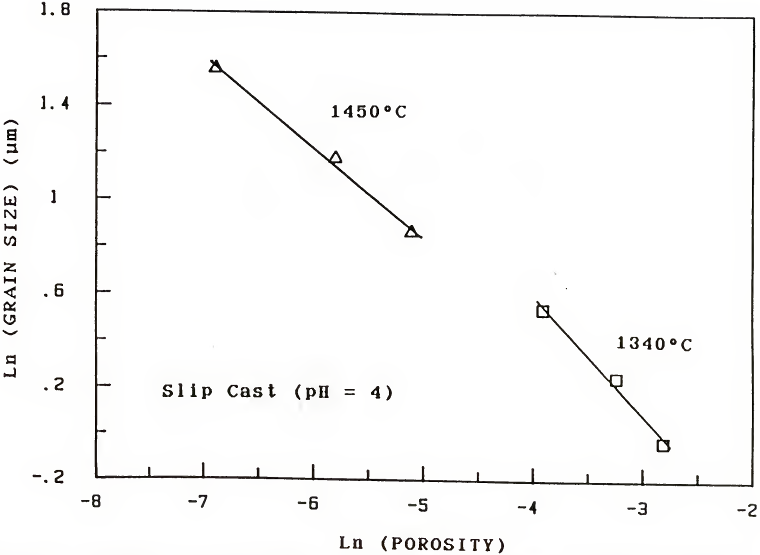

Figure 4.131 Plots of Ln (grain size) vs. Ln (porosity) for SCD samples sintered at 1340 and 1450°C.

(2/3) + x_2. Using the x_2 values obtained above, n_2 would equal 0.206 and -0.189 for samples sintered at 1340 and 1450°C, respectively. However, these n_2 values do not give a linear relation between $(P_0/P)^{n_2} - 1$ and t.

Grain growth kinetics. As discussed in chapter II, when pore drag controls the grain boundary migration and surface diffusion controls the pore mobility, Brook et al. [Bro82, How81] and Harmer et al. [Ber86, Har84, Zha87] proposed that the following equations

$$G^4 - Go^4 = \frac{K}{(1 - D)^{4/3}}$$

or

$$\frac{dG}{dt} = \frac{K}{G^3 (1 - D)^{4/3}}$$

should give the best fit to the grain growth data. However, the grain growth data in the present study did not fit the above equations. Instead, they fit the well-known grain growth equation

$$G^n - Go^n = K t.$$

Figures 4.132 to 4.135 show the grain size data plotted in this form for samples sintered at 1340 and 1450°C. Both n = 3 (Figures 4.132 and 4.134) and n = 4 (Figures 4.133 and 4.135) gave good linear fits.

An Arrhenius-type equation

$$G^n - Go^n = K_a \cdot t \cdot \exp(-Q/RT)$$

can be used to represent the above grain growth data, where K_a is a constant, Q is the apparent activation energy, R is the gas constant,

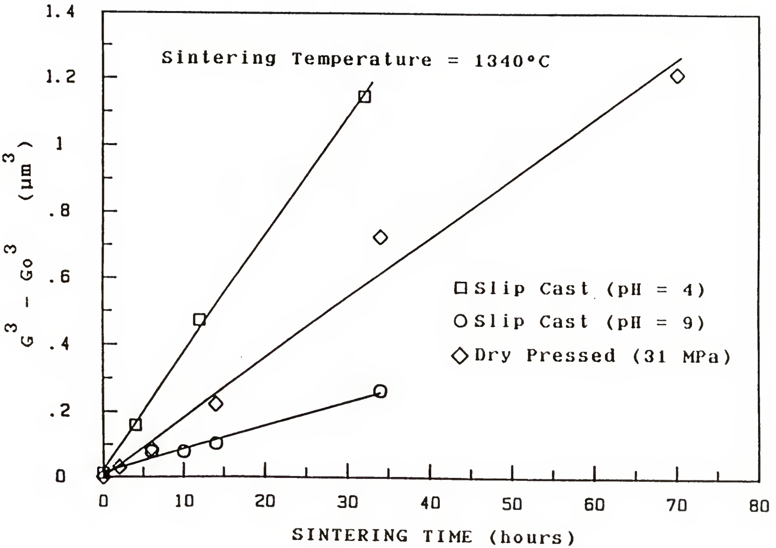

Figure 4.132 Plots of G^3-Go^3 vs. sintering time at 1340°C for SCD, SCF, and DPH samples.

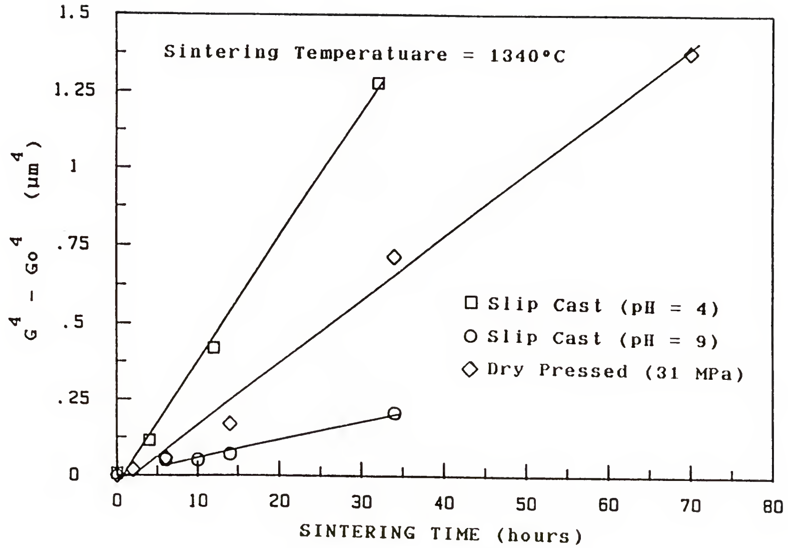

Figure 4.133 Plots of G^4-Go^4 vs. sintering time at 1340°C for SCD, SCF, and DPH samples.

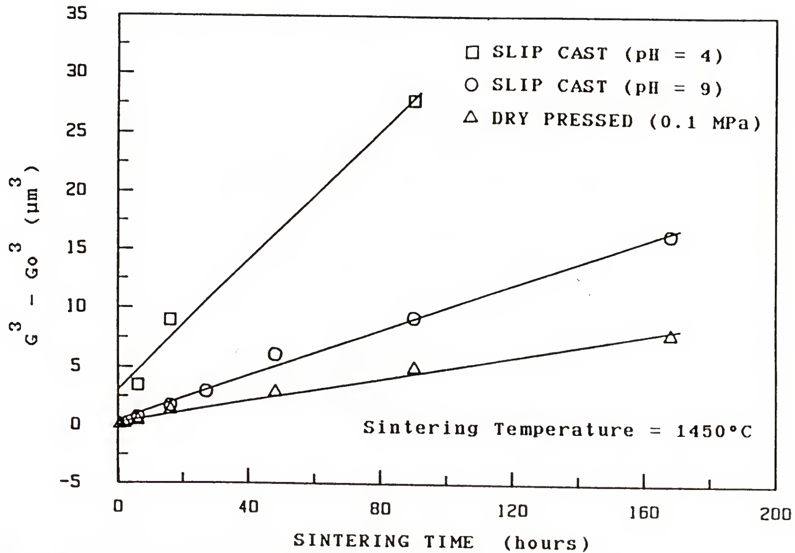

Figure 4.134 Plots of G^3-Go^3 vs. sintering time at 1450°C for SCD, SCF, and DPL samples.

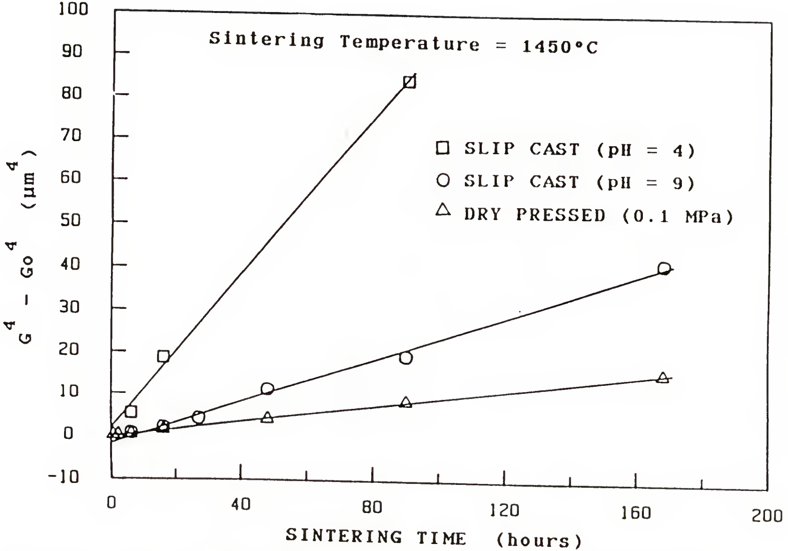

Figure 4.135 Plots of G^4-Go^4 vs. sintering time at 1450°C for SCD, SCF, and DPL samples.

and T is the absolute temperature. Therefore, by plotting Ln $(Gn - Go^{n})$ vs. reciprocal absolute temperature for the grain intercept sizes obtained at a constant sintering time at 1340 and 1450°C, the apparent activation energy of grain growth can be obtained from the slope. The calculated apparent activation energies are ~575 and 586 KJ/mole for the SCD and SCF samples, respectively, for $n = 3$. For $n = 4$, the apparent activation energies are ~711 and 528 KJ/mole for the SCD and SCF samples, respectively. Because only two data points were used to calculate the slope, significant variation in activation energy was expected. However, these values still agreed very well with the value reported by Venkataraman and DiMilia (~690* KJ/mole) [Ven89]. The values also agreed very well with values calculated earlier in this chapter using other approaches.

Even though the current grain growth data also showed a good fit to the kinetics equation $G^n - Go^n = kt$, great caution need to be taken in interpreting the grain growth kinetics. The grain size data showed in Figures 4.132 to 4.135 are obtained from samples over a wide range of density--near fully dense for SCD samples sintered at 1450°C and very porous for DPL samples. The SCD sample may approach some of the geometrical assumptions adopted in the grain growth models (e.g., spherical closed pores). However, the pore structure of the DPL sample is far away from the geometrical assumptions in the models. Most models assumed pores are located at planar grain boundaries (i.e., two grain interface) so that the interaction forces between pores and grain

---

[*] The original value reported in their paper was 230 KJ/mole. However, a factor of 3 was left out in their derivation; therefore, the correct value should be 690 KJ/mole.

boundaries can therefore be derived. In a real sintered body, most pores are located in the three grain intersections (i.e., grain edges) or even four grain intersections (i.e., grain corners).

Samples also showed great differences in microstructure homogeneities--very homogeneous for SCD samples and extremely heterogeneous for DPH and DPL samples. As proposed by Greskovich and Lay [Gre71], the grain growth mechanism for very porous compacts might be significantly different from the high density samples which are the focus of most grain growth models. Furthermore, it has been clearly shown in this study that the pore size remained relatively constant (except the DPL sample) over the entire range of sintering process which is in conflict with the assumptions made in model development.

From the above discussion, it can be concluded that the grain growth kinetic data of samples with varieties of particle packing conditions can all be represented with the empirical equation $(D^n - Do^n) \alpha k t$. However, this good fit should not be used to support the applicability of any proposed model.

CHAPTER V
EFFECT OF PARTICLE SIZE DISTRIBUTION

Introduction

Although sintering has been investigated extensively in the past forty years or so, the effect of particle size distribution on densification and microstructural evolution has received relatively little attention. Most of the studies concerning the effect of particle size distribution on sintering have involved powders with bimodal size distribution [Han84, Oha69, Pos60, Smi84] or powders with different mean sizes [Cho71, Dav71]. Investigations which compare the sintering behavior of ceramic powders with the same average size, but varying width of the size distribution, are particularly limited. Only a few studies using dry-pressed compacts of metal powders were reported by Patterson et al. [Pat83, Pat84, Pat86].

In this study, an attempt has been made to prepare powders and powder compacts with model characteristics; therefore, the effect of particle size distribution can be clearly studied.

Background

Previous investigations on the effect of particle size distribution on suspension rheology, particle packing and green microstructure, sintering and microstructural evolution during sintering will be reviewed below.

Suspension Rheology

The particle size distribution of the powder in a suspension has significant effect on the viscosity of the suspension. For a two-dimensional configuration, Reed [Ree86] illustrated that a large fraction of suspending liquid can be immobilized in a concentrated suspension prepared from monosized spheres resulting in high viscosities. At constant solids loading, the amount of immobilized liquid can be significantly reduced for a suspension prepared from a broad size distribution powder. Fine particles can fit in the interstices formed by larger particles and more efficient particle packing can be achieved. This will result in lower suspension viscosity.

It was shown that the fine particles in a bimodal suspension behaves like a fluid with respect to the coarser particles in that suspension [Cho62, Fid61]. Based on this concept, Farris [Far68] assumed that the behavior of particles of each size is completely independent of the others. From this assumption he developed a theory to predict the relationship between viscosity and solids loading for polydisperse suspensions. In order to use this theory, the relationship between viscosity and solids loading for a monodisperse suspension must be known. At a given solids loading, he showed that the viscosity of a monodispersed suspension could be decreased by adding another powder with different particle size. The differences in viscosity increased with increasing particle size ratio. The minimum viscosity for a binary suspension was predicted to be achieved when approximately 60 - 70 vol% of coarse powder was used. He also showed that at high solids loading, the viscosity of optimally blended multicomponent suspensions decreased when the number of composing components was increased. However, at lower solids loadings (<20 vol%), the viscosity of the multicomponent suspensions approached the viscosity of monodispersed suspensions.

The flow characteristics for concentrated alumina suspensions prepared from powders with various particle size distribution were measured with a capillary tube viscometer by Phelps and McLaren [Phe78]. They showed that adding 4% fine alumina (~0.5 μm median size) to a coarse alumina (~5 μm median size) significantly decreased the apparent viscosity of the suspension. In the same study, they also showed that suspensions of a broader size distribution quartz powder, obtained by blending equal amounts of two narrower size distribution powders, had much higher flow rates than suspensions prepared from either component powder.

In summary, there are several advantages for using broad size distribution powder in suspension processing :

(1) At a given solids loading, the suspension viscosity is lower, i.e., the flowability is higher; therefore, less power is needed for transporting or mixing.

(2) At a constant viscosity, suspension with higher solids loading can be prepared. The advantages of higher solids loading are : (a) higher throughput of the process, (b) lower usage of solvent, (c) less solvent removal and shrinkage in the drying process.

(3) Highly-loaded suspensions showed less dilatancy which can make suspension processing more efficient.

Particle Packing and Green Microstructure

Typically, a randomly close-packed compact of mono-sized hard spheres, without the complication of the inter-particle forces, shows a packing density of 60 - 64% [McG61, Sco60, Wes30]. A large amount of interstitial voids exist. In order to increase the packing density, the simplest approach would be to fill the interstices with finer particles so that the void space can be decreased.

Furnas [Fur29, Fur31] and Westman and Hugill [Wes30] are among the earliest investigators to systematically study the effect of particle size distribution on the packing density of powder compact. By using a simple graphical procedure, they predicted and also experimentally confirmed that binary powder mixtures can have much higher packing densities. Furnas showed that the maximum packing density of a binary compact could be obtained at the composition where the proportion of larger size is $1/(1 + V)$, where V is the porosity of monosized packing. Westman and Hugill showed that the maximum packing density was obtained for powder mixtures containing ~70% coarse particles, where the packing density of a single component system is ~60% [Wes30]. The achievable maximum packing density depended on the ratio of the diameters of the two component powders. McGeary [McG61] showed that more than 80% packing density could be obtained for powders with diameter ratio larger than 10. The packing density rapidly decreased if the diameter ratio of the two component became smaller than 7.

By using powders with particle sizes that can fit into progressively smaller interstices in the powder compact, the packing density can be further increased. It was demonstrated by McGeary that packing densities of ~90% and ~95% for ternary and quaternary powder mixtures, respectively, could be obtained [McG61]*. Based on his work on binary system, Furnas [Fur31] developed a procedure to formulate continuous size distributions for maximum packing density. He also pointed out that the optimal distribution depended on (1) the maximum packing density of each mono-sized component, (2) the ratio of largest diameter to smallest diameter. However, investigations which compare the packing behavior of powders with same mean size but varying width of the distribution have not been reported.

In practical ceramic processing, fine powders with irregular shape are used. Agglomeration and particle size segregation may occur which will make the investigation of the effect of particle size distribution on particle packing even more difficult. It was shown by Hauth that green densities higher than 80% could be obtained for slip cast alumina compacts prepared from well-dispersed suspensions with particle sizes in the range 0.1 to 80 μm [Hau49]. For alumina compacts prepared with two submicron powders having 0.78 and 0.21 μm medium size, Han et al. [Han84] obtained a maximum packing density of ~72% for compact containing ~70 wt% coarse powder. They also showed that the pore channel sizes measured by mercury porosimetry continuously decreased with increasing amount of fine particles in the binary mixtures.

---

* It should be noted that the extremely high packing density was achieved only by a multiple infiltration processes. Initially, the coarsest powder by itself was placed in a container and vibrated until the minimum volume was obtained. Vibration was stopped and the next size component was poured into the container and again vibrated until minimum volume was reached. The same procedure was followed for the successive ternary and quaternary components. Lower packing density will be obtained if pre-mixed powders are used.

Sintering and Microstructural Evolution

O'Hara and Cutler [OHa69] were among the earliest to study the isothermal sintering behavior of binary powder mixtures. They showed that the linear shrinkage of bimodal alumina powder compacts continuously decreased as the proportion of coarse powders increased. Similar results were also reported by Smith and Messing [Smi84]. Since surface energy is the driving force for sintering, it is not surprising to observe a decrease in densification kinetics when coarse particles which have lower specific surface area and small surface curvature are introduced into the fine particle matrix. Furthermore, as pointed out by O'Hara and Cutler [OHa69], for a dense large particle embedded in fine particle matrix, the fine particles surrounding the large particle will experience tensile hoop stresses during sintering. These stresses can also cause retardation of the densification of the fine particle matrix.

On the other hand, when fine particles are introduced into coarse powder compacts, as illustrated by Coble [Cob73] in a two-dimensional array, fine particles can fit into the interstices of large particles. Because sintering between the small and large particles occurs more rapidly than sintering between large particle alone, compressive stresses will be developed at the contacts between large particles. The sintering of the large particles will be enhanced if the contacts between small and large particles remain. The sintering behavior of compacts prepared from powders having broad size distribution becomes complicated due to the existence of stresses as discussed above.

Based on the sintering models for monosized particle pairs, Coble [Cob73] developed a sintering model for particle pairs with varied sizes and applied it to calculate the linear shrinkage for a linear array of particles with various sizes. According to his one-dimensional model, the number-basis size distribution rather than volume-basis size distribution must be used to predict the initial-stage sintering behavior of a compact prepared from broad size distribution powder. The effective size which can represent the shrinkage behavior of a broad size distribution sample is much smaller than the median size obtained from volume-basis size distribution.

Since the discovery of methods for synthesizing monodispersed spherical ceramic powders, a number of studies on the sintering of such powders have been reported. Frequently, it was proposed that narrow size distribution powders are preferable for producing dense, uniform, fine-grained microstructures at low sintering temperatures [Bar82, Bar84, Yan83]. However, experimental evidence to support this supposition is lacking.

Yan et al. [Yan83] developed a model to analyze the conditions of pore separation from grain boundary during sintering. Kelvin's tetrakaidecahedron was used to represent the grain structure with spherical pores located at the four grain corners. It was concluded that a critical density existed and pore-grain boundary separation will occur when the sintered density becomes larger than the critical density. For samples with a narrow grain size distribution, the critical density is above 99% relative density. However, for samples with a broad grain size distribution, the critical density decreases to about 90% relative density. Because densification rate becomes extremely low when the pores break away from grain boundaries, densification essentially stops. Therefore, they concluded that a narrow grain size distribution is imperative to obtain a high sintered density. However, the equation used to describe the pore drag on grain boundary in their model was developed for geometric configurations where spherical pores are located at two-grain interfaces. This may not be applicable in their initial geometrical assumption (i.e., pores are located at four grain corners). Furthermore, monosized tetrakaidecahedron can be used to construct a space-filling structure. However, they did not explain how to construct a coherent three-dimensional structure with broad size distribution polyhedrons. They also did not consider the differences in pore size distribution and interpore distances when the grain size distributions of samples were different. In addition, packing defects which are normally obtained in a real powder compact can significantly affect the densification and microstructural evolution of the compact. Therefore, their conclusion about the critical density may not be applicable in a real powder compact.

Chappell et al. [Cha86] developed a model to describe the effects of particle size distribution on densification kinetics for the initial and intermediate stages of sintering. According to their model, shrinkage rate should decrease significantly with increasing width of particle size distribution. The grain growth rate should significantly increase as the width of particle size distribution increases. The shrinkage equation used in their model to describe the shrinkage behavior of a broad size distribution compact were derived with the geometrical configuration of two contacting monosized spheres (initial stage sintering) or monosized polyhedron (intermediate stage sintering). However, as pointed out by Coble [Cob73], the shrinkage kinetics of a particle strongly depend on the particle sizes of its neighboring particles. The packing density and green microstructures, which can strongly influence the sintering behavior of a compact, are strongly dependent on the particle size distribution and these were not taken into consideration in their model. Furthermore, the validity of the equation used to describe the particle size dependence of rate constant was not demonstrated in their paper. Therefore, the applicability of their model need further evaluation.

Gattuso and Bowen [Gat84] and Roosen and Bowen [Roo88] compared the sintering behavior of a classified narrow size distribution alumina powder with an as-received broad size distribution powders and observed that higher densification kinetics, finer sintered microstructures and higher final sintered densities were obtained for the classified powders. They concluded that narrow size distribution powders produced better sintering results. However, their conclusions are somewhat misleading because : (1) The narrower size distribution powders were obtained by collecting the fine fractions of the as-received powder, therefore, the classified powders had finer particle sizes (e.g., 0.38 and 0.61 μm Stokes diameters for classified and as-received powders, respectively) and higher surface areas (e.g., 11.4 and 7.9 m^2/g for the classified and as-received powders, respectively). (2) The as-received powders contained large hard agglomerates but the classified powders were agglomerate-free. Therefore, it is not surprising to obtain higher densification kinetics and finer microstructures for their classified powders.

Liniger and Raj [Lin87] investigated the packing and sintering of two-dimensional structures made from bimodal polystyrene spheres. They reported that monosized spherical particles formed hexagonal close-packed domains with lower packing density regions between these domains.

During sintering, faster densification rates obtained within the domains led to the opening-up of domain boundaries (i.e., large pores or cracks were generated). They also showed that binary mixtures of spherical particles can be used to produce dense random packing which showed more homogeneous sintering without the formation of large pores.

Patterson and Benson [Pat83] investigated the sintering behavior of loose-stacked tungsten powders which had similar weight-basis geometric mean sizes but varied widths of particle size distribution. They reported that broad size distribution powders had higher green density and significantly higher densification kinetics. At a constant sintered density, the broad size distribution sample also showed higher specific pore-solid interfacial area. They converted the weight-basis size distribution into number-basis size distribution and showed that the broad size distribution powders had much smaller number-basis mean sizes which implied that these powders contained large number of fine particles. For powders with similar number-basis geometric mean size, they showed that the weight-basis geometric size of broad size distribution powder became much larger and the densification kinetics of broad size distribution samples became slower. They also observed significant particle size segregation in the broad size distribution samples which might significantly affect their results.

Effect of particle size distribution on the sintering of constant green density (~65% relative density) compacts of copper and tungsten powders were reported by Patterson et al. [Pat86]. For coarse (~45 μm mean size) spherical copper powder, they showed that an enhanced densification kinetics was obtained in broad size distribution samples. However, for finer (~7 μm mean size) tungsten powders, no consistent trend was observed. Because agglomerated powders were used for dry-pressing compacts, heterogeneous green bodies might be produced which could significantly interfere their investigation. Furthermore, broad size distribution powders normally have higher packing densities. In order to produce green compacts with similar density from powders with various particle size distributions, more plastic deformation will be introduced for the narrow size distribution samples. The plastic deformation may significantly affect sintering kinetics.

It was proposed that exaggerated grain growth during sintering occurs more easily for compacts prepared from broad size distribution powders because large grains existing in these powders can act as seeds for exaggerated grain growth [Bar82, Bar84]. Smith and Messing [Smi84] studied the sintering of a bimodally distributed alumina powders. They showed that rapid densification and grain growth occurred for the fine powders due to their high specific surface area and large surface curvature. In contrast, the coarse powder densified little and no grain growth was observed. The microstructure of the binary powder compacts became more uniform upon sintering. They suggested that the large grains adjacent to locally dense, fine-grained regions did not grow because the driving force for the large grains to grow into the fine-grained regions was frequently diminished due to the existence of pores at the grain boundaries between the large grains and the fine-grained regions.

Results and Discussion

Powder Characterization

Figure 5.1 shows the particle size distributions obtained by gravitational x-ray sedimentation for the NSD-30, ISD, and BSD powders.

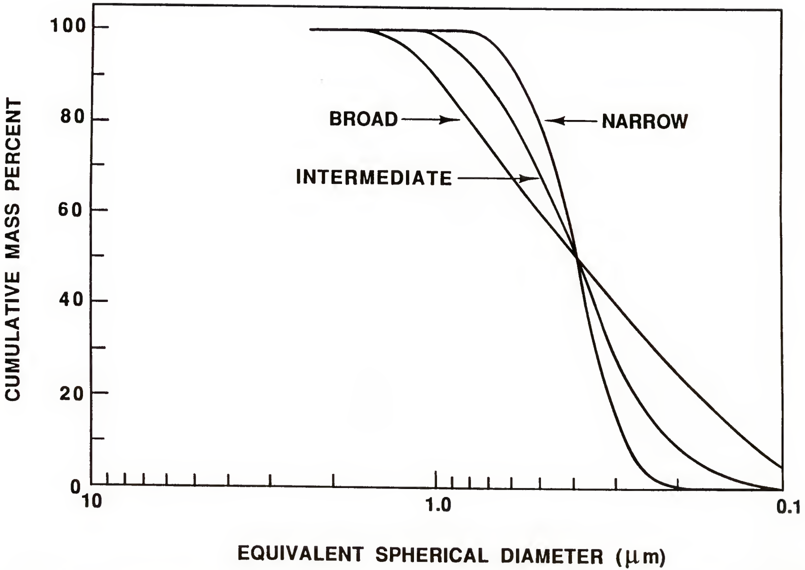

Figure 5.1 Gravitational X-ray sedimentation data for the NSD-30, ISD, and BSD powders.

The median Stokes diameter was ~0.39 μm for each powder. The NSD-30 powder had an excellent fit to the log-normal distribution over the entire particle size range. This can be seen in Figure 5.2 where the size distribution data are plotted on a log-probability scale. The geometric standard deviation*, σ_g, of the NSD-30 powder was ~1.3. The ISD and BSD powders fit the log-normal distribution over most of the particle size range (Figure 5.2) although a substantial divergence for the BSD powder was observed at the larger sizes. σ_g was ~1.7 and ~2.4 for the ISD and BSD powder, respectively, in the size range over which the fit was good.

The particle size distribution histograms determined by the centrifugal photosedimentation method are shown in Figures 5.3, 5.4, and 5.5 for NSD-30, ISD, and BSD powders, respectively. The volume-basis median size and geometric standard deviation for each powder are shown in Table 5.1. In order to have a direct comparison, the particle size distribution curves determined by x-ray sedimentation method (Figure 5.1) were converted into distribution histograms as shown in Figures 5.6 to 5.8. The results obtained from both sedimentation methods agreed very well except slightly larger median size and smaller geometric standard deviation were observed for the BSD powder using centrifugal photo-sedimentation method.

The number-basis distribution histograms of equivalent area diameters (D_A) and equivalent perimeter diameter (D_p) determined from projected images on SEM photographs are shown in Figures 5.9 to 5.11 and Figures 5.12 to 5.14, respectively, for each particle size distribution.

---

* σ_g was calculated by dividing the particle diameter at the 84.13 percentile by the median (50 percentile) diameter.

Table 5.1

Characterization Method		NSD	ISD	BSD
X-ray Sedimentation (Volume-Basis)	Median Size	0.39	0.39	0.39
	σ_g**	1.3	1.7	2.4
Centrifugal Photo-Sedimentation (Volume-Basis)	Median Size	0.38	0.39	0.44
	σ_g**	1.3	1.6	1.9
Equivalent Area Diameter (SEM) (Number-Basis)	Median Size	0.47	0.42	0.25
	σ_g*	1.3	1.6	1.9
Equivalent Perimeter Diameter (SEM) (Number-Basis)	Median Size	0.62	0.53	0.32
	σ_g*	1.3	1.6	1.9
Equivalent Area Diameter (SEM) Volume-Basis	Median Size	0.48	0.56	0.78
	σ_g**	1.2	1.4	1.6

* Geometric standard deviation (σ_g) was obtained by using the equation

$$\text{Log}\ \sigma_g = \left(\frac{\sum_{i=1}^{N} (\text{Log}\ d_i - \text{Log}\ d_g)^2}{N - 1} \right)^{1/2}$$

where N is the number of particles, d_i is the diameter of particle i, and d_g is the geometric mean diameter.

** σ_g was calculated by dividing the particle diameter at the 84.13 percentile by the median (50 percentile) diameter.

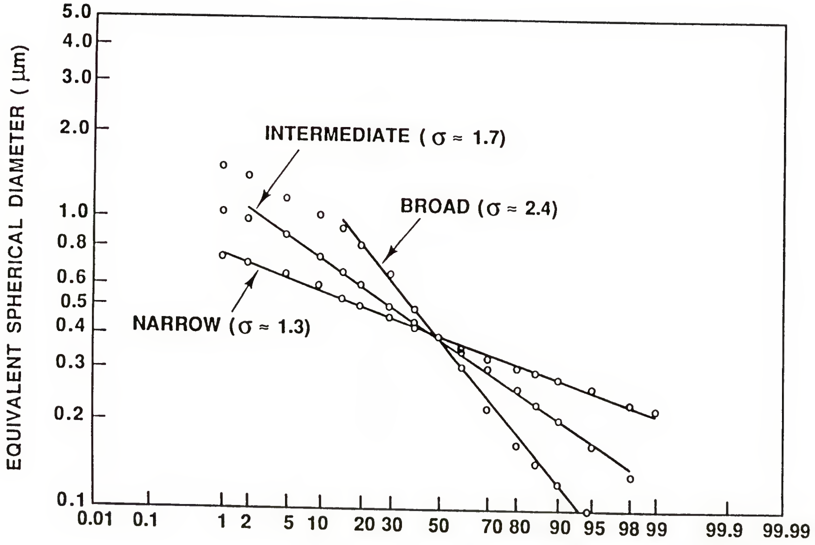

Figure 5.2 Particle size distributions plotted on a log-probability scale for the various powders in Figure 5.1.

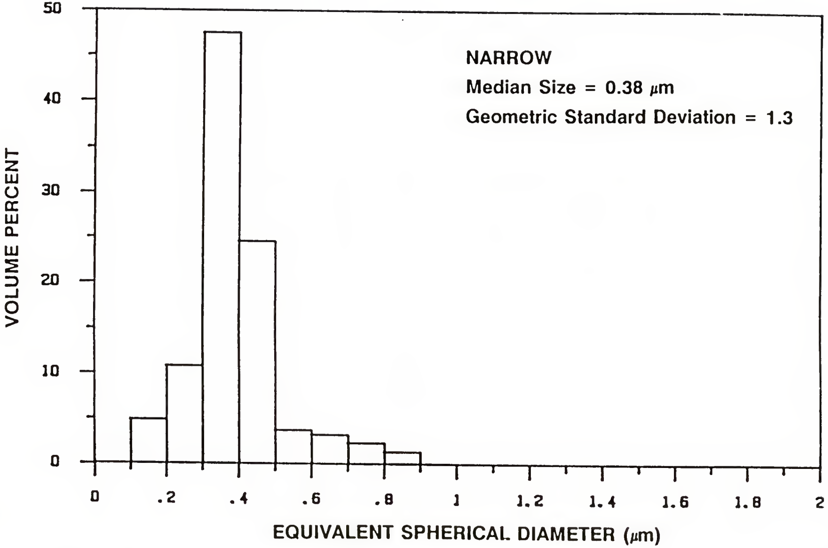

Figure 5.3 Histogram plot of the particle size distribution determined by centrifugal photosedimentation method for the NSD-30 powders.

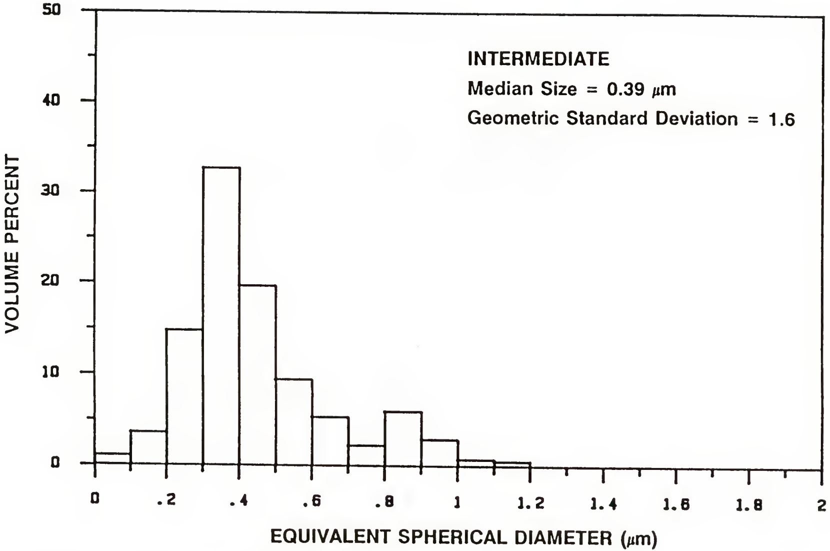

Figure 5.4 Histogram plot of the particle size distribution determined by centrifugal photosedimentation method for the ISD powders.

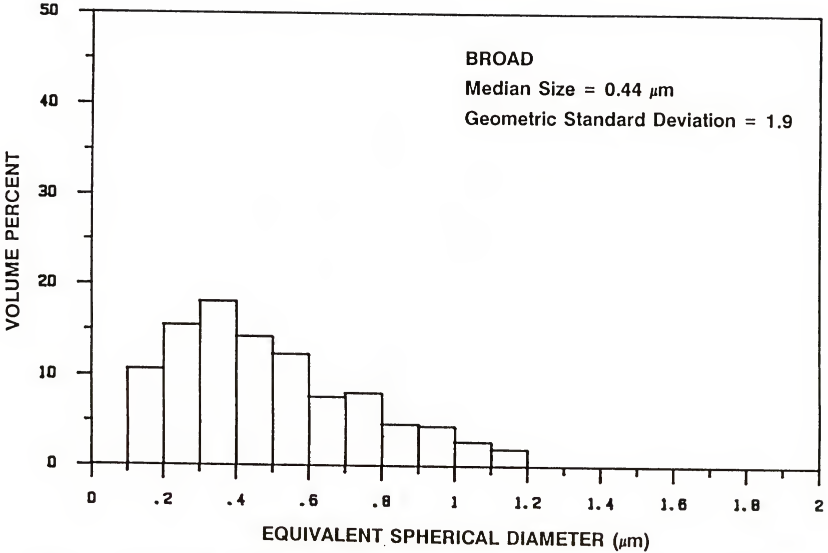

Figure 5.5 Histogram plot of the particle size distribution determined by centrifugal photosedimentation method for the BSD powders.

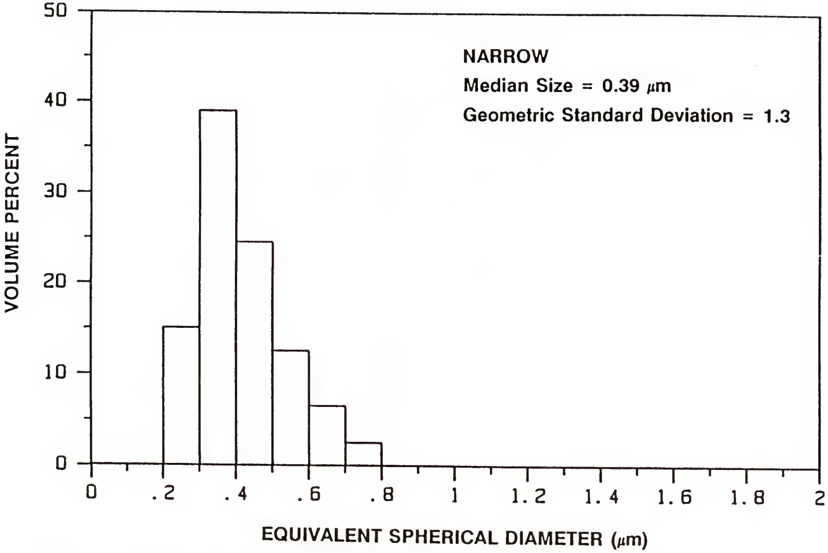

Figure 5.6 Histogram plot of the particle size distribution determined by gravitational x-ray sedimentation method for the NSD-30 powders.

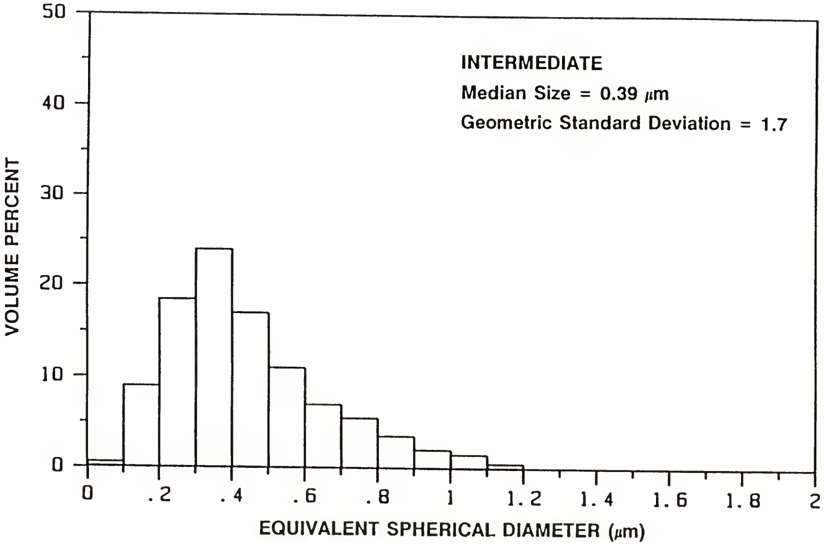

Figure 5.7 Histogram plot of the particle size distribution determined by gravitational x-ray sedimentation method for the ISD powders.

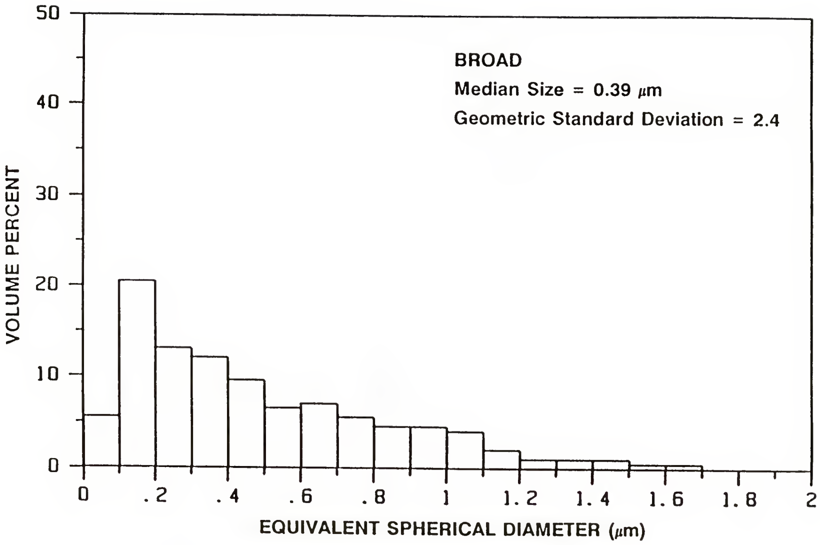

Figure 5.8 Histogram plot of the particle size distribution determined by gravitational x-ray sedimentation method for the BSD powders.

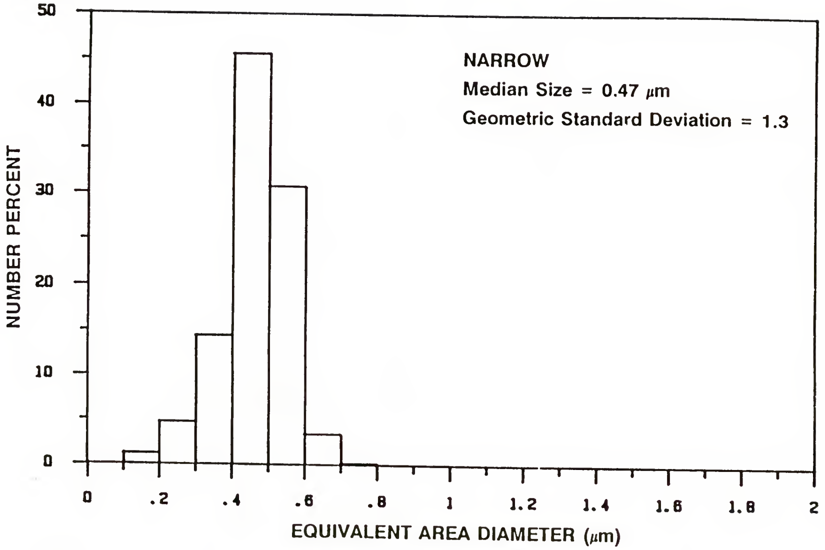

Figure 5.9 Histogram plot of the number-basis distribution of equivalent area diameter determined by SEM for the NSD-30 powders.

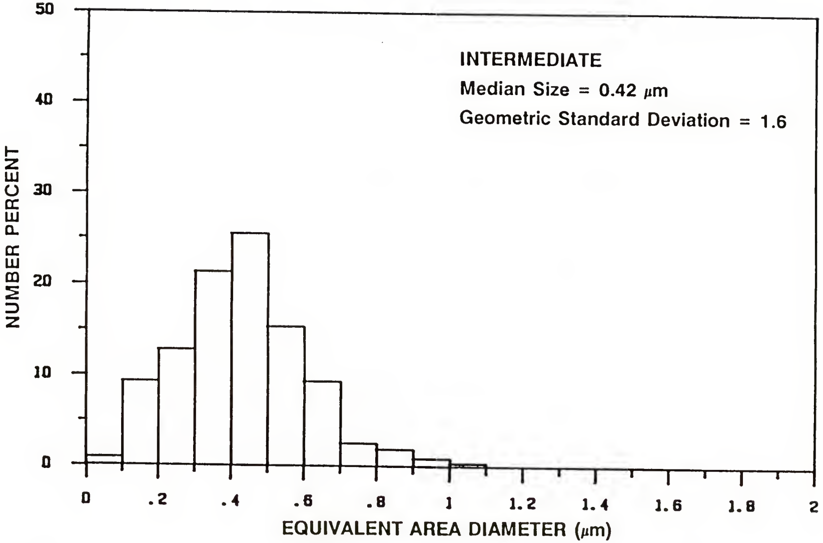

Figure 5.10 Histogram plot of the number-basis distribution of equivalent area diameter determined by SEM for the ISD powders.

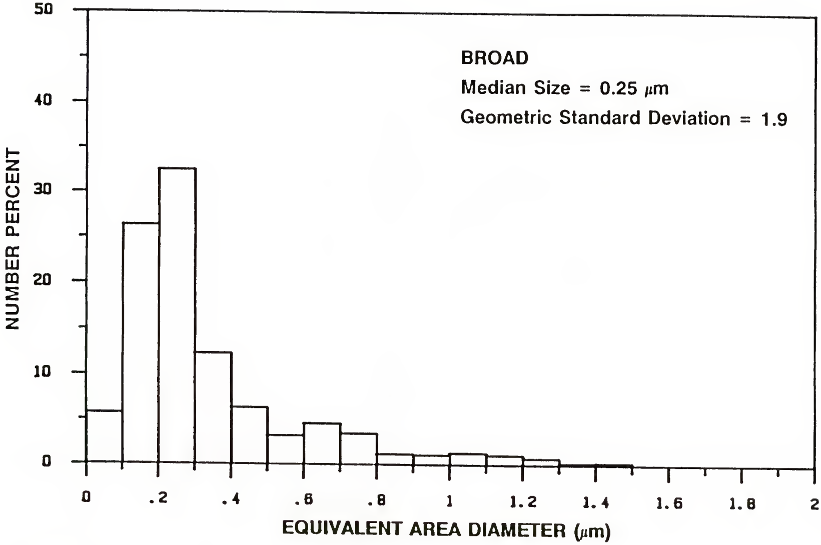

Figure 5.11 Histogram plot of the number-basis distribution of equivalent area diameter determined by SEM for the BSD powders.

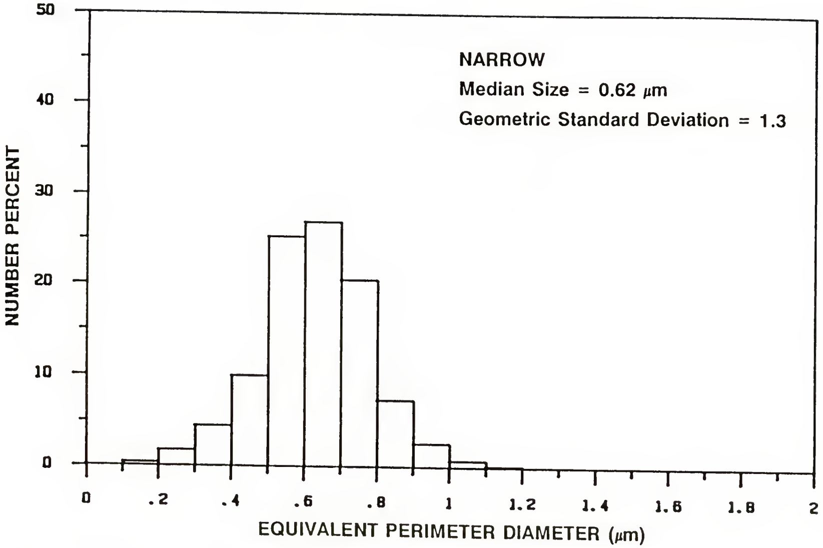

Figure 5.12 Histogram plot of the number-basis distribution of equivalent perimeter diameter determined by SEM for the NSD-30 powders.

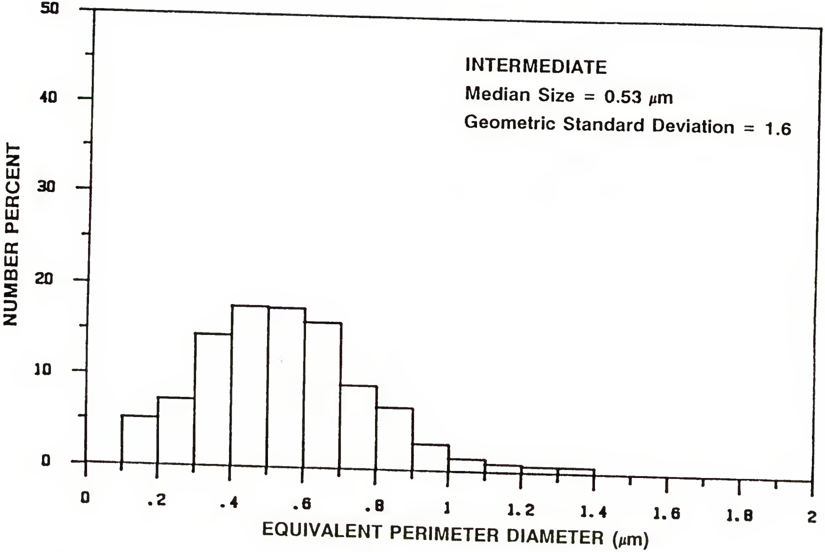

Figure 5.13 Histogram plot of the number-basis distribution of equivalent perimeter diameter determined by SEM for the ISD powders.

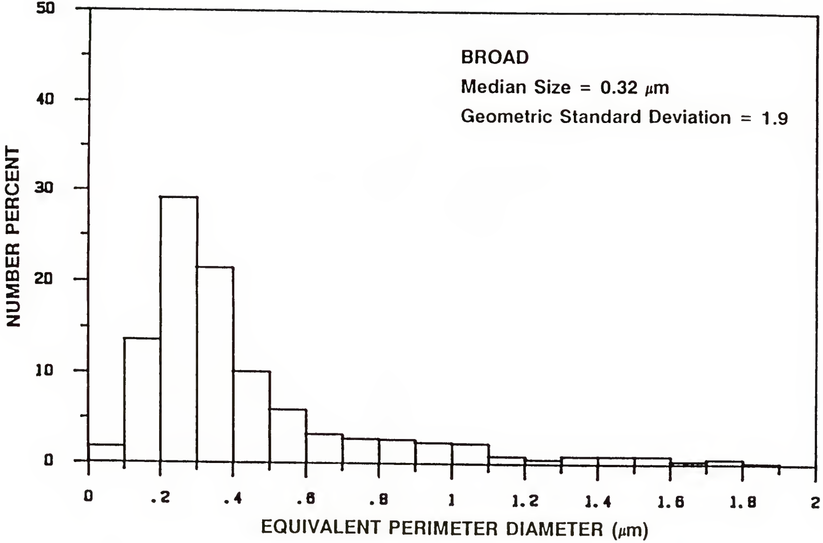

Figure 5.14 Histogram plot of the number-basis distribution of equivalent perimeter diameter determined by SEM for the BSD powders.

The median sizes and geometric standard deviations are shown in Table 5.1. The D_p's were significantly larger than the D_A's. This implied that these powders were not equiaxed simple shapes (e.g., sphere). Because the geometric standard deviations were similar in both characterization methods, the distribution histograms for D_A's and D_p's were similar except that the histograms for D_p's simply shifted to larger sizes. It should be noted that the number-basis median size decreased as the width of the particle size distribution increased. This is because the number of particles needed to comprise a constant weight increases as the particle size decreases, therefore, fine particles dominate in the number-basis size distribution. When the width of the particle size distribution increases, the number of fine particle increases significantly. Therefore, the number-basis median size decreases.

In order to have a comparison on same frequency basis with the particle size distribution determined by sedimentation methods, the number-basis distribution histograms of D_A (Figures 5.9 to 5.11) were converted to volume-basis distribution histograms (Figures 5.15 to 5.17). The volume-basis median sizes and geometric standard deviations are also shown in Table 5.1. Compared to the particle size results obtained by sedimentation methods, the volume-basis D_A's were significantly larger. This suggested that the equivalent area diameters were over-estimated since the particles were non-equiaxed. In the samples prepared for SEM observations, particles tend to rest on the plane with its maximum stability, i.e., the plane which gives the largest cross sectional area. This phenomena becomes even more severe for the largest particles which normally showed the most deviation from equiaxed shapes. Because the largest particles are actually "mini"

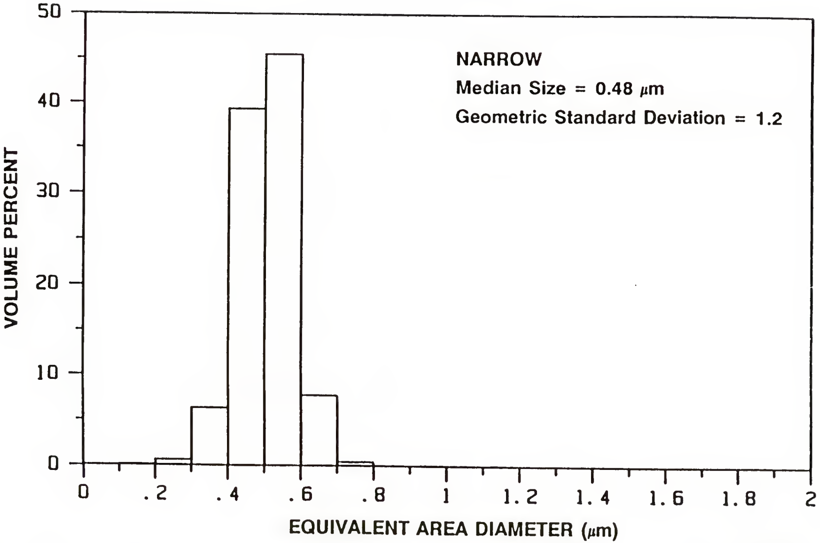

Figure 5.15 Histogram plot of the volume-basis distribution of equivalent area diameter determined by SEM for the NSD-30 powders.

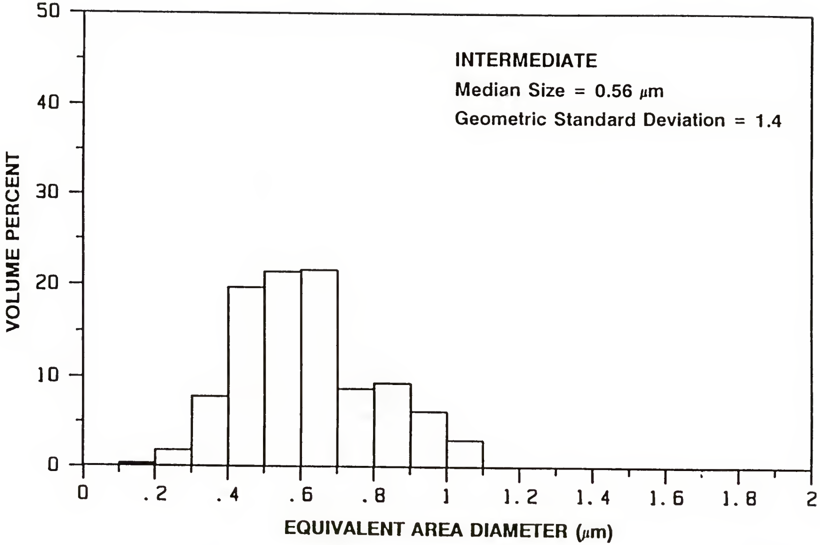

Figure 5.16 Histogram plot of the volume-basis distribution of equivalent area diameter determined by SEM for the ISD powders.

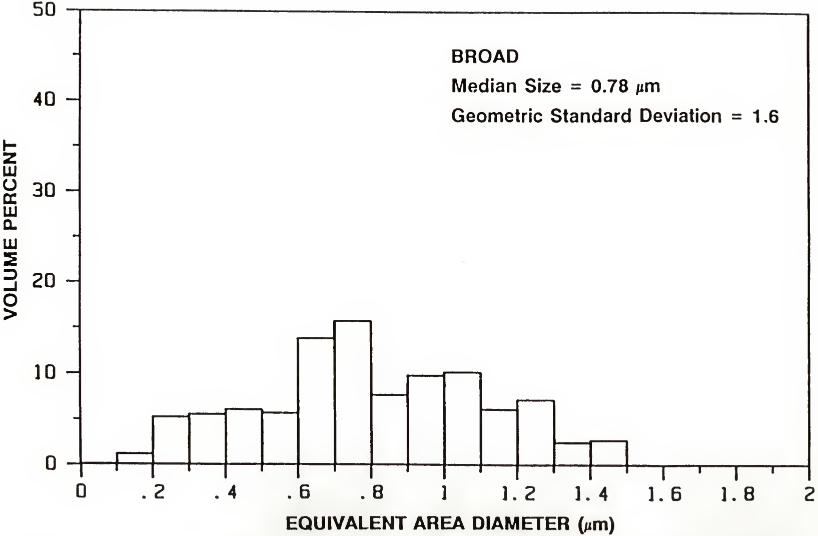

Figure 5.17 Histogram plot of the volume-basis distribution of equivalent area diameter determined by SEM for the BSD powders.

aggregates which are comprised of several primary particles. The overestimation of the D_A results is again amplified when the number-basis results are converted to volume-basis distributions. For example, the volume of a 1 μm particle is about 1000 times of the volume of 0.1 μm. Overestimation of the large particles can significantly increase the volume fraction of large particle and further shift the volume-basis median size to larger values. Therefore, the discrepancies among the median sizes determined by sedimentation methods and SEM method became more significant when the particle size distribution became broader (i.e., had more large particles.)

The surface areas determined by BET method are 7.0, 6.9 and 7.6 m^2/g for NSD-30, ISD, and BSD powders, respectively. The similar surface area obtained for each powder further demonstrated that model powders were obtained in the present study and particle size distribution can be isolated as the only variable for investigation. Slightly larger surface area obtained for the BSD powder may be due to the deviation from the ideal log-normal distribution in the coarse size regions (Figure 5.2) (i.e., the deficiency in the large particles).

Suspension Characterization

Figure 5.18 shows plots of viscosity vs. shear rate for 45 vol% suspensions at pH ~ 4 prepared with NSD-30, ISD and BSD powder, respectively. All suspensions showed slightly shear thinning behavior which is normally observed for high solids loading suspensions. Due to the lower packing efficiency, the suspension prepared from NSD-30 powder showed relatively higher viscosity. The particle packing efficiency becomes better when the width of particle size distribution increases.

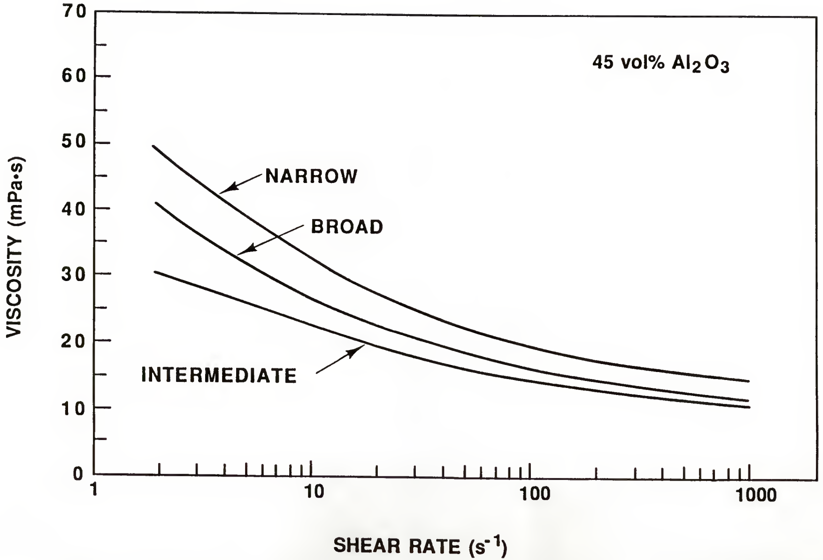

Figure 5.18 Plots of viscosity vs. shear rate for 45 vol% suspensions at pH ≈ 4 prepared with NSD-30, ISD, and BSD powders.

Therefore, the suspension prepared from ISD powder showed slightly lower viscosity. However, it is surprising that the suspension prepared from BSD powder had higher viscosity than the suspension prepared from ISD powder. As will be demonstrated in the next chapter, Brownian motion and electroviscous effects can significantly increase the viscosity when the suspension contains very fine particles. The BSD powder had a much larger fraction of fine particles (i.e., ~26 wt% of the particles measured by x-ray sedimentation method in BSD powder are $\leq 0.2\ \mu m$, whereas only ~10 wt% of the particles in ISD powder are $\leq 0.2\ \mu m$). Therefore, the suspension prepared from the BSD powder showed higher viscosities.

Green Compact Characterization

Plots of the pore size distributions determined by mercury porosimetry for slip cast compacts prepared from the NSD-30, ISD, and BSD powders are shown in Figure 5.19. Green compact characteristics (e.g., green density, median pore channel radius, and BET surface area)

Table 5.2

Property	Sample		
	NSD-30	ISD	BSD
Green Density (%)	65	70	73
Median Pore Channel Radius (nm)	50	40	29
Surface Area (m^2/g)	7.1	6.7	7.5
Surface Area ($m^2/c.c.$)	18.1	18.6	21.5

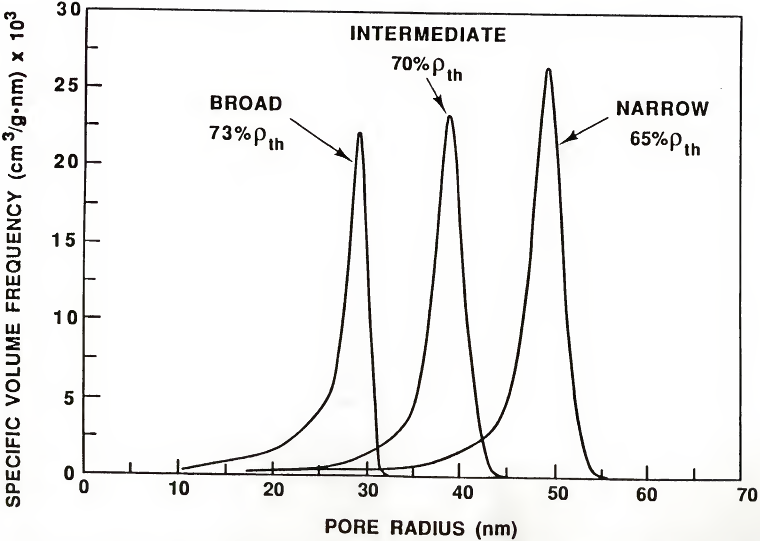

Figure 5.19 Plots of specific pore volume frequency vs. pore channel radius obtained by mercury porosimetry for the NSD-30, ISD, and BSD samples.

are shown in Table 5.2. All samples showed high relative green density as a result of using well-dispersed suspensions for casting. Due to the narrow particle size distribution, the NSD-30 sample had the lowest green density and largest mean pore channel radius. As the width of the particle size distribution increased, the green density increased and the mean pore channel radius decreased. These results indicate that fine particles are filling the interstices formed by larger particles in the broader size distribution samples and more efficient particle packing was obtained. The finer pore channel sizes indicated that the average curvature in the neck regions between particles is higher; as a consequence, the average driving forces for sintering is also higher.

The SEM photographs of the top surfaces and fracture surfaces are shown in Figures 5.20, 5.21, and 5.22 for NSD-30, ISD, and BSD slip cast compacts, respectively. As seen from the microstructures of the top surfaces, all samples showed very homogeneous packing. The differences in the width of the particle size distributions can be clearly identified in the micrographs. The increase in packing density anddecrease in pore channel sizes with increasing width of the particle size distribution can be clearly seen and this is consistent with the results obtained from mercury porosimetry.

The surface area per unit weight for each sample is also shown in Table 5.2 which agreed very well with the values obtained from loose-stacked powders. When the weight-basis surface areas were converted to volume-basis, it was found that higher surface areas per unit volume were obtained for the compacts prepared from powders having broader particle size distributions. This is because the higher packing densities were obtained for samples having broader particle size

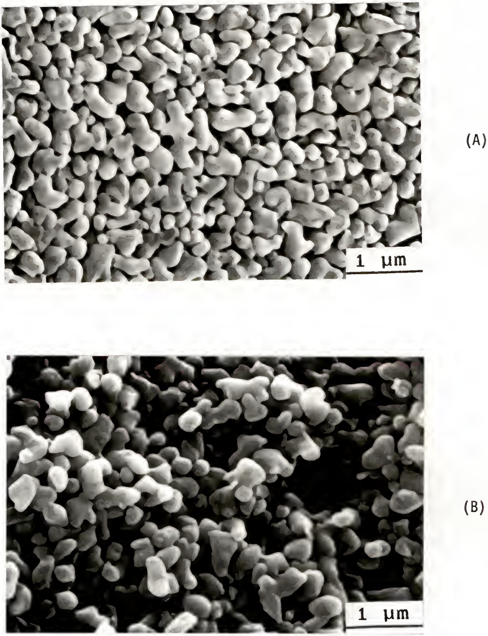

Figure 5.20 SEM micrographs for (A) top surface and (B) fracture surface of NSD-30 sample.

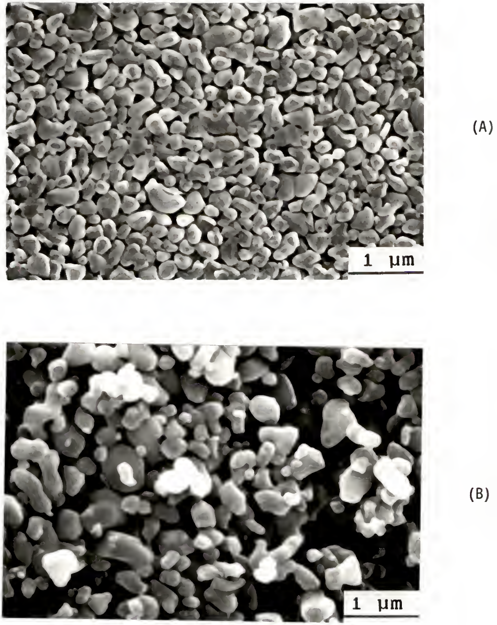

Figure 5.21 SEM micrographs for (A) top surface and (B) fracture surface of ISD sample.

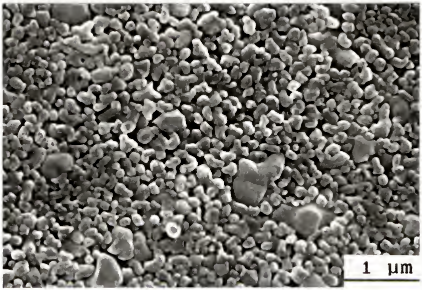

(A)

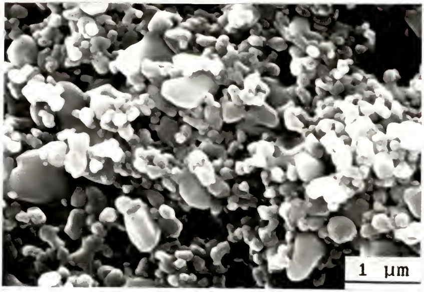

(B)

Figure 5.22 SEM micrographs for (A) top surface and (B) fracture surface of BSD sample.

distributions. It is expected that the initial stage densification kinetics of the BSD sample should be enhanced due to the higher packing density, finer pore size and higher specific surface area per unit volume.

Plot of relative green density vs. geometric standard deviation of the particle size distribution determined by x-ray gravitational sedimentation for NSD-30, ISD, BSD, and SCD (from chapter IV) samples is shown in Figure 5.23. Initially, the relative green density linearly increased with the increasing geometric standard deviation. Beyond ~70% relative density, the rate of green density increase gradually levelled off. This is confirmed by the results reported by Sacks and Scheiffele [Sac85] where ~75% green density was obtained for slip cast compacts prepared from very broad size distribution silicon powder (particle sizes ranged from ~20 μm to ~0.15 μm). It should be noted that the extrapolated green density at geometric standard deviation equals one (i.e., monosized powder) is ~61% which agrees very well with thereported packing density for randomly close-packed monosized spherical powder [McG61, Sco60].

Densification Kinetics

Plots of relative density vs. sintering time at the temperatures of 1100, 1180, 1260, and 1340°C are shown in Figures 5.24, 5.25, 5.26A, and 5.26B, respectively. Compacts with broader size distribution showed higher densification rate during the early stages of sintering. For example, after sintering for 2 h at 1180°C, the relative densities increased 13.8 and 13.1% for the BSD and ISD samples, respectively. However, the relative density of NSD-30 sample only increased ~11.7% for

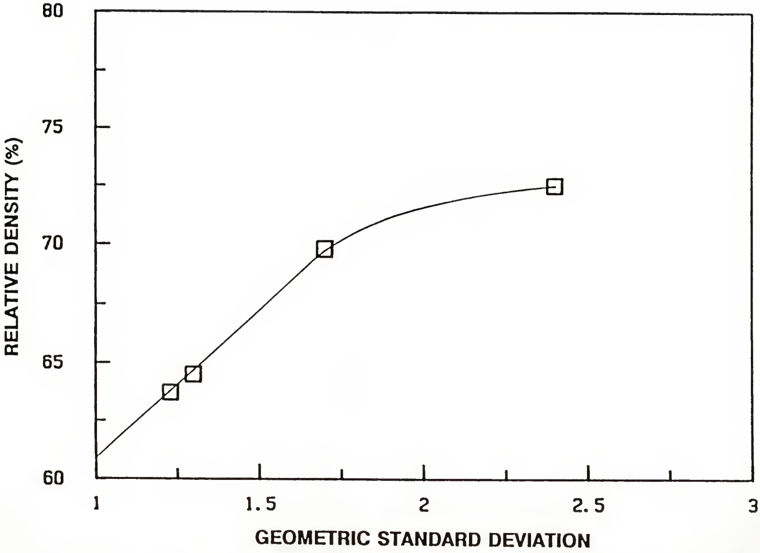

Figure 5.23 Plot of relative density of slip cast compacts prepared from well-dispersed suspensions vs. geometric standard deviation of the powders in the suspensions.

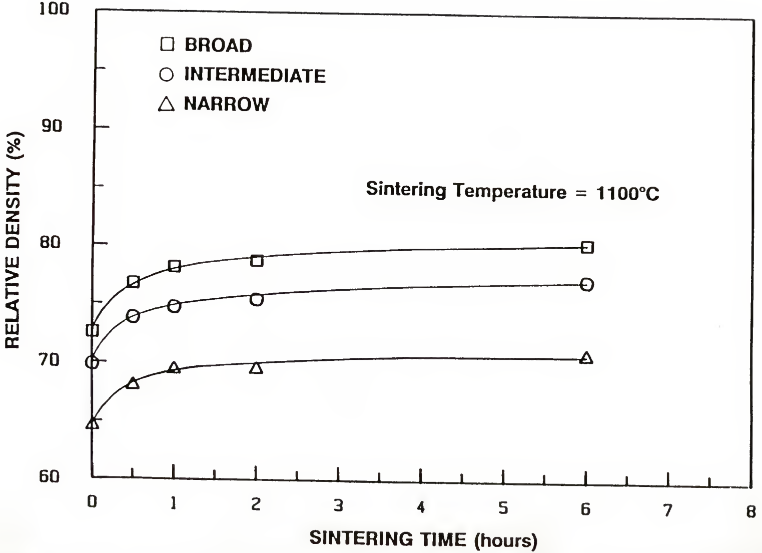

Figure 5.24 Plot of relative density vs. sintering time at 1100°C for the NSD-30, ISD, and BSD samples.

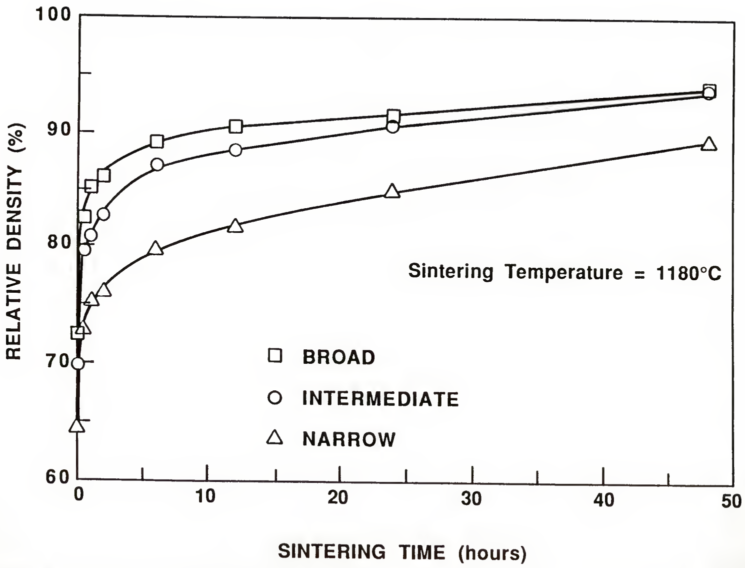

Figure 5.25 Plot of relative density vs. sintering time at 1180°C for the NSD-30, ISD, and BSD samples.

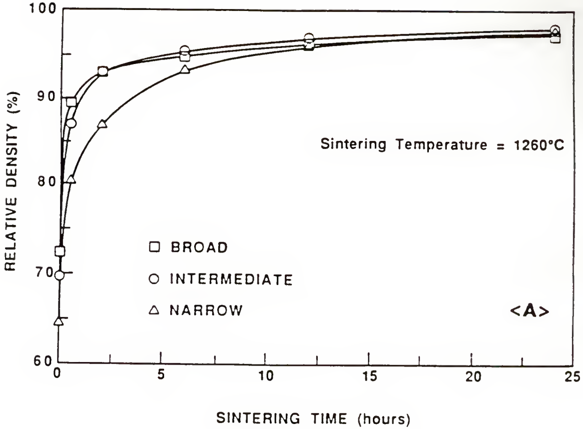

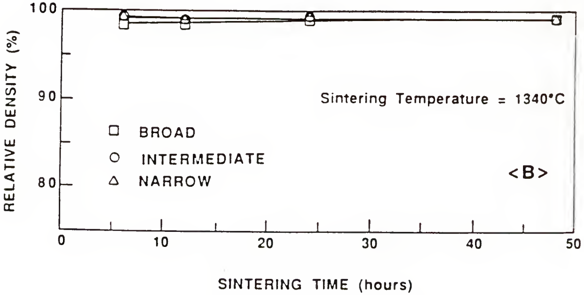

Figure 5.26 Plot of relative density vs. sintering time at (A) 1260°C and (B) 1340°C for the NSD-30, ISD, and BSD samples.

the same sintering schedule. The enhancement in the early-stage densification kinetics increased as the width of the particle size distribution increased. This is consistent with the green compact characteristics discussed before. According to Coble's model [Cob73], number-basis size distribution should be used to determine the initial stage sintering kinetics. As shown before, the number-basis medium size decreased as the width of the particle size distribution increased. Again, this also suggested that in the early stage sintering the ISD sample should have higher densification kinetics and the BSD sample should have the highest densification kinetics. The slower densification rates predicted by Chappell et al. [Cha86] for the samples with broader size distribution were not observed in the present study.

The BSD sample showed the fastest decrease in densification rate at longer sintering times. Hence, after 48 h at 1180°C or 2 h at 1260°C, the ISD sample had similar density as the BSD sample. The density differences between the BSD and NSD-30 samples also decreased (e.g., ~8% relative density difference at the green state; ~4.6% and ~6% relative density differences after 48 h at 1180°C and 2 h at 1260°C, respectively). The NSD-30 sample showed minimum decrease in densification rate. After 12 h at 1260°C, all samples reached similar density (~96%). With longer sintering times at 1260°c (Figure 5.26A) or at higher sintering temperatures (Figure 5.26B), the relative densities of all samples remained the same. (Even though slightly lower density was obtained for the BSD sample in the late stage of sintering, it was within the experimental error.) The low limiting density (~90%) predicted by Yan et al. [Yan83] for compacts prepared from broad size distribution powder was not observed in the present study.

As discussed in Chapter IV, densification rate can also be determined by taking the slopes of the smoothed curves in the plots of relative density vs. sintering time. Plots of densification rate vs. sintering time for various samples sintered at 1100, 1180, and 1260°C are shown in Figures 5.27, 5.28, and 5.29, respectively. The evolution of densification rate for each sample can be clearly seen in these figures. The faster decrease in densification rate for the ISD and BSD samples became more significant (i.e., occurred in shorter time) when the sintering temperature was increased (Figure 5.29).

The more rapid decrease in densification rate for the ISD sample and especially for the BSD sample are probably associated with a rapid elimination of the finest grains, resulting in a decrease in the average driving force and an increase in average diffusion distance. For example, stereological measurements on BSD sample showed that the percentage of grain intercepts which were < 0.2 μm decreased from ~59% to ~35% as sintering time at 1180°C increased from 0.5 h to 12 h. A similar trend was also observed for the ISD sample, except the ISD sample had less fine grains initially. In contrast, the NSD-30 samples showed virtually no change in grain size distribution during the same period. In addition, due to the higher green density and higher densification rate in the early stages of sintering, the ISD and BSD samples reached high density in short sintering time. For example, after 2 h sintering at 1260°C, the relative densities of BSD and ISD samples were ~93%; however, the NSD-30 sample only had ~87% relative density. As discussed in Chapter IV, high density samples normally show lower densification rate. Therefore, the NSD-30 sample could still have

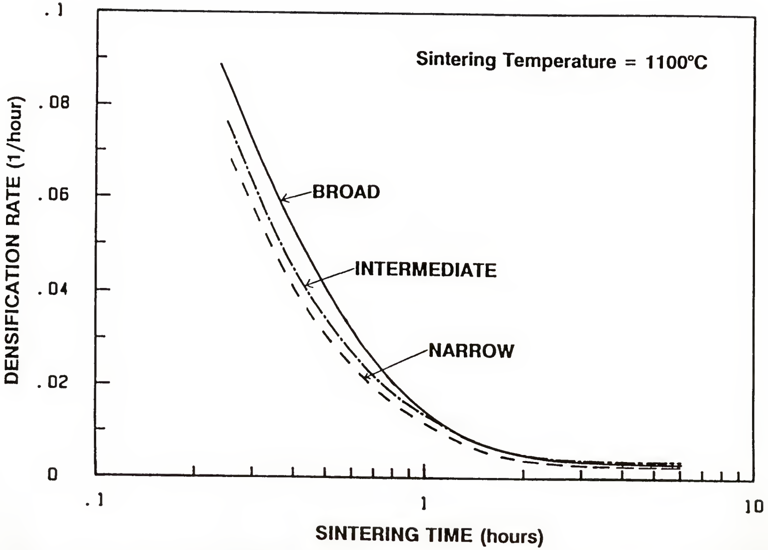

Figure 5.27 Plots of densification rate vs. sintering time at 1100°C for the NSD-30, ISD, and BSD samples.

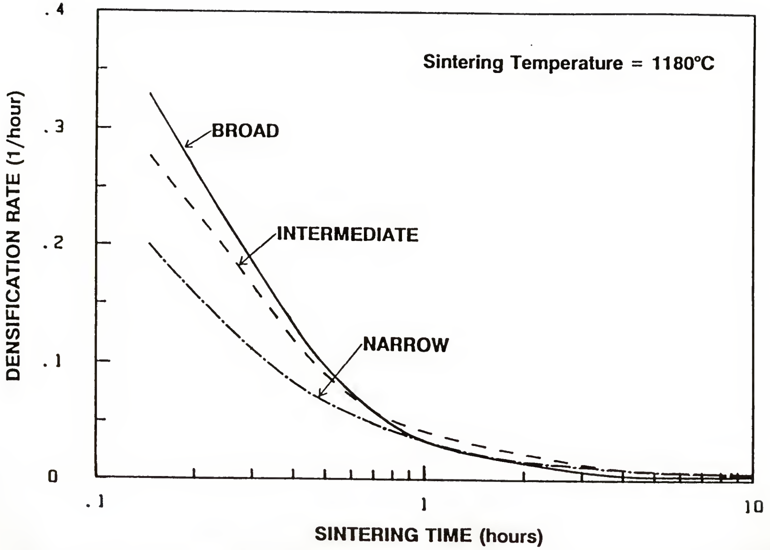

Figure 5.28 Plots of densification rate vs. sintering time at 1180°C for the NSD-30, ISD,and BSD samples.

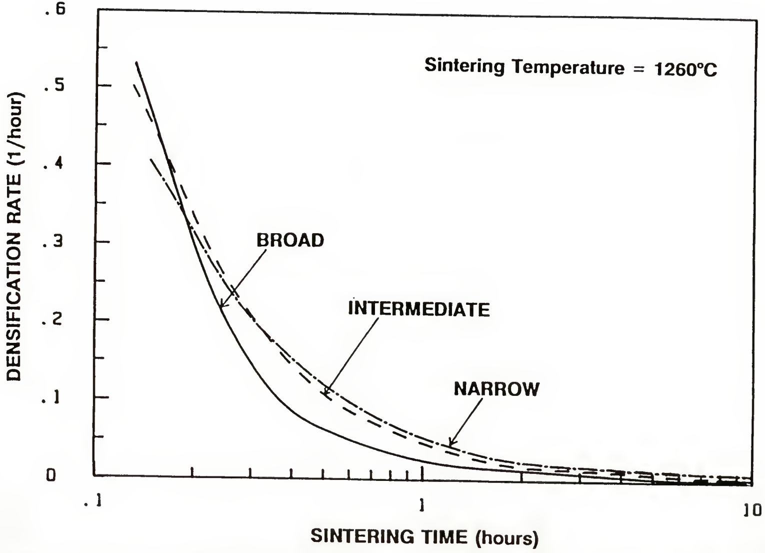

Figure 5.29 Plots of densification rate vs. sintering time at 1260°C for the NSD-30, ISD,an BSD samples.

relatively higher densification rate when the densification rate of BSD and ISD samples decreased.

Plots of densification rate vs. relative density for samples sintered at 1180°C and 1260°C are shown in Figures 5.30 and 5.31, respectively. Comparing at a constant relative density, generally speaking, the densification rate was higher as the width of the particle size distribution increased. However, at high densities, especially above ~96% relative density, similar densification rates were obtained for all samples despite the differences in the initial particle size distribution.

Activation Energy

The apparent activation energies for samples with various particle size distributions can be obtained by using the method discussed in Chapter IV. After 0.5 h sintering at 1260°C, the densities obtained were 80.6, 87.1 and 98.6% relative density for the NSD-30, ISD, and BSD sample, respectively. For samples sintered at 1180°C, it was found that same sintering time (~ 6 h) was needed for each sample to obtain the respective densities mentioned above. This suggested that samples with various particle size distributions had similar apparent activation energy for sintering. By using the above data of sintering temperatures and times and plotting in the form of Ln (reciprocal time) vs. reciprocal absolute temperature, the apparent activation energy calculated from the slope is ~ 573 KJ/mole. This value agrees very well with the values obtained in Chapter IV. This result shows that particle size and particle size distribution have little effect on the apparent activation energy of densification.

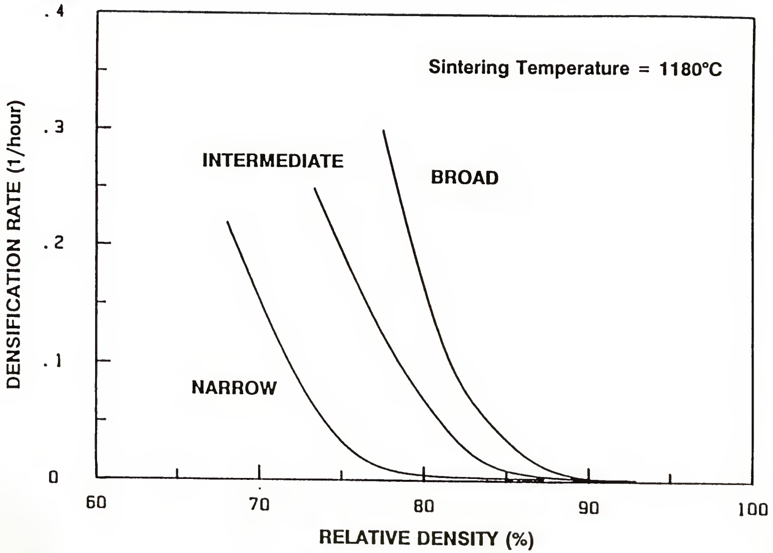

Figure 5.30 Plots of densification rate vs. relative density at 1180°C for the NSD-30, ISD, and BSD samples.

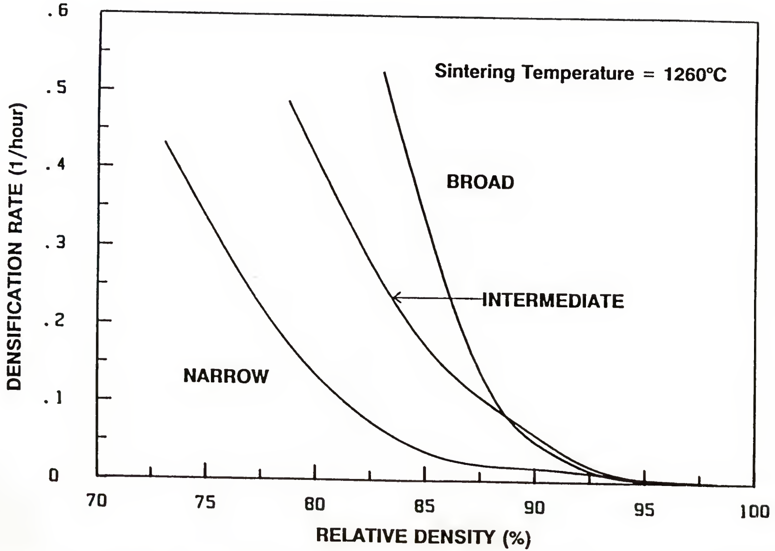

Figure 5.31 Plots of densification rate vs. relative density at 1260°C for the NSD-30, ISD, and BSD samples.

Volume Shrinkage

Plots of volume shrinkage vs. sintering time for samples sintered at 1100, 1180, and 1260°C are shown in Figures 5.32, 5.33, and 5.34, respectively. In the early stages of sintering (e.g., 1100°C or < 6 h at 1180°C) all samples showed similar shrinkage kinetics. However, different volume shrinkage was obtained for each sample at longer sintering schedules (e.g., > 6 h at 1260°C) where similar densities was obtained for all samples. Because the NSD-30 sample had the lowest green density, the highest volume shrinkage was needed for this sample to reach the same density levels as other samples. On the other hand, the BSD sample showed the lowest volume shrinkage due to its high green density.

Effect of Particle Size Distribution on Microstructural Evolution

Figures 5.35 to 5.45 show the SEM photographs with low magnification (Figures 5.35 to 5.39) and high magnification (Figures 5.40 to 5.45) for NSD-30, ISD, and BSD samples sintered to various density levels. Figure 5.46 show plot of relative density obtained by stereological measurement on the SEM photographs vs. relative density obtained by water displacement measurements. Very good agreement between these two values suggests that representative microstructures were obtained for quantitative characterization. Quantitative characterization and detailed comparison of the effects of particle size distribution on the evolution of grain size and grain size distribution, pore size and pore size distribution, as well as pore-solid interfacial area are discussed below.

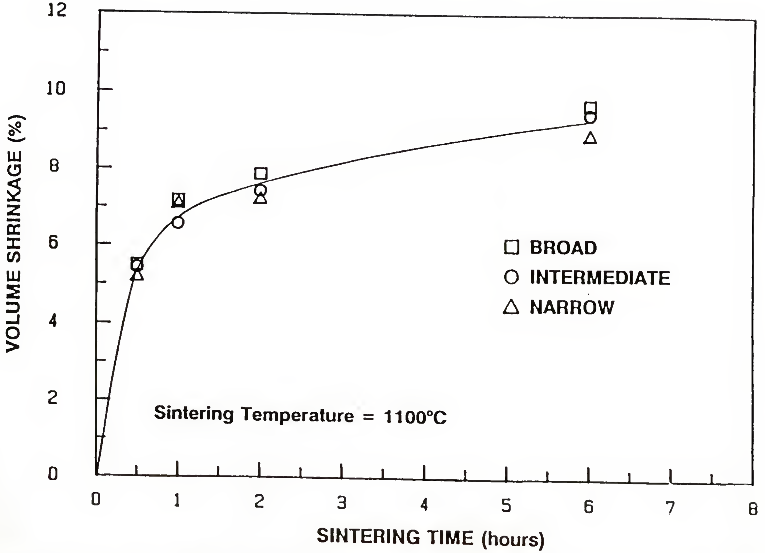

Figure 5.32 Plots of volume shrinkage vs. sintering time at 1100°C for the NSD-30, ISD, and BSD samples.

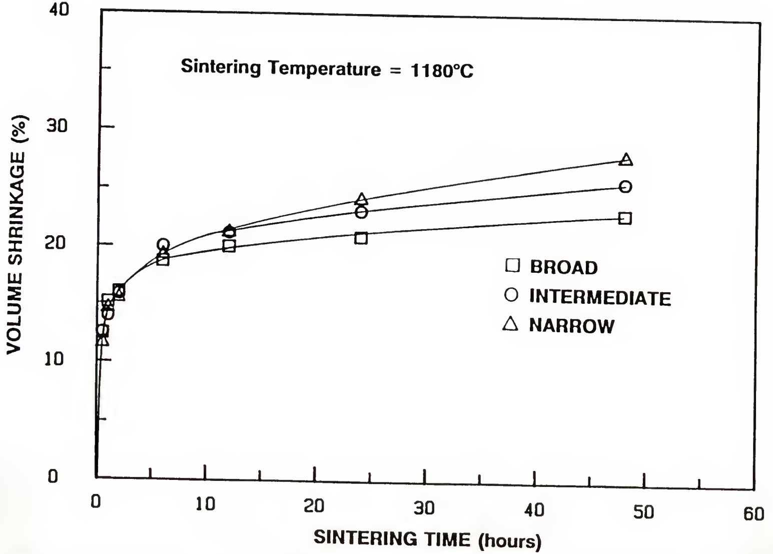

Figure 5.33 Plots of volume shrinkage vs. sintering time at 1180°C for the NSD-30, ISD, and BSD samples.

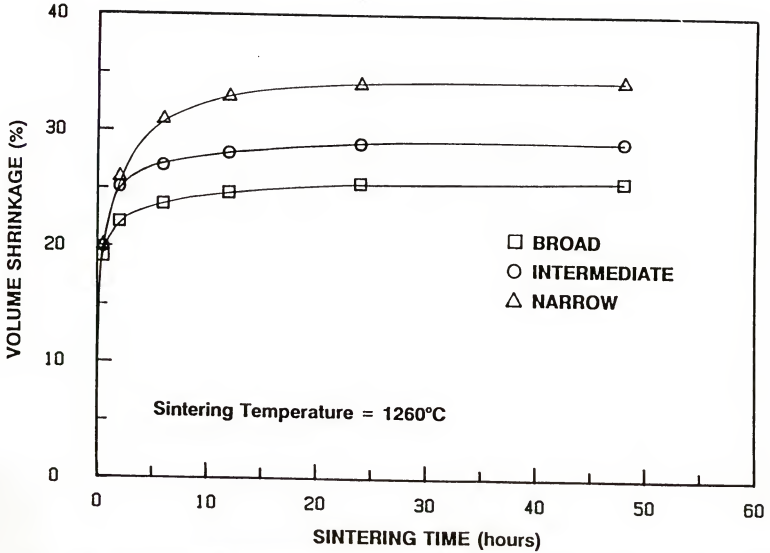

Figure 5.34 Plots of volume shrinkage vs. sintering time at 1260°C for the NSD-30, ISD, and BSD samples.

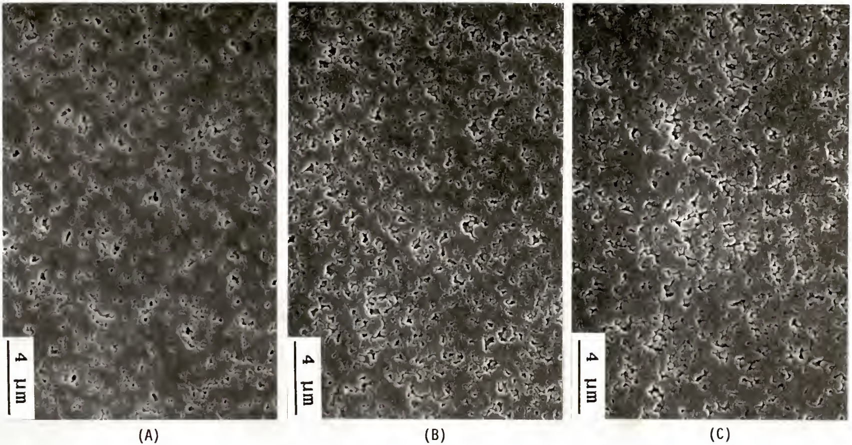

Figure 5.35 SEM micrographs of (A) BSD sample sintered at 1100°C, 1 h to 78.1% relative density, (B) ISD sample sintered at 1100°C, 1 h to 74.7% relative density, and (C) NSD-30 sample sintered at 1180°C, 1 h to 75.4% relative density.

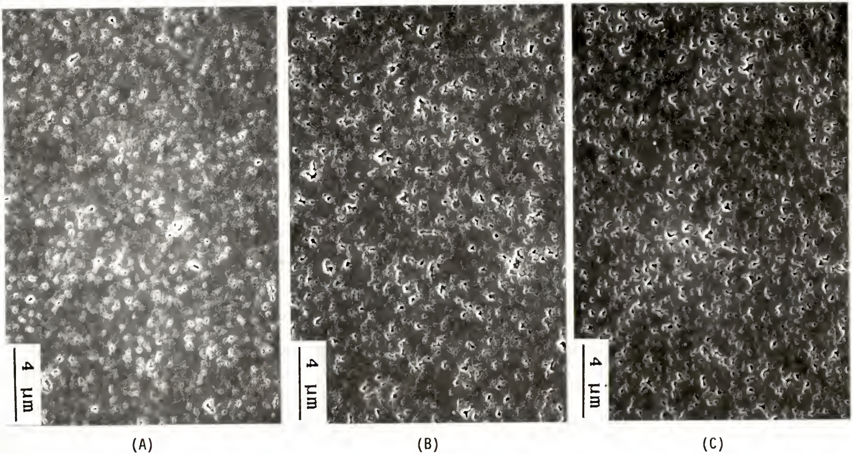

Figure 5.36 SEM micrographs of (A) BSD sample sintered at 1180°C, 0.5 h to 82.8% relative density, (B) ISD sample sintered at 1180°C, 1 h to 81.1% relative density, and (C) NSD-30 sample sintered at 1180°C, 12 h to 81.9% relative density.

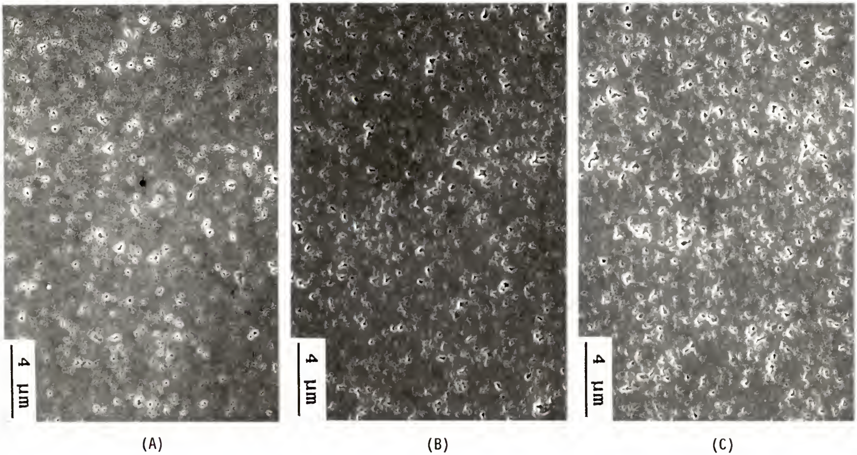

Figure 5.37 SEM micrographs of (A) BSD sample sintered at 1180°C, 2 h to 86.3% relative density, (B) ISD sample sintered at 1180°C, 6 h to 87.3% relative density, and (C) NSD-30 sample sintered at 1260°C, 2 h to 87.0% relative density.

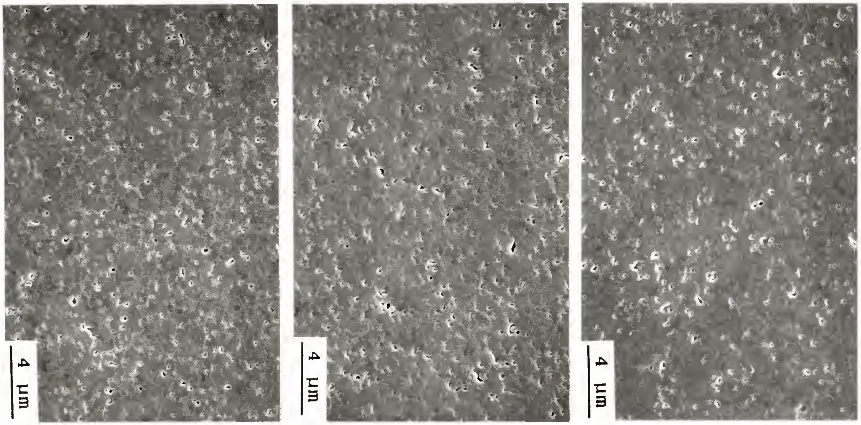

(A) (B) (C)

Figure 5.38 SEM micrographs of (A) BSD sample sintered at 1260°C, 2 h to 93.1% relative density, (B) ISD sample sintered at 1260°C, 2 h to 93.2% relative density, and (C) NSD-30 sample sintered at 1260°C, 6 h to 93.4% relative density.

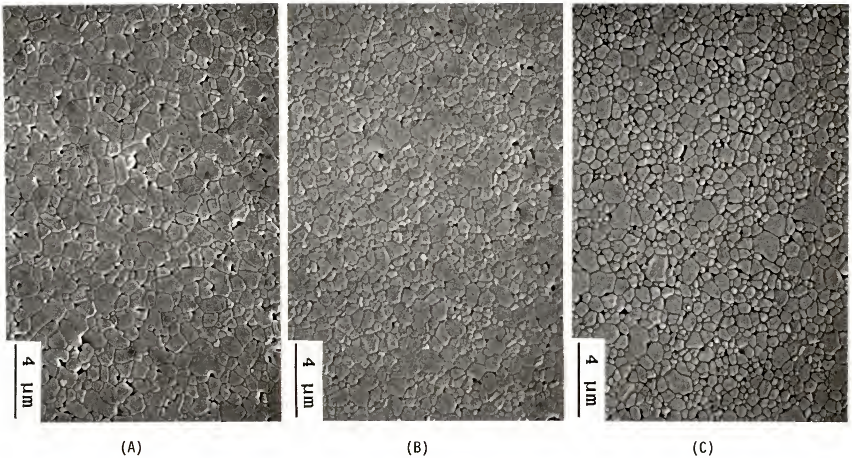

Figure 5.39 SEM micrographs of (A) BSD sample sintered at 1260°C, 16 h to 96.6% relative density, (B) ISD sample sintered at 1260°C, 16 h to 97.4% relative density, and (C) NSD-30 sample sintered at 1260°C, 16 h to 96.7% relative density.

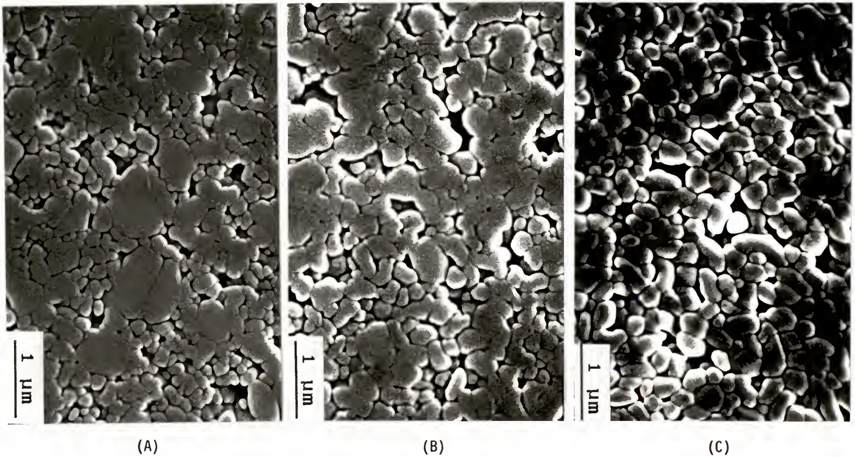

Figure 5.40 SEM micrographs of (A) BSD sample sintered at 1100°C, 1 h to 78.1% relative density, (B) ISD sample sintered at 1100°C, 1 h to 74.7% relative density, and (C) NSD-30 sample sintered at 1180°C, 2 h to 76.2% relative density.

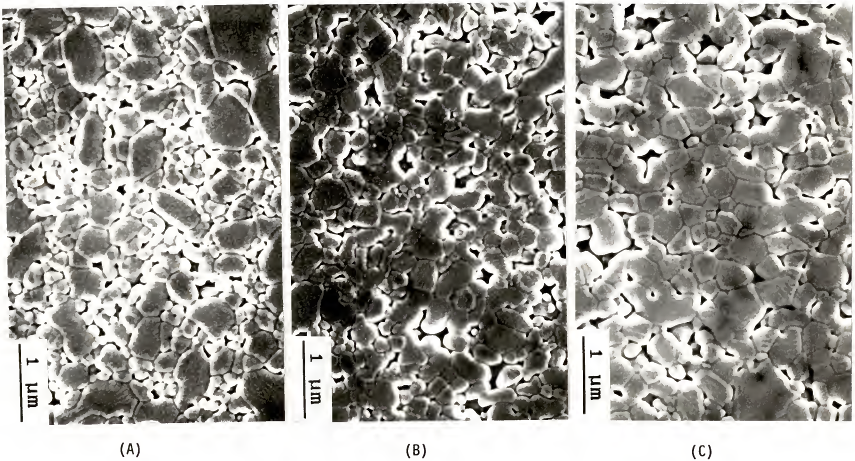

Figure 5.41 SEM micrographs of (A) BSD sample sintered at 1180°C, 0.5 h to 82.8% relative density, (B) ISD sample sintered at 1180°C, 2 h to 82.9% relative density, and (C) NSD-30 sample sintered at 1180°C, 12 h to 81.9% relative density.

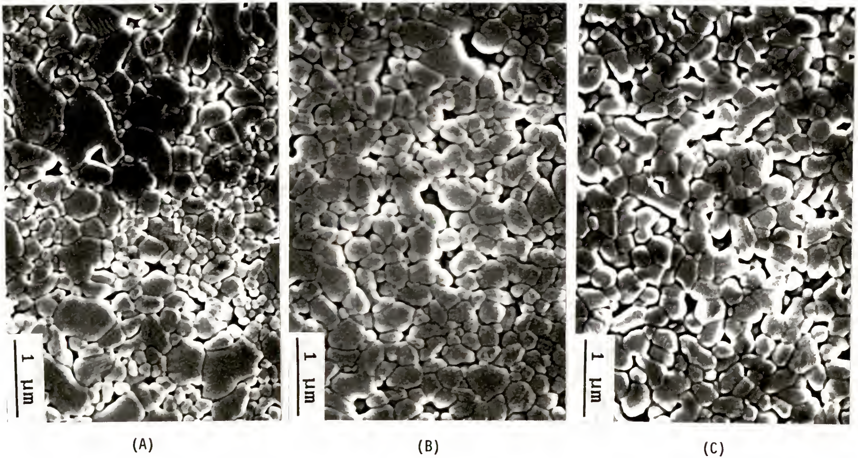

(A) (B) (C)

Figure 5.42 SEM micrographs of (A) BSD sample sintered at 1180°C, 2 h to 86.3% relative density, (B) ISD sample sintered at 1180°C, 6 h to 87.3% relative density, and (C) NSD-30 sample sintered at 1260°C, 2 h to 87.0% relative density.

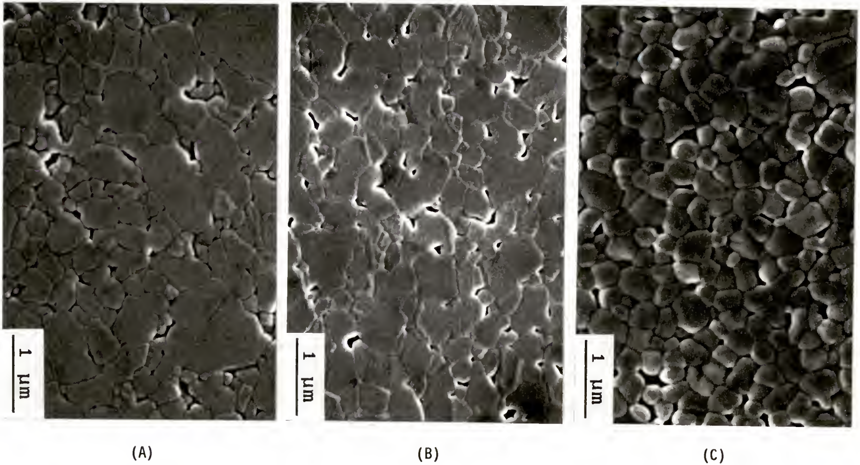

Figure 5.43 SEM micrographs of (A) BSD sample sintered at 1260°C, 2 h to 93.1% relative density, (B) ISD sample sintered at 1260°C, 2 h to 93.2% relative density, and (C) NSD-30 sample sintered at 1260°C, 6 h to 93.4% relative density.

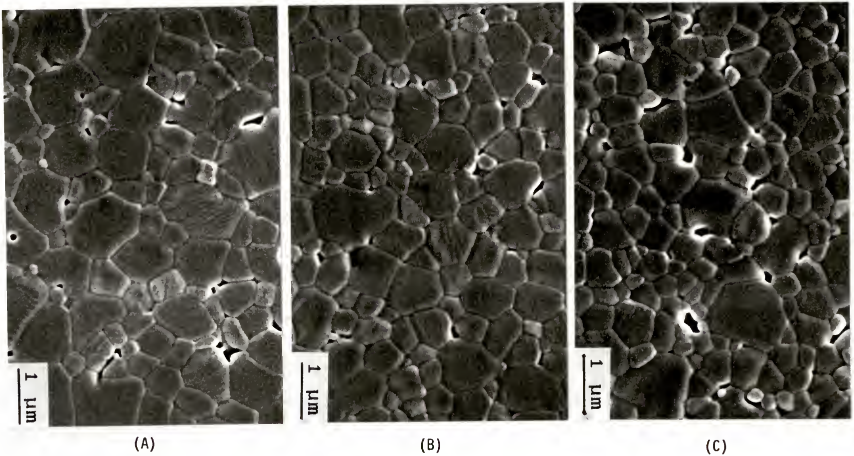

Figure 5.44 SEM micrographs of (A) BSD sample sintered at 1260°C, 16 h to 96.6% relative density, (B) ISD sample sintered at 1260°C, 16 h to 97.4% relative density, and (C) NSD-30 sample sintered at 1260°C, 16 h to 96.7% relative density.

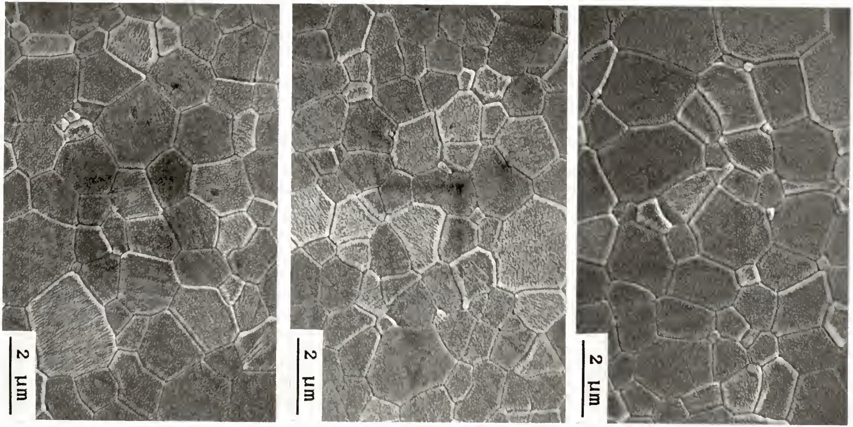

(A) (B) (C)

Figure 5.45 SEM micrographs of (A) BSD sample sintered at 1340°C, 48 h to 99.1% relative density, (B) ISD sample sintered at 1340°C, 48 h to 99.2% relative density, and (C) NSD-30 sample sintered at 1340°C, 48 h to 99.0% relative density.

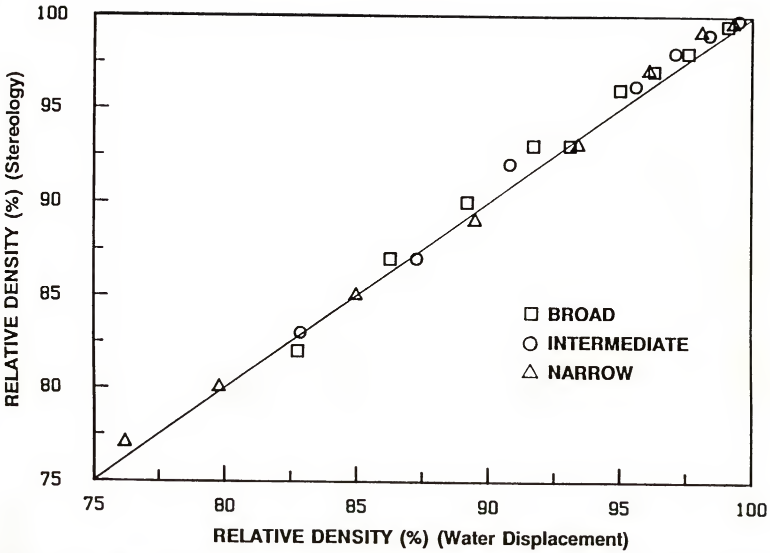

Figure 5.46 Comparison of relative densities determined by quantitative stereology and Archimedes water displacement method for the NSD-30, ISD, and BSD samples.

Grain size and grain size distribution. Plots of average grain intercept size vs. relative density at the sintering temperatures of 1180°C and 1260°C are shown in Figures 5.47* and 5.48, respectively, for NSD-30, ISD, and BSD samples. Similar grain intercept sizes were obtained over the entire density range for samples with varied breadths of particle size distributions. Even though slightly larger grain intercept sizes were observed for the BSD samples at > 95% relative density, it is still within the experimental error. For the samples sintered at 1180°C, the grain intercept sizes showed essentially no change until the relative density became higher than ~90%. For samples sintered at 1260°C, the densities at which grain coarsening began were slightly higher (i.e., about 93% relative density). Therefore, in the high density region, the samples sintered at 1260°C had slightly smaller grain intercept size compared to samples sintered at 1180°C. This observation agreed with Brook's proposition that higher sintering temperature enhanced the densification/coarsening ratio [Bro82]. However, the differences in grain intercept size observed in the present study were not very significant. By using samples sintered to higher densities (i.e., longer sintering time at 1180°C) or by increasing the differences in sintering temperature, more significant difference in grain size may be observed; therefore, more conclusive results may be obtained on the effect of temperature on densification/coarsening ratio.

In the density range where the average grain intercept sizes of each size distribution series were relatively constant, the grain size distributions of each sample series also remained relatively unchanged. This was demonstrated in Figures 5.49 to 5.60 where particle size

---

* Solid symbols denote samples sintered at 1100°C for 1 h.

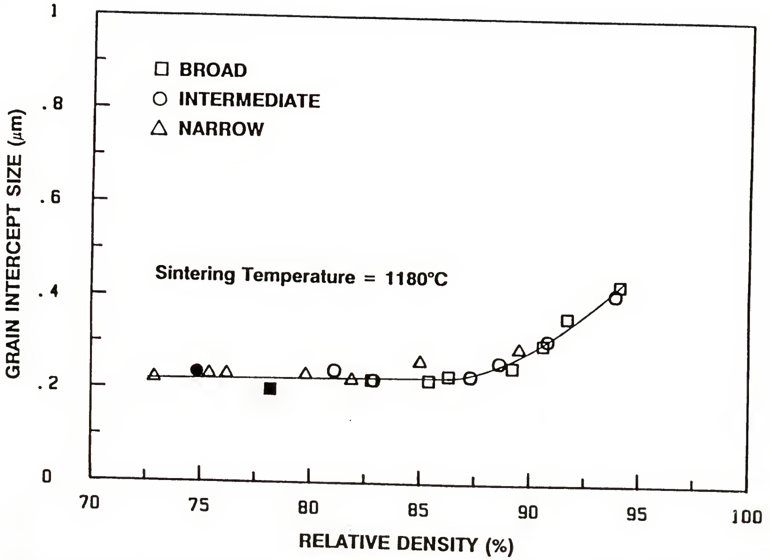

Figure 5.47 Plots of average grain intercept size vs. relative density for the NSD-30, ISD, and BSD samples sintered at 1180°C. (Solid symbols denote samples sintered at 1100°C.)

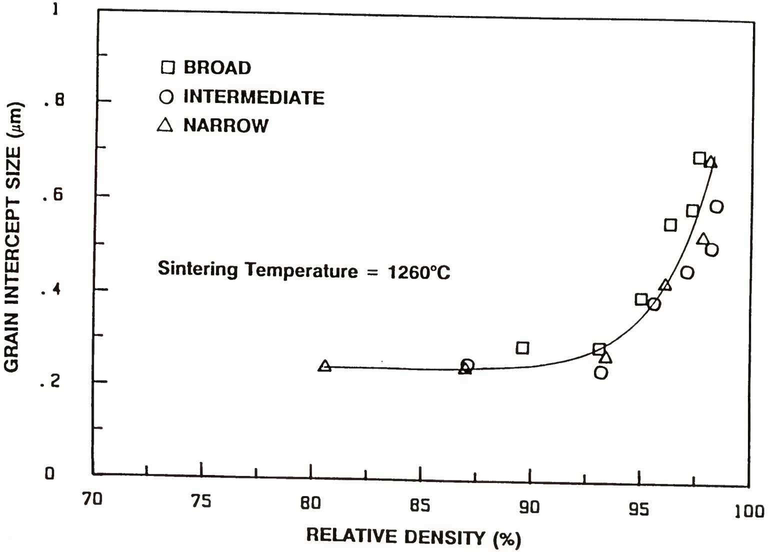

Figure 5.48 Plots of average grain intercept size vs. relative density for the NSD-30, ISD, and BSD samples sintered at 1260°C.

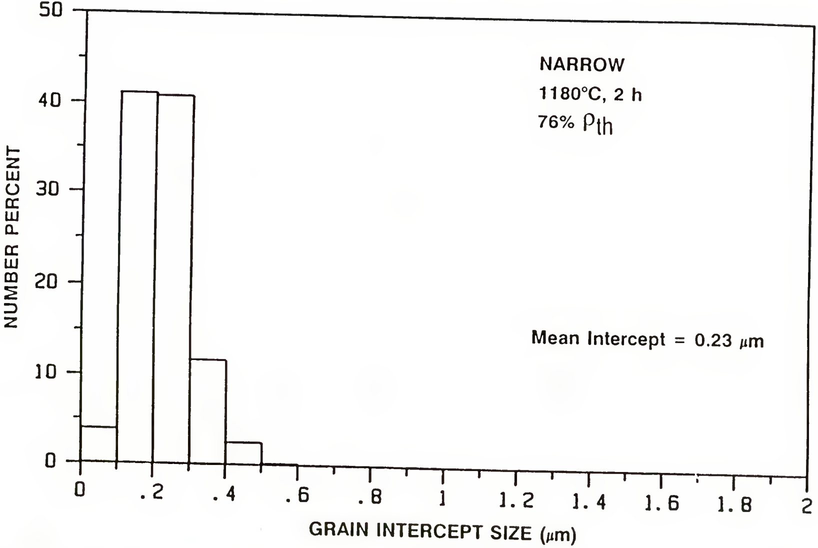

Figure 5.49 Histogram plot of the grain intercept size distribution for the NSD-30 sample sintered at 1180°C, 2 h to 76.2% relative density.

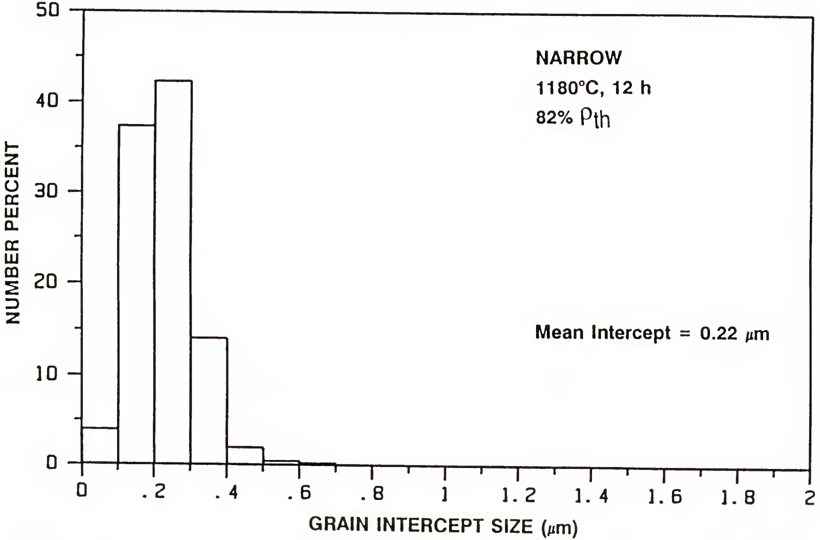

Figure 5.50 Histogram plot of the grain intercept size distribution for the NSD-30 sample sintered at 1180°C, 12 h to 81.9% relative density.

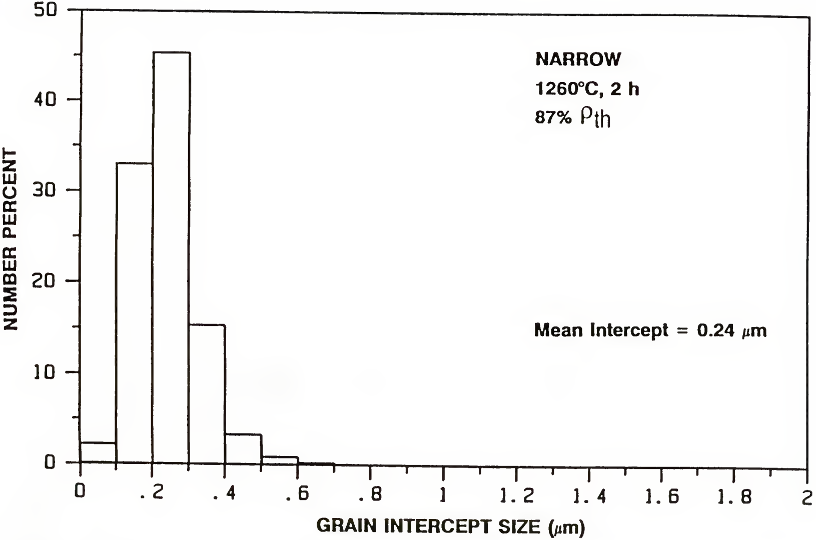

Figure 5.51 Histogram plot of the grain intercept size distribution for the NSD-30 sample sintered at 1260°C, 2 h to 87.0% relative density.

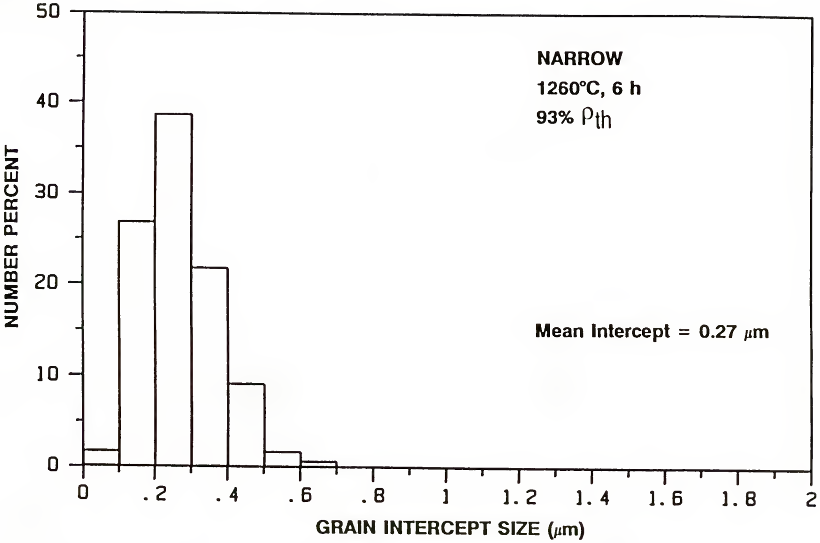

Figure 5.52 Histogram plot of the grain intercept size distribution for the NSD-30 sample sintered at 1260°C, 6 h to 93.4% relative density.

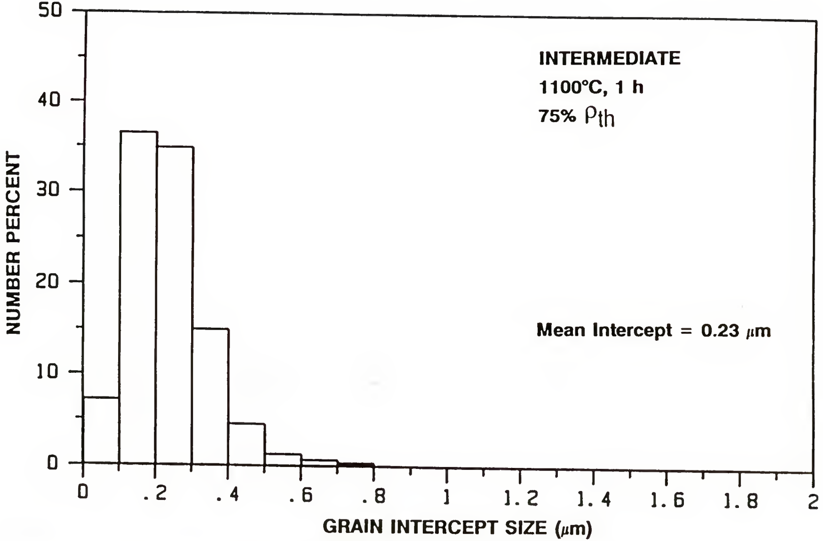

Figure 5.53 Histogram plot of the grain intercept size distribution for the ISD sample sintered at 1100°C, 1 h to 74.7% relative density.

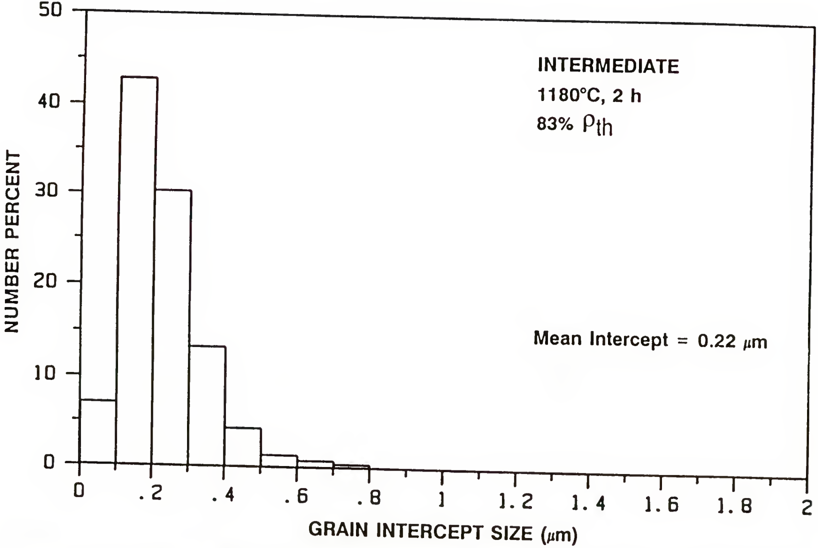

Figure 5.54 Histogram plot of the grain intercept size distribution for the ISD sample sintered at 1180°C, 2 h to 82.9% relative density.

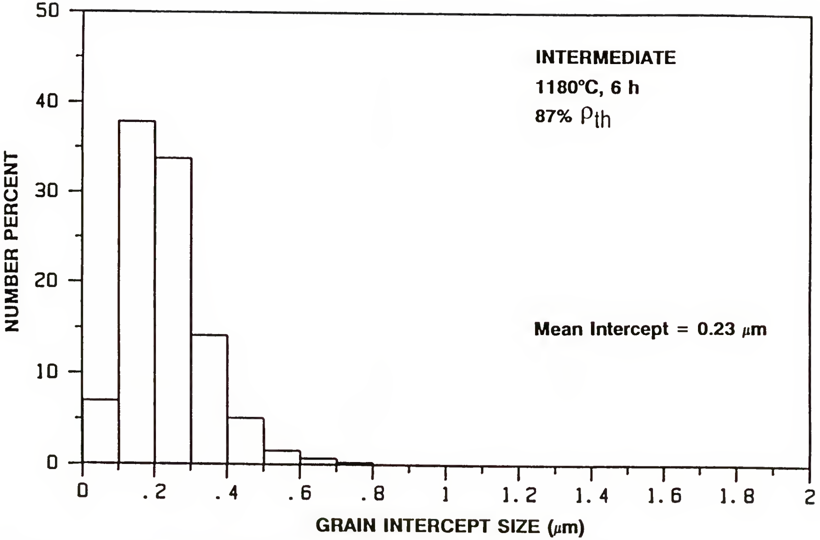

Figure 5.55 Histogram plot of the grain intercept size distribution for the ISD sample sintered at 1180°C, 6 h to 87.3% relative density.

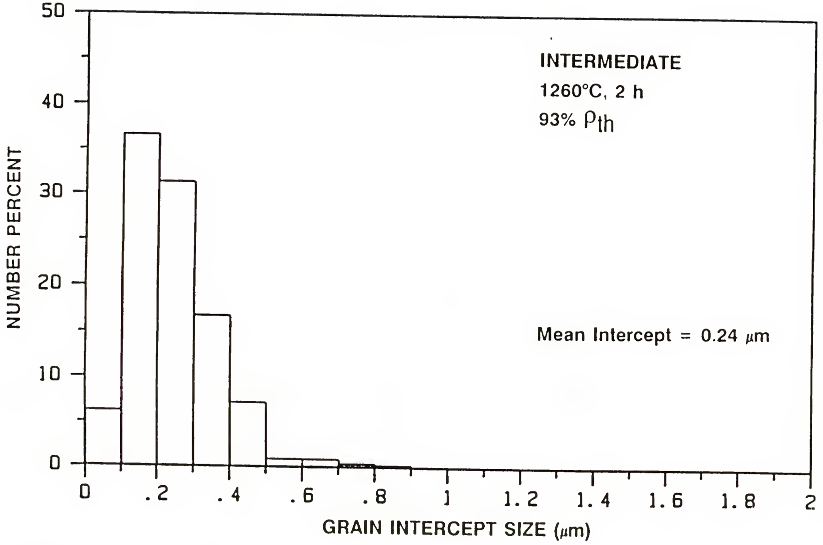

Figure 5.56 Histogram plot of the grain intercept size distribution for the ISD sample sintered at 1260°C, 2 h to 93.2% relative density.

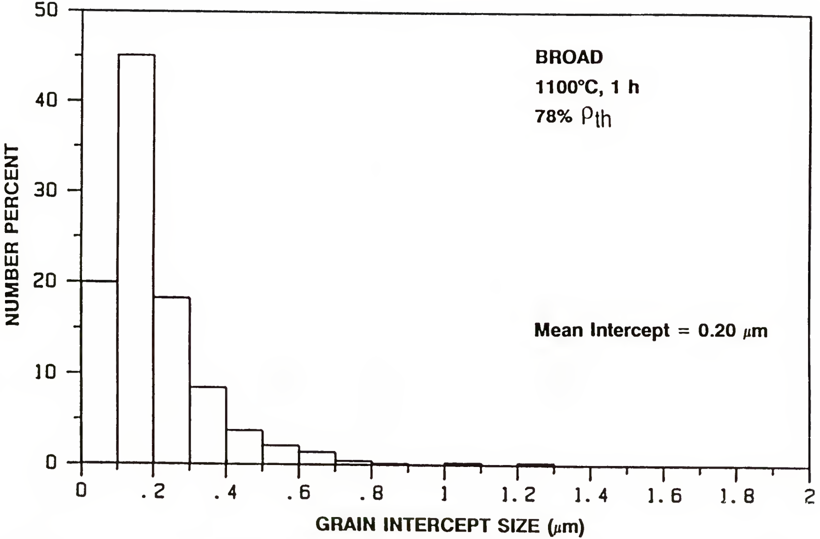

Figure 5.57 Histogram plot of the grain intercept size distribution for the BSD sample sintered at 1100°C, 1 h to 78.1% relative density.

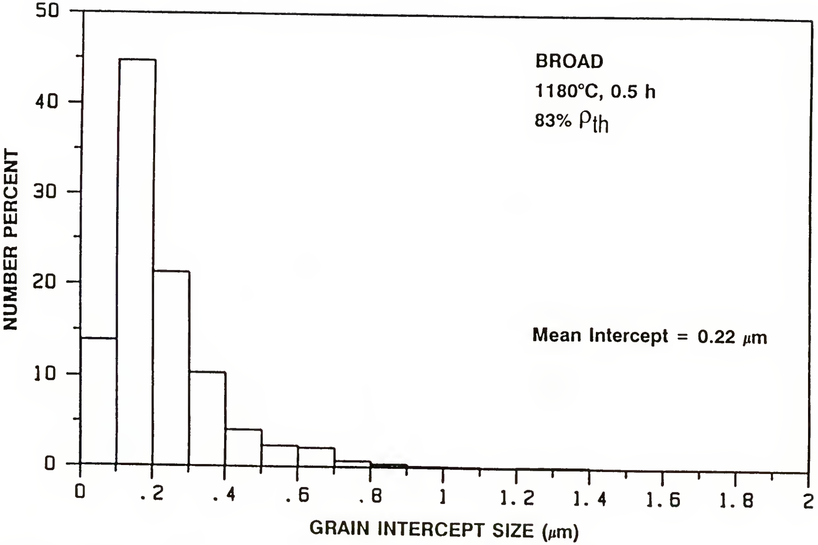

Figure 5.58 Histogram plot of the grain intercept size distribution for the BSD sample sintered at 1180°C, 0.5 h to 82.8% relative density.

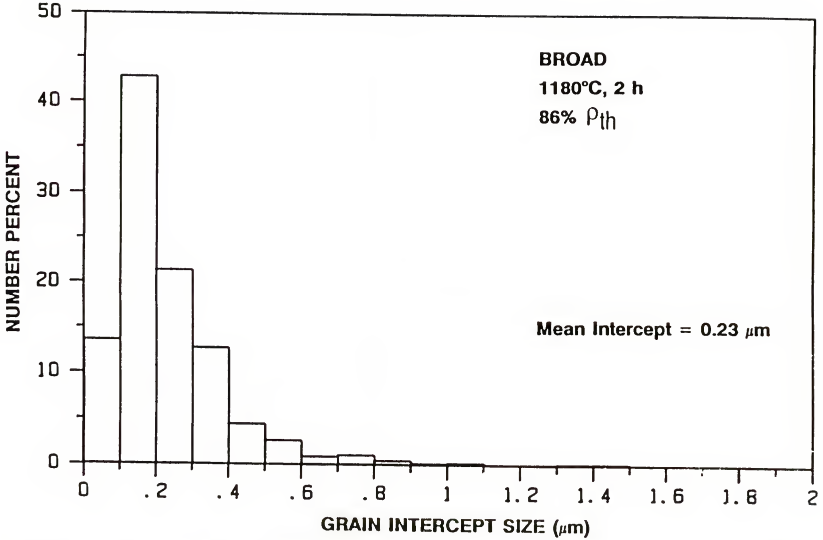

Figure 5.59 Histogram plot of the grain intercept size distribution for the BSD sample sintered at 1180°C, 2 h to 86.3% relative density.

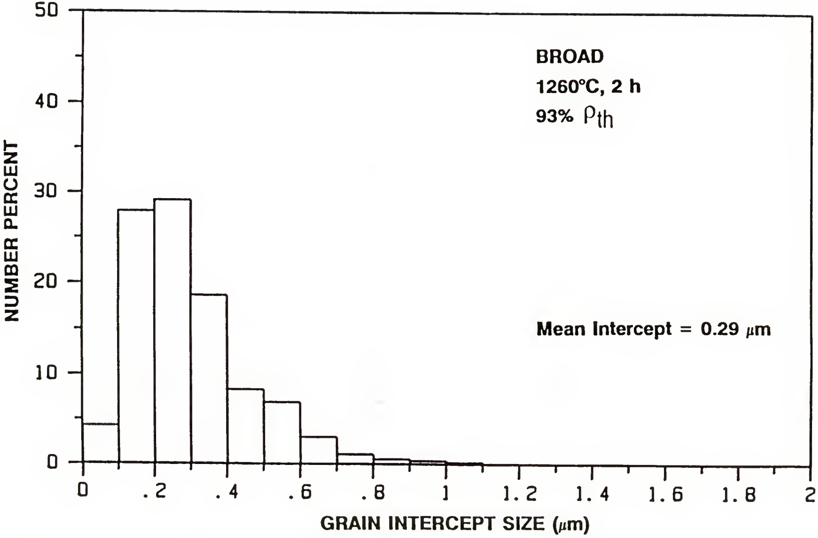

Figure 5.60 Histogram plot of the grain intercept size distribution for the BSD sample sintered at 1260°C, 2 h to 93.1% relative density.

distribution histograms for NSD-30, ISD, and BSD samples are shown. Slight decrease in the fine intercept sizes (<0.2μm) was observed in the NSD-30 and ISD samples. A more significant decrease in the fine intercept sizes was observed for the BSD sample. This was consistent with the densification kinetic results. However, increases in the size of largest grains were not observed in any of the size distribution series. The distinct differences in the width of size distribution of each sample remained. This also can be clearly seen in the SEM photographs as shown in Figures 5.40 to 5.43.

Plots of percentage of open porosity vs. relative density for NSD-30, ISD, and BSD samples are shown in Figure 5.61. Similar to the slip cast samples discussed in Chapter IV, the connected three-dimensional pore channels started to pinch off and form isolated pores when relative density became larger than ~90%. Only closed pores remained when the relative density became larger than ~95%. As discussed in chapter IV, when the connected pore channels start to collapse into isolated pores, they become less effective in preventing grain boundary migration. The grain sizes started to increase as the samples reached > 90% density (Figure 5.47). Rapid grain growth was observed for samples with > 95% relative density (Figure 5.48). The rapid grain growth can also be clearly demonstrated in Figure 5.62 to 5.64 where the histograms of grain intercept size distributions for NSD-30, ISD, and BSD samples at ~97% density are shown. For various samples at ~93% relative density only the BSD sample had few grain intercept sizes larger than 1 μm (Figures 5.52, 5.56 and 5.60). At ~97% relative density, all samples had significant percentage of grain intercepts larger than 1 μm. It should be noted that the grain intercept size distributions for the NSD-30 and

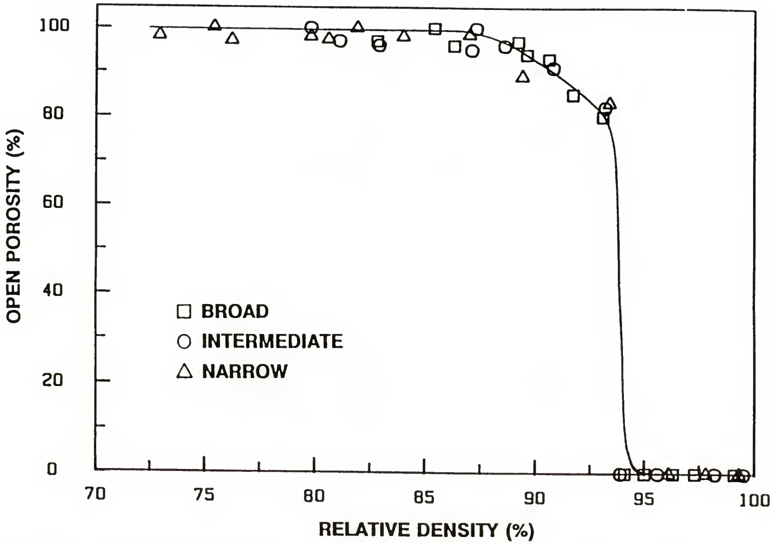

Figure 5.61 Plots of percentage of open porosity vs. relative density for the NSD-30, ISD, and BSD samples.

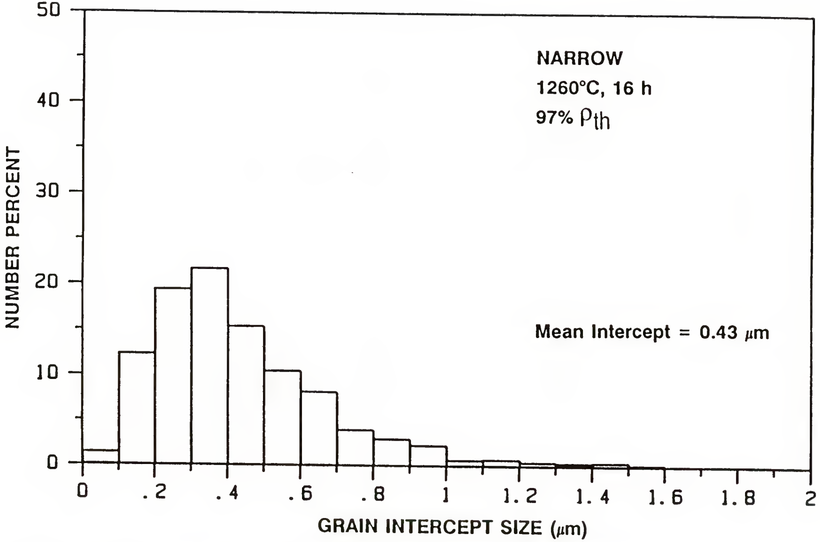

Figure 5.62 Histogram plot of the grain intercept size distribution for the NSD-30 sample sintered at 1260°C, 16 h to 96.7% relative density.

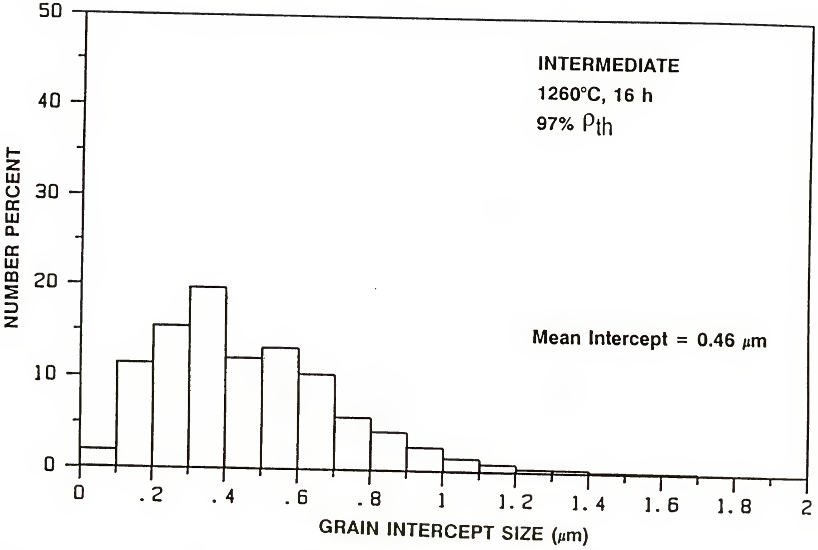

Figure 5.63 Histogram plot of the grain intercept size distribution for the ISD sample sintered at 1260°C, 16 h to 97.4% relative density.

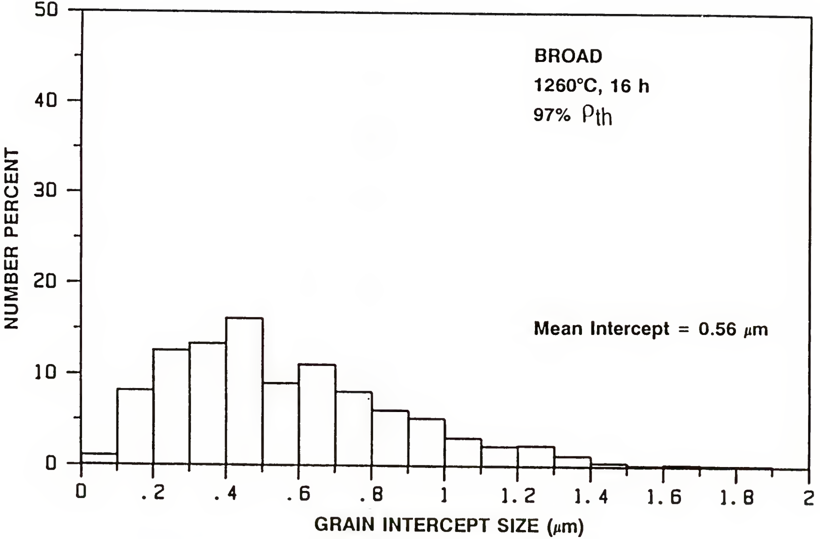

Figure 5.64 Histogram plot of the grain intercept size distribution for the BSD sample sintered at 1260°C, 16 h to 96.6% relative density.

ISD samples became significantly broader and approached the size distribution of BSD sample. SEM photographs of the above samples (Figure 5.44) also showed that microstructures of various samples became similar even though the particle size distributions of the starting powders were significantly different. In order to further confirm the above finding, investigation on samples having >99% density (sintered at 1340°C for 48 h) was carried out. Again, very similar microstructures (Figure 5.45) and grain intercept size distributions (Figures 5.65 to 5.67) were obtained. No exaggerated grain growth was observed in any sample despite the long sintering times. The large grains in the BSD sample did not act as seeds for exaggerated grain growth. This is consistent with the results of Smith and Messing [Smi84] and Handwerker et al. [Han89]. The powders used in the present study had very high purity which could eliminate the possibility of forming liquid phases in the grain boundaries and decrease the possibility of exaggerated grain growth [Ben85, Han89].

From the above results, it can be concluded that the amount and morphology of pores have the most significant effect on the grain growth behavior of a homogeneous powder compact. Before the open pore channels of a sample breakdown into isolated pores, very little grain growth can occur. The grain size distribution of the sample is determined by its initial particle size distribution (i.e., sample prepared from narrow size distribution powder will show narrow grain size distribution; sample prepared from broad size distribution powder will have broad grain size distribution). For sample sintered to high density (> 95% relative density), a majority of pores become closed and rapid grain growth occurs. The average grain intercept sizes and size distributions

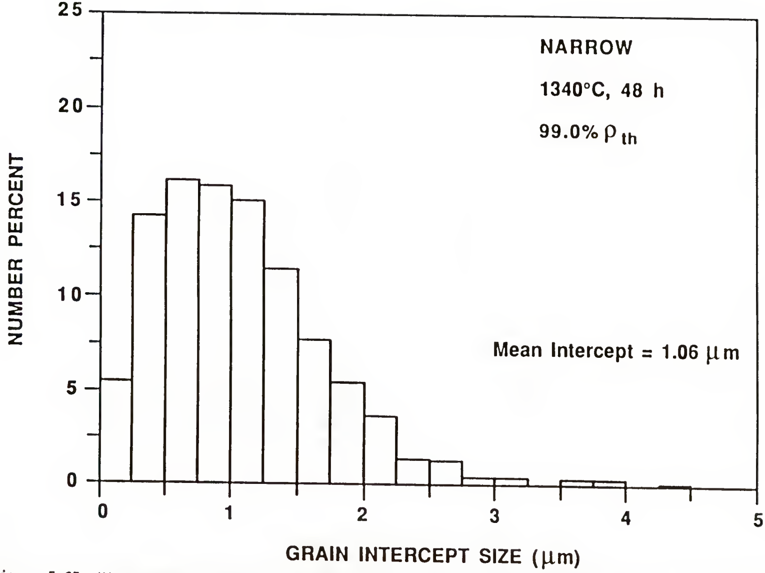

Figure 5.65 Histogram plot of the grain intercept size distribution for the NSD-30 sample sintered at 1340°C, 48 h to 99.0% relative density.

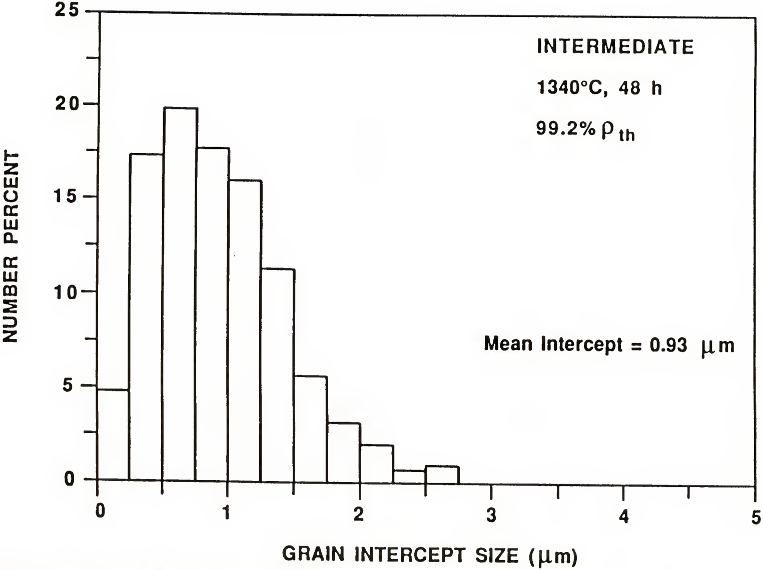

Figure 5.66 Histogram plot of the grain intercept size distribution for the ISD sample sintered at 1340°C, 48 h to 99.2% relative density.

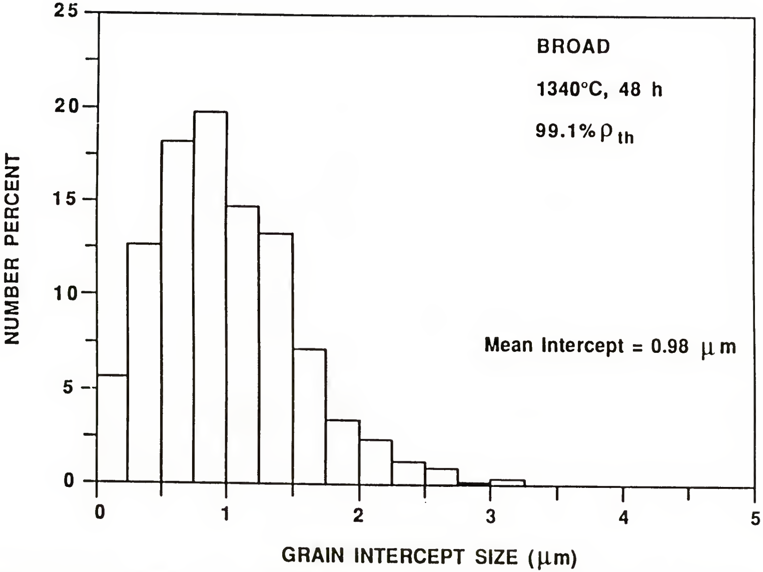

Figure 5.67 Histogram plot of the grain intercept size distribution for the BSD sample sintered at 1340°C, 48 h to 99.1% relative density.

of samples prepared from powders having various particle size distributions become similar if the initial powders have similar average sizes.

Despite the careful preparation of the powders and green bodies used in the present study, in the microscopic point of view, the powder compacts still contain localized packing inhomogeneities and packing density gradients*. Although these heterogeneities are considerably less severe than observed in compacts prepared by more conventional processing routes, they still have an important influence on the sintering behavior and microstructure evolution. It is well known that regions in a powder compact with the highest packing density undergo the most rapid densification (i.e., pore volume reduction) during sintering [Lan84, Sac82, Sac84]. Grain growth occurs more readily in these regions due to the elimination of the pore drag force on grain boundaries. Since different regions of the sample undergo different rates of grain growth, there is a tendency for the grain size distribution to broaden during the sintering process for samples prepared from powders with narrower size distributions.

In addition, depending on the orientation and the mismatch angle of a grain boundary, the grain boundary energy become different. This can result in a significant difference in the migration speed of the grain boundary. Therefore, some grains can grow while their neighbor grains were "consumed" and decrease in size. This process can also result in the broadening of the grain size distribution. This was demonstrated in a theoretical study by Grest et al. [Gre85] in which a Monte Carlo computer simulation of the effect of anisotropic grain boundary energy on grain growth was reported. In the present study, the NSD-30 and ISD samples (especially the NSD-30 sample) undergo more broadening of the grain size distribution during sintering. This is evident from the fact that the final grain size distributions are similar despite the difference in the initial particle size distributions.

---

* Microstructural heterogeneities can be due to the imperfections in sample preparation or simply due to the statistical fluctuation. Only "perfect" ordered packing can produce a homogeneous particle compact with uniform pore size and particle coordination number. However, it is impossible to achieve. Even atomic packing contains packing defects. For a random closed-packing, local packing density gradient always exists.

It has been discussed in Chapter IV that the geometric standard deviation (σ_g) of the grain intercept size distribution approached stable range of values (1.8 - 2.0) as the grain growth proceeded during sintering. The same stable range of values for the σ_g were also observed for the NSD-30, ISD, and BSD samples even though these samples had significant differences in σ_g for their initial particle size distributions. Plots of σ_g of the grain intercept size distribution vs. relative density for the NSD-30, ISD, and BSD samples are shown in Figure 5.68. The σ_g of the BSD sample remained at the stable range of values over the entire density range. For relative densities less than ~90% (i.e., before the onset of grain growth), the σ_g for the NSd-30 and ISD samples were also relatively constant. It is not surprising that the NSD-30 sample had the smallest σ_g (~1.45) and the ISD sample had intermediate σ_g value (~1.6) which were consistent to the σ_g values of the particle size distribution of each powder. As the relative density increased to higher than ~90% (i.e., grain growth started), the σ_g's of the ISD and NSD-30 samples began to increase and approached the stable range of values (i.e., ~ 1.8 - 2.0).

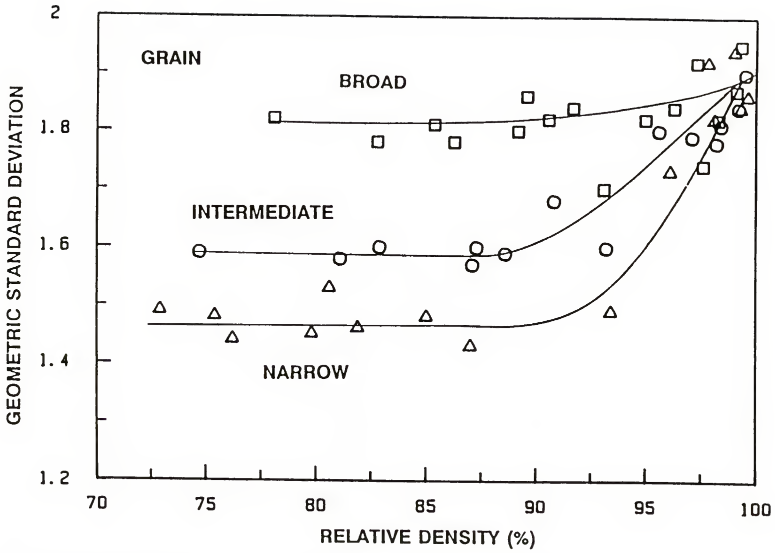

Figure 5.68 Plots of geometric standard deviation of grain intercept size distribution vs. relative density for the NSD-30, ISD, and BSD samples.

The effect of grain growth on the σ_g of the grain intercept size distribution can be clearly seen in the plots of the σ_g of the grain intercept size distribution vs. grain intercept size as shown in Figure 5.69. For the BSD sample, a relatively constant σ_g was observed over the entire grain intercept size range. On the other hand, the σ_g's were about 1.6 and 1.45 for the ISD and NSD-30 samples, respectively, before the onset of grain growth. After the grain growth began, the σ_g's of the ISD and NSD-30 samples rapidly increased to the stable range of values.

In order to further confirm the existence of a stable range of values for the σ_g of the grain intercept size distribution, intercept size measurements were carried out on samples sintered at 1450°C for 48 h where significant grain growth occurred. The BSD, ISD, and NSD samples had similar grain intercept size (~2.3 μm). The σ_g of each sample was still in the range 1.8 to 2.0 (i.e., 1.95, 1.89 and 1.86 for the BSD, ISD, and NSD-30 samples, respectively).

As mentioned in Chapter IV, σ_g value shows the width of a grain intercept size distribution plotted on the logarithmic scale. From the above discussion, it is clear that a broadening of the grain intercept size distribution (in log scale) was obtained for the NSD-30 and ISD samples after the onset of grain growth. Relative constant σ_g values were obtained as the grain intercept sizes were > 0.5 μm. This indicates that a similar distribution function will be obtained if each size distribution is normalized with respect to its mean size (i.e., each grain intercept size is divided by the mean size).

Plots of arithmetic standard deviation (σ_a) of grain intercept size distribution vs. grain intercept size for the NSD-30, ISD, and BSD samples are shown in Figure 5.70. Before the onset of grain growth, the

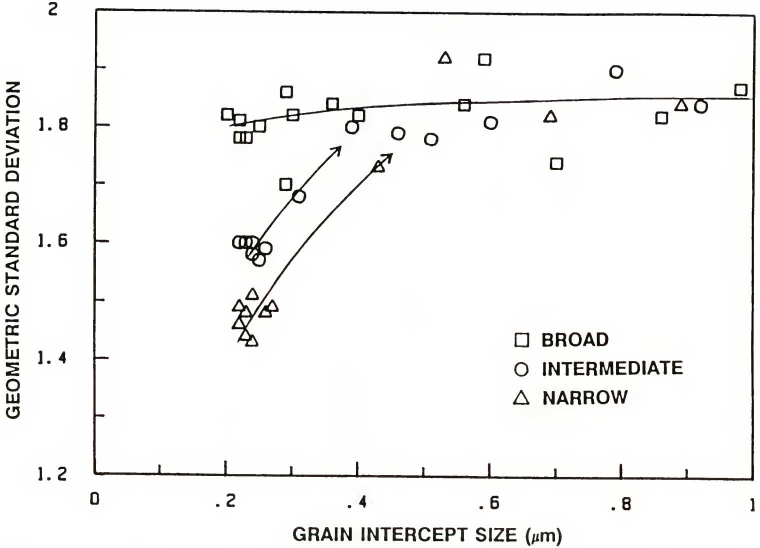

Figure 5.69 Plots of geometric standard deviation of grain intercept size distribution vs. grain intercept size for the NSD-30, ISD, and BSD samples.

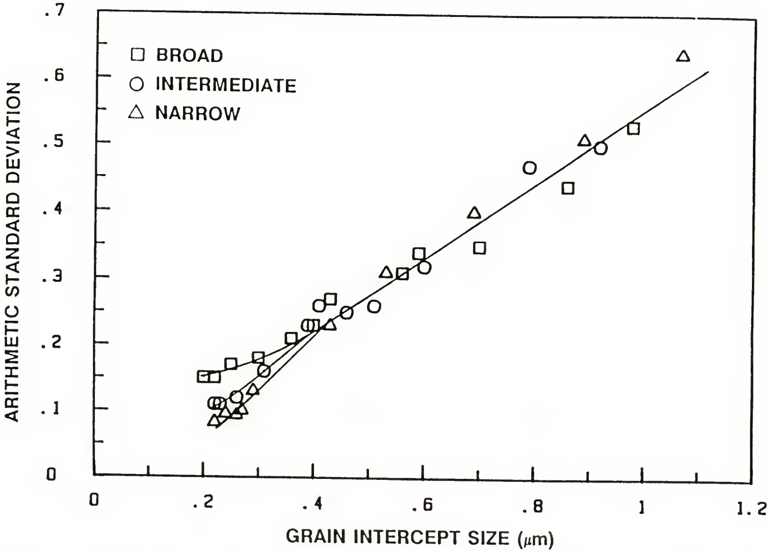

Figure 5.70 Plots of arithmetic standard deviation of grain intercept size distribution vs. grain intercept size for the NSD-30, ISD, and BSD samples.

BSD samples had the highest σ_a values and the NSD-30 samples had the lowest σ_a values. These results are consistent with the widths of the particle size distributions of the starting powders. The differences between the σ_a values decreased as the grain growth proceeded. For grain intercept size > 0.5 μm, a common linear relation between σ_a and grain intercept size was obtained for all samples. The above trend can be more clearly seen in Figure 5.71 in which plots of the ratio of σ_a of grain intercept size distribution to mean intercept size vs. grain intercept size for the NSD-30, ISD, and BSD samples are shown. The ratios of σ_a to grain intercept size were ~0.35-0.4 and ~0.45-0.5 for the NSD-30 and ISD samples, respectively, before the onset of grain growth. After the grain growth began, the ratios for the NSD-30 and ISD samples rapidly increased. A stable range of values (~0.5 to 0.6) for the ratio of σ_a to grain intercept size were obtained for all samples with intercept size >0.5 μm. This is consistent with the results in geometric standard deviation (Figure 5.69). However, higher ratio of σ_a to mean intercept size was observed for the BSD samples at grain intercept size < 0.25 μm. Higher ratio suggested that the normalized grain intercept size distributions for the BSD samples were initially broader. This may be due to the larger percentage of fine intercept size (Figures 5.57 to 5.59). After the onset of grain growth (i.e., >90% relative density), fine particles were more rapidly eliminated (Figures 5.59 and 5.60). This resulted in an increase of grain intercept size and decrease of the ratio of σ_a to grain intercept size (i.e., the width of the normalized grain intercept size distribution). However, the above trend was not observed in Figure 5.69.

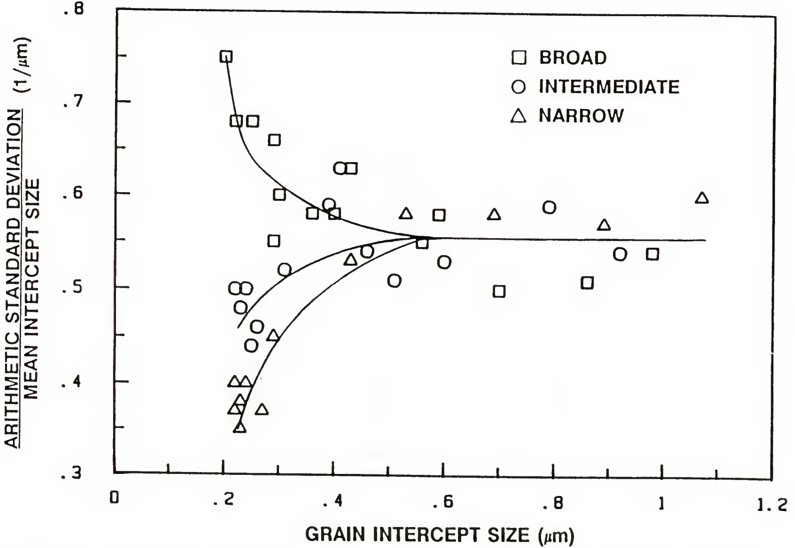

Figure 5.71 Plots of the ratio of arithmetic standard deviation of grain intercept size distribution to mean intercept size vs. grain intercept size for the the NSD-30, ISD, and BSD samples.

Figure 5.72 shows plots of the ratio of σ_a of grain intercept size distribution to mean intercept size vs. relative density for the NSD-30, ISD, and BSD samples. The trend in the broadening of normalized grain intercept size distribution for the NSD-30 and ISD samples are consistent with the results in geometric standard deviation (Figure 5.68). However, as discussed previously, a slightly higher ratio of σ_a to grain intercept size was observed for the BSD sample in the early stages of sintering.

From the grain intercept size distribution results in Chapters IV and V, it is clear that the σ_g and the ratio of σ_a to grain intercept size rapidly approach a relative constant value (i.e., ~ 1.8 - 2.0 for σ_g and ~ 0.5 - 0.65 for the ratio of σ_a to grain intercept size) after the onset of grain growth. The σ_g and the ratio of σ_a to grain intercept size remain relative constant when the grain growth proceeds. This indicates that when the grain intercept size distributions are plotted on either a linear scale or log scale, a relatively constant distribution function is observed if the grain intercept size is normalized with respect to the mean size. This result is consistent with the assumption adopted in most models of normal grain growth [Atk88, Fel57, Hil65, Kur80a] and is also widely observed for metals [And85, Fel57, Hu74] and ceramics [Abo69, Car78b, Kur80b]. Recently, Sroloritz et al. reported an extensive study on the Monte Carlo computer simulation of grain growth [And85, Gre85, Sro83, Sro84a, Sro84b, Sro85]. They also showed that the grain size distribution function is time invariant when the grain size is normalized by the mean size. They found that "the normal grain size distribution is very robust and strongly resistant to perturbations" [Sro85]. Similar size distribution functions

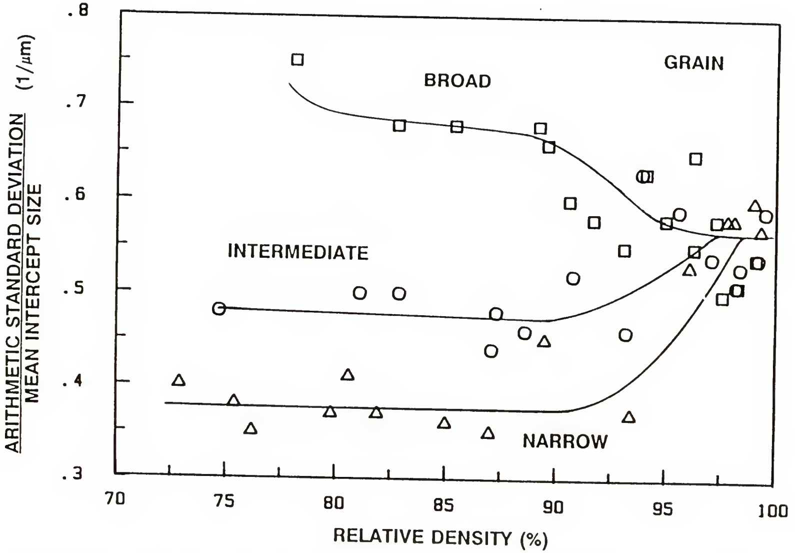

Figure 5.72 Plots of the ratio of arithmetic standard deviation of grain intercept size distribution to mean intercept size vs. relative density for the NSD-30, ISD, and BSD samples.

were obtained even though abnormally large grains were introduced initially [Sro85]. This is consistent with the present results for the BSD samples. They also showed that the derived grain size distribution functions were dependent upon the degree of anisotropy of grain boundary energy [Gre85]. The distribution function became broader as the anisotropy was increased. For the present study, the normalized grain intercept size distributions of those samples which had reached the stable distribution showed a very good fit with the distribution function developed by Monte Carlo procedure. This is demonstrated in Figures 5.73 where the normalized grain intercept size distributions for NSD-30, ISD, and BSD samples sintered at 1340°C for 48 h are compared with the distribution function obtained by Monte Carlo simulation for the case that the grain boundary energy had a moderate anisotropy* [Gre85]. This is reasonable because alumina is known to have anisotropical grain boundary energy.

It should be noted that homogeneous, equiaxed grains (without exaggerated grain growth) were obtained in the present study. If the exaggerated grain growth does occur, it is possible to obtain larger values on the σ_g and the ratio of σ_a to mean intercept size. In fact, slightly larger values on the σ_g and the ratio of σ_a to mean intercept size were obtained for the DPL sample which was sintered at high temperature (e.g., 1600°C, 48 h) and had extremely heterogeneous microstructure.

---

* The grain size distribution function obtained by Monte Carlo simulation was derived for the case that the grain boundary energy was described by Read-Shockley potential and the anisotropy parameter was 0.6π [Gre85].

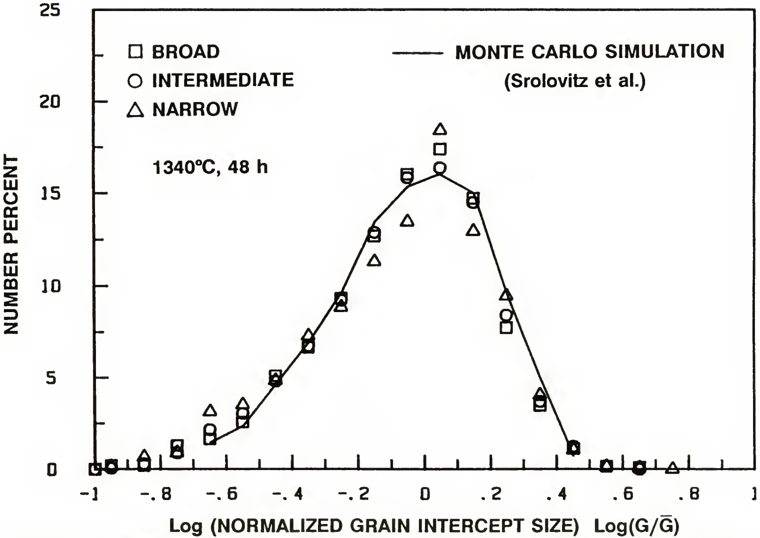

Figure 5.73 Normalized grain intercept size distribution plotted in log scale for the NSD-30, ISD, and BSD samples sintered at 1340°C, for 48 h. For comparison, plot of normalized grain size distribution from Monte Carlo simulation [Gre85] is also shown.

Pore intercept size and size distribution. Plots of the pore intercept size vs. relative density for the NSD-30, ISD, and BSD samples are shown in Figure 5.74. Similar to the SCD sample in Chapter IV, the pore intercept size distribution of the NSD-30 sample also remained relatively constant over the entire density range. However, the BSD sample, and to a lesser extent the ISD sample, showed finer pore intercept size in the early stages of sintering. This is consistent with the mercury porosimetry results for the green compacts. As the densification proceeded, an increase in the average pore intercept size for the BSD and ISD samples was observed. This was due to the more rapid removal of fine size pores which had higher driving force for densification. The increase in pore intercept sizes also explained the more rapid decrease in densification rates for the BSD and ISD samples.

Histograms of pore intercept size distribution for the NSD-30, ISD, and BSD samples are shown in Figures 5.75 to 5.87. The pore intercept size distributions of the NSD-30 samples remained relatively unchanged over the entire density range (Figures 5.75 to 5.79). For the BSD sample, initially, significantly large percentage of fine intercepts was observed (Figure 5.84). As discussed previously, due to the large amounts of fine-sized particles, more efficient packing, and higher packing density, the BSD sample had significantly large quantities of fine-sized pores. In Figures 5.84 and 5.85, it is also shown that the BSD samples had smaller percentage of large pores and the maximum size of large pores was also smaller. This is partly due to the fact that the BSD sample had higher packing density which decreased the probability of forming large pores. This was confirmed in the SEM photographs in Figures 5.36 and 5.37. Another factor which contributed to this

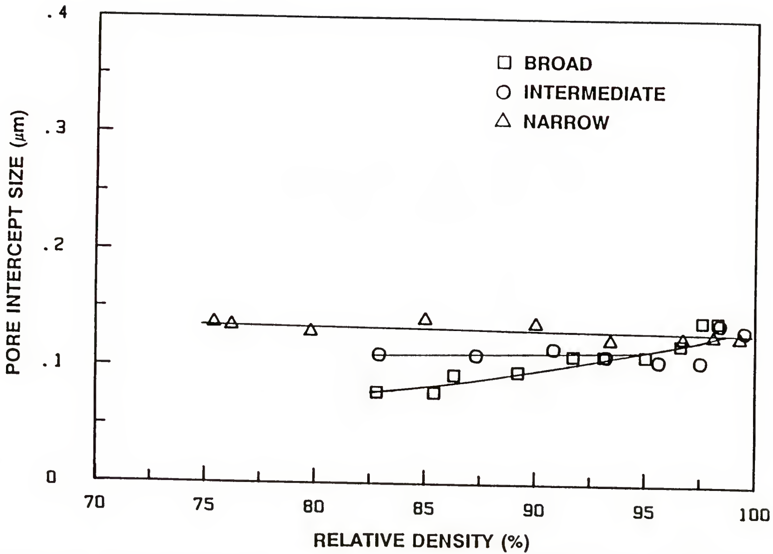

Figure 5.74 Plots of average pore intercept size vs. relative density for the NSD-30, ISD, and BSD samples.

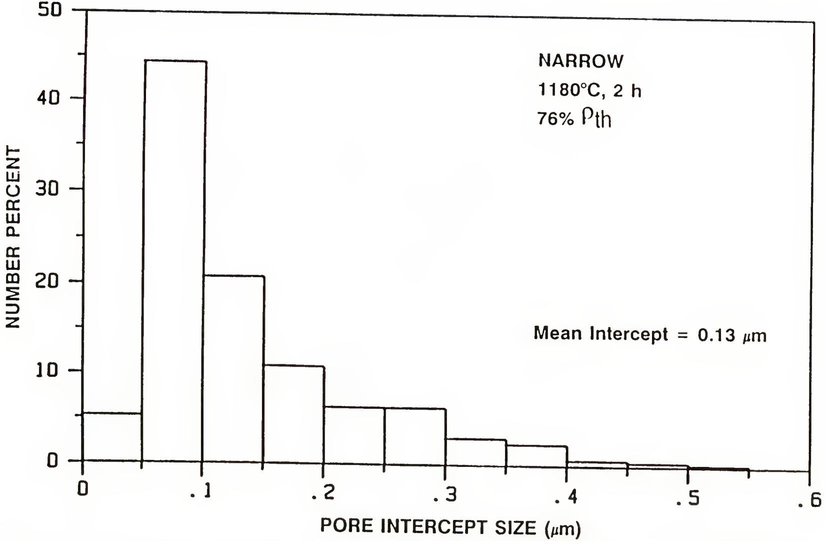

Figure 5.75 Histogram plot of the pore intercept size distribution for the NSD-30 sample sintered at 1180°C, 2 h to 76.2% relative density.

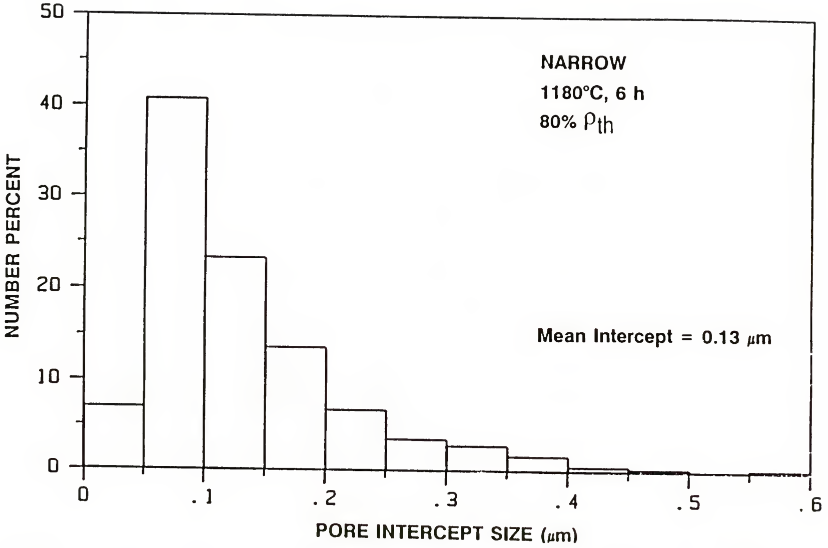

Figure 5.76 Histogram plot of the pore intercept size distribution for the NSD-30 sample sintered at 1180°C, 6 h to 79.8% relative density.

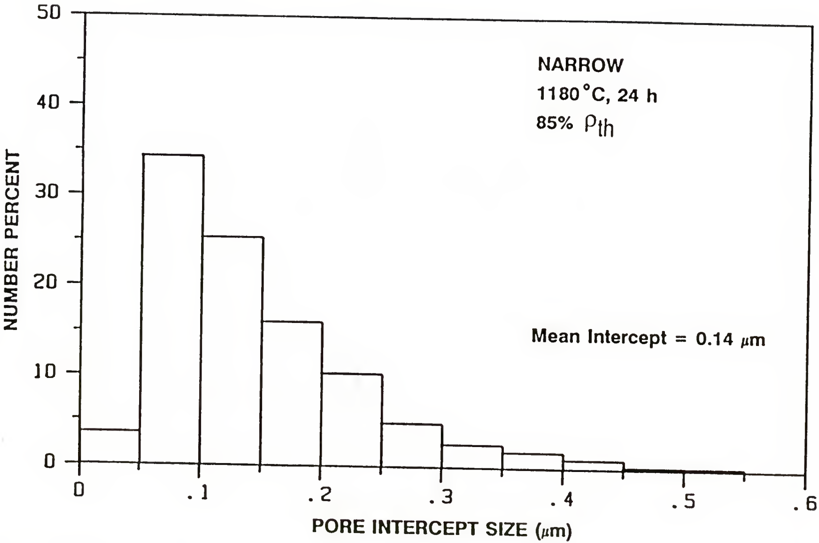

Figure 5.77 Histogram plot of the pore intercept size distribution for the NSD-30 sample sintered at 1180°C, 24 h to 85.0% relative density.

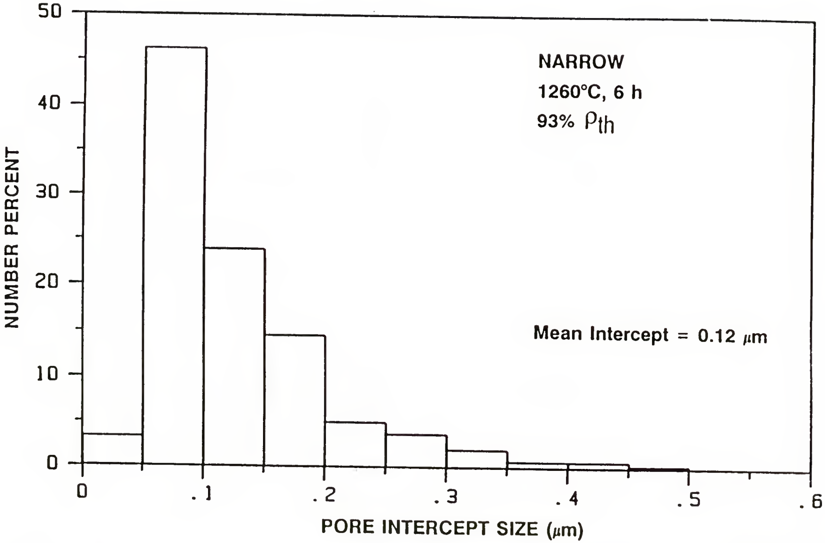

Figure 5.78 Histogram plot of the pore intercept size distribution for the NSD-30 sample sintered at 1260°C, 6 h to 93.4% relative density.

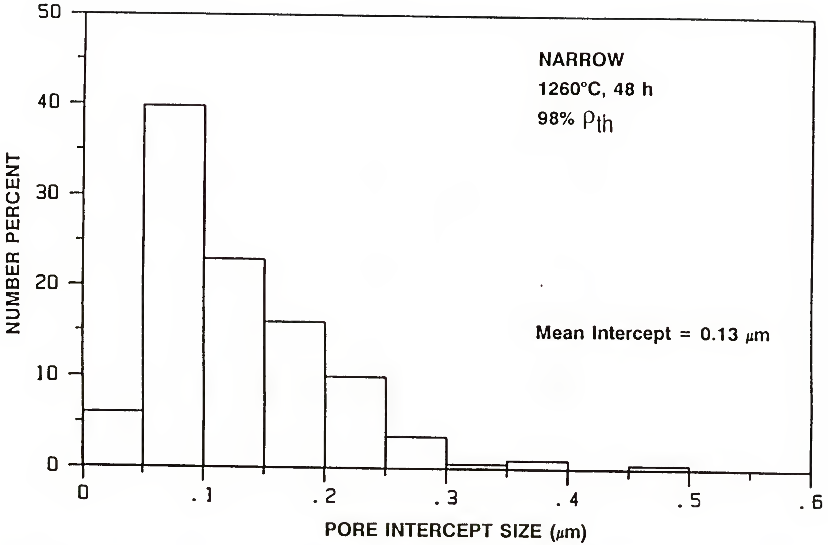

Figure 5.79 Histogram plot of the pore intercept size distribution for the NSD-30 sample sintered at 1260°C, 48 h to 98.1% relative density.

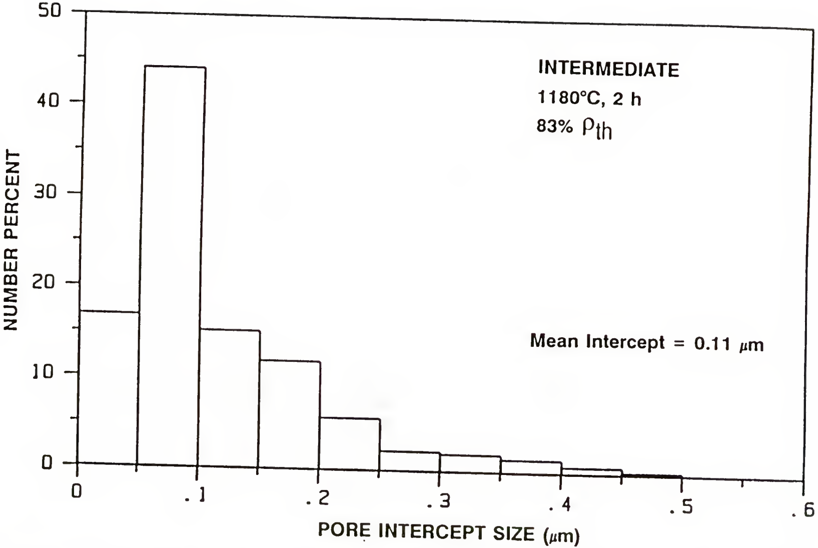

Figure 5.80 Histogram plot of the pore intercept size distribution for the ISD sample sintered at 1180°C, 2 h to 82.9% relative density.

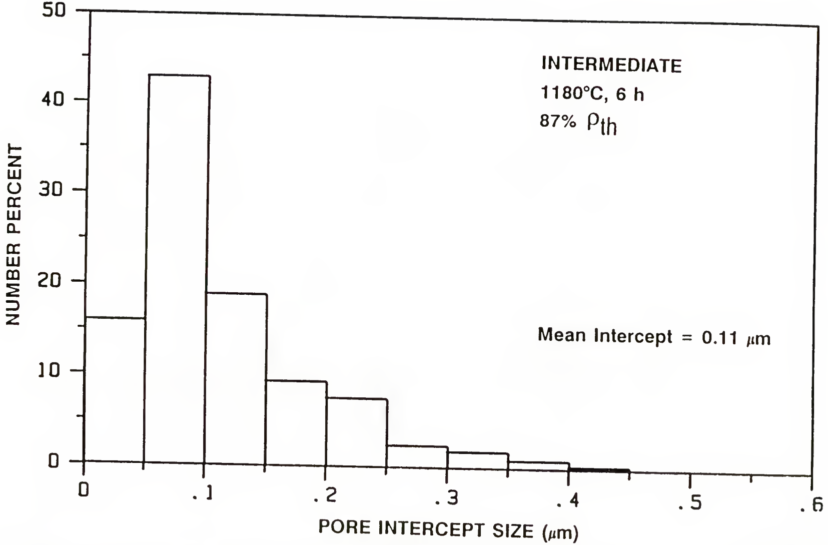

Figure 5.81 Histogram plot of the pore intercept size distribution for the ISD sample sintered at 1180°C, 6 h to 87.3% relative density.

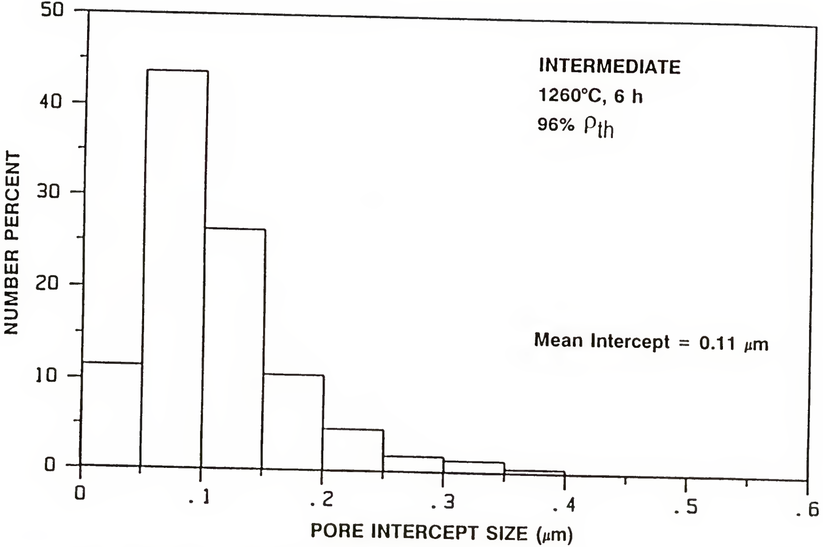

Figure 5.82 Histogram plot of the pore intercept size distribution for the ISD sample sintered at 1260°C, 6 h to 95.6% relative density.

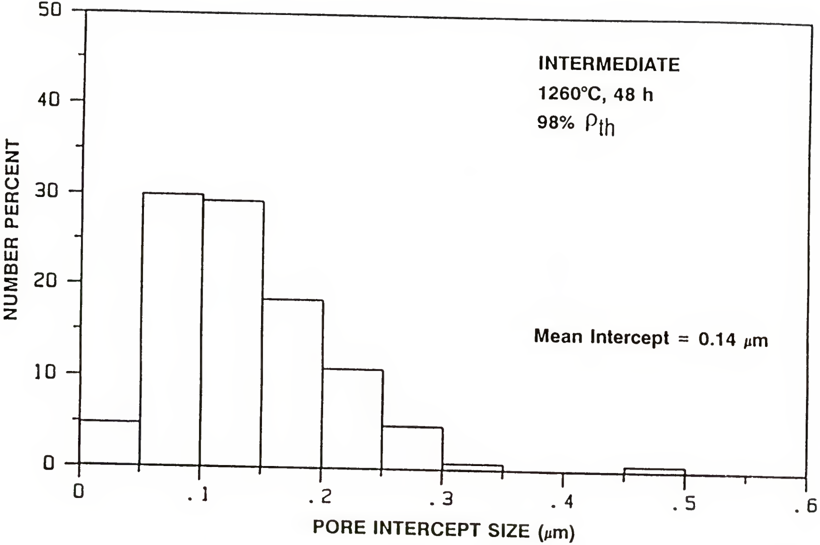

Figure 5.83 Histogram plot of the pore intercept size distribution for the ISD sample sintered at 1260°C, 48 h to 98.4% relative density.

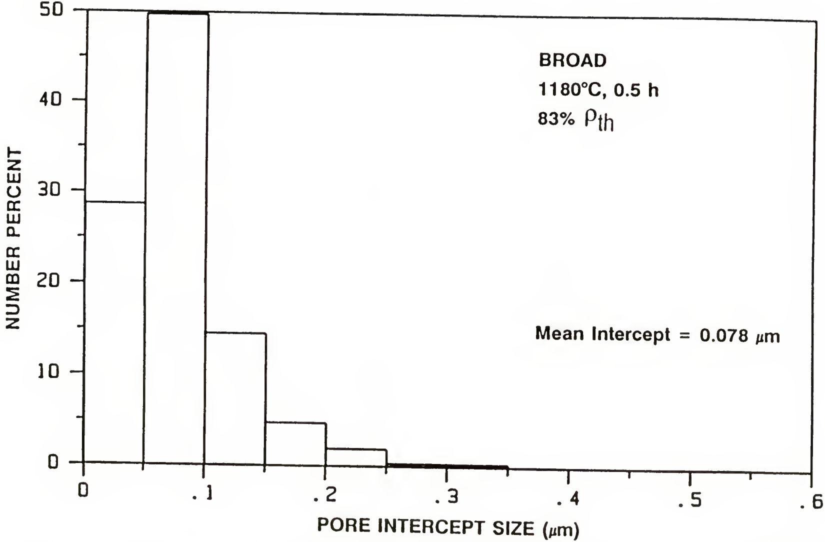

Figure 5.84 Histogram plot of the pore intercept size distribution for the BSD sample sintered at 1180°C, 0.5 h to 82.8% relative density.

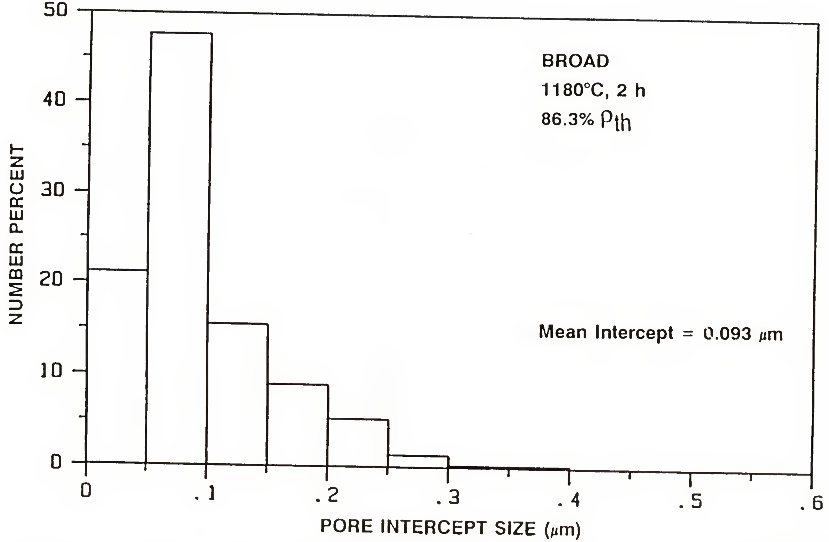

Figure 5.85 Histogram plot of the pore intercept size distribution for the BSD sample sintered at 1180°C, 2 h to 86.3% relative density.

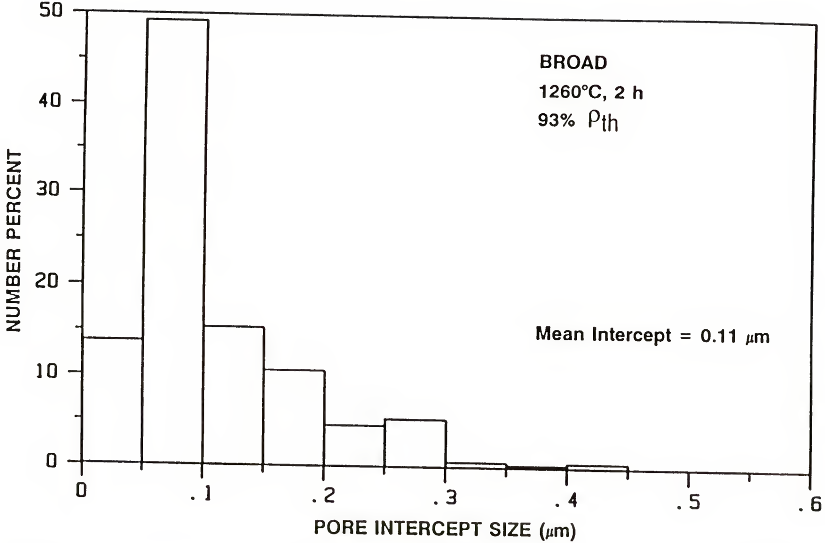

Figure 5.86 Histogram plot of the pore intercept size distribution for the BSD sample sintered at 1260°C, 2 h to 93.1% relative density.

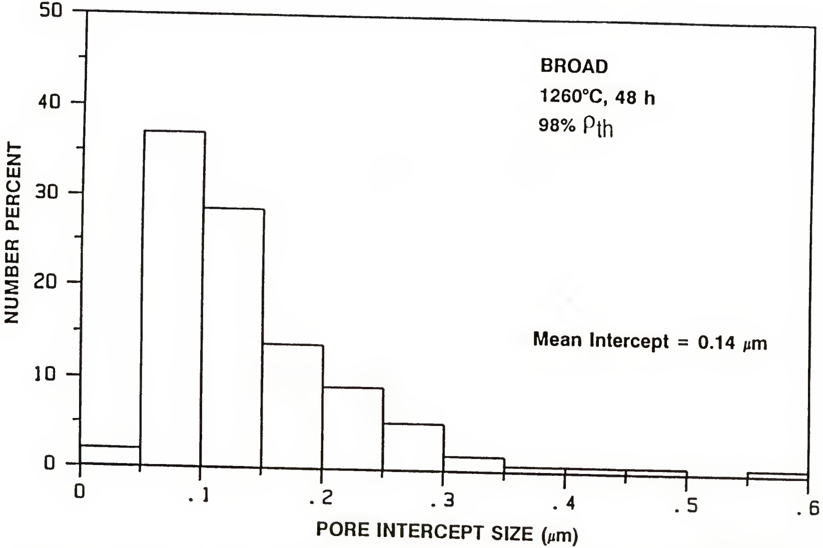

Figure 5.87 Histogram plot of the pore intercept size distribution for the BSD sample sintered at 1260°C, 48 h to 97.6% relative density.

observation is that the BSD sample had significantly large numbers of fine-sized pores; therefore, the number percentage of large pores became very small. Because the fine-sized pores were much easier to be removed, the percentage of fine intercepts rapidly decreased as the densification proceeded (Figures 5.85 to 5.87). On the other hand, the number percentage of large pores became more significant and started to show up in the pore intercept size histograms of high density samples (Figures 5.86 and 5.87). This also resulted in the increase of average pore intercept size as shown in Figure 5.74. The pore intercept size and pore intercept size distributions of the BSD sample approached that of the NSD-30 sample in the high density range. The ISD sample showed a similar trend, but less in extent, as that of the BSD samples. Therefore, all samples showed similar pore intercept size distribution at ~98% relative density (Figures 5.79, 5.83, and 5.87).

The geometric standard deviations (σ_g) of pore intercept size distributions are plotted as a function of relative density for the NSD-30, ISD, and BSD samples in Figure 5.88. Similar and relatively constant σ_g values (~ 1.6 to 1.8) were obtained for each sample over the entire density range. However, slightly lower σ_g values were observed for samples with > 95% relative density. This suggested that the width of the normalized pore intercept size distribution when plotted in log scale became slightly narrower in the closed pore stages.

Plots of σ_a of pore intercept size distribution vs. relative density for the NSD-30, ISD, and BSD samples are shown in Figure 5.89. For relative density < 95%, the highest σ_a values were obtained for the NSD-30 samples and lowest σ_a values were obtained for the BSD samples. However, in this density range, the NSD-30 samples also had highest pore

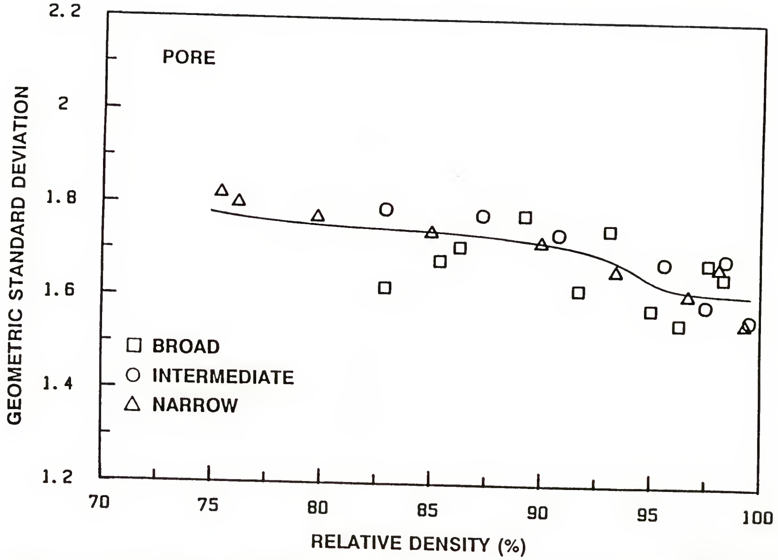

Figure 5.88 Plots of geometric standard deviation of pore intercept size distribution vs. relative density for the NSD-30, ISD, and BSD samples.

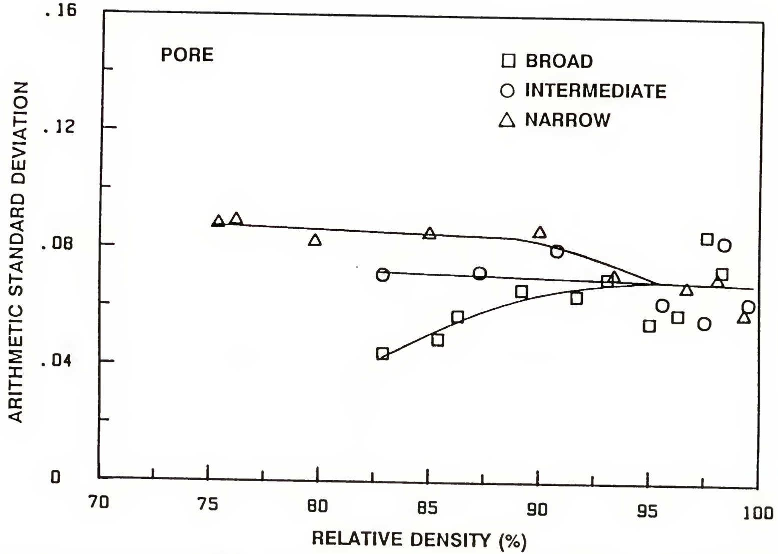

Figure 5.89 Plots of arithmetic standard deviation of pore intercept size distribution vs. relative density for the NSD-30, ISD, and BSD samples.

intercept sizes and the BSD samples had the lowest. Therefore, similar ratio of σ_a of pore intercept distribution to mean intercept size were obtained for each sample as shown in Figure 5.90. A relatively constant ratio of σ_a to mean pore intercept size was observed, although the ratio decreased slightly in the closed pore stages (> 95% relative density). This also indicated that the normalized pore intercept size distribution (in linear scale) of each sample remained relatively unchanged in the open-pore stages (<95% relative density). However, the normalized pore intercept size distributions became narrower* in the closed-pore stages (>95% relative density). This is consistent with the σ_g results in Figure 5.88.

Pore-solid interfacial area (surface area). Plots of specific pore-solid interfacial area vs. relative density for the NSD-30, ISD, and BSD samples are shown in Figures 5.91 and 5.92 where solid symbols denote values determined by BET method and open symbols denote values obtained by quantitative stereological measurements. Comparing at a constant density, higher specific pore-solid interfacial area was obtained as the width of the particle size distribution of the sample was increased. This is consistent with the observed finer pore intercept sizes for samples prepared from broader size distribution powders.

In the high density regions where the pore-solid interfacial areas were determined by stereological methods (Figure 5.92), linear relationships between interfacial area and density were observed.

---

* In the pore intercept size histograms of the BSD sample (Figures 5.84 to 5.87), it seems that the pore intercept size distribution (in linear scale) became broader in the high density range. However, in the same time, the mean intercept size also increased significantly. Therefore, the normalized pore intercept size distributions (with respect to the mean size) became narrower.

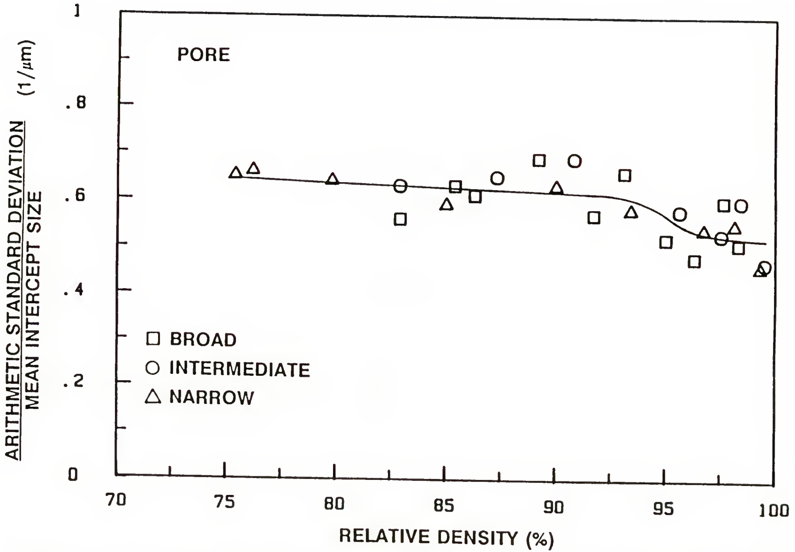

Figure 5.90 Plots of the ratio of arithmetic standard deviation of pore intercept size distribution to mean pore intercept size vs. relative density for the NSD-30, ISD, and BSD samples.

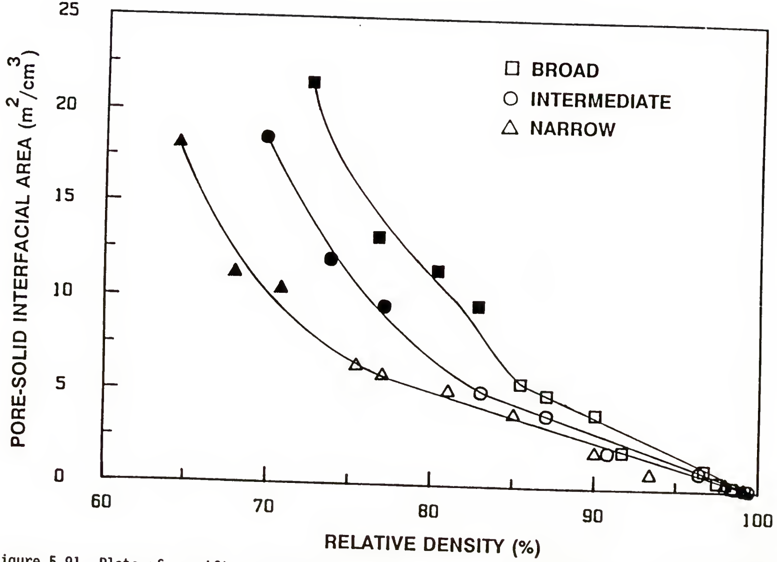

Figure 5.91 Plots of specific pore-solid interfacial area determined by quantitative stereology (open symbols) and surface area determined by BET method (solid symbols) vs. relative density for the NSD-30, ISD, and BSD samples.

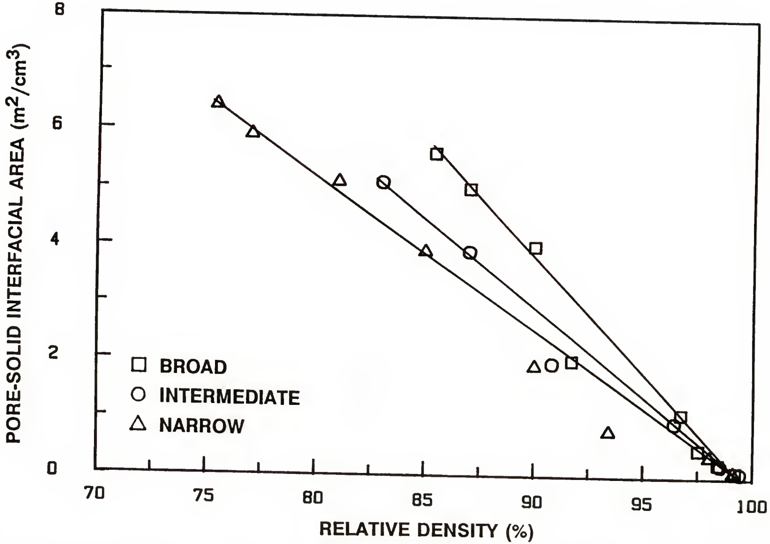

Figure 5.92 Plot of specific pore-solid interfacial area determined by quantitative stereology vs. relative density for the NSD-30, ISD, and BSD samples in expanded scale.

According to DeHoff et al. [DeH66], this linear relationship indicates a constant pore intercept. This was observed for the NSD-30 sample; however, increases in pore intercept size were observed for the ISD and BSD samples (Figure 5.74). Furthermore, each curve appeared to show a "dip" (sharper decrease) around 90 to 95% relative density. In the same density range, the interconnected pore channels started to pinch off and formed closed pores (Figure 5.61) which have more round geometry. At a constant volume, the spherical geometry has the smallest surface area. Therefore, the sharper decrease in pore-solid interfacial area may be related to the formation of closed pores.

The surface area determined by BET method for the low density samples did not follow the same linear relationship. Instead, surface area decreased at a much faster rate in the early stages of sintering. According to Burke's proposition [Bur80], this phenomena represent larger ratio of coarsening to densification rate. However, grain size measurement carried out in these density ranges showed that no significant grain growth was observed. The decrease of surface area in the early stages of sintering should be associated with surface rounding, neck formation and densification of fine particles. These processes could significantly reduce the surface area with relatively little increase in density and little change in grain size. Because the low density samples used for BET measurement were sintered at low temperatures (i.e., 1100 and 1180°C), surface diffusion which is more significant at low sintering temperature may play a more important role in these samples. This can also contribute to the more rapid reduction of surface area.

Effect of Particle Size on Sintering and Microstructural Evolution

Surface curvatures which determine the magnitude of the driving forces for densification are inversely proportional to particle size. The distance of mass transport during sintering is also closely related to particle size. Herring was the first to propose scaling laws [Her50]

$$\frac{t_2}{t_1} = \left(\frac{G_2}{G_1} \right)^n$$

to describe the densification kinetic relations of two compacts with different particle size, where t is the sintering time needed to reach a given density, G is the initial particle size, and subscript 1 and 2 represent two different powders. The exponent n is determined by the densification mechanisms (e.g., n = 1 for viscous flow, n = 2 for evaporation and condensation, n = 3 for volume diffusion, n = 4 for surface diffusion or grain boundary diffusion). In order to have a proper comparison between two systems, it is required that the two samples have similar path of microstructural evolution and same sintering mechanism.

In the present study, two homogenous green compacts (i.e., NSD-30, SCD) were prepared from two narrow size distribution powders which had similar geometric standard deviations but different median sizes (~0.39μm for NSD-30 and ~0.87μm for SCD). Similar green densities were also obtained (i.e., ~64% for SCD and ~65% for NSD-30). These two samples offered the opportunity to properly examine the applicability of Herring's scaling laws. Before comparing the densification kinetics of these two samples, it is necessary to ensure that paths of microstructural evolution were similar. Figures 5.93 shows plots of normalized grain size (i.e., G/Go, where G is the grain intercept size

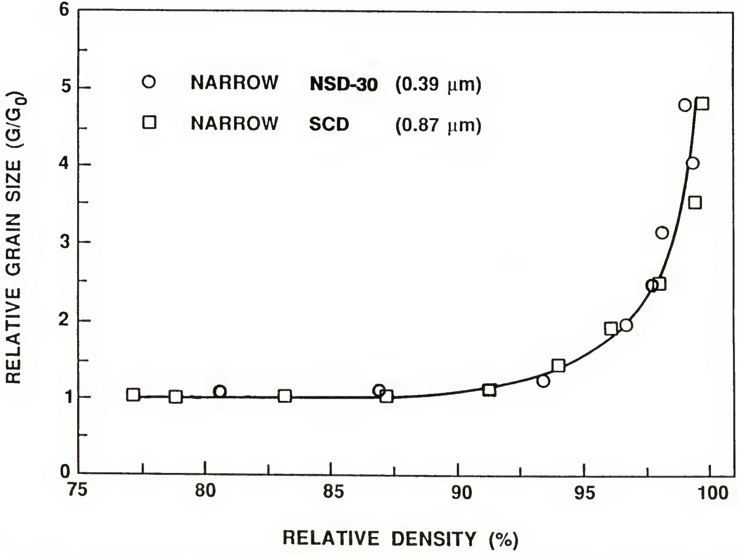

Figure 5.93 Plots of the ratio of grain intercept size to initial grain intercept size vs. relative density for the NSD-30 and SCD samples.

at each density level and Go is the initial grain intercept size before grain growth started) vs. relative density for the NSD-30 and SCD samples. Figure 5.94 shows plot of the ratio of the pore intercept size to the initial grain intercept size vs. relative density. Figure 5.95 shows plots of the ratio of the grain intercept size to the pore intercept size vs. relative density. From the above microstructural results, it is clear that both samples had very similar path of microstructural evolution*. It also suggested that both samples densified with same mass transport mechanism.

Plots of the relative density vs. sintering time at 1260°C for the SCD and NSD-30 samples are shown in Figure 5.96. It is not surprising that NSD-30 sample showed much faster densification rate due to the finer particle size. The sintering time needed for each sample to reach a given density and the values of exponent n in the scaling law are shown in Table 5.3. The exponents were found to be ~3.

Song et al. [Son84] proposed another method to derive the average value of the exponent n . They showed that if the logarithm of density increase (i.e., $\log(\rho-\rho_0)$, where ρ is the relative density at time t and ρ_0 is the relative green density) was plotted as a function of the logarithm of sintering time (log(t)), the exponent n could be calculated as follow

---

* In Figures 5.93 to 5.95, the microstructural results for the NSD-30 samples were obtained from the samples which were sintered at 1260 and 1340°C. The microstructural results for the SCD samples were obtained from samples sintered at 1300, 1340, and 1450°C. Despite the significant differences in sintering temperature, the paths of microstructural evolution still showed excellent agreement. This indicated that the surface diffusion which might be important at lower sintering temperatures (e.g., 1180°C) and smaller particle size materials (i.e., NSD-30 in this study) became less significant at higher sintering temperatures (i.e., ≥ 1260°C).

Table 5.3

Relative Density (%)	Sintering Time (h)		n
	SCD	NSD	
80	5.5	0.5	3.00
83	9	1	2.74
85	12	1.5	2.60
87	18.5	2	2.78
90	33	3.4	2.83

$$n = \frac{(I_1 - I_2) / P}{\log (G_2 / G_1)}$$

where I is the intercept of the linear curve at the y axis, P is the slope of the linear curve, G is the particle (grain) size, and subscripts 1, 2 designate two samples with different particle size. Figure 5.97 shows plots in this form and the corresponding linear equations for the NSD-30 and SCD samples*. The value of the exponent was found to be 3.0.

The value of the exponent obtained in Song's studies [Son84] was 4.7 which was significantly higher than the theoretical values for volume diffusion (n=3) or grain boundary diffusion (n=4). Several possible explanations were proposed. For example, simultaneous grain growth during densification process could significantly increase the

---

* Densification data up to ~92-93% relative density (in which the grain size still remained relative constant) were used in this plot. Significant grain growth was observed for samples with higher sintered density which may cause changes in the ratio of grain sizes. Therefore, these samples can not be used to evaluate the exponent of the scaling law.

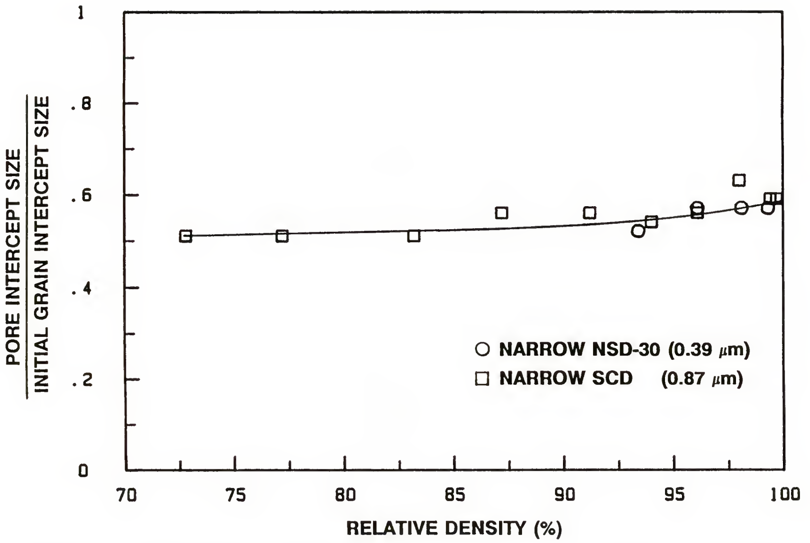

Figure 5.94 Plots of the ratio of pore intercept size to initial grain intercept size vs. relative density for the NSD-30 and SCD samples.

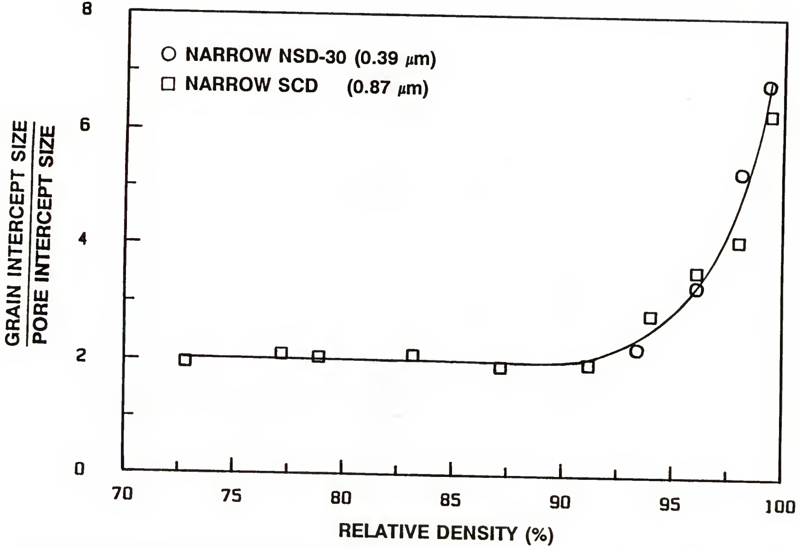

Figure 5.95 Plots of the ratio of grain intercept size to pore intercept size vs. relative density for the NSD-30 and SCD samples.

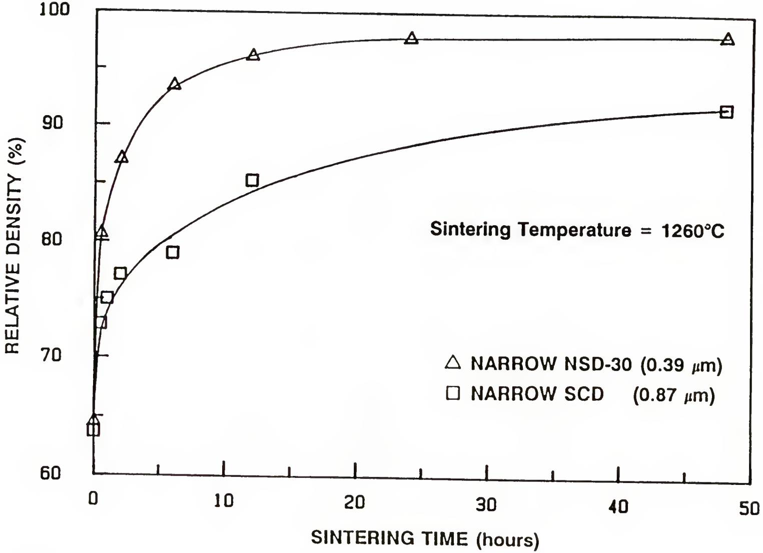

Figure 5.96 Plot of the relative density vs. sintering time at 1260°C for the NSD-30 and SCD samples.

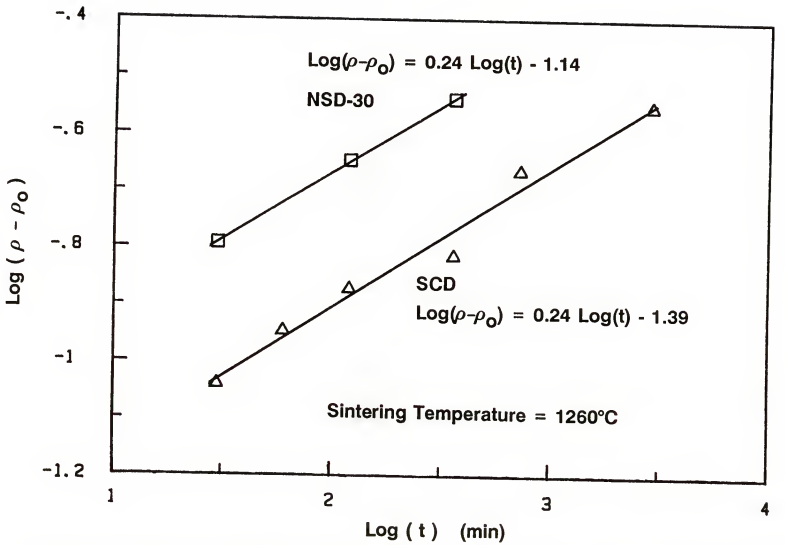

Figure 5.97 Plots of logarithm of density increase ($\log(\rho-\rho_o)$) vs. logarithm of sintering time ($\log(t)$) at 1260°C for the NSD-30 and SCD samples.

grain size ratio (e.g., grain size ratio increased from 2.5 to 4.0 in their studies) which could result in the deviation of the exponent. Due to the homogeneous green microstructure and high densification rate obtained in the present study, constant grain size was observed in the density range where Herring's scaling law was applied. This suggested that a more reliable exponent can be obtained in the present studies.

According to Herring's scaling law, n=3 indicated that the volume diffusion was the dominant mechanism for densification. The activation energies for densification and grain growth obtained in the present study (i.e., ~570-630 KJ/mole) also agreed very well with the activation energy for volume diffusion reported by other workers [Can80, Ois60, Raj73, War62]. Normally, lower activation energy (~400-500 KJ/mole [Can80, Ois60]) was observed for grain boundary diffusion. Therefore, it can be concluded that volume diffusion is the dominant mechanism for the densification of the alumina samples in the present studies.

Based on Coble's model [Cob61] and Herring's scaling law [Her50], Harmer and co-workers [Ber86, Zha87] proposed that the densification rate should be linearly related to $1/G^m$, where G is the grain size, and m is a constant. The grain size exponent m equals 3 when volume diffusion is the dominant mechanism for densification and equals 4 when grain boundary diffusion is the dominant mechanism. Berry and Harmer [Ber86] investigated the densification and grain growth kinetics of a high purity (99.99%) alumina samples. The grain size exponent obtained in their studies were ~4; therefore, they concluded that grain boundary diffusion was the dominant densification mechanism. Zhao and Harmer [Zha87] performed a similar study and showed that the grain size exponent was ~3.5. They suggested that both volume and grain boundary diffusion contributed to the densification of their samples. However, as discussed previously, a good fit with Coble's equation can not be used as a criterion to conclude that volume diffusion is the dominant mechanism for densification. Further evaluation is also needed to determine whether m=4 can be used as a criterion to conclude that grain boundary diffusion is the dominant mechanism for densification.

CHAPTER VI
LOW TEMPERATURE SINTERING OF ALUMINA

Introduction

Messing and co-workers have recently described a method for producing high relative density (~99%) α-Al_2O_3 at sintering temperatures of ~1200°C [Kum84, Kum85, Mes86]. The fabrication process involved the preparation of boehmite sol-gel samples containing small additions ($\leq$2.0 wt%) of fine (~0.1 μm) α-Al_2O_3 seed particles. The α-Al_2O_3 particles acted as nucleation sites for the θ- to α-Al_2O_3 phase transformation, resulting in a significant enhancement of the transformation kinetics. Furthermore, the microstructure after the transformation consisted of relatively aggregate-free, fine-grained α-Al_2O_3 and sintering occurred at much lower temperatures compared to unseeded sol-gel samples. However, it was reported that preparation of boehmite sol-gel monoliths was difficult; gels undergo large shrinkages during drying and cracking tends to occur. In this chapter, it is shown that high relative density (>99%) α-Al_2O_3 can be produced at temperatures <1200°C by controlled suspension processing of α-Al_2O_3. Shrinkage during drying and sintering is considerably reduced compared to the boehmite sol-gel process.

Results and Discussion

Powder Characterization

The volume-basis median particle size determined by the centrifugal photosedimentation method for the CSD sample was 0.10 μm.

The particle size distribution histogram is shown in Figure 6.1. It should be noted that the maximum particle size obtained was only 0.2 µm. When the data is transformed to a number basis, the median diameter is 0.07 µm. The number-basis average diameter determined from SEM measurements was 0.06 µm. The powder specific surface area was 23.8 m^2/g which gives an equivalent surface area diameter of 0.06 µm. The good agreement between the equivalent surface area diameter and the other particle diameters indicates that the powder is essentially aggregate-free.

X-ray diffraction shows that the powder is predominantly alpha alumina (α-Al_2O_3), although a trace amount of theta alumina (θ-Al_2O_3) was detected [PDFa]. (The amount was estimated to be ~1% or less. The most intense θ-Al_2O_3 peaks were approximately the same height as those α-Al_2O_3 peaks having intensities of 1% or less of the most intense alpha peak [PDFb].)

Suspension Characterization

Electrophoresis measurements on a sample with pH ≈ 4 and 3.2×10^{-3} M KCl gave an average mobility of 3.9×10^{-4} $cm^2s^{-1}V^{-1}$. In order to calculate the zeta potential from the mobility, the value of ka need to be determined, where k is the Debye-Hückel parameter and a is the particle radius. Since the ionic strength was known, the value of k was determined readily (1.9×10^6 cm^{-1}). Two different particle radii were used in the zeta potential calculation: the volume-basis median radius from the centrifugal photosedimentation measurement (0.05 µm) and the number-basis average radius from the microscopy measurement (0.03 µm). Both radii were used in order to provide an upper and lower limit for

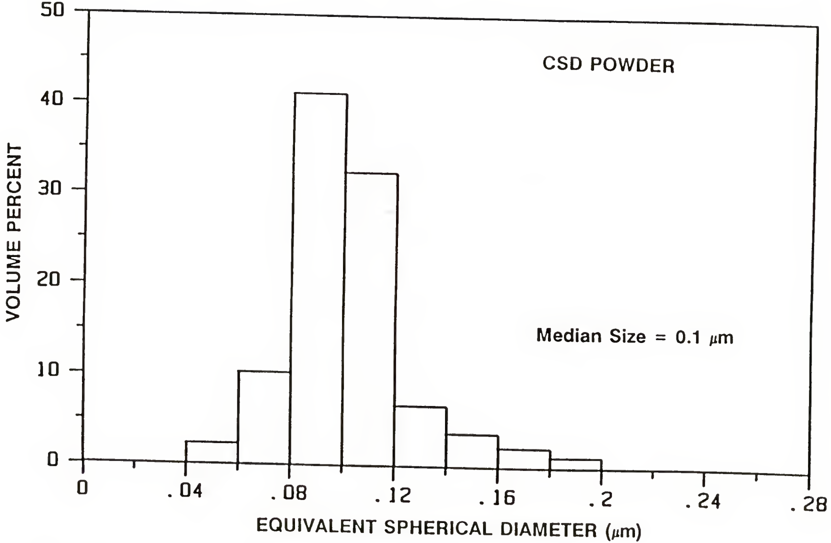

Figure 6.1 Histogram plot of the particle size distribution determined by centrifugal photosedimentation method for the CSD powders.

the calculations. Thus, the ka values used were 9.3 and 5.6, respectively. Using the treatment by Wiersema et. al. [Wie66], the calculated zeta potentials are 77 and 87 mV, respectively.

A slightly higher electrophoretic mobility (4.0×10^{-4} $cm^2s^{-1}V^{-1}$) was determined for a suspension with no KCl addition. The Debye-Hückel parameter was crudely estimated by assuming that the ionic strength was controlled by the nitric acid addition which was used to adjust the pH. (This approach neglects other ions of unknown concentration, such as aluminum-bearing ions that result from the limited solubility of the Al_2O_3 particles in water at pH ≈ 4. Therefore, the calculated zeta potentials probably are overestimates.) Based on a nitric acid concentration of ~3×10^{-4} M, the ka values for the two particle radii estimates (0.05 and 0.03 μm) are 2.8 and 1.7, respectively. This gives zeta potentials of 103 and 100 mV, respectively.

Figure 6.2 shows a plot of viscosity vs. shear rate for a suspension prepared at pH ≈ 4 with ~38 vol% of the CSD powder. The suspension shows shear thinning behavior, i.e. the viscosity decreases with increasing shear rate. Although this behavior can often be attributed to particle flocculation [Sac86, Sac87], alternative explanations must be considered in this case because the electrokinetic results indicate that the suspension should be well-dispersed. The high zeta potential and moderate ionic strength in this suspension result in relatively strong repulsive forces between the particles. For example, DLVO [Ove52] pair potential calculations give repulsive energy maxima in the range 38-106 kT. (In these calculations, the effective Hamaker constant for Al_2O_3 in water was assumed to be 4×10^{-20} J [Vis72]. Calculations were made using the various zeta potentials (77-103 mV) and

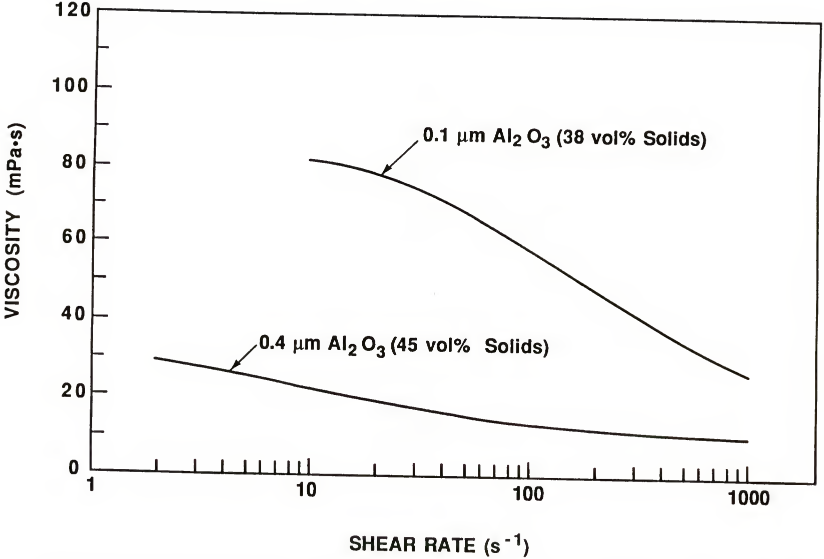

Figure 6.2 Plots of viscosity vs. shear rate for suspensions prepared with the indicated solids concentration and particle size of Al_2O_3.

ka values (1.7-9.3) discussed earlier for suspensions with and without KCl additions. It should be emphasized, however, that rheology and slip casting experiments were carried out using suspensions _without_ KCl, i.e. under conditions in which the interparticle repulsive force was maximized.) Another indication that the CSD suspension is well-dispersed is the observation that slip cast samples have a very high packing density (~ 69% relative density). This is discussed in more detail below in the section on green body characterization.

The shear thinning behavior in Figure 6.2 can be attributed to two phenomena that become increasingly important as the particle size decreases--Brownian motion and electroviscous effects. The effect of Brownian motion on viscosity was clearly demonstrated by Krieger et al. [Kri72, Pap70, Woo70] using "neutrally stable" suspensions of monodisperse latex particles. (In these experiments, the surface charge and ionic strength were adjusted to minimize the effects of interparticle forces on the suspension rheology.) Below ~20 vol% solids concentration, Krieger et al. [kri72, pap70] observed Newtonian flow behavior over a wide range of shear rates. At higher solids concentrations, suspensions showed shear thinning behavior with low-shear and high-shear Newtonian limits. In the present study, the CSD suspension also appears to be approaching low- and high-shear limiting viscosities (Figure 6.2), although measurements over a broader range of shear rates are needed to confirm this. In the study by Krieger et al. [Kri72, pap70], the low-shear viscosity was approximately twice the high-shear viscosity for suspensions with 50 vol% solids and ~0.15 μm particle size. The difference between the two limiting viscosity values decreased rapidly with decreasing solids loading and increasing particle size. In Figure 6.2, the viscosity for CSD suspension (with only 38 vol% solids) ranges from ~83 mPa·s at 10 s^{-1} to ~27 mPa·s at 1000 s^{-1}, i.e. an approximately threefold difference. These results indicate that the shear thinning behavior cannot be attributed entirely to the effect of Brownian motion, especially since the limiting viscosity at high-shear rate is probably much lower than the value at 1000 s^{-1}.

The other factor which accounts for the shear thinning behavior in Figure 6.2 is the second electroviscous effect [Con60]. Electroviscous effects become increasingly important as the zeta potential increases, the surface charge density increases, the ionic strength decreases, and the particle size decreases [Bro65, Kri76, Sto68]. Electroviscous contributions to the viscosity can be much larger than effects due to Brownian motion; changes in viscosity of several orders of magnitude between low and high shear rates are possible [Bro65, Kri76]. Yield stresses are also observed if the ionic strength is decreased sufficiently [Bro65, Kri76]. Based on the limited data collected in the present study, we cannot quantitatively assess the relative contributions of electroviscous effects and Brownian motion to the viscosity of the CSD suspension. This can be done in a relatively straightforward fashion, however, by following procedures described by Krieger et al. [Kri72, Woo70].

As noted earlier, Brownian motion and electroviscous contributions to the viscosity become increasing significant as the particle size decreases. Figure 6.2 also shows viscosity vs. shear rate data for the suspension prepared with 45 vol% ISD powder (~0.4 μm) as discussed in Chapter V. As expected, suspensions are less shear thinning and viscosities are much lower compared to CSD suspension. This occurs despite the higher solids loading in the ISD suspension.

The results in Figure 6.2 illustrate one of the practical problems associated with processing ultrafine particles. As the particle size decreases, it becomes increasingly difficult to prepare suspensions with high solids loading while still maintaining suitable rheological properties for processing operations (e.g. casting).* For example, suspensions with 54 vol% solids were easily prepared and slip cast using a ~0.4 μm Al_2O_3 [Sac88b]. In contrast, it is difficult to prepare castable suspensions beyond ~45 vol% with the CSD powder used in this study.

Green Body Characterization

The green density of the slip cast CSD samples prepared from well-dispersed (pH=4) suspensions was determined by two methods--mercury porosimetry and Archimedes displacement. In the latter technique, compacts had to be calcined at 500°C for 1 h in order to have sufficient handling strength for the measurement. A relative density of ~70% was obtained by the Archimedes method, while mercury porosimetry gave a value of ~69%. These high green densities are consistent with our earlier argument that the CSD suspension is well-dispersed. The values are also similar to the slip cast ISD samples (~ 70% relative density).

---

* This effect is not limited to electrostatically stabilized suspensions, such as used in the present study. In sterically stabilized systems, the ratio of the thickness of the adsorbed polymer layer to the radius of the particle tends to increase as the particle size decreases. Thus, the "effective" volume (i.e. hydrodynamic volume) fraction of solids in suspension tends to increase with decreasing particle size.

Figure 6.3 shows the pore size distribution (obtained by mercury porosimetry) for the slip cast CSD sample. The median pore radius is only ~10 nm. In addition, almost all the pore radii are less than 20 nm, indicating that particle packing in the compacts is very homogeneous.

It should be noted that one practical difficulty associated with slip casting of extremely fine particles is that consolidation rates are relatively slow. (Liquid filtration rates through the cast layer decrease rapidly with decreasing particle size.) Casting rates can be enhanced, however, by applying additional pressure during consolidation (e.g. pressure filtration or centrifugal casting).

Sintering

Figure 6.4 shows plots of relative density vs. sintering time at 1150°C for the slip cast samples prepared in this study and the α-Al_2O_3-seeded boehmite samples prepared by Messing et al. [Mes86]. It is evident that the slip cast samples have a considerably higher densification rate. In addition, these samples reach a higher "final" density, i.e. 3.95 ± 0.01 g/cm^3 (~ 99.2% relative density) after 2 h and 3.97 ± 0.01 (~ 99.7% relative density) after 6 h. Figure 6.5 shows a micrograph of a slip cast sample which was sintered for 2 h at 1150°C, cross-sectioned and polished, and thermally etched for 4 h at 1150°C. The average intercept grain size is only 0.16 μm.

The enhanced densification for the slip cast samples can be attributed, at least in part, to the improved green microstructure, i.e. the particle packing density is higher and the microstructure is more homogeneous. In the gel samples, the "packing units" are actually boehmite aggregates. The size of these "packing units" is on the order

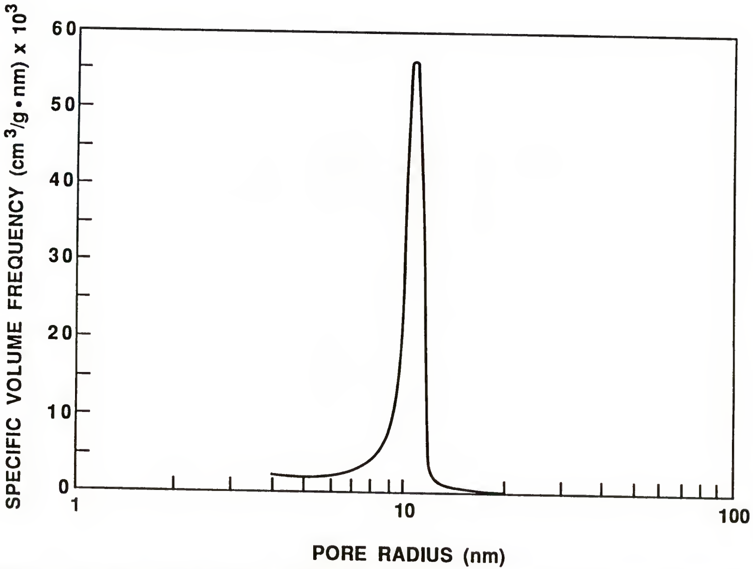

Figure 6.3 Plot of specific pore volume frequency function vs. pore radius obtained by mercury porosimetry for a sample prepared by slip casting the ~0.1 μm Al_2O_3 suspension.

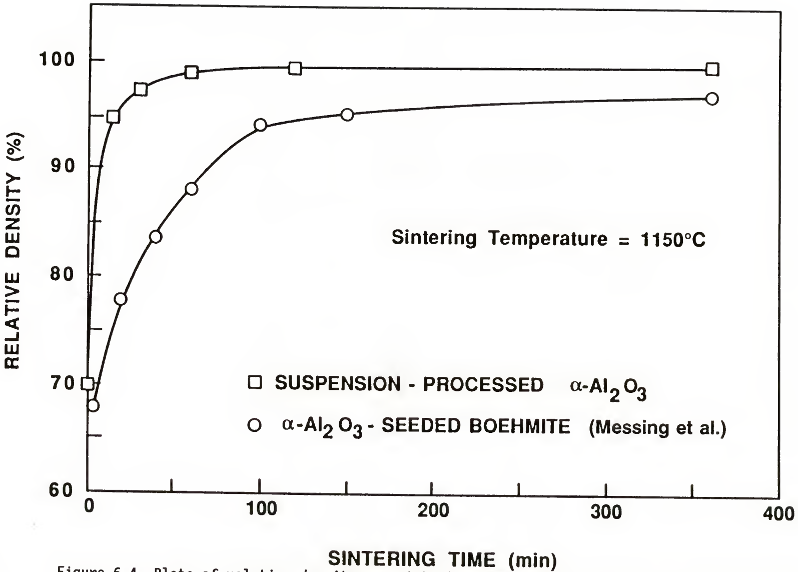

Figure 6.4 Plots of relative density vs. sintering time at 1150°C for suspension-processed samples in this study and boehmite sol-gel samples reported by Messing et al. [Mes86].

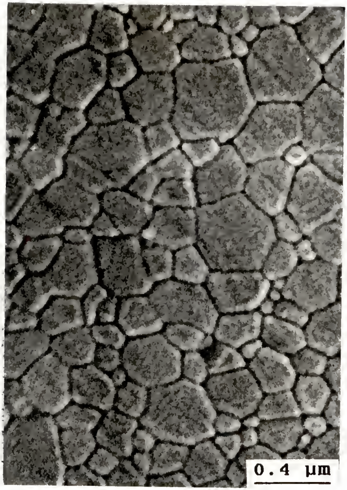

Figure 6.5 Scanning electron micrograph of a polished section of a suspension-processed sample which was sintered for 2 h at 1150°C and etched for 4 h at 1150°C.

of ~20-100 nm, but specific surface area measurements indicate that the primary particle, or crystallite, size is on the order of ~5-10 nm [Kum84, Kum85]. These porous aggregates are probably the main reason for the relatively low green density of the dried gels (~50-60%). In contrast, the high green density achieved in slip cast samples (~69%) indicates that aggregates were effectively eliminated during the powder preparation (i.e. sedimentation) process.

The sol-gel samples also develop heterogeneities during heat treatment. Boehmite undergoes a decomposition reaction (i.e. dehydroxylation) and a succession of phase transformations [Mes86]:

$$\text{boehmite} \rightarrow \gamma\text{-} \rightarrow \delta\text{-} \rightarrow \theta\text{-} \rightarrow \alpha\text{-AL}_2\text{O}_3$$

Thus, the dried gel undergoes substantial changes in volume (prior to sintering) due to weight loss (i.e. water removal) and increases in true density as the phase transformations occur. Differential shrinkages arise during these volume changes due to local variations in the kinetics of the decomposition reaction and the phase transformations. Thus, Messing et al. [Kum85, Mes86] observed "clusters" of ~0.05-0.10 μm particles and "cracklike structures" in samples which were transformed to α-Al_2O_3. These defects should affect densification the same way as powder agglomerates; particles in the regions of locally dense packing tend to sinter rapidly, whereas large voids "open up" in the regions of more porous packing [Sac82, Sac84]. The latter development is particularly detrimental since these porous regions have much lower densification rates. Hence, Messing et al. [Mes86] found that the "cracklike structures" persisted to relative densities as high as 99%.

Another factor which could contribute to the different densification rates observed in Figure 6.4 are differences in particle size. Unfortunately, this factor cannot be evaluated readily since quantitative particle size measurements were not available for the gel samples. However, Messing et al. [Kum85, Mes86] did report that the α-Al_2O_3 particle size was ~0.05-0.10 μm for gel samples in which the θ to α transformation was nearly complete. The particles used in the present study are in the same size range, suggesting that the enhanced densification for the slip cast samples is due almost exclusively to the higher green density and more homogeneous green microstructure.

The low sintering temperature and small grain size obtained in the present study with α-Al_2O_3 are similar to results reported by Rhodes [Rho81] using high green density (~ 74% relative density) Y_2O_3-stabilized ZrO_2 powder compacts prepared from well-dispersed suspensions of fine, unagglomerated particles. In the latter study, samples were sintered at 1100° C (1 h) to a relative density of 99.5% and average grain size of 0.2 μm.

Presumably, the sintering temperature for densifying Al_2O_3 could be further reduced if particles with smaller size were available and if a homogeneous, high relative density green structure was maintained after consolidation.* When the particles are smaller than the size used in the present study (i.e. $\lesssim$0.05-0.10 μm), the shape-forming method is generally referred to as a "sol-gel" process. Xerogels formed by sol-gel processing invariably have much lower relative densities than the values obtained in the present study. This suggests that the magnitude of the interparticle repulsive forces that operate in the sol-gel systems is inadequate. Several researchers [Sch86, Wei85] have demonstrated that particle consolidation under conditions of low repulsive force (e.g. rapid coagulation) tends to produce more porous and highly ramified structures (with lower fractal dimension), while more compact structures (with higher fractal dimension) tend to form under conditions with higher interparticle repulsive forces (e.g. reaction-limited coagulation). Thus, future investigations into processing of ultrafine particles (i.e. smaller than used in the present study) should focus on improving our understanding of the factors which determine the magnitude of the interparticle forces.

---

*This assumes that shrinkage-producing mechanisms, i.e. grain boundary and/or volume diffusion, still dominate as the particle size is reduced and the sintering temperature is lowered. However, surface diffusion tends to become more important under these conditions and this can lead to particle coarsening, instead of densification.

CHAPTER VII
SUMMARY AND SUGGESTIONS FOR FUTURE WORK

Summary

Alumina powders and powder compacts with model characteristics were prepared in order to investigate the effects of green microstructures (i.e., particle packing, pore characteristics, particle size, and particle size distribution) on densification and microstructural evolution during sintering.

Particle Packing

Green compacts prepared from slip casting of well-dispersed suspensions had very homogeneous green microstructure with high packing density and fine pore size. High densification rate as well as uniform sintered microstructure with fine grain and pore sizes were observed for these samples. No grain growth was observed up to 90% relative density. The above results were consistent with other microstructural characteristics such as higher specific pore-solid interfacial area, higher grain boundary area, higher absolute value of integral mean curvature, and shorter inter-pore distance. This is apparently a direct consequence of the meticulous procedures used to prepare uniform green compacts from well-dispersed suspensions (i.e., removing hard agglomerates, using ultrasonication to break down soft agglomerates, optimizing the pH to maximize the interparticle electrostatic repulsive forces in suspensions, using concentrated suspensions to avoid segregation of particles with different sizes, etc.).

Compacts slip cast from flocculated suspensions had lower green density and larger pore size. Lower densification rate was observed for these samples. Macroscopically, the green microstructures of the SCF samples were still homogeneous; however, small close-packed clusters were observed which could locally densify in the earlier stages of sintering and support grain growth. Hence, grain growth began at lower bulk density. Compared to the SCD sample, coarser sintered microstructure was obtained--larger grain and pore size, lower pore-solid interfacial area, lower grain boundary area, smaller absolute value of integral mean curvature, and larger inter-pore distance. All of these microstructural features were consistent with the initial packing characteristics and sintering behavior.

Dry-pressed samples showed heterogeneous green microstructure and bimodal pore size distribution--fine pore size for the close-packed agglomerates and large pore size for the more porous regions. Differential sintering was observed which resulted in broad and bimodal distributions in grain and pore sizes. High sintered density, fine pore size, and extensive grain growth were obtained for the close-packed agglomerates; lower densification kinetics, large residual pores, and smaller grain size for the porous regions. Due to large pores and low packing density, the DPL samples showed very low bulk densification rate. At a given relative density, the DPL samples had the largest grain sizes and smallest grain boundary and pore-solid interfacial areas. Even after extensive sintering (e.g., 48 h at 1600°C), only ~90% relative density was obtained for the DPL samples. Extremely heterogeneous microstructures were obtained and large pores remained.

The DPH sample had a green density similar to that of the SCF sample. They also had similar paths of evolution for most bulk (average) microstructural properties (e.g., pore intercept size, pore-solid interfacial area, grain boundary area, integral mean curvature, etc.). However, it should be noted that the DPH samples had much severer microstructural heterogeneities which were clearly seen in the SEM micrographs. These microstructural inhomogeneities could result in significant retardation on densification at high density (> 90%) range. Therefore, longer sintering time was needed and larger grain intercept size was obtained for the DPH sample with high sintered density. For the DPH sample, the number percentage of intragranular pores also started to increase at lower sintered densities. Significantly larger percentage of intragranular pores was obtained at high sintered density.

For most samples (except the DPL sample), the pore intercept size and pore intercept size distribution remained relatively constant over the entire density range. This indicated a balance between the mechanisms which tend to decrease the average pore size (e.g., densification) and the mechanisms which tend to increase the average pore size (e.g., elimination of fine pores, pore coalescence). However, slight increase of pore intercept sizes were observed at high density range. This indicated that pore coarsening mechanisms may become more important in the high density range. An significant increase in pore intercept size was observed for the DPL sample over the entire density range investigated. This may be due to the fact that the large pores are thermodynamically stable and remain unchanged while the fine pores are eliminated.

Even though particle packing characteristics had significant influence on densification kinetics, similar volume shrinkage kinetics were obtained in the earlier stages of sintering for samples with significant difference in particle packing. In the late stage of sintering, the volume shrinkage was determined by the green density, i.e., samples with higher green density had lower volume shrinkage.

The slip cast sample prepared from well-dispersed suspension showed very homogeneous microstructure which approached the geometric assumption proposed in most sintering models. However, the sintering results of this sample did not give a good fit to the intermediate and final stages sintering models proposed by Rosolowski and Greskovich [Ros75], Ikegami et al. [Ike78], and Kuczynski [Kuc77]. Most of the densification data had a good linear fit when they were plotted against logarithm of sintering time. However, a good fit should not be used to support any sintering model (e.g., Coble's model). Grain growth data also followed the empirical grain growth equation $D^n - D_0^n \alpha t$. Again, it can not be used to confirm any grain growth model.

Particle Size Distribution

The ISD suspension showed lower viscosity compared to the NSD-30 suspension. This is the direct result of the broader particle size distribution obtained in the ISD powder. However, the BSD suspension showed higher viscosity compared to the ISD suspension. This is because that the BSD suspension had large amounts of fine-sized particles. The Brownian motion and electroviscous effects, which are important for suspensions prepared with fine-sized particles, can significantly increase the viscosity of suspension.

The packing density increased, the pore size decreased, and the volume fraction of fine particles increased as the width of the particle size distribution of a green compact increased. This green microstructure characteristics resulted in the higher densification kinetics in the early stages of sintering for samples prepared from powders with broad particle size distribution. The sintered microstructure (e.g., pore size and pore size distribution, grain size and grain size distribution) for samples in the early stages of sintering resembled the initial green microstructures. However, due to the faster elimination of fine particles in the BSD samples and the broadening of grain size distribution in the NSD and ISD samples, similar sintered microstructures were obtained in the late stages of sintering (> 96% relative density).

Even though particle size distribution had significant influence on densification kinetics. Similar volume shrinkage kinetics were obtained in the earlier stages of sintering.

For samples prepared from powder with broad particle size distribution (i.e., BSD powder), the widths of the normalized grain intercept size distributions in log scale remained relatively constant over the entire densification process. However, the widths of the grain intercept size distributions in linear scale decreased in the early stages of sintering. This may be associated with the elimination of the fine particles. For samples prepared from powders with narrower particle size distributions (i.e., NSD-15, NSD-30, and ISD powders), the widths of the normalized grain intercept size distributions (either in linear scale or log scale) increased as grain growth began and reached the same widths as the BSD distributions. Then the normalized grain intercept size remained relatively unchanged with further densification.

The pore intercept size of the NSD-30 sample remained relatively constant over the entire densification process. The BSD and ISD samples had finer pore intercept sizes in the early stages of sintering. As the densification proceeded, the pore intercept size increased and approached the value of NSD-30 sample.

For the range of conditions investigated in this study, green compacts prepared from either broad or narrow size distribution powders could be sintered to high density (> 99%) with fine grain size and no exaggerated grain growth. Broad size distribution powders, however, provide several advantages compared to using powders with narrow size distribution : (1) The green density is higher and, therefore, less shrinkage is required to reach full density. This is helpful in achieving dimensional tolerances and in minimizing differential shrinkage in large sintered bodies. (2) The viscosity of suspensions is lower and suspensions with higher solids loading can be prepared. This is useful in (a) increasing the throughput of a process, (b) decreasing the power needed for mixing or transporting, (c) decreasing the amount of solvents used, and (d) decreasing shrinkage in the drying process.

Both of the narrow size distribution samples prepared from well-dispersed suspensions (i.e., SCD and NSD-30) had similar paths of grain size and pore size evolution during sintering even though the median particle size of the SCD sample was approximately twice than that of the NSD sample. Densification results at 1260°C for the above two samples were used to examine the applicability of Herring's scaling law.

Exponent values of ~ 3 were obtained which indicated that the volume diffusion was the dominant densification mechanism.

Low Temperature Sintering

By using homogeneous, high green density compacts with fine particle size (~0.1 μm), it was possible to sinter alumina at 1150°C to near-theoretical density (> 99.5%) and extremely fine grain size. Due to the Brownian motion and electroviscous effects, the viscosity of suspensions prepared from fine-sized powders was significant higher. This is consistent with the viscosity results of the BSD samples.

Suggestions for Future Work

Particle Packing

(1) The effect of MgO dopant on sintering for samples with various packing could be studied. MgO could be added into low temperature calcined compacts by impregnation of Mg-containing salts and subsequent calcination. Densification and microstructural evolution results for the MgO-doped samples could be compared with the results for the undoped samples obtained in this study.

(2) Mercury porosimetry could be used to investigate the evolution of pore structure during sintering for samples with various particle packing. These results could be compared with the pore intercept size results obtained in this study.

(3) The effect of sintering temperature on microstructural evolution could be studied. For the present study, only a few of the samples sintered at each temperature were examined to obtain microstructural properties. Therefore, comparison on the microstructural

results for samples with a constant density but varying sintering temperature could not be obtained. Further work could be done to characterize the remaining samples and thus provide sufficient data for studying the effect of sintering temperature. Long sintering times at low temperature (e.g., 1260°C) may be needed to obtain samples with higher density, therefore, comparisons over a wide density range can be made.

(4) Powders with low density agglomerates could be obtained by breaking up and grinding of powder cake prepared from flocculated suspensions. Densification and microstructural evolution of dry-pressed compacts prepared from the above powders could be compared with the dry-pressed samples obtained in the present study (which contained close-packed agglomerates).

(5) The effect of particle packing on the mechanical properties of samples at various sintered densities could be studied.

Particle Size Distribution

(1) Slightly lower sintered densities were observed for the BSD samples at long sintering times (e.g., > 12 h at 1260°C). Because the differences in density were small, it is not clear whether they were due to experimental error or due to the differences in particle size distribution. By preparing powders with even broader particle size distribution and investigating its effect on densification and microstructural evolution, more conclusive results may be obtained.

(2) Powder compacts with various width of particle size distribution, but constant green density may be obtained by slip casting flocculated suspensions. Therefore, investigation on the effect of

particle size distribution on densification and microstructural evolution for samples with constant green density could be carried out. Comparisons between these results and the results obtained in the present study could be obtained.

(3) The effect of MgO dopant on the densification and microstructural evolution of samples with various particle size distribution could be studied.

(4) Slight differences in grain size trajectories were observed for samples sintered at 1180 and 1260°C. By using samples sintered to higher densities at 1180°C or by increasing the differences in sintering temperature, more conclusive results may be obtained. The effect of sintering temperature on other microstructure properties could also be studied.

(5) Mercury porosimetry could be used to investigate the evolution of pore structures for samples with various particle size distribution. These results could be compared with the pore intercept size results reported in this study.

(6) The effect of particle size distribution on the mechanical properties of samples at various sintered densities could be studied.

Ultra-Fine Powder

(1) Agglomerate-free powders with even finer particle size could be prepared. Its effect on suspension properties and densification behaviors could be studied.

(2) Studies on the mechanical properties of samples with extremely fine grain size could be carried out.

APPENDIX A
PROCEDURE FOR POWDER FRACTIONATION

1. Narrow Size Distribution Powder from AKP-15 (NSD-15)

a. Prepared ~30 vol% suspensions with 960 grams of as-received AKP-15 powders, 545 ml D.I. water, and 15 ml 3 wt % HNO_3.

b. Adjusted pH to 3.7 with 3 wt% HNO_3.

c. Ultrasonicated 100 ml of suspension at a time for 30 min. at output 8.

d. Diluted into 2 vol% suspensions.

e. Let settle in 4000 ml graduated PMMA cylinders (height = 55 cm, I.D. = 10.2 cm).

f. After 72 hours, withdrew the top 15 cm of suspensions (save this fraction for making ISD and BSD powders).

g. Withdrew another 21 cm--Fraction N.

h. Repeated steps b to g for the suspensions left in the bottom of cylinders to obtain as much Fraction N as possible.

i. Adjusted the pH of the Fraction N to 3.7.

j. Let settle in 4000 ml graduated cylinders.

k. After 100 hours, withdrew the top 50 cm of suspensions (save this fraction for making ISD and BSD powders).

l. Redispersed the bottom fraction (pH adjustment and sonication) and diluted to 4000 ml.

m. Repeated steps j to l about 10 times to obtain a very narrow particle size distribution.

2. Narrow Size Distribution Powder from AKP-30 (NSD-30)

a. Prepared ~30 vol% suspension with 1280 grams of as-received AKP-30 powders, 720 ml D.I. water, and 25 ml 3 wt% HNO_3.

b. Adjusted pH to 3.7 with 3 wt% HNO_3.

c. Ultrasonicated 100 ml of suspension at a time for 30 min. at output 8.

d. Diluted into 2 vol% suspension.

e. Let settle in 4000 ml graduated PMMA cylinders (height = 55 cm, I.D. = 10.2 cm).

f. After 400 hours, withdrew the top 20 cm of suspensions (save this fraction for making ISD and BSD powders).

g. Withdrew another 20 cm--Fraction R.

h. Repeated steps b - g for the suspensions left in the bottom of cylinders to obtain as much Fraction R as possible.

i. Adjusted the pH of the Fraction R to 3.7.

j. Let settle in 4000 ml graduated cylinders.

k. After 450 hours, withdrew the top 45 cm of suspensions (save this fraction for making ISD and BSD powders).

l. Redispersed the bottom fraction (pH adjustment and sonication) and diluted to 4000 ml.

m. Repeated steps j to l about 10 times to obtain a very narrow particle size distribution.

3. Ultra-fine powder from AKP-50 (CSD)

a. Prepared ~30 vol% suspensions with 960 grams of as-received AKP-50 powders, 535 ml D.I. water, and 25 ml 3 wt% HNO_3.

b. Adjusted pH to 3.7 with 3 wt% HNO_3.

c. Ultrasonicated 100 ml of suspension at a time for 30 min. at output 8.

d. Diluted into 2 vol% suspensions.

e. Let settle in 4000 ml PE bottles (height = 23 cm, I.D. = 15 cm).

f. After 60 days, withdrew the top 14.4 cm of suspensions--CSD powder.

g. Repeated steps b to f for the suspensions left in the bottom of PE bottles to obtain as much of CSD powder as possible.

4. ISD and BSD Powders

During the process of preparing NSD-15, NSD-30, and CSD powders, suspensions with various particle size distributions were generated and collected. Some of these suspensions (Figures A.1 and A.2) were used to produce suspensions with intermediate and broad particle size distribution (i.e., ISD and BSD). The ISD suspension was obtained using a mixture of 10 wt% of B, 20 wt% of C and of D, and 50 wt% of E. The BSD suspension was obtained using a mixture of 18 wt% of A, 20 wt% of D, 25 wt% of E and of F, and 12 wt% of G. After homogeneous mixtures were obtained, a small amount of the ISD and BSD suspensions were used to determine the particle size distributions. Depending on the particle size distribution obtained, small amounts of powders with suitable particle size distributions were added to modify the overall particle size distribution in order to obtain the same median size (0.39 μm).

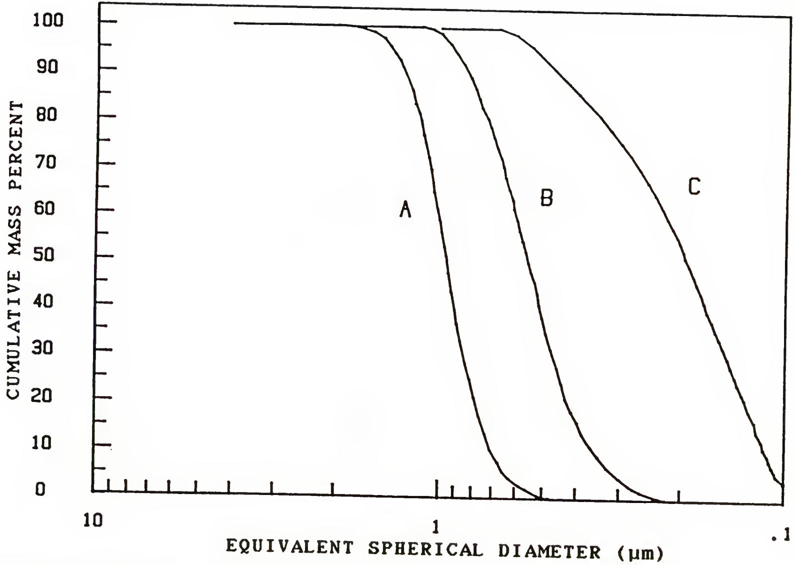

Figure A.1 Gravitational x-ray sedimentation data for powder batches (A to C) used for making ISD and BSD powders.

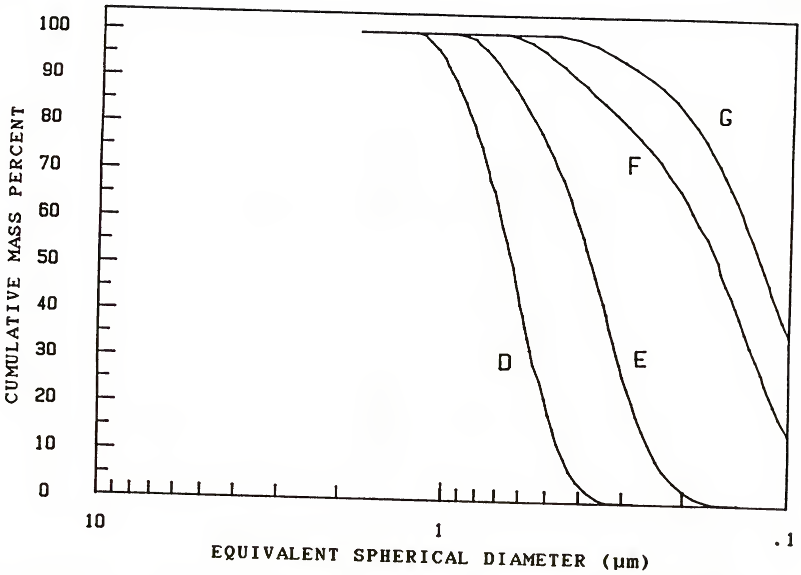

Figure A.2 Gravitational x-ray sedimentation data for powder batches (D to G) used for making ISD and BSD powders.

APPENDIX B
IMPREGNATION OF POROUS BODY FOR POLISHING

Recently, there has been an increased interest in the investigation of the effect of green microstructure on the sintering and microstructural evolution during sintering. It is desirable to obtain a flat polished surface for microstructural characterization using optical or electron microscopy. However, due to the fragility of green compacts (or slightly sintered porous compacts), impregnation is needed to strengthen the porous compacts and to preserve microstructural details during polishing.

Impregnation of porous compacts using molten sulfur [Gre72], metal amalgams [Lau80], and low melting point glass [Lau81] was proposed. Recently, Pickles and Lilley [Pic85] described an impregnation technique using an epoxy* first developed by Spurr [Spu69]. However, a complicated and laborious procedure for dehydration and infiltration is needed. Furthermore, the viscosity of the Spurr polymer is still relative high (~60 cp [Pic85]) and may fail to fill fine cavities especially when fine powders are used to form the green compacts. A novel impregnation method was developed by this author, the detailed procedure and some remarks about this method are described as follows.

---

* Spurr low-viscosity embedding media, Polyscience, Warrington, PA.

Procedure

a. A mixture of monomer* and initiator** in the ratio of 8 to 12 mg of initiator per 5 ml monomer was prepared. The solution was stirred for 5 to 10 min to obtain a complete dissolution of initiator in the monomer.

b. The porous sample was then put in a glass bottle and approximately 3 ml of monomer solution was poured into the bottle. The bottle was sealed with a metal lined cap.

c. The bottle was then placed in an oven and the temperature was set at 50 to 65°C. After the polymerization was complete (about 3-10 hours), the bottle was removed from the oven.

d. The above procedure gives a mount about 2 cm diameter and 0.5 cm thick. By repeating the same procedure, the thickness of the mount was increased. However, other mounting materials (for example, Quickmount) can also be poured on top of the solidified polymer mount to increase the thickness of mounting for easy handling.

e. The sample mount was then removed from the glass bottle and could be clamped onto a sample holder for polishing.

Remarks

a. Because the monomer has very low viscosity (less than 1 cp) and can wet most oxide materials, strong capillary force will ensure fast and complete impregnation of any pore cavity. No vacuum or pressure are needed in the impregnation process.

---

* Methyl Methacrylate, Fisher Scientific Co., Springfield, NJ.

** 2,2'-Azobis [2-methyl-propionitrile], Eastman Kodak Co., Rochester, NY.

b. Solidification takes place at low temperatures (50 - 65°C) and can be done in any oven.

c. The solidified mount (PMMA) is hard and strong which is suitable for preserving microstructural details during grinding and polishing.

d. Complete burn-out of impregnating materials can be easily achieved at 800 - 900°C. Clean SEM micrographs can be obtained.

e. Glass containers are recommended for containing monomer because monomer may react with plastic ware.

f. Because auto-acceleration will occur during polymerization process, only a small quantity (about 3 ml) of monomer should be used each time. If a large quantity is used, bubbles may be generated during the polymerization process and a foamed body may be obtained. Decreasing the polymerization temperature to around 50°C can decrease the reaction rate and solve the foaming problem; however, very long polymerization time (several days) will be needed.

g. Polymerization rate can be controlled by choosing optimum combination of polymerization temperature and initiator concentration.

h. This method (i.e., impregnation of porous silica bodies with PMMA polymer) has also been used to produce transparent PMMA-silica composites [Liu80, Pop86a, Pop86b].

APPENDIX C1
DENSIFICATION DATA FOR PACKING STUDY

Sintering Schedule	Bulk Density g/cm^3 (Relative Density %)			
	SCD	SCF	DPL	DPH
1260°C, 0.5 h	2.90 (72.8)	2.34 (58.9)	-	-
1 h	2.99 (75.0)	2.38 (59.8)	-	-
2 h	3.07 (77.1)	2.43 (61.0)	2.04 (51.3)	2.63 (66.0)
6 h	3.14 (79.0)	2.56 (64.4)	2.14 (53.7)	2.76 (69.4)
12 h	3.40 (85.3)	-	-	-
48 h	3.65 (91.8)	-	-	-
1300°C, 0.5 h	3.70 (77.2)	-	-	-
1 h	3.14 (78.9)	2.49 (62.6)	1.95 (49.1)	-
6 h	3.43 (86.1)	2.73 (68.7)	2.13 (53.5)	-
12 h	3.57 (89.6)	2.85 (71.5)	2.22 (55.9)	-
24 h	3.69 (92.6)	2.95 (74.2)	2.45 (61.5)	-
72 h	3.84 (96.6)	3.20 (80.4)	2.49 (62.5)	-
168 h	3.87 (97.3)	3.26 (81.9)	2.69 (67.5)	-
1340°C, 1 h	3.31 (83.2)	2.64 (66.4)	2.18 (54.7)	2.81 (70.6)
2 h	3.47 (87.2)	2.73 (68.7)	2.27 (57.1)	2.89 (72.5)
4 h	3.63 (91.2)	2.88 (72.4)	2.39 (60.0)	3.14 (79.0)
8 h	3.74 (94.0)	2.98 (74.9)	2.44 (61.2)	3.26 (81.8)
12 h	3.79 (95.3)	3.11 (78.1)	2.52 (63.4)	3.31 (83.2)
16 h	3.82 (96.1)	3.23 (81.2)	2.62 (65.8)	3.40 (85.4)
24 h	3.85 (96.8)	3.34 (83.8)	2.71 (68.2)	3.47 (87.1)
36 h	3.90 (98.0)	3.41 (85.6)	-	3.56 (89.4)
72 h	3.94 (99.0)	3.58 (90.0)	2.91 (73.2)	3.67 (92.2)
168 h	3.96 (99.6)	3.64 (91.5)	2.95 (74.1)	-
1375°C, 155 h	3.96 (99.6)	3.78 (95.1)	3.19 (80.1)	3.83 (96.3)
1450°C, 0.5 h	3.75 (94.3)	2.97 (74.6)	2.60 (65.4)	-
2 h	3.91 (98.2)	3.40 (85.5)	2.78 (69.8)	-
6 h	3.96 (99.4)	3.63 (91.1)	2.94 (73.8)	-
16 h	3.97 (99.7)	3.70 (93.0)	3.13 (78.6)	-
27 h	-	3.78 (95.0)	-	-
48 h	3.98 (100.0)	3.91 (98.3)	3.24 (81.4)	-
90 h	3.99 (100.0)	3.94 (99.0)	3.39 (85.2)	3.85 (96.8)
168 h	3.98 (100.0)	3.95 (99.3)	3.50 (88.0)	3.89 (97.8)
1600°C, 24 h	-	-	3.55 (89.2)	3.95 (99.3)
48 h	-	-	3.55 (89.2)	-

APPENDIX C2
OPEN POROSITY RESULTS FOR PACKING STUDY

Sintering Schedule	Open Porosity (%)			
	SCD	SCF	DPL	DPH
1260°C, 0.5 h	100.0	100.0	-	-
1 h	100.0	100.0	-	-
2 h	100.0	100.0	100.0	100.0
6 h	100.0	100.0	100.0	100.0
12 h	100.0	-	-	-
48 h	100.0	-	-	-
1300°C, 0.5 h	100.0	-	-	-
1 h	100.0	100.0	100.0	-
6 h	100.0	100.0	100.0	-
12 h	100.0	100.0	100.0	-
24 h	100.0	100.0	100.0	-
72 h	0.0	100.0	100.0	-
168 h	2.0	98.3	100.0	-
1340°C, 1 h	96.7	99.7	100.0	100.0
2 h	99.2	98.7	98.7	98.7
4 h	88.7	99.3	99.3	94.7
8 h	50.4	98.4	99.4	98.4
12 h	3.5	98.1	98.9	97.9
16 h	2.6	98.3	99.6	97.6
24 h	5.3	100.0	100.0	96.7
36 h	1.0	97.6	-	-
72 h	0.0	98.0	100.0	87.1
168 h	0.0	97.6	100.0	-
1375°C, 155 h	0.0	9.0	99.7	35.2
1450°C, 0.5 h	96.6	100.0	100.0	-
2 h	1.0	100.0	100.0	-
6 h	0.0	91.0	100.0	-
16 h	0.0	58.0	100.0	-
27 h	-	0.0	-	-
48 h	0.0	0.0	100.0	-
90 h	0.0	0.0	100.0	34.4
168 h	0.0	0.0	100.0	31.4
1600°C, 24 h	-	-	92.2	0.0
48 h	-	-	91.3	-

APPENDIX C3
MICROSTRUCTURAL PROPERTIES OF SCD SAMPLES

Sintering Schedule		RD*	GI*	PI*	S_V^{P}*	S_V^{B}*	M_V*	P/A*	%IP*
1260°C,	0.5 h	72.8	0.41	0.21	4.50	1.31	-9.04	1.48	0
1300°C,	0.5 h	77.2	0.44	0.21	3.39	2.01	-9.05	1.48	0
	1 h	78.9	0.43	0.21	3.18	-	-	-	-
1340°C,	1 h	83.2	0.44	0.21	2.42	3.06	-7.95	1.28	0
	2 h	87.2	0.44	0.23	1.72	3.54	-7.70	1.23	0
	4 h	91.2	0.45	0.23	1.24	3.35	-5.96	0.95	0.1
	8 h	94.0	0.62	0.22	0.60	2.98	-3.20	0.51	0.4
	16 h	96.1	0.82	0.23	0.38	2.29	-1.99	0.32	1.3
	36 h	98.0	1.07	0.26	0.32	1.72	-1.40	0.22	7.1
1450°C,	6 h	99.4	1.52	0.24	0.12	1.28	-0.63	0.1	32.2
	16 h	99.7	2.08	0.24	0.07	1.04	-0.41	0.06	55.8
	90 h	100.0	3.03	0.29	0.05	-	-	-	-

* RD = Relative Density (%)
GI = Grain Intercept Size (μm)
PI = Pore Intercept Size (μm)
S_V^{P} = Pore-Solid Interfacial Area (m^2/cm^3)
%OP = Percentage of open porosity
%IP = Number Percentage of Intragranular Pores

S_V^{B} = Grain Boundary Area (m^2/cm^3)
M_V = Integral Mean Curvature ($1/\mu m^2$)
P/A = Number of Pores / Area ($1/\mu m^2$)
BD = Bulk Density (g/cm^3)

APPENDIX C4
MICROSTRUCTURAL PROPERTIES OF SCF SAMPLES

Sintering Schedule	RD*	GI*	PI*	S_V^{P}*	S_V^{B}*	M_V*	P/A*	%IP*
1300°C, 1 h	62.6	0.44	-	-	-	-	-	-
12 h	71.5	0.46	0.41	2.57	1.40	-4.65	0.85	0
1340°C, 1 h	66.4	0.43	-	-	-	-3.66	0.70	0
8 h	74.9	0.54	0.38	2.49	1.92	-4.40	0.73	0
12 h	78.1	0.54	-	-	2.13	-4.10	0.67	0
16 h	81.2	0.57	0.40	1.53	2.30	-3.70	0.60	0
36 h	85.6	0.70	0.42	1.38	1.98	-3.31	0.53	0.1
1450°C, 6 h	91.1	0.92	0.45	0.93	1.50	-2.32	0.37	0.6
16 h	93.0	1.21	0.46	0.62	1.30	-1.54	0.24	3.1
27 h	95.0	1.44	-	-	1.06	-1.08	0.17	0.80
48 h	98.3	1.83	0.46	0.23	0.84	-0.63	0.10	12.5
90 h	99.0	2.10	0.47	0.17	-	-0.40	0.07	-
168 h	99.3	2.54	0.54	0.11	0.79	-0.31	0.05	22.6

* See APPENDIX C3

APPENDIX C5
MICROSTRUCTURAL PROPERTIES OF DPH SAMPLES

Sintering Schedule	RD*	GI*	PI*	S_V^{P}*	S_V^{B}*	M_V*	P/A*	%IP*
1340°C, 1 h	70.6	0.43	0.29	3.09	1.38	-5.02	0.82	0.3
2 h	72.5	0.43	0.37	2.77	1.60	-5.22	0.85	0
4 h	79.0	0.48	0.35	2.32	2.43	-4.87	0.79	0.2
8 h	81.8	0.55	-	1.78	2.35	-3.57	0.57	0.3
16 h	85.4	0.67	0.40	1.56	2.17	-3.19	0.51	0.6
36 h	89.4	0.93	0.41	0.80	2.04	-2.25	0.36	1.1
72 h	92.2	1.09	0.47	0.64	1.35	-1.54	0.25	2.8
1375°C, 155 h	96.3	1.94	0.49	0.30	1.02	-0.73	0.12	4.3
1450°C, 168 h	97.8	2.24	0.52	0.23	0.77	-0.50	0.08	23.1
1600°C, 24 h	99.3	4.14	0.40	0.07	0.69	-0.29	0.05	73.2

* See APPENDIX C3

APPENDIX C6
MICROSTRUCTURAL PROPERTIES OF DPL SAMPLES

Sintering Schedule	RD*	GI*	PI*	S_V^{P}*	S_V^{B}*	M_V*	P/A*	%IP*
1450°C, 0.5 h	65.4	0.50	-	-	-	-	-	-
2 h	69.8	0.56	-	-	-	-	-	-
6 h	73.8	0.76	0.68	1.48	1.25	-	-	-
16 h	78.6	1.11	0.75	1.0	1.09	-1.61	0.26	0.5
48 h	81.4	1.43	0.99	0.70	0.75	-0.87	0.14	4.6
90 h	85.2	1.71	1.10	0.47	0.37	-0.68	0.11	8.5
168 h	88.0	1.99	-	-	0.38	-0.51	0.08	15.2
1600°C, 48 h	89.2	2.79	1.35	0.31	0.33	-0.33	0.05	25.8

* See APPENDIX C3

APPENDIX D1
DENSIFICATION DATA AND MICROSTRUCTURAL PROPERTIES OF NSD-30 SAMPLES

Sintering Schedule	BD*	RD*	%OP*	GI*	PI*	S_V^{P*}
1100°C, 0.5 h	2.71	68.0	97	-	-	-
1 h	2.76	69.4	99	0.24	-	-
2 h	2.77	69.5	97	-	-	-
6 h	2.82	70.8	100	-	-	-
1180°C, 0.5 h	2.90	72.9	98	0.22	-	-
1 h	3.00	75.4	100	0.23	0.14	6.4
2 h	3.03	76.2	97	0.23	0.13	5.9
6 h	3.18	79.8	98	0.23	0.13	5.1
12 h	3.26	81.9	100	0.22	-	-
24 h	3.38	85.0	98	0.26	0.14	3.9
48 h	3.56	89.5	89	0.29	0.14	1.9
1260°C, 0.5 h	3.21	80.6	97	0.24	-	-
2 h	3.46	87.0	99	0.24	-	-
6 h	3.72	93.4	83	0.27	0.12	1.8
16 h	3.85	96.7	0	0.43	0.13	-
24 h	3.89	97.8	0	0.53	-	-
48 h	3.90	98.1	0	0.69	0.13	0.37
1340°C, 6 h	3.95	99.3	0	0.89	0.13	0.11
12 h	3.93	98.7	0	-	-	-
24 h	3.96	99.6	0	-	-	-
48 h	3.94	99.0	0	1.06	-	-
1450°C, 48 h	3.96	99.6	0	2.3	-	-

* See APPENDIX C3

APPENDIX D2
DENSIFICATION DATA AND MICROSTRUCTURAL PROPERTIES OF ISD SAMPLES

Sintering Schedule	BD*	RD*	%OP*	GI*	PI*	S_V^{P*}
1100°C, 0.5 h	2.94	73.8	99	-	-	-
1 h	2.97	74.7	97	0.23	-	-
2 h	3.00	75.4	100	-	-	-
6 h	3.07	77.1	96	-	-	-
1180°C, 0.5 h	3.18	79.8	100	-	-	-
1 h	3.23	81.1	97	0.24	-	-
2 h	3.30	82.9	96	0.22	0.11	5.1
6 h	3.47	87.3	100	0.23	0.11	3.9
12 h	3.53	88.6	96	0.26	-	-
24 h	3.61	90.8	91	0.31	0.12	2.0
48 h	3.74	93.9	0	0.41	-	-
1260°C, 0.5 h	3.47	87.1	95	0.25	-	-
2 h	3.71	93.2	82	0.24	-	-
6 h	3.80	95.6	0	0.39	0.11	1.0
16 h	3.88	97.4	1	0.46	0.11	-
24 h	3.91	98.2	0	0.51	-	-
48 h	3.92	98.4	0	0.60	0.14	0.23
1340°C, 6 h	3.96	99.5	0	0.79	0.13	0.10
12 h	3.94	99.0	0	-	-	-
24 h	3.95	99.3	0	-	-	-
48 h	3.95	99.2	0	0.93	-	-
1450°C, 48 h	3.96	99.5	0	2.3	-	-

* See APPENDIX C3

APPENDIX D3
DENSIFICATION DATA AND MICROSTRUCTURAL PROPERTIES OF BSD SAMPLES

Sintering Schedule	BD*	RD*	%OP*	GI*	PI*	S_V^{P*}
1100°C, 0.5 h	3.05	76.7	98	-	-	-
1 h	3.11	78.1	100	0.20	-	-
2 h	3.13	78.7	98	-	-	-
6 h	3.20	80.3	96	-	-	-
1180°C, 0.5 h	3.30	82.8	97	0.22	0.078	-
1 h	3.40	85.4	100	0.22	0.078	5.6
2 h	3.43	86.3	96	0.23	0.093	5.0
6 h	3.55	89.2	97	0.25	0.096	4.0
12 h	3.61	90.6	93	0.30	-	-
24 h	3.65	91.7	85	0.36	0.11	2.0
48 h	3.75	94.1	0	0.43	-	-
1260°C, 0.5 h	3.57	89.6	94	0.29	-	-
2 h	3.71	93.1	80	0.29	0.11	-
6 h	3.78	95.0	0	0.40	0.11	1.1
16 h	3.84	96.6	0	0.56	0.12	0.49
24 h	3.87	97.3	0	0.59	-	-
48 h	3.88	97.6	0	0.70	0.14	0.25
1340°C, 6 h	3.91	98.3	0	0.86	0.14	0.12
12 h	3.92	98.4	0	-	-	-
24 h	3.94	98.9	0	-	-	-
48 h	3.94	99.1	0	0.98	-	-
1450°C, 48 h	3.95	99.3	0	2.4	-	-

* See APPENDIX C3

REFERENCES

[Abo69] D.A. Aboav and T.G. Langdon, Metallography, [1] 333 (1969).

[Aks84] I.A. Aksay and C.H. Schilling, pp. 439 in Ultrastructure Processing of Ceramics, Glasses, and Composites. Edited by L.L. Hench and D.R. Ulrich. Wiley-Interscience, New York, 1984.

[Ale57] B.H. Alexander and R.W. Baluffi, Acta Met., 5 666 (1957).

[And85] M.P. Anderson, G.S. Grest, and D.J. Sroloritz, Scripta Metall., 19 [2] 225 (1985).

[Atk88] H.V. Atkinson, Acta Metall., 36 [3] 469 (1988).

[Aus50] C.R. Austin, U.S. Pat 2,494,276 (1950).

[Bag70] R.D. Bagley, I.B. Cutler, D.L. Johnson, J. Am. Ceram. Soc., 53 136 (1970).

[Bai85] S. Baik, D.E. Fowler, J.M. Blakely, and R. Raj, J. Am. Ceram. Soc., 68 [5] 281 (1985).

[Ban80] M.J. Bannister, Am. Ceram. Soc., 63 [3-4] 229 (1980).

[Bar82] E.A. Barringer and H.K. Bowen, J. Am. Ceram. Soc., 65 [12] C-199 (1982).

[Bar84] E.A. Barringer, N. Jubb, B. Fegley, R.L. Pober, and H.K. Bowen, pp. 315 in Ultrastructure Processing of Ceramics, Glasses, and Composites. Edited by L.L. Hench and D.R. Ulrich. Wiley-Interscience, New York, 1984.

[Ben73] R.B. Bennett and D.E. Niesz, Final Report,Office of Naval Research, Contract No. N00014-68-C0342, NR032-511 (July 1973).

[Ben83] S.J. Bennison and M.P. Harmer, J. Am. Ceram. Soc., 66 [5] C-90 (1983).

[Ben85] S.J. Bennison and M.P. Harmer, J. Am. Ceram. Soc., 68 [1] C-22 (1985).

[Ber86] K.A. Berry and M.P. Harmer, J. Am. Ceram. Soc., 69 [2] 143 (1986).

[Bro65] J. G. Brodnyan and E. L. Kelly, J. Colloid. Sci., 20 7 (1965).

[Bro76] R.J. Brook, pp. 331 in Ceramic Fabrication Processes. Edited by F.F.Y. Wang, Academic Press, New York, 1976.

[Bro82] R.J. Brook, Proc. Br. Ceram. Soc., 32 7 (1982).

[Bru62] C.A. Bruch, Am. Ceram. Soc. Bull., 41 [12] 799 (1962).

[Bur52] J.E. Burke and D. Turnbull, Progr. Metal Phys. 3 220 (1952).

[Bur57] J.E. Burke, J. Am. Ceram. Soc., 40 [1] 80 (1957).

[Bur80] J.E. Burke, L.W. Lay and S. Prochazka, pp. 417 in Sintering Processes. Edited by G.C. Kuczynski. Plenum Press, New York, (1980).

[Cah56] H.P. Cahoon and C.J. Christensen, J. Am. Ceram. Soc., 39 [10] 337 (1956).

[Cah62] J.W. Cahn, Acta. Metall., 10 [9] 789 (1962).

[Cah67] J.W. Cahn, TMS-AIME, 239 May, 610 (1967).

[Cam88] C.P. Cameron and R. Raj, J. Am. Ceram. Soc., 71 [12] 1032 (1988).

[Cam89] C.P. Cameron and R. Raj, submitted to J. Am. Ceram. Soc..

[Can80] R.M. Cannon, W.H. Rhodes, and A.H. Heuer, J. Am. Ceram. Soc., 63 [1] 46 (1980).

[Car78a] T.J. Carbone and J.S. Reed, Am. Ceram. Soc. Bull., 57 [8] 748 (1978).

[Car78b] F.M.A. Carpay and S.K. Kurtz, pp. 217 in Processing of Crystalline Ceramics. Edited by H. Palmour, R.F. Davis, and T.M. Hare, Plenum Press, New York, 1978.

[Car84] E. Carlstrom and F.F. Lange, J. Am. Ceram. Soc., 67 [8] C-169 (1984).

[Cha86] J.S. Chappell, T.A. Ring, and J.D. Birchall, J. Appl. Phys., 60 [1] 383 (1986).

[Cho71] G.R. Chol, J. Am. Ceram. Soc., 54 [1] 34 (1971).

[Cob58] R.L. Coble, J. Am. Ceram. Soc., 41 [2] 55 (1958).

[Cho62] J.S. Chong, Ph.D. Dissertation, University of Utah, 1962.

[Cob61] R.L. Coble, J. Appl. Phys., 32 [5] 787 (1961).

[Cob62a] R.L. Coble, U.S. Pat. 3,026,210, March 21, 1962.

[Cob62b] R.L. Coble, J. Am. Ceram. Soc., 45 [3] 123 (1962).

[Cob63] R.L. Coble and J.E. Burke, pp. 197 in Progress in Ceramic, Science Vol. 3, Edited by J.E. Burke, The Macmillan Company, New York, 1963.

[Cob67] R.L. Coble and T.K. Gupta, pp. 423 in Sintering and Related Phenomena. Edited by G.C. Kuczynski, N.A. Hooton and C.F. Gibbon. Gordon and Breach, Science Publishers, New York, 1967.

[Cob73] R.L. Coble, J. Am. Ceram. Soc., 56 [8] 461 (1973).

[Com52] G.E. Comstock III, U.S. Pat. 2618,567 (1952).

[Con60] B. E. Conway and A. Dobry-Duclaux, pp. 83 in Rheology: Theory and Applications, Vol. 3. Edited by F. R. Eirich. Academic Press, New York, 1960.

[Dav71] J.E. Davis, V.G. Carithers and D.R. Watson, Am. Ceram. Soc. Bull., 50 [11] 906 (1971).

[DeH66] R.T. DeHoff, R.H. Rummel, H.P. LaBuff and F.N. Rhines, pp. 310 in Modern Developments in Powder Metallurgy. Vol.1, Fundamentals and Methods. Edited by H.H. Hausner. Plenum Press, New York, (1966).

[DeH67] R.T. DeHoff, TMS-AIME, 239 May, 617 (1967).

[DeH68] R.T. DeHoff and F.N. Rhines, Editors, Quantitative Microscopy, McGraw-Hill, New York, 1968.

[DeH77] R.T. DeHoff, Microstructural Science, 5 331 (1977).

[Dyn83] F.W. Dynys and J.W. Halloran, J. Am. Ceram. Soc., 66 [9] 655 (1983).

[Dyn84] F.W. Dynys and J.W. Halloran, J. Am. Ceram. Soc., 67 [9] 596 (1984).

[Eit54] W. Eitel, The Physical Chemistry of the Silicates, University of Chicago Press, 1954.

[Eva82] A.G. Evans, J. Am. Ceram. Soc., 65 [10] 497 (1982).

[Exn72] H.E. Exner, Int. Met. Rev., 17 25 (1972).

[Exn73] H.E. Exner, G. Petzow and P. Wellner, pp. 351 in Sintering and Related Phenomena. Edited by G.C.Kuczynski, Plenum Press, New York, 1973.

[Exn79] H.E. Exner, Rev. Powder Metall. Phys. Ceram., 1 [1-4] 1 (1979).

[Exn80] H.E. Exner and G. Petzow, pp. 107 in Sintering Processes. Edited by G.C. Kuczynski, Plenum Press, New York, 1980.

[Far68] R.J. Farris. Trans. Soc. Rheol., 12 [2] 281 (1968).

[Fel57] P. Feltham, Acta Metall., 5 [1] 97 (1957).

[Fid61] V. Fidleris and R.V. Whitmore, Rheol. Acta., 1 [4-6] (1961).

[Flo78] W.M. Flock, pp. 85 in Ceramic Processing Before Firing, Edited by G.Y. Onoda, Jr. and L.L Hench. John Wiley & Sons, New York, 1978.

[Fre45] J. Frenkel, J. Phys. USSR, 9 [5] 385 (1945).

[Fur29] C.C. Furnas, Bur. Mines, Bull., 307 74 (1929).

[Fur31] C.C. Furnas, Ind. Eng. Chem., 23 [9] 1052 (1931).

[Gat84] T. R. Gattuso and H.K. Bowen, pp. 644 in Structure and Properties of MgO and Al_2O_3 Ceramics. Edited by W.D. Kingery, Am. Ceram. Soc., Columbus, OH, 1984.

[Gre69] R. Gregg, Ph.D. Dissertation, University of Florida, 1969.

[Gre71] C. Greskovich and K.W. Lay, J. Am. Ceram. Soc., 55 [3] 142 (1972).

[Gre85] G.S. Grest, D.J. Srolovitz, and M.P. Anderson, Acta Metall., 33 [3] 509 (1985).

[Gup72] T.K. Gupta, J. Am. Ceram. Soc. 55 [5] 276 (1972).

[Han84] C. Han, I.A. Aksay, and O.J. Whittemore, pp. 339 in Advances in Materials Characterization II. Edited by R.L. Snyder, R.A. Condrate, Sr. and P.F. Johnson. Plenum Press, New York, 1984.

[Han89] C.A. Handwerker, P.A. Morris, and R.L.Coble, J. Am. Ceram. Soc., 72 [1] 130 (1989).

[Har79] M.P. Harmer, E.W. Roberts, and R.J. Brook, Trans. J. Br. Ceram. Soc., 78 [1] 22 (1979).

[Har84] M.P. Harmer, pp. 679 in Structure and Properties of MgO and Al_2O_3 Ceramics. Edited by W.D. Kingery, Am. Ceram. Soc., Columbus, OH, 1984.

[Hau49] W.E. Hauth, Jr., J. Am. Ceram. Soc., 32 [12] 394 (1949).

[Her50] C. Herring, J. Appl. Phys., 21 [4] 301 (1950).

[Her86] S.M. Her, Ph.D. Dissertation, University of Florida (1986).

[Heu79] A.H. Heuer, Am. Ceram. Soc. 62 [5-6] 317 (1979).

[Hie77] P.C. Hiemenz, Principles of Colloid and Surface Chemistry, Marcel Dekker, New York, 1977.

[Hil65] M. Hillert, Acta Metall., 13 [3] 227 (1965).

[How81] S.P. Howlett, Ph.D. Dissertation, University of Leeds (1981).

[Hsu86] C.H. Hsueh, A.G. Evans, and R.M. McMeeking, J. Am. Ceram. Soc., 69 [4] C-64 (1986).

[Hu74] H. Hu, Can Metal. Q., 13 275 (1974).

[Hun81] R.J. Hunter, Zeta Potential in Colloid Science, Academic Press, London, 1981.

[Hun87] R.J. Hunter, Foundations of Colloid Science, Vol.1, Clarendon Press, Oxford, 1987.

[Ike78] T. Ikegami, M. Tsutsumi, S. Matsuda, S. Shirasaki and H. Suzuki, J. Appl. Phys. 49 [7] 4238 (1978).

[Ike87] T. Ikegami, K. Kotani and K. Eguchi, J. Am. Ceram. Soc., 70 [12] 885 (1987).

[Jan89] M.A. Janney and H.D. Kimrey, to be published in Sintering of Advanced Ceramics, Am. Cera. Soc., Westerville, OH, 1989.

[Jef42] J.A. Jeffery, U.S. Pat. 2,274,067 (1942).

[Joh69] D.L. Johnson, J. Appl. Phys., 40 [1] 192 (1969).

[Joh70] D.L. Johnson, J. Am. Ceram. Soc., 53 [10] 574 (1970).

[Joh72] D.W. Johnson, Jr., D.J. Nitti and L. Berrin, Am. Ceram. Soc. Bull., 51 [12] 896 (1972).

[Joh78] W.C. Johnson, and R.L. Coble, J. Am. Ceram. Soc., 61 [3-4] 110 (1978).

[Jor64] P.J. Jorgensen and J.H. Westbrook, J. Am. Ceram. Soc., 47 [7] 332 (1964).

[Kel84] B. Kellett and F. F. Lange, J. Am. Ceram. Soc., 67 [5] 369 (1984).

[Kep05] G. Kepler, Die Chemische Ind. Nachrechten Ausgabe, 28 232 (1905).

[Kes65] J.R. Keski and I.B. Cutler, J. Am. Ceram. Soc., 48 653 (1965).

[Kes68] J.R. Keski and I.B. Cutler, J. Am. Ceram. Soc., 51 [8] 440 (1968).

[Kha88] C.S. Khadilkar, Ph.D. Dissertation, University of Florida (1988).

[Kim87] T.Kimura, Y. Matsuda, M. Oda, and T. Yamaguchi, Ceramics International, 13 27 (1987).

[Kin76] W.D. Kingery, H.K. Bowen, and D.R. Uhlmann, Introduction to Ceramics, Second Edition, John Wiley and Sons, New York, 1976.

[Kin67] W.D. Kingery and B. Francois, pp. 471 in Sintering and Related Phenomena. Edited by G.C. Kuczynski, N.A. Hooton, and G.F. Gibbon. Gordon Breach, New York, 1967.

[Kri72] I. M. Krieger, Adv. Colloid Interface Sci, 3 111 (1972).

[Kri76] I. M. Krieger and M. Equiluz, Trans. Soc. Rheol., 20 [1] 29-45 (1976).

[Kru52] H.R. Kruyt Editor, Colloid Science, Elsevier, Amsterdam, 1952.

[Kuc76] G.C. Kuczynski, pp. 233 in Ceramic Microstructures'76. Edited by R.M. Fulrath and J.A. Pask. Westview Press, Boulder, Co, 1977.

[Kuc77] G.C. Kuczynski, Science of Sintering, 9 [3] 243 (1977).

[Kum84] M. Kumagai and G. L. Messing, J. Am. Ceram. Soc., 67 [11] C-230 (1984).

[Kum85] M. Kumagai and G. L. Messing, J. Am. Ceram. Soc., 68 [9] 500 (1985).

[Kur80a] S.K. Kurtz and F.M.A. Carpay, J. Appl. Phys., 51 [11] 5725 (1980).

[Kur80b] S.K. Kurtz and F.M.A. Carpay, J. Appl. Phys.,51 [11] 5745 (1980).

[Lac79] C. Lacour, Phys. Stat. Sol. (b) 96 785 (1979).

[Lan84a] F.F. Lange and B.I. Davis, pp. 714 in Science and Technology of Zirconia II. Edited by N. Claussen, M. Reuhle and A.H. Heuer, Am. Ceram. Soc., Columbus, OH, 1984.

[Lan84b] F.F. Lange, J. Am. Ceram. Soc., 67 [2] 83 (1984).

[Lan87] F.F. Lange and K.T. Miller, J. Am. Ceram. Soc., 70 [12] 896 (1987).

[Lau80] R.J. Lauf and H. Keating, pp. 196 in 38th Annual Proceeding of the Electron Microscopy Society of America. Edited by G.W. Bailey, Claitor's, Baton Rouge, LA, 1980.

[Lau81] R.J. Lauf and S.S. Rawlston, pp. 132 in 39th Annual Proceeding of the Electron Microscopy Society of America. Edited by G.W. Bailey, Claitor's, Baton Rouge, LA, 1981.

[Lin87] E. Liniger and R. Raj, J. Am. Ceram. Soc., 70 [11] 843 (1987).

[Liu80] C.C. Liu, Ph.D. Dissertation, University of California, Los Angeles, CA, 1980.

[Luk78] S.J. Lukasiewicz and J.S. Reed, Bull. Am. Ceram. Soc., 57 [9] 798 (1978).

[Lyk68] J. Lyklema, Adv. Colloid Interface Sci., 2 65 (1968).

[Mas80] Y. Masuda and R. Watanabe, pp. 3 in Sintering Processes. Edited by G.C. Kuczynski, Plenum Press, New York, 1980.

[McD38] T.G. McDougal, A.H. Fessler, and K. Schwartzwalder, U.S. Pat. 2,120,338 (1938).

[McD41] T.G. McDougal, A.H. Fessler, and H.B. Barlett, U.S. Pat. 2,232,860 (1941).

[McG61] R.K. McGeary, J. Am. Ceram. Soc., 44 [10] 513 (1961).

[Mes81] G.L. Messing and G.Y. Onoda, Jr., J. Am. Cera. Soc., 64 [8] 468 (1981).

[Mes86] G. L. Messing, M. Kumagai, R. A. Shelleman, and J. L. McArdle, pp. 259 in Science of Ceramic Chemical Processing. Edited by L. L. Hench and D. R. Ulrich. John Wiley and Sons, New York, 1986.

[Mis68] R.E. Mister and R.L. Coble, J. Am. Ceram. Soc., 39 [4] 237 (1968).

[Nic66] F.A. Nichols, J. Appl. Phys. 37 [13] 4599 (1966).

[Nic68] F.A. Nichols, J. Am. Ceram. Soc. 51 468 (1968).

[Nor71] L.D. Norman, E.E. Maust, Jr., and L.P. Sholnic, Computer Simulation of Particulate Systems, U.S.Bureau of Mines Bulletin, No. 658, 1971.

[Occ84] M.A. Occhionero and J.W. Halloran, pp. 89 in Sintering and Heterogeneous Catalysis. Edited by G.C. Kuczynski, A.E. Miller and G.A. Sargent. Plenum Press, New York, 1984.

[Occ86] M.A. Occhionero, Ph.D. Dissertation, Case Western Reserve University (1986).

[OHa69] M.J. O'Hara and I.B. Cutler, Proc. Brit. Ceram. Soc., 2 [12] 145 (1969).

[Ois60] Y. Oishi and W.D. Kingery, J. Chem. Phys., 33 480 (1960).

[Oka86] H. Okamura, E.A. Barringer, and H.K. Bowen, J. Am. Ceram. Soc., 69 [2] C-22 (1986)

[Ono77] G.Y. Onoda, Jr., pp. 163 in Ceramic Microstructures '76. Edited by R.M. Fulrath and J.A. Pask. Westview Press, Boulder, Co, 1977.

[Orr69] C. Orr, Jr., Powder Technol. 3 117 (1969).

[Ove52] J.Th.G. Overbeek, pp. 245 in Colloid Science, Edited by H.R. Kruyt, Elsevier, Amsterdam, 1952.

[Ove82] J.Th.G. Overbeek, Adv. Colloid Interface Sci., 16 17 (1982).

[Pae88] Y.-K. Paek, K.-Y. Eun, and S.-J. L. Kang, J. Am. Ceram. Soc., 71 [8] C-380 (1988).

[Pag88] R.A. Page, S. Spooher, W.B. Sanderson and D.L. Johnson, J. Am. Ceram. Soc., 71 [12] 1125 (1988).

[Pap70] Y. S. Papir and I. M. Krieger, J. Colloid Interface Sci., 34 [1] 126 (1970).

[Par73] G.D. Parfitt, Editor, Dispersion of Powders in Liquids, Applied Science Publishers, London, 1973.

[Pat83] B.R. Patterson and L.A. Benson, Progress in Powder Metallurgy, 39 215 (1983).

[Pat84] B.R. Patterson and J.A. Griffin, Modern Developments in Powder Metallurgy, 15 279 (1984).

[Pat86] B.R. Patterson, V.D. Parkhe and J.A. Griffin, pp. 43 in Sintering'85. Edited by G.C. Kuczynski, D.P. Uskokovic, H. Palmour III and M.M. Ristic. Plenum Press, New York, 1986.

[PDFa] Powder Diffraction File, Card No. 11-517, Joint Committee on Powder Diffraction Standards, Swarthmore, PA.

[PDFb] Powder Diffraction File, Card Nos. 10-173 and 11-661, Joint Committee on Powder Diffraction Standards, Swarthmore, PA.

[Phe78] G.W. Phelps and M.G. McLaren, pp. 211 in Ceramic Processing Before Firing. Edited by G.Y. Onoda, Jr. and L. L. Hench. John Wiley & Sons, New York, 1978.

[Pic85] D.G. Pickles and E. Lilley, J. Am. Ceram. Soc., 68 [9] C-222 (1985).

[Pop86a] E.J.A. Pope and J.D. Mackenzie, pp 809 in Better Ceramics Through Chemistry II. Edited by C.J. Brinker, D.E. Clark, and D.R. Ulrich, Mat. Res. Soc., Pittsburgh, PA. 1986.

[Pop86b] E.J.A. Pope and J.D. Mackenzie, pp 187 in Tailoring Multiphase and Composite Ceramics. Edited by R.E. Tressler, G. L. Messing, C.G. Pantano, and R.G. Newnham, Plenum Press, New York, 1986.

[Pos60] A.R. Poster, C.T. Waldo, and H.H. Hausner, Progress in Powder Metallurgy, 16 56 (1960).

[Rah87] M.N. Rahaman and L.C. De Jonghe, J. Am. Ceram. Soc., 70 [12] C-348 (1987).

[Raj73] W. Rajarao and I.B. Cutler, J. Am. Ceram. Soc., 56 [11], 588 (1973).

[Raj84] R. Raj and R.K. Bordia, Acta Metall., 32 [7] 1003 (1984).

[Ree73] R.E. Reed-Hill, Physical Metallurgy Principles, pp. 304, Second Edition, D. Van Nostrand Co., N.J., 1973.

[Ree76] J.S. Reed and R.B. Runk, pp. 71 in Ceramic Fabrication Process. Edited by F.F.Y. Wang, Academic Press, New York, 1976.

[Ree86] J.S. Reed, Introduction to the Principles of Ceramic Processing, pp. 243, John Wiley & Sons, New York, 1986.

[Rei31] R. Reichman, U.S. Pat. 1,799,225 (1931).

[Rhi62] F.N. Rhines, R.T. DeHoff, and R.A. Rummel, pp. 351 in Agglomeration. Edited by W.A. Knepper, Interscience Publishers, N.Y. 1962.

[Rhi69] F.N. Rhines, R.T. DeHoff, and J. Kronsbein, Final Report, A.E.C. Contract NO. AT-(40-1)-2581, 1969.

[Rho81] W.H. Rhodes, J. Am. Ceram. Soc., 64 [1] 19 (1981).

[Rod89] J. Rodel and A.M. Glaeser, to be published in the Proceedings of the Symposium on Sintering of Advanced Ceramics, American Ceramic Society.

[Roo67] H.M. Rootare and C.F. Prenzlow, J. Phys. Chem. 71 2734 (1967).

[Roo88] A. Roosen and H. K. Bowen, J. Am. Ceram. Soc., 71 [11] 970 (1988).

[Ros73] G. Rossi, J.E. Burke, J. Am. Ceram. Soc. 56 654 (1973).

[Ros75] J.H. Rosolowski and C. Greskovich, J. Am. Ceram. Soc., 58 [5-6] 177 (1975).

[Sac82] M.D. Sacks and J.A. Pask, J. Am. Ceram. Soc., 65 [2] 70 (1982).

[Sac84] M.D. Sacks and T.-Y. Tseng, J. Am. Ceram. Soc., 67 [8] 532 (1984).

[Sac85] M.D. Sacks and G.W. Scheiffele, Ceram. Eng. Sci. Proc., 6 [7-8] 1109 (1985).

[Sac86] M. D. Sacks, pp. 522 in Science of Ceramic Chemical Processing. Edited by L. L. Hench and D. R. Ulrich. Wiley, New York, 1986.

[Sac87] M. D. Sacks, C. S. Khadilkar, G. W. Scheiffele, A. V. Shenoy, J. H. Dow, and R. S. Sheu, pp. 495 in Ceramic Powder Science, Advances in Ceramics, Vol. 21. Edited by G. L. Messing, K. S. Mazdiyasni, J. W. McCauley, and R. A. Haber. The American Ceramic Society, Westerville, OH, 1987.

[Sac88a] M.D. Sacks, H.W. Lee, and O.E. Rojas, pp. 440 in Ceramic Powder Science II. Edited by G.L. Messing, E.R. Fuller, Jr. and H. Hausner. Am. Ceram. Soc., Westerville, OH, 1988.

[Sac88b] M. D. Sacks, H. W. Lee, and O. E. Rojas, J. Am. Ceram. Soc., 71 [5] 370 (1988).

[Sal67] S.A. Saltykov, pp. 163 in Stereology. Edited by H. Elias, Springer, New York, 1967.

[Sat84] T. Sato and R. Ruch, Stabilization of Colloidal Dispersions by Polymer Adsorption, Marcel Dekker, New York, 1984.

[Sch86] D. W. Schaefer and K. D. Keefer, pp. 277 in Better Ceramics Through Chemistry, II, Materials Research Society Symposia Proceedings, Volume 73. Edited by C. J. Brinker, D. E. Clark, and D. R. Ulrich. North-Holland, New York, 1986.

[Sco60] G.D. Scott, Nature, 188 [4754] 908 (1960).

[Sha86] N.J. Shaw and R.J. Brook, J. Am Ceram. Soc., 69 [2] 107 (1986).

[Smi23] R. Smith, J. Chem. Soc., 123 2088 (1923).

[Smi84] J.P. Smith and G.L. Messing, J. Am. Ceram. Soc. 67 [4] 238 (1984).

[Smo54] W.J. Smothers and H.J Reynolds, J. Am. Ceram. Soc., 37 [12] 588 (1954).

[Son84] H. Song R.L. Coble, and R.J. Brook, pp 63 in SIntering and Heterogeneous Catalysis. Edited by G.C. Kuczynski, A.E. Miller, and G.A. Sargent, Plenum Press, New York, 1984.

[Spu69] A.R. Spurr, J. Ultrastruct. Res., 26 31 (1969).

[Sro83] D.J. Srolovitz, M.P. Anderson, G.S. Grest, and P.S. Sahni, Scripta Metall., 17 [2] 241 (1983).

[Sro84a] D.J. Srolovitz, M.P. Anderson, P.S. Sahni, and G.S. Grest, Acta Metall., 32 [5] 793 (1984).

[Sro84b] D.J. Srolovitz, M.P. Anderson, G.S. Grest, and P.S. Sahni, Acta Metall., 32 [9] 1429 (1984).

[Sro85] D.J. Srolovitz, G.S. Grest, and M.P. Anderson, Acta Metall., 33 [12] 2233 (1985).

[Sto68] J. Stone-Masui and A. Watillon, J. Colloid Interface Sci., 28 [2] 187 (1968).

[Tad80] Th. T. Tadros, Adv. Colloid Interface Sci., 12 141 (1980).

[Tay74] R.I. Taylor, J.P. Coad, R.J. Brook, J. Am. Ceram. Soc., 57 539 (1974).

[Tuo72] W.D. Tuohig, Ph.D. Dissertation, University of Florida (1972).

[Und70] E.E. Underwood, Quantitative Stereology, Addison-Wesley Publishing, Reading, MA, 1970.

[Var83] J.A. Varela and O. J. Whittemore, J. Am. Ceram. Soc., 66 [1] 77 (1983).

[Ven89] K.S. Venkataraman and R.A. Dimilia, J. Am. Ceram. Soc., 727 [1] 33 (1989).

[Ver48] E.J. Verwey and J.Th.G. Overbeek, Theory of the stability of Lyophobic Colloids, Elsevier, Amsterdam, 1948.

[Vis72] J. Visser, Adv. Colloid Interface Sci., 3 331 (1972).

[Vor84] S.D. Vora, Master's Thesis, University of Florida (1984).

[Wan76] D.N.K. Wang, Ph.D. Dissertation, University of California, Berkeley, 1976.

[War62] S.I. Warsaw and F.H. Norton, J. Am. Ceram. Soc., 45 [10] 479 (1962).

[War67] M.O. Warman, D.W. Budworth, Trans. Br. Ceram. Soc., 66 253 (1967).

[Wat83] A.S. Watwe, Doctoral Dissertation, University of Florida (1983).

[Wei85] D. A. Weitz, J. S. Huang, M. Y. Lin, and J. Sung, Phys. Rev. Lett., 54 [13] 1416 (1985).

[Wei86] M.W. Weiser and L.C. De Jonghe, J. Am. Ceram. Soc., 69 [11] 822 (1986).

[Wes30] A.E.R. Westman and H.R. Hugill, J. Am. Ceram. Soc., 13 [10] 767 (1930).

[Whi74] O.J. Whittemore and J.J. Sipe, Powder Tech., 9 155 (1974).

[Whi78] O.J. Whittemore, Materials Science Research, 11 125 (1978).

[Whi80] O.J. Whittemore and J.A. Varela, pp. 51 in Sintering Processes. Edited by G.C. Kuczynski. Plenum, New York, 1980.

[Wie66] P.H. Wiersema, A.L. Loeb, and J.Th.G. Overbeek, J. Colloid Interface Sci., 22 78 (1966).

[Woo70] M. E. Woods and I. M. Krieger, J. Colloid Interface Sci., 34 [1] 91 (1970).

[Woo72] J.L. Woolfrey, J. Am. Ceram. Soc., 55 [8] 383 (1972).

[Wu84] S.Wu, E. Gilbart, and R.J. Brook, pp. 574 in Structure and Properties of MgO and Al_2O_3 Ceramics. Edited by W.D. Kingery. The Am. Ceram. Soc., Columbus, OH, 1984.

[Yan77] M.F. Yan, R.M. Cannon,and H.K. Bowen, pp. 276 in Ceramic Microstructures. Edited by R.M. Fulrath and J.A. Pask. Westview Press, Boulder, CO, 1977.

[Yan81] M.F. Yan, Mater. Sci. Eng. 48 53 (1981).

[Yan83] M.F. Yan, R.M. Cannon, H.K. Bowen, and U. Chowdhry, Mater. Sci. Eng., 60 275 (1983).

[Yeh85] T.-S. Yeh and S.D. Vora, unpublished work.

[Yeh88a] T.-S. Yeh and M.D. Sacks, J. Am. Ceram. Soc., 71 [10] 841 (1988).

[Yeh88b] T.-S. Yeh and M.D. Sacks, J. Am. Ceram. Soc., 71 [12] C-484 (1988).

[You82] R.A. Youshaw and J.W. Halloran, Bull. Am. Ceram. Soc., 61 [2] 227 (1982).

[Zha87] J. Zhao and M.P. Harmer, J. Am. Ceram. Soc., 70 [12] 860 (1987)

[Zha88] J. Zhao and M.P. Harmer, J. Am. Ceram. Soc., 71 [7] 530 (1988)

[Zhe89] J. Zheng and J.S. Reed, J. Am. Ceram. Soc., 72 [5] 810 (1989).

BIOGRAPHICAL SKETCH

Tsung-Shou Yeh was born in Taiwan, Republic of China, on March 12, 1956. In 1978, he received the Bachelor of Science in Materials Science and Engineering from National Tsing-Hua University in Hsin-Chu, Taiwan, R.O.C. After a two-year tour of duty in the Army, he joined China Steel Corporation, Kao-Hsiung, Taiwan, as a metallurgical engineer. In August, 1983, he enrolled in the Department of Materials Science and Engineering of the University of Florida and received the Master of Science in 1986. Upon completion of this study, he will return to his country and serve as a research scientist in the Materials Research Laboratories of the Industrial Technology Research Institute, Hsin-Chu.

I certify that I have read this study and that in my opinion it conforms to acceptable standards of scholarly presentation and is fully adequate, in scope and quality, as a dissertation for the degree of Doctor of Philosophy.

Michael D. Sacks

Dr. Michael D. Sacks, Chairman
Associate Professor of Materials
Science and Engineering

I certify that I have read this study and that in my opinion it conforms to acceptable standards of scholarly presentation and is fully adequate, in scope and quality, as a dissertation for the degree of Doctor of Philosophy.

Robert T. DeHoff

Dr. Robert T. DeHoff
Professor of Materials Science and
Engineering

I certify that I have read this study and that in my opinion it conforms to acceptable standards of scholarly presentation and is fully adequate, in scope and quality, as a dissertation for the degree of Doctor of Philosophy.

D. O. Shah

Dr. Dinesh O. Shah
Professor of Chemical Engineering

I certify that I have read this study and that in my opinion it conforms to acceptable standards of scholarly presentation and is fully adequate, in scope and quality, as a dissertation for the degree of Doctor of Philosophy.

Joseph H. Simmons

Dr. Joseph H. Simmons
Professor of Materials Science and Engineering

I certify that I have read this study and that in my opinion it conforms to acceptable standards of scholarly presentation and is fully adequate, in scope and quality, as a dissertation for the degree of Doctor of Philosophy.

E. Dow Whitney

Dr. E. Dow Whitney
Professor of Materials Science and Engineering

This dissertation was submitted to the Graduate Faculty of the College of Engineering and to the Graduate School and was accepted as partial fulfillment of the requirements for the degree of Doctor of Philosophy.

December, 1989

Winfred M. Phillips
Dean, College of Engineering

Madelyn M. Lockhart
Dean, Graduate School